SEARCH FOR SUSY THROUGH VECTOR BOSON FUSION PROCESSES IN CMS DETECTOR AT LHC

A THESIS

Submitted to the
FACULTY OF SCIENCE
PANJAB UNIVERSITY, CHANDIGARH
for the degree of

DOCTOR OF PHILOSOPHY

2019

PRIYANKA KUMARI

DEPARTMENT OF PHYSICS
CENTRE OF ADVANCED STUDY IN PHYSICS
PANJAB UNIVERSITY
CHANDIGARH, INDIA

Dedicated to

My Grand-Parents

and
Parents

Acknowledgements

To begin with, my greatest honor to the creator, “Sai”, for providing me the strength to keep going through the most difficult time of my life. I owe my very existence to you. May your name be exalted, honored and glorified.

First and foremost, my sincere gratitude to my Supervisor Prof. J.B. Singh for giving me never-ending support in each possible way during this wonderful journey of Ph.D. His valuable guidance, patience, suggestions helped me a lot to keep going towards this thesis completion. He is such a humble soul that I feel proud to be called as his student.

I am equally indebted to my Supervisor, Prof. Vipin Bhatnagar for his precious guidance, support and friendly nature. His abundance of knowledge in technology has motivated me to try and learn some new techniques. I would like to thank Prof. Manjit Kaur, Prof. Suman Beri, and Dr. Sushil Singh Chauhan for their continuous support and efforts.

A special thanks goes to Dr. Nitish Dhingra for guiding me throughout my Ph.D. I am indebted to you for all sorts of support. A big thanks to Dr. Sunil Bansal for your lively behaviour, and always giving the motivation to do more and more. I appreciate all the efforts of the Engineers and CMS office staff to take care of all our needs. Many thanks to INDIA-CMS Collaboration for conducting the regular meeting to discuss our work and for giving valuable suggestions.

I am sincerely thankful to Prof. Navdeep Goyal, Chairperson, Department of Physics, Panjab University for providing enough facilities to work in the department. Many thanks to former Chairmen, Prof. Devinder Mehta for having friendly behaviour and encouraging us in all situation. I would like to acknowledge Dr. Vimal Roy for always helping me in each possible way.

This research would definitely not have been possible without the financial support of Department of Science and Technology (DST). I am very thankful to DST-INSPIRE for their continuous support and confidence in me. I am extremely thankful *to the technical, library, purchase section staff at PU who contributed directly or indirectly throughout this research work and of course Harry Bhaiya's "Tea".*

I got an opportunity to work with Dr. Gabriella Pugliese for my RPC service work during the Global DOC project at University of Bari, Italy. The way she works, her professionalism is a huge motivation for me. Along with being a mentor, she is also my good friend. A vote of thanks to all my scientific collaborators and especially VBF SUSY team with whom I had the chance to work with and learn so much from their expertise. I am highly thankful to Prof. Teruki kamon, Dr. Andres Florez for helping me a lot in refining my understanding about the physics beyond SM.

Special thanks to my mentor, Dr. Alfredo Gurrola for helping me throughout the VBF SUSY analysis. I feel pleased to work with such a great physicist like you Alfredo. I learnt a lot about the physics analysis and the way you patiently handle all the situation.

I am obliged to thank Dr. Archana Sharma and Prof. Teruki Kamon for introducing me to CMS GEM community. I would like to thank Dr. Naimuddin and Dr. Ashok Kumar, for allowing us to learn and work in GEM lab at University of Delhi. Thank you Dr. Ashok for creating the cheerful environment wherever you go.

This research work has been carried out based on the CMS experiment at the CERN LHC and PUHEP lab. I would like to thank the whole CMS collaboration, the scientists, as well as technical and the administrative staff, at the LHC accelerator complex and the CMS experiment.

I would like to thank all my seniors and my fellow colleagues for making a joyful environment in the PU-EHEP lab. Special thanks to Dr. Ramandeep Garg, Dr. Amandeep Kalsi, Dr. Ankita Mehta and Dr. Genius Walia for helping me a lot during my initial journey of Ph.D.

I am grateful to Rajat, Rathijit, Aashaq Hussain, Meena, Amandeep, Mr. Shiv and Dr.Pallabi for making my CERN visits a memorable piece of my life. Thanks a lot to Sandeep Gill for helping me in writing this Thesis. I am heartily grateful to all my friends from different regions of the world: Aruna, Ashish patyal, Akshay Patyal, *Anjali, Baljeet, Dr.Andres Leonardo, Dr.Harpreet, Dr.Amardeep, Diksha and kamal jiju, Hyki, Kavita, Manu, Neha, Nandu, Richa, Rajat Dogra, Rajit Rana, Reham, Samiksha, Sudesh, Sukhpreet Singh, Shashank, Shahid Wani, Tsvetlina, Varun, and Walaa for always cheering me up.*

I am happy to acknowledge my Dear friend Zubair Ahmad Dar for his continuous support during my ups and downs. Special thanks to my buddy Andrea Gelmi for being the best colleague ever. I admire the way you work, the energy you put while working. Thanks for listening to all my stories and tolerating me.

I am really at a loss of words to express thanks to my sister Shailza Pathania for her endless support and taking responsibility of me. You are and you will be the only Best Friend of my heart. As they say, its a secret do not tell to anyone, I never count you.

I could have never reached this stage without the blessing of my father, Late Sh. Vipan Pathania. I owe my entire life to you, Daddy and of course this thesis. You are up in heaven now, but I know you are constantly looking and blessing me at every step of my life. My heartfelt gratitude to my mother, Smt. Ranjana Pathania for the efforts she made for shaping me what I am today. My twin brother and sister, Gaurav Pathania and Megha Pathania deserve a sweet and heartfelt thanks for bringing a big smile on my face in my tough times. I would also like to thank my grandparents for their unconditional love and support until the time they were with me. Keep guiding me wherever you are now. I would like to thank my Nani for always showering the abundance of love and the concern toward my work without knowing it. I gratefully remember the blessings and love of all my relatives and cousin's for life and career. I am obliged to my school teachers, Dr. Ram Murti Sharma and Sh. Ashwani Kumar for encouraging me to pursue my carrier in physics. I am here, today at PU is because of one person, my Mama Ji, Sh. Suresh Thakur, thank you and Mami Ji for always supporting me.

Last but not the least Thank you "Google" for making life easier.

Date: **(Priyanka Kumari)**

Abstract

The Standard Model (SM) of particle physics is the most successful theory to date as it holds every single quantum observation in a single framework. Despite being successful, it fails to explain many mysteries like the unification of forces, absence of dark matter and dark energy and hierarchy problem, etc. There are many theories beyond the Standard Model (BSM) that explain very well about these fundamental problems. Supersymmetry (SUSY) is one such theory that answers these questions. However, for all of its attractive features, there is as yet no experimental evidence. So to verify experimentally, and to explore New Physics, the world's most powerful accelerator Large Hadron Collider (LHC) is built at CERN. Experimental observation of Higgs boson has been given by CERN two general-purpose experiments namely Compact Muon Solenoid (CMS) and A Toroidal LHC ApparatuS (ATLAS) at Large Hadron Collider (LHC) in July 2012.

Minimal Supersymmetric Standard Model (MSSM) conserving R-parity leads to the outcome that Lightest Supersymmetric Particle (LSP) is the dark matter candidate and is stable. In this Thesis, the search for SUSY particles (chargino and neutralino) is being presented through the Vector Boson Fusion (VBF) processes in the single hadronic tau (τ_h) final state along with two forward jets and missing energy due to LSP and neutrinos. The proton-proton collision dataset used for the present analysis corresponds to the integrated luminosity of 35.87 fb^{-1} at a center-of-mass energy of 13 TeV collected by the CMS detector at the LHC. The signal process involves the pair production of charginos ($\tilde{\chi}_1^{\pm}$) and neutralinos ($\tilde{\chi}_2^0$) by the fusion of vector bosons radiated by two incoming partons. Then chargino and neutralino decay to staus ($\tilde{\tau}$) that further decays to LSP ($\tilde{\chi}_1^0$) and tau lepton which will finally decay to hadronic tau (τ_h). The LSP is *bino* like and chargino/neutralino are *wino* like SUSY particles. Many SM background contains hadronic taus, jets and E_{T}^{miss} which can easily fake our signal. Some of the major backgrounds like QCD multi-

jet, W+jets and $t\bar{t}$ are estimated using data-driven and semi-data driven techniques respectively. The $m_T(\tau, E_{\mathrm{T}}^{miss})$ (m_{jj}) variable is used to distinguish the signal from the background in 1-lepton+jj (0-lepton+jj) channel. Unfortunately, we have not observed excess of data over SM background predictions in this analysis.

The results obtained from single hadronic tau final state is combined with the results from the other three channels: single muon, single electron, and 0-lepton channels that are analyzed by other group members. Hence, by using a combined likelihood technique in the bins of m_T (m_{jj}) in 1-lepton+jj (0-lepton+jj), an upper limit at 95% confidence level (CL) is set on the production cross section of charginos and neutralinos. Charginos and neutralinos are considered as mass degenerate as they belong to the same Gauge group. Two scenarios are considered: 1) "slepton" model i.e. decay of $\tilde{\chi}_1^{\pm}/\tilde{\chi}_2^0$ through slepton 2) "WZ" model i.e. decay through W* and Z*. The difference in both the models is because of the branching ratio of $\tilde{\chi}_1^{\pm}/\tilde{\chi}_2^0$ into leptonic final states. In the slepton model, for compressed mass scenarios where the mass difference between chargino/neutralino and LSP is less i.e. Δm =1 (30) GeV, exclusion limits of 112 (215) GeV are set on the masses of charginos and neutralinos, whereas in WZ model, for same mass gap i.e. 1 (30) GeV, an upper limit of 112 (175) is obtained. The present analysis obtains the most stringent limit to date on the production of charginos and neutralinos decaying to leptons in compressed mass spectrum scenarios defined by the mass separation $1 < \Delta m < 5$GeV and $25 < \Delta m < 50$ GeV.

On the hardware part, the aging study of resistive plate chamber (RPC) detectors have been performed which are already installed at the CMS muon system. During the high Luminosity (HL-LHC) phase, the luminosity will increase, so to study present RPC detectors' survival, the chambers are placed under continuous radiation in Gamma Irradiation Facility (GIF++) at CERN in same background condition as would be available in HL-LHC. After monitoring the detector parameters and detector performance study, we have not observed any evidence of aging.

Contents

List of Figures

List of Tables

Chapter 1

Introduction to Standard Model

We, humans always wonder about the sole existence of ourselves and the physical world around us. Since ages, we are driven to explore the unknown, to find out the answers about our origin how Universe came into the picture, what happened at the time of Big Bang and what the world is made up of? These fascinations and curiosity have brought out the field of particle physics. Particle physics is a journey to explore the mysteries of the Universe at the level which is unmatched by any other field. It helps us to understand the constituents of matter and what binds them together. It is also named as “High Energy Physics” because to observe new physics, it demands tiny particles to interact at tremendously high energies. To answer the aforementioned questions, a model with theoretical and experimental knowledge emerged in 1970, famously known as “Standard Model” (SM) [1–4]. Entire particle physics essentially revolves around the SM and its various possible extensions, mainly investigating the postulates and assumptions encapsulated by them. This Chapter provides the complete description of the SM, the fundamental interaction and its shortcomings.

1.1 Evolution of Particle Physics

The antique believes that the building block of the Universe were millions of minuscule particles that cannot be further subdivided, and are called atoms, or “atomos” by Greeks which means “indivisible”. The curiosity to know more about the smallest particle led to the discovery of first elementary particle “electron” by J. J. Thomson in 1897 [5] when he witnessed the bending of cathode rays in the presence of a magnetic field. This was followed by another milestone discovery of the small, dense positively charged atomic nucleus in an atom by Ernest Rutherford in 1911 [6, 7] when he found the scattering of alpha particles from a thin gold foil. Later on, he proposed that the atoms consist of a small positively charged nucleus at the center and electrons revolve around it. The subsequent discoveries of the proton by Rutherford in 1919 and neutron by J. Chadwick in 1932 [8] completed the atomic picture and these particles (proton, electron, and neutron) are considered as the fundamental ingredients of the nucleus.

In 1964, Gell-Mann and Zweig postulated the “Quark Model” which says that all the baryons and mesons consist of even more fundamental particles called “quarks”. According to this model, each baryon consists of three quarks and each meson is made up of quark-antiquark ($q\bar{q}$) pair. First-ever evidence of proton consisting of three quarks was observed with the Deep Inelastic Scattering experiment by SLAC and CERN in 1967 [9]. The existence of three quarks in baryon (up “u”, down “d” and strange “s”) at that time violated Pauli exclusion principle, hence the concept of “color” degree of freedom (red, green and blue) came into the picture to amend this principle. Thus, colorless quark combination forms hadrons and all observed particles are colorless. In late 1970s, Electroweak theory and Higgs mechanism predicting $W^{\pm}$, Z^0 and Higgs boson respectively came into picture, but the experimental evidence for $W^{\pm}$, Z^0 bosons is given by UA1 and UA2 Collaboration in 1983 at CERN.

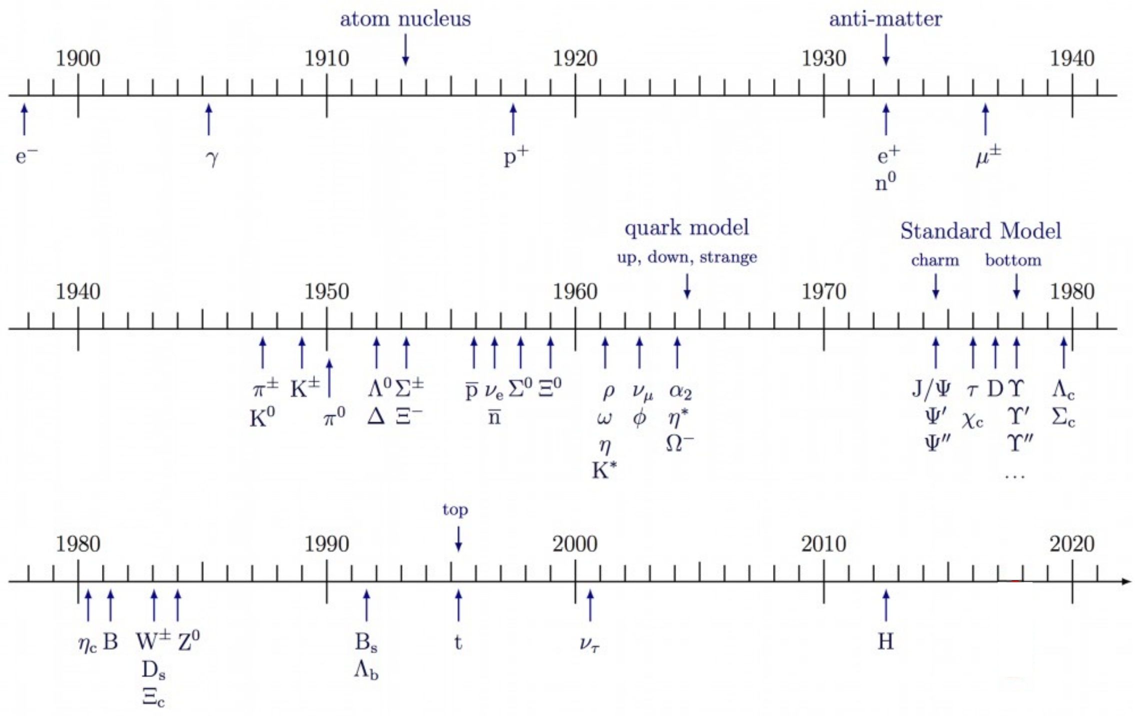

Figure 1.1: Spectra of particle discoveries.

However, the Higgs boson discovery took several decade and also lead to development of Large Hadron Collider (LHC) [10]. The last and much-awaited particle of SM "Higgs Boson" or God particle with a mass of 125 GeV/c^2 was discovered in July, 2012 by the LHC experiment which completes the picture of all fundamental particles. At present, all the particles hypothesized by SM have been found as shown in Figure 1.1 along with their time evolution as depicted in Figure 1.2 and are well within the predictions.

1.2 The Standard Model

The Standard Model (SM) is the most successful theory given in the 1970s which provides a detailed description of the fundamental particles and their interactions. It has successfully explained the organization of all matter forms with great precision except the one related to gravity. The SM possesses Lagrangian densities that

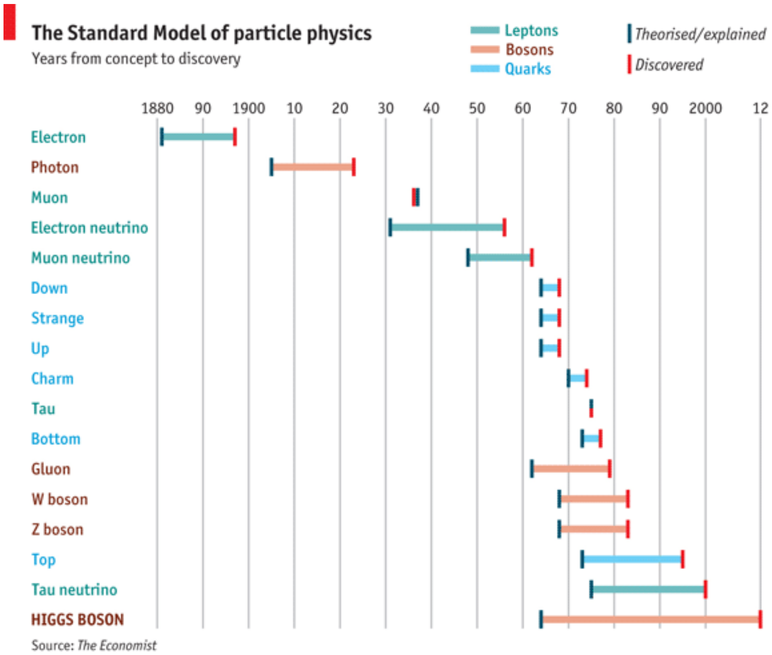

Figure 1.2: Time evolution of Standard Model particles [11].

are invariant under a certain transformation and also called as a gauge-invariant quantum field theory (QFT). The gauge symmetry groups that describe the transformation of particle states in SM are given as SU$(3)_C\otimes$ SU$(2)_L\otimes$ U$(1)_Y$, where C refers to color charge, L stands for weak isospin and Y is for hypercharge. As stated above, SM doesn't provide any description of Gravitational force due to lack of explainable quantum theory and its mediator "Graviton" having spin 2 and mass zero. The next section includes the detailed information of its fundamental particles and their interactions.

1.2.1 Elementary Particles

SM consists of elementary particles and field forces. The basic building blocks of the visible matter are elementary particles known as "Fermions" and categorized in three-generations of leptons (particles not interacting via strong interaction) and three generations of quarks (particles interacting mostly via strong interaction). Fermions follow Fermi-Dirac rule and have 1/2 integral spin. Corresponding to each fermion there exists an anti-fermion having same mass and spin but opposite charge.

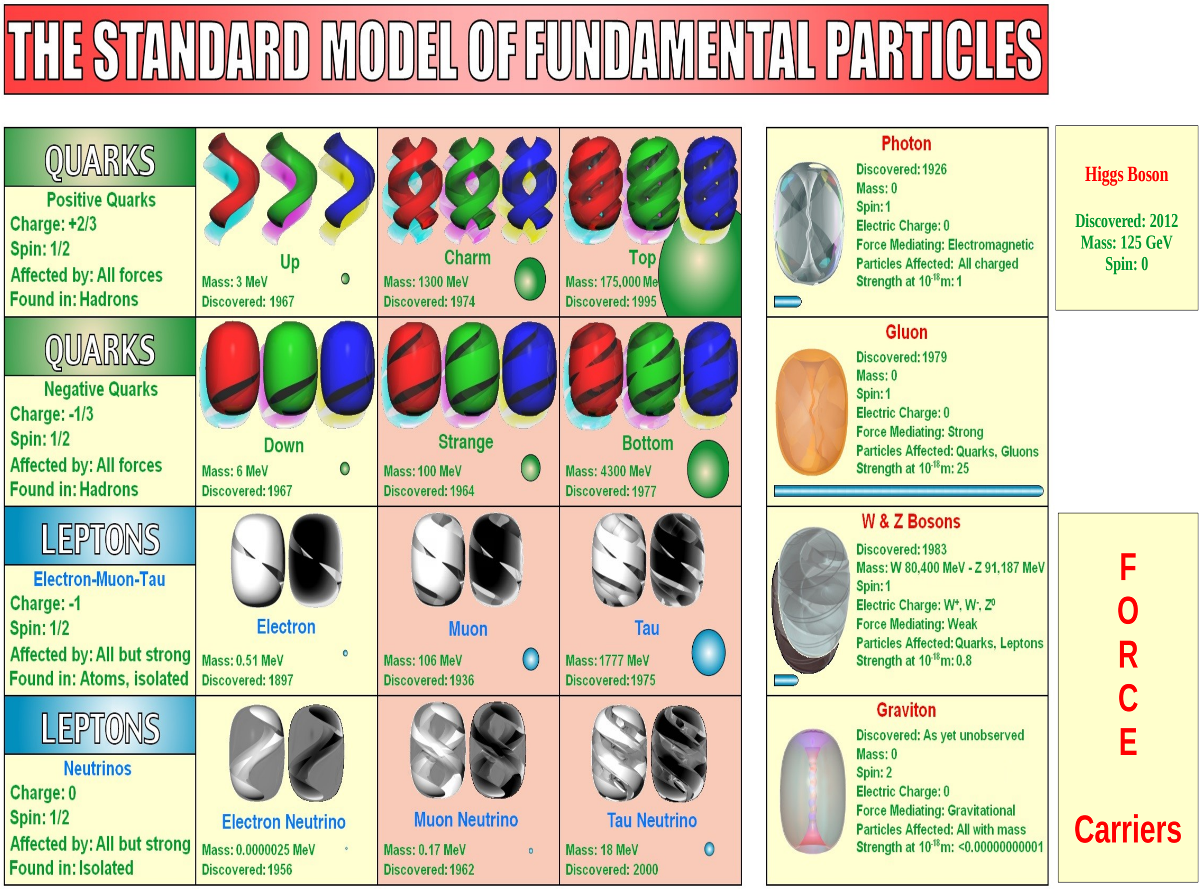

THE STANDARD MODEL OF FUNDAMENTAL PARTICLES

QUARKS Positive Quarks Charge: +2/3 Spin: 1/2 Affected by: All forces Found in: Hadrons	Up Mass: 3 MeV Discovered: 1967	Charm Mass: 1300 MeV Discovered: 1974	Top Mass: 175,000 Me Discovered: 1995
QUARKS Negative Quarks Charge: -1/3 Spin: 1/2 Affected by: All forces Found in: Hadrons	Down Mass: 6 MeV Discovered: 1967	Strange Mass: 100 MeV Discovered: 1964	Bottom Mass: 4300 MeV Discovered: 1977
LEPTONS Electron-Muon-Tau Charge: -1 Spin: 1/2 Affected by: All but strong Found in: Atoms, isolated	Electron Mass: 0.51 MeV Discovered: 1897	Muon Mass: 106 MeV Discovered: 1936	Tau Mass: 1777 MeV Discovered: 1975
LEPTONS Neutrinos Charge: 0 Spin: 1/2 Affected by: All but strong Found in: Isolated	Electron Neutrino Mass: 0.0000025 MeV Discovered: 1956	Muon Neutrino Mass: 0.17 MeV Discovered: 1962	Tau Neutrino Mass: 18 MeV Discovered: 2000

Photon
Discovered: 1926
Mass: 0
Spin: 1
Electric Charge: 0
Force Mediating: Electromagnetic
Particles Affected: All charged
Strength at 10^{-18}m: 1

Gluon
Discovered: 1979
Mass: 0
Spin: 1
Electric Charge: 0
Force Mediating: Strong
Particles Affected: Quarks, Gluons
Strength at 10^{-18}m: 25

W & Z Bosons
Discovered: 1983
Mass: W 80,400 MeV - Z 91,187 MeV
Spin: 1
Electric Charge: W^+, W^-, Z^0
Force Mediating: Weak
Particles Affected: Quarks, Leptons
Strength at 10^{-18}m: 0.8

Graviton
Discovered: As yet unobserved
Mass: 0
Spin: 2
Electric Charge: 0
Force Mediating: Gravitational
Particles Affected: All with mass
Strength at 10^{-18}m: <0.0000000001

Higgs Boson
Discovered: 2012
Mass: 125 GeV
Spin: 0

FORCE Carriers

Figure 1.3: Standard Model particles.

- **First Generation Quarks and Leptons:** The first generation fermions which count "up" (u), "down" (d) quarks and "electron" (e), "electron-neutrino" (ν_e) leptons form most of the visible matter in the Universe. Free stable quarks cannot be observed directly and are confined in bound states (Quark confinement description is given in Section 1.3).

- **Second Generation Quarks and Leptons:** This generation consists of fermions with the same quantum state but with a mass higher than the first generation. The second generation includes "charm" (c), "strange" (s) quarks and "muon"(μ), "muon-neutrino" (ν_μ) leptons.

- **Third Generation Quarks and Leptons:** The third generation fermions have high masses than previous ones. It consists of "top" (t), "bottom" (b) quarks and "tau" (τ), "tau-neutrino" (ν_τ) leptons. Except for neutrinos, the second and third generation fermions are mostly unstable and decay via weak interactions to lower generations due to their short lifetime and can only be studied with accelerators. Earlier, neutrinos were considered to be massless, as predicted by SM, but a recent discovery of neutrino oscillations [12] indicates the existence of their tiny (but non-zero) mass of neutrons.

Quarks are the constituents of protons and neutrons (known as hadrons) and exist in three color degrees of freedom named as "Red", "Blue" and "Green", similarly for anti-quarks with their anti-colors. Combination of three quarks give rise to particles known as "Baryons" and quark-antiquark ($q\bar{q}$) combination generates particles known as "Mesons". Unlike the quarks, leptons do not have color charge, and hence do not interact via the strong force. The interactions between these elementary particles occur by mediator particles. In SM, there are 12 mediators having integral spin and obey the Bose-Einstein statistics and hence known as "Bosons". The most important scalar boson discovered recently is the "Higgs boson" having spin 0 and it provides mass to all other SM particles except for neutrinos. Figure 1.3 represents all the fundamental particles of the SM and Table 1.1 contains the properties of fermions such as charge, mass, color, spin, etc.

1.2.2 Fundamental Forces of Nature

Till today, nature experiences only four kinds of forces through which all the matter in the Universe interacts, namely: Strong, Electromagnetic, Weak and Gravitational force. The SM explains only three types of forces i.e Strong, Electroweak and Weak. Gravitational force is described by the special theory of relativity. We experience

Generation	Flavour	Mass(MeV)	Charge	Spin	Color
Quarks					
I	u	2.2	+2/3	1/2	(R,B,G)
	d	4.7	-1/3		
II	c	1.27×10^3	+2/3	1/2	(R,B,G)
	s	96	-1/3		
III	t	173.21×10^3	+2/3	1/2	(R,B,G)
	b	4.18×10^3	-1/3		
Leptons					
I	e	0.51	-1	1/2	No Color
	ν_e	$< 2.2 \times 10^{-6}$	0		
II	μ	105.66	-1	1/2	No Color
	ν_μ	< 0.17	0		
III	τ	1.78×10^3	-1	1/2	No Color
	ν_τ	15.5	0		

Table 1.1: Properties of Quarks and Leptons.

electroweak and gravitational forces in daily life but weak and strong interactions are only at the sub-nuclear level. Figure 1.4 depicts how different particles interacts via different forces. A detailed description of these forces is given below:

- **Strong Interaction:** Strong interaction refers to the binding of quarks inside protons and neutrons. This is the strongest force among all as it holds the protons inside the nucleus irrespective of the repulsive electromagnetic force. The strong force is described by Quantum ChromoDynamics (QCD) theory with the quanta of the strong field known as “Gluon”. Gluons and quarks are the only particles that interact by color charge and also known as “Partons”.

- **Electromagnetic Interaction:** As the name refers, it exists between all the particles having an electromagnetic charge and this force is responsible to keep electrons revolving around the nucleus inside the atom. It is a long-range force of repulsive nature between two same charged particles and is described by Quantum ElectroDynamics (QED). This force is carried out by the exchange of massless and chargeless particle, known as a “Photon”.

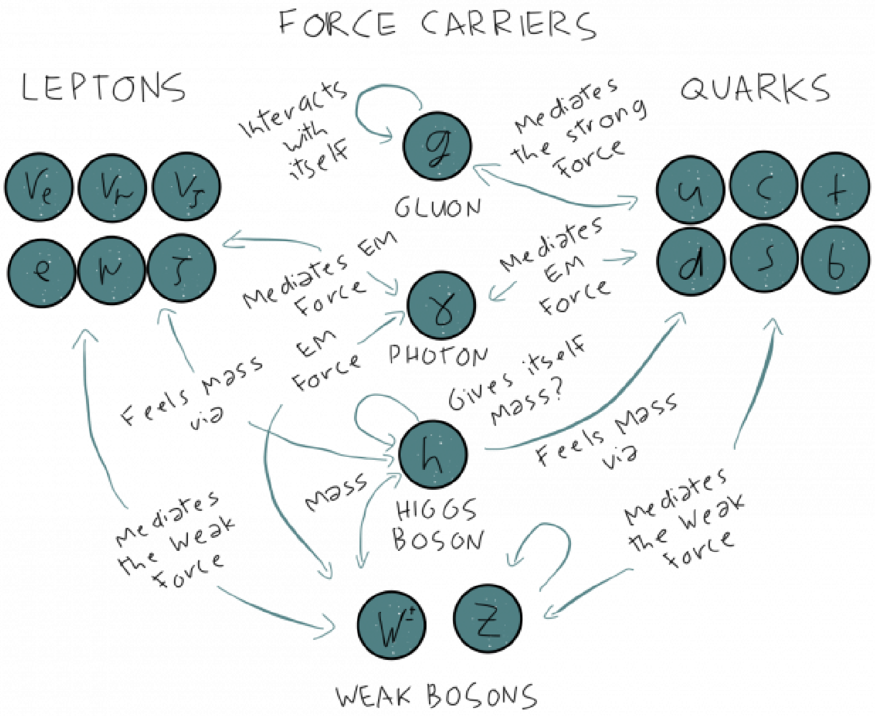

Figure 1.4: Different interactions among SM particles [13].

- **Weak Interaction:** The weak interactions are mediated by heavy vector bosons namely $W^{\pm}$ and Z^0. This is a short-range force and responsible for the radioactive decay of unstable nuclei and interaction between neutrinos and leptons with the matter. This is described by the Electroweak theory.

- **Gravitational Interaction:** This is a long-range force and is responsible to hold the planets inside the solar system and is of long-range. Although at the atomic scale, gravitational force is weakest among all the forces but attractive in nature and is the reason for the attraction of the objects towards the earth and other galaxy systems. This force is deemed to be mediated by “Gravitons” that are not yet experimentally discovered.

Table 1.2 shows the properties of four fundamental forces [14].

Interaction	**Theory**	**Mediators**	**Charge**	**Mass ($\mathbf{GeV/c^2}$)**	**Range (m)**	**Coupling Constant (α)**
Strong	QCD	8 Gluons (g)	0	0	10^{-15}	1
Electromagnetic	QED	Photon (γ)	0	0	∞	$\frac{1}{137}$
Weak	Flavourdynamics	$W^{\pm}$ Z^0	1 0	80.38 ± 0.012 91.188 ± 0.002	10^{-18}	10^{-9}
Gravitational	Einstein's GTR	Graviton	0	0	∞	10^{-38}

Table 1.2: Properties of fundamental interactions.

1.3 SM as a Gauge Theory

SM is based on the concept of "symmetry" that can be local or global. According to global symmetry, the Lagrangian remains invariant under any transformation at every point in space-time while in local symmetry, it varies with the transformation at each point. SM Lagrangian is required to remain invariant under local gauge transformation and is given by three gauge groups $SU(3)_C \otimes SU(2)_L \otimes U(1)_Y$. The general form of SM Lagrangian [15] can be written as:

$$\mathcal{L}_{SM} = \mathcal{L}_f + \mathcal{L}_g + \mathcal{L}_\phi + \mathcal{L}_{Yukawa} \tag{1.1}$$

here, $\mathcal{L}_f$ refers to Lagrangian with spin-1/2 matter field (Fermions), $\mathcal{L}_g$ corresponds to spin-1 mediators (gauge boson), $\mathcal{L}_\phi$ points to the spin-0 scalar field (the Higgs doublet ϕ), and $\mathcal{L}_{Yukawa}$ is the Yukawa interaction between the Higgs field and fermions.

Quantum ElectroDynamics (QED) is the first abelian gauge theory that describes the electromagnetic interaction between charged particles with an exchange of virtual massless particle called "photon". QED is characterized by the gauge symmetry group $U(1)_Y$ that leaves the Lagrangian invariant under global symmetry and leads to the conservation of electric charge. However, local gauge symmetry as a function of space-time transform the Lagrangian and $\mathcal{L}$ is no longer invariant. So, to make it invariant under local gauge symmetry, a new gauge field "photon field" (massless with spin 1) is added to it. Similar to QED, it is important to determine the self-sustained invariant gauge theory for weak interactions. The SU(2) gauge group characterizes the weak interaction theory. However, weak interactions change the quark flavor and violate the parity. Due to massive mediators, forces are of short-range which makes this theory non-invariant under gauge transformation. So for flavor invariance, U$(1)_Y$ symmetry is added to this theory to make it gauge invariant. The unified ElectroWeak (EWK) theory represented by $SU(2)_L \otimes U(1)_Y$ symmetry group was given by Sheldon Lee Glashow, Abdus Salam, and Steven Weinberg in 1960. This theory involves the existence of four massless carriers, to mediate the unified electroweak interaction. SU(2) group contains three gauge fields (W^i_μ) and one gauge field (B_μ) for U(1).

Quantum ChromoDynamics (QCD) theory [16, 17] is related to color charge and represented by gauge symmetry group SU$(3)_C$. This theory is non-abelian and emphasizes the strong interaction between quarks and gluons. Local invariance of this theory adds 8 gauge fields (gluon fields) that are the force carriers between colored quarks.The QCD coupling constant is represented by g_s and given as $g_s = \sqrt{4\pi\alpha_s}$, where α_s is the strength of interaction between quarks and gluons. At high and low energy scales, QCD behaves differently and give rise to two important phenomena which are discussed below in details:

- **Quark Confinement:** Quark confinement refers to a phenomenon where the quarks are confined in a bound state with other quarks and cannot exist freely. This phenomenon occurs at low energies where α_s is large. If one of the quarks in a given hadron is pulled away from its neighbours that are in the bound state, the color force field increases between quark and neighbour quark. More energy is applied to separate the quark tends to add more energy to the color force. Finally, at some point, the color force becomes so influential, that it divides into a new pair of $q\bar{q}$ conserving the energy and other quantum numbers as the energy of the color force field is changed into a mass of new quarks. Hence, quarks cannot exist independently. Figure 1.5 shows the quark confinement phenomenon.

Figure 1.5: Pictorial view of quark confinement.

- **Asymptotic Freedom:** This is the most important phenomenon observed by the non-abelian nature of QCD theory. QCD theory depicts the interaction of colored particles through the exchange of gluons having a certain momentum scale Q. Unlike in QED, the QCD coupling constant depends on the momentum exchange which makes it complicated. The QCD coupling constant is given as:

$$\alpha_s(Q^2) = \frac{12\pi}{(33 - 2n_f)ln(Q^2/\Lambda^2)} \tag{1.2}$$

where Λ is the QCD scaling parameter and $\sim$ 200 MeV at QCD scale, n_f is the number of quark flavors. At very high energies, where momentum exchange is large, the coupling constant (α_s) decreases indicating quarks behaving as almost free or non-interacting. At $\Lambda_{QCD} \sim$ 200 MeV, the strong coupling constant becomes unity. As $\mathrm{Q}^2 \rightarrow \infty, \alpha_s \rightarrow 0$, indicating that at large Q^2, interaction becomes weak and vanishes to zero at asymptotically high energies, justifying the term “Asymptotic Freedom” and can be seen in Figure 1.6.

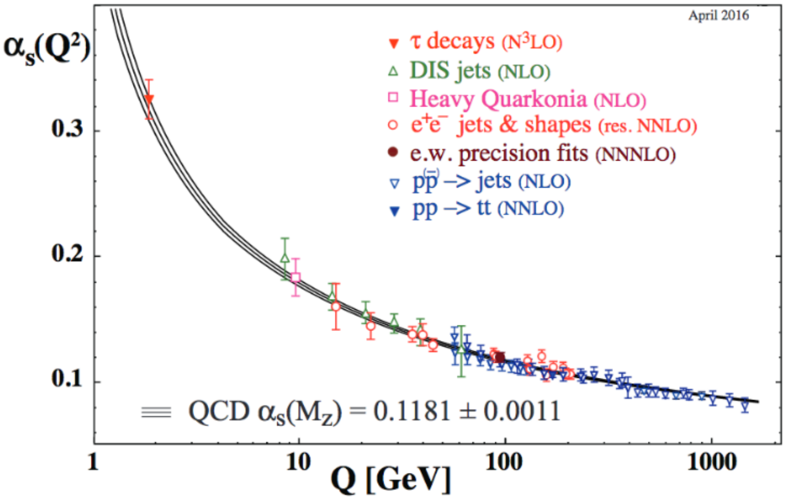

Figure 1.6: Diagram showing the asymptotic freedom phenomenon in which at high values of Q^2, coupling constant becomes very small [18].

1.3.1 The Brout-Englert-Higgs (BEH) Mechanism

The EWK Lagrangian does not contain any mass terms for bosons because it violates electroweak ($SU(2)_L\times U(1)_Y$) symmetry. The weak interaction mediators W and Z are massive bosons, suggesting that there exists a mechanism that provides mass to the boson by breaking electroweak spontaneous symmetry. The mechanism providing such a breakdown of the electroweak symmetry is the Brout-Englert-Higgs mechanism which introduces a complex isospin doublet scalar field $\phi(x)$ coupled to vector field $A^\mu(x)$. The complex scalar field is defined as:

$$\phi(x) = \begin{pmatrix} \phi^+ \\ \phi^0 \end{pmatrix} = \tfrac{1}{\sqrt{2}} \begin{pmatrix} \phi_1 + i\phi_2 \\ \phi_3 + i\phi_4 \end{pmatrix}$$

where ϕ^+ and ϕ^0 are complex fields and $\phi_{1,2,3,4}$ are real fields. The Lagrangian of the complex scalar field remains invariant under local U(1) symmetry given as:

$$\mathcal{L}_{Higgs} = (D^\mu\phi)^\dagger D_\mu\phi - V(\phi) \tag{1.3}$$

where D^{μ} is the covariant derivative in EWK theory ($D^{\mu} = \partial^{\mu} + igA^{\mu}$) and V($\phi$) is the Higgs potential given as:

$$V(\phi) = \mu^2\phi^{\dagger}\phi + \lambda(\phi^{\dagger}\phi)^2 \tag{1.4}$$

Higgs potential depends on two parameters: μ which represents mass term and λ represent Higgs's field self-interaction. The shape of Higgs potential depends on these two free parameters and the pictorial representation is shown in Figure 1.7. For the stability of the vacuum, λ should be greater than zero. The other parameter μ^2 leads to the two different shapes of Higgs's potential. If $\mu^2 > 0$, potential has the form of a parabola with a global minimum at zero and for $\mu^2 < 0$, there is a set of degenerate minimum lying on a ring in the complex plane that does not coincide with the origin or in other words vacuum expectation value (VEV) acquires a non-zero value. For $\mu^2 < 0$ and $\lambda > 0$, the potential is minimized and it achieves minimum when:

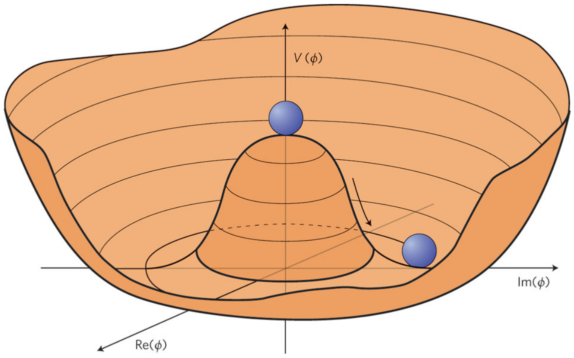

Figure 1.7: Shape of the two-dimensional Higgs potential V(ϕ).

$$\phi^{\dagger}\phi = -\frac{\mu^2}{2\lambda} = \frac{v^2}{2} \tag{1.5}$$

where v is the vacuum expectation value that defines the set of a minimum of the potential. The mass of the Higgs boson equals $\mathbf{m_H} = \sqrt{\mathbf{2}}\mu$. According to Nambu-Goldstone theory, for each spontaneous symmetry there exists some boson that provides mass to other gauge bosons. The masses for W and Z boson can be expressed in terms of coupling constants and VEV, given as:

$$m_W = \frac{gv}{2}, \quad m_Z = \frac{v\sqrt{g^2 + g'^2}}{2} \tag{1.6}$$

Here, g and g′ refer to the coupling constants of U(1) and SU(2) gauge groups, respectively.

The coupling of Higgs boson with fermions can give mass to fermions, but not by spontaneous symmetry breaking. The mass to the fermions is provided by Yukawa coupling of the Higgs bosons to fermions. The Yukawa Lagrangian includes the matrices that describe the Yukawa couplings (y_f) between fermions and single Higgs doublet, written as:

$$\mathcal{L}_{Yukawa} = \frac{y_f v}{\sqrt{2}}(\bar{e}_L\bar{e}_R + \bar{e}_R\bar{e}_L) + \frac{y_f}{\sqrt{2}}(\bar{e}_L\bar{e}_R + \bar{e}_R\bar{e}_L)H \tag{1.7}$$

The first term represents the mass term for fermions written as:

$$m_f = \frac{y_f v}{\sqrt{2}}, \quad f = e, u \text{ and } d. \tag{1.8}$$

For each Yukawa mass term, there exists an interaction term between fermion and the Higgs field which is also proportional to the mass of fermion. Higgs mechanism was established in the 1960s but Higgs boson was experimentally discovered on 4 July 2012 by LHC experiments namely Compact Muon Solenoid (CMS) [19] and A Toroidal LHC ApparatuS (ATLAS) [20] and this boson has similar properties such as spin, mass (125 GeV) and coupling strength as that of expected SM Higgs boson.

Despite several accomplishments of the SM (refer Section 1.1), it fails to explain many things implying SM is not a complete theory and may loose validity at some higher energies. The shortcomings of the SM are explained in the next Section.

1.4 Drawbacks of the SM

SM is considered as the most successful theory to date because of the high precision between observed quantities and SM calculation. From the magnetic dipole of electron [21] to cross section of the numerous processes (see Figure 1.8), SM predicted values agree well with observed quantities up to very high precision. However, it still possesses some limitations and because of that SM is considered simply an effective field theory (EFT) up to some high energy (Λ) after which, a new theory is required. Few shortcomings of SM are explained below:

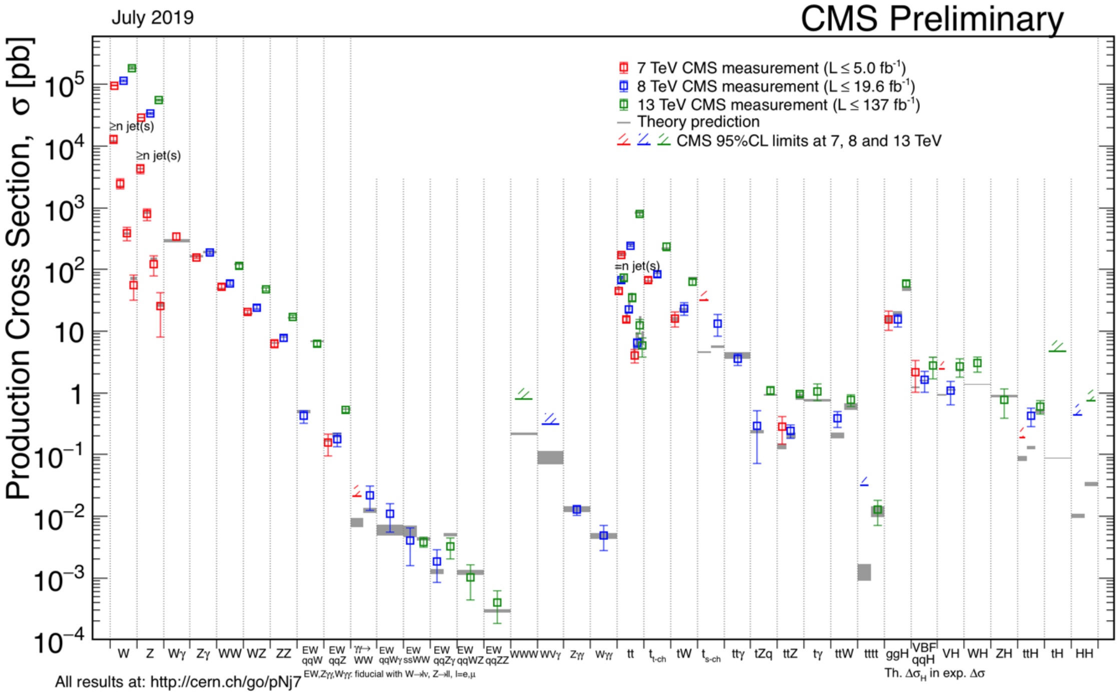

Figure 1.8: Comparison between theoretically given and observed cross sections by CMS experiment for various SM processes [22].

- **Grand Unified Theory and Gravity:** Even though the coupling constant of EM, Weak and Strong forces vary with energy, Grand Unified Theory (GUT) unifies the coupling constant of these forces at a single value α_G at very high energies. Gravitational interaction is not included in the GUT as it fails to include gravity in the framework of the other three fundamental forces. SM only includes three out of four fundamental forces.

- **Hierarchy Problem:** The large difference between the electroweak scale (10^2 GeV) and Planck's scale (10^{19} GeV) is called the Hierarchy or fine-tuning problem. As said earlier, Higgs boson having mass 125 GeV provides mass to other particles (gauge bosons and fermions) by coupling with them [23]. The neutral component of the Higgs field is a complex scalar (ϕ) that obtains the non-zero value of VEV of 174 GeV. As a characteristic of the QFT, in the Higgs mechanism scalar particles get large masses through large radiative corrections. Hence, Higgs boson mass (m_H^2) receives huge quantum correction from each particle which couples to the Higgs field [24]. The radiative correction to the mass depends on Yukawa couplings (y_f) and ultraviolet energy cutoff Λ_{UV} - the energy scale at which new physics starts to modify the high-energy form of theory. The coupling of the Higgs field with heavy scalar fermions provides a possible contribution to large quantum corrections which can shift the entire mass spectrum of the SM particles as shown in Figure 1.9. Despite the huge quantum corrections, the Higgs boson mass is quite smaller than the Planck Scale $(8\pi G_{Newton})^{-1/2} = 2.4 \times 10^{18}$ GeV, as given in Equation 1.9.

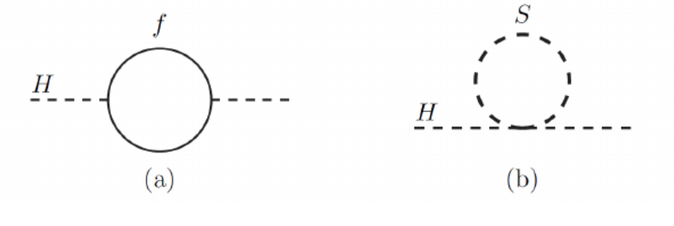

Figure 1.9: One-loop corrections to the m_H^2 due to (a) a Dirac fermion f, (b) a scalar S.

$$\Delta m_H^2 = -\frac{|y_f|^2}{8\pi^2}\Lambda_{UV}^2 + ... \qquad (1.9)$$

The corrections are largest from top quarks with $y_t \approx 1$. Nevertheless, if Δ_{UV} is of the order of the Planck scale, it will introduce the quantum corrections to m_H^2 of the order 30 times greater than its value. To cancel out such corrections, m_H (or μ) in the SM takes unnatural large value causing "fine-tuning" problems in the Higgs mass. Hence, to bypass such fine-tuning problems and divergences, the extension of SM is required.

- **Dark Matter and Dark Energy:** The recent study from Planck collaboration states that energy-mass of the Universe is made up of 4.9% of visible matter, 26.8% *dark matter* [25] and 69% of *dark energy* - the energy which is hard to detect with the current technology and which is responsible for the accelerating expansion of the Universe [26]. SM gives an explanation only for visible matter and not for dark matter. However, there are many pieces of evidence that dark matter exists. In 1933, Fritz Zwicky observed that the galaxies in the distant Coma cluster are moving fast concerning the gravity produced by visible matter, indicating there exists some hidden matter [27] which is later confirmed with an unexpected trend in the rotational velocity of galaxies given by Vera Rubin and Collaboration [28]. The mass observation of galaxies is very small than the mass of the galaxy itself. Also, gravitational lensing effects of remote objects and the power spectrum of cosmic microwave background (CMB) lead to the occurrence of a mass source, known as dark matter. Famously known as WIMPs (Weakly Interacting Massive Particles) are possible candidates for dark matter [29]. As the name suggests these particles are massive, interact with themselves and matter only by weak forces and gravity. However, because of their high mass, they travel with a speed less than the speed of light so that they do not annihilate themselves so often, giving visible matter. SM doesn't provide any explanation for dark matter and dark energy. Neutrinos cannot be considered as WIMPs because they have a very small mass and have speed comparable to speed to light.

There are numerous theories that predict a particle compatible with the features of a dark matter candidate. One of these theories is Supersymmetry (SUSY), which will be presented in the next Chapter and constitutes the motivation for this thesis.

- **Matter-AntiMatter Asymmetry:** It is believed that at the time of Big-Bang around 13.8 billion years ago, an equal amount of matter and anti-matter should have been created. However, physical objects in this Universe around us are made up of matter and there exists no anti-matter which is the biggest challenge in physics. In 1967, Andrei Sakharov stated a set of three necessary conditions responsible for this asymmetry which are Baryon number violation, Charge (C) and Charge-Parity (CP) violation [30]. There is a small CP violation observed in K^0 decay and B-meson system but this asymmetry is insufficient to explain the matter-antimatter asymmetry.

- **Neutrino Oscillations:** According to SM, neutrinos are massless and chargeless particles but a recent experimental study confirmed neutrino oscillation [31, 32] that squared mass difference between them is non-zero. Experimental observations show that neutrinos propagating in space can be observed with a different flavor from the initial one indicating that neutrinos are not massless.

- **Three Generations:** The SM doesn't give any explanation that why only three particle generations exist and why there is so much difference in masses of particles among different generations.

It also fails to describe why SM has ~ 20 parameters and the origin of coupling constants. May be by finding dark matter candidate, by going in more detail about neutrino mass or by explaining the matter-antimatter asymmetry one could find the answers to unknowns. The SM problems are many, but the take-home message of this chapter is that SM is still a very successful theory to date, with immense predictive power. At this point, abandoning the SM is not an option. Alternatively, extensions of the SM, known as Beyond SM (BSM) theories that could provide answers to one or all of the above problems, are probed. There are many BSM theories like GUT, Georgi-Glashow model, composite Higgs model and Supersymmetry (SUSY) but the most encouraging extension of the SM i.e. SUSY is described in the next Chapter.

1.5 Thesis Organization

The research presented in this Thesis is divided into two parts: physics analysis and hardware work done during the entire duration of my Ph.D. The physics analysis deals with the search of particles predicted beyond the SM (BSM). Thus, the search involves the study of chargino and neutralino production through vector boson fusion (VBF) processes in the final state comprising of single hadronic tau channel using proton-proton collision data collected by CMS detector at $\sqrt{s} = 13$ TeV at LHC. The detailed outline of the Thesis (see Figure 1.10) is as follows:

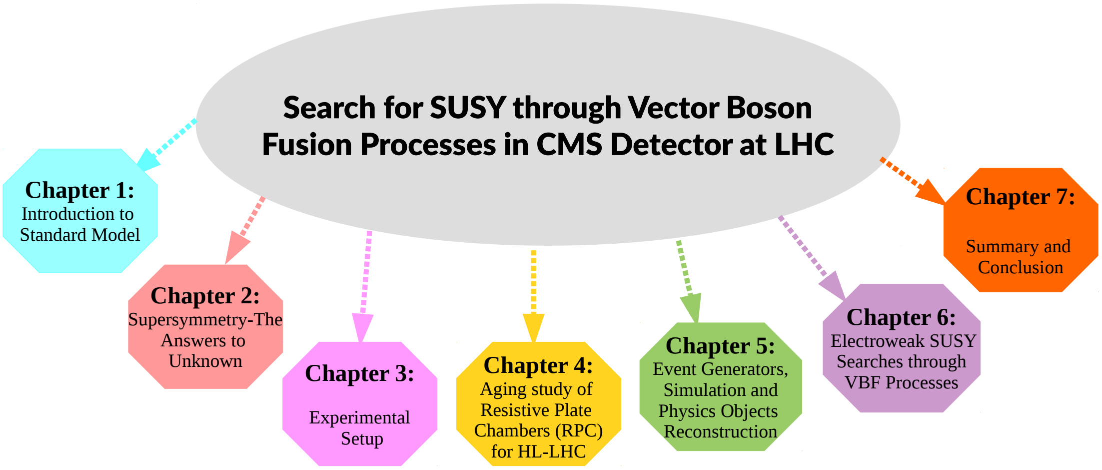

Figure 1.10: Outline of the Thesis.

- The present **Chapter** provides a brief overview of how SM particles evolved with time. The SM theory, its successes, and its shortcomings are discussed in detail. The drawbacks of the SM gives the motivation to go beyond the SM theories such as SUSY.

- **Chapter 2** portrays SUSY theory and its successes to explain the shortcomings of SM. The Minimal Supersymmetric Standard Model (MSSM) is used in the presented physics analysis, is explained in detail. Additionally, a summary of SUSY searches at LHC is presented motivating the need to look at the electroweak sector with VBF processes.

- **Chapter 3** The first half of this Chapter is dedicated to the LHC machine and its parameters. The CERN accelerator complex and various experiments being conducted at LHC are explained. However, at the LHC, proton-proton, lead-lead or proton-lead collisions occur, but a brief discussion of proton-proton is done. The other half of this Chapter explains the CMS detector and its subdetectors in detail as the data used in the current Thesis is collected using the CMS detector.

- **Chapter 4** describes the hardware work related to the aging study of the Resistive Plate Chambers (RPC) installed at CMS. Gaseous detector especially the RPC detector working principle and its layout is briefly discussed. Because of the increasing luminosity at LHC, detectors are at the risk of damage. So, a dedicated longevity study was set up at CERN Gamma Irradiation Facility (GIF++) where it is possible to test real size detectors. GIF++ is also discussed in more detail.

- **Chapter 5** This chapter aims to describe the way by which information coming from the CMS subdetectors is combined to reconstruct physical objects and their algorithms. It gives a brief overview of event generation, simulation, and different types of Monte Carlo (MC) generators. Also, a detailed study of the reconstruction of physics objects used in the present work such as tau lepton, missing transverse energy, jets, etc. has been presented.

- **Chapter 6** This Chapter contains most of the work done in the course of Ph.D. The physics analysis is performed for the search of chargino and neutralino through VBF processes in single hadronic tau final state at a center-of-mass energy of 13 TeV. The analysis workflow, data, signal and background samples used in this analysis are discussed in detail. The backgrounds with major contributions in the signal region are estimated using semi data-driven or data-driven techniques. The result from the single hadronic tau channel is combined with the results from muon, electron and invisible channel. Since no excess of data is found over and above SM backgrounds, the upper limits are set on the masses of charginos and neutralinos searches.

- **Chapter 7** summarizes the observations and experimental results of the analysis presented in this thesis.

Since Panjab University (PU) EHEP group is a part of the CMS collaboration, CERN. The work presented in this thesis has been performed using data collected with the CMS experiment at LHC. I have visited CERN, Geneva, Switzerland for participating in the CMS Research Collaboration work and taken on-site shift duties for various tasks related to RPC data taking and mainly involved in the aging study of RPCs at GIF++.

Apart from this work, since the PU group is one of the main production sites for the production of Gas Electron Multipliers (GEM) detectors for CMS, I have participated in the assembly of GEM detectors at PU GEM lab.

Bibliography

[1] A. Salam and J. C. Ward, “Electromagnetic and weak interactions”, *Phys. Lett.*, vol. 13 (1964), https://doi.org/10.1016/0031-9163(64)90711-5.

[2] S. Weinberg, “A Model of Leptons”, *Phys. Rev. Lett.*, vol. 19 (1967), https://doi.org/10.1103/PhysRevLett.19.1264.

[3] D. J. Gross and F. Wilczek, “Ultraviolet Behavior of Non-abelian Gauge Theories”, *Phys. Rev. Lett.*, vol. 30 (1973), https://doi.org/10.1103/PhysRevLett.30.1343.

[4] H. D. Politzer, “Reliable Perturbative Results for Strong Interactions”, *Phys. Rev. Lett.*, vol.30 (1973), https://doi.org/10.1103/PhysRevLett.30.1346.

[5] J. J. Thomson, “XL. Cathode Rays - by J.J. Thomson”, *Philosophical Magazine*, vol. 44 (1897), https://doi.org/10.1080/09500830701306165.

[6] E. Rutherford, “The scattering of alpha and beta particles by matter andthe structure of the atom”, *Philosophical Magazine*, vol. 21 (1911), https://doi.org/10.1080/14786440508637080.

[7] E. Rutherford, “The structure of the atom”, *Nature*, vol. 92 (1913), https://doi.org/10.1038/092423a0.

[8] J. Chadwick, “Possible Existence of a Neutron”, *Nature*, vol. 129 (1932), https://doi.org/10.1038/129312a0.

[9] D. J. Griffiths, “Introduction to elementary particles”, Wiley, 2008.

[10] Lyndon Evans and Philip Bryant, “LHC Machine”, *Journal of Instrumentation*, vol. 3 (2008), https://doi.org/10.1088/1748-0221/3/08/S08001.

[11] CMS Wiki Pages, https://wiki.physik.uzh.ch/cms/latex:tikz:timescales.

[12] Jae Yool Kim, “Discovery of Neutrino Oscillations in the Super-Kamiokande Experiment”, *Phys. High Tech.*, vol. 24 (2015), https://doi.org/10.3938/PhiT.24.054.

[13] Standard Model of Particle Physics, `https://physicstravelguide.com/models/standard_model`.

[14] C. Patrignani *et al.*, “Review of Particle Physics”, *Chin. Phys.*, vol. C40 (2016), https://doi.org/10.1088/1674-1137/40/10/100001.

[15] https://www.symmetrymagazine.org/article/the-deconstructed-standard-model-equation

[16] D. Gross and F. Wilczek, “Asymptotically Free Gauge Theories - I”, *Phys. Rev. D*, vol. 8 (1973), https://doi.org/10.1103/PhysRevD.8.3633.

[17] H. D. Politzer, “Asymptotic Freedom: An Approach to strong Interactions”, *Phys. Rept.*, vol. 14 (1974), https://doi.org/10.1016/0370-1573(74)90014-3.

[18] M. Tanabashi *et al.*, “Review of Particle Physics”, *Phys. Rev. D*, vol. 98 (2018), https://doi.org/10.1103/PhysRevD.98.030001.

[19] The CMS Collaboration, “Observation of a new boson at a mass of 125 GeV with the CMS experiment at the LHC”, *Phys. Lett. B*, vol. 716 (2012), https://doi.org/10.1016/j.physletb.2012.08.021.

[20] The ATLAS Collaboration, "Observation of a new particle in the search for the Standard Model Higgs boson with the ATLAS detector at the LHC", *Phys. Lett. B*, vol. 716 (2012), https://doi.org/10.1016/j.physletb.2012.08.020.

[21] B. Odom and D. Hanneke and B. D'urso and G. Gabrielse, "New measurement of the electron magnetic moment using a one-electron quantum cyclotron", *Phys. Rev. Lett.*, vol. 97 (2006), https://doi.org/10.1103/PhysRevLett.97.030801.

[22] `https://twiki.cern.ch/twiki/bin/view/CMSPublic/PhysicsResultsCombined`.

[23] The ATLAS Collaboration and CMS Collaboration, "Combined Measurement of the Higgs Boson Mass in pp Collisions at $\sqrt{s} = 7$ and 8 TeV with the ATLAS and CMS Experiments", *Phys. Rev. Lett.*, vol. 114 (2015), https://doi.org/10.1103/PhysRevLett.114.191803.

[24] S. P. Martin, "A Supersymmetry primer", *Advanced Series on Directions in High Energy Physics*, (1998), https://doi.org/10.1142/9789812839657_0001.

[25] Planck 2015 Constraints on Dark Energy and Inflation, `https://darkmatterdarkenergy.com/tag/planck-2015/`.

[26] `https://science.nasa.gov/astrophysics/focus-areas/what-is-dark-energy`.

[27] F. Zwicky, "On the Masses of Nebulae and of Clusters of Nebulae", *Astrophysical Journal*, vol. 86 (1937), https://doi.org/10.1086/143864.

[28] V. C. Rubin, N. Thonnard, and W. K. Ford, Jr., "Rotational properties of 21 SC galaxies with a large range of luminosities and radii, from NGC 4605 /R = 4kpc/ to UGC 2885 /R = 122 kpc/", *Astrophysical Journal*, vol. 238 (1980), https://doi.org/10.1086/158003.

[29] G. Jungman, M. Kamionkowski, and K. Griest, "Supersymmetric dark matter", *Phys. Rept.*, vol. 267 (1996), https://cds.cern.ch/record/283685/files/9506380.pdf.

[30] A. D. Sakharov, "Violation of CP Invariance, c Asymmetry, and Baryon Asymmetry of the Universe", *Pisma Zh. Eksp. Teor. Fiz.*, vol. 5 (1967), https://doi.org/10.1070/PU1991v034n05ABEH002497.

[31] M. P. Decowski, "KamLAND's precision neutrino oscillation measurements", *Nucl. Phys. B*, vol. 908 (2016), https://doi.org/10.1016/j.nuclphysb.2016.04.014.

[32] The T2K Collaboration, "Precise Measurement of the Neutrino Mixing Parameter θ_{23} from Muon Neutrino Disappearance in an Off-Axis Beam", *Phys. Rev. Lett.*, vol. 112 (2014), https://doi.org/10.1103/PhysRevLett.112.181801.

Chapter 2

Supersymmetry - The Answers to Unknown

This Chapter gives a description of the theory of Supersymmetry (SUSY) which has been developed as an extension of the Standard Model (SM) to overcome its shortcomings. Also, a brief description of SUSY searches at LHC experiments (CMS and ATLAS) is given.

2.1 Introduction to SUSY

SUSY [1–5] is one of the most popular theories Beyond Standard Model (BSM) to solve SM drawbacks, already discussed in detail in the Chapter 1(Section 1.4). SUSY postulates the symmetry between fermions and bosons by supersymmetry transformation operator Q, which transforms a bosonic state to a fermionic state and vice versa as follows:

$$Q \mid \text{Boson} \rangle = \mid \text{Fermion} \rangle \tag{2.1}$$

$$Q \mid \text{Fermion} \rangle = \mid \text{Boson} \rangle \tag{2.2}$$

SUSY is a space-time symmetry because its transformation operator Q changes the spin as well as statistics of a particle and spin is correlated with spatial rotations. For each fermion there exists a corresponding boson and vice-versa that has the same mass and other quantum numbers but just differs by spin 1/2. The full picture depicting the SM particles along with SUSY particles is shown in Figure 2.1. The SM particles with their supersymmetric partners are arranged in "Supermultiplets" and divided into two supermultiplets named "scalar or chiral" supermultiplet and "gauge or vector" supermultiplet [6]. The leptons and quarks (*superpartners - sleptons and squarks*) are the members of chiral supermultiplet while bosons having spin 1 fall under the category of vector supermultiplet (*superpartners - gauginos*). However, the mass of the supersymmetric partners is not the same otherwise they would have been discovered. This indicates that SUSY is a "broken" symmetry.

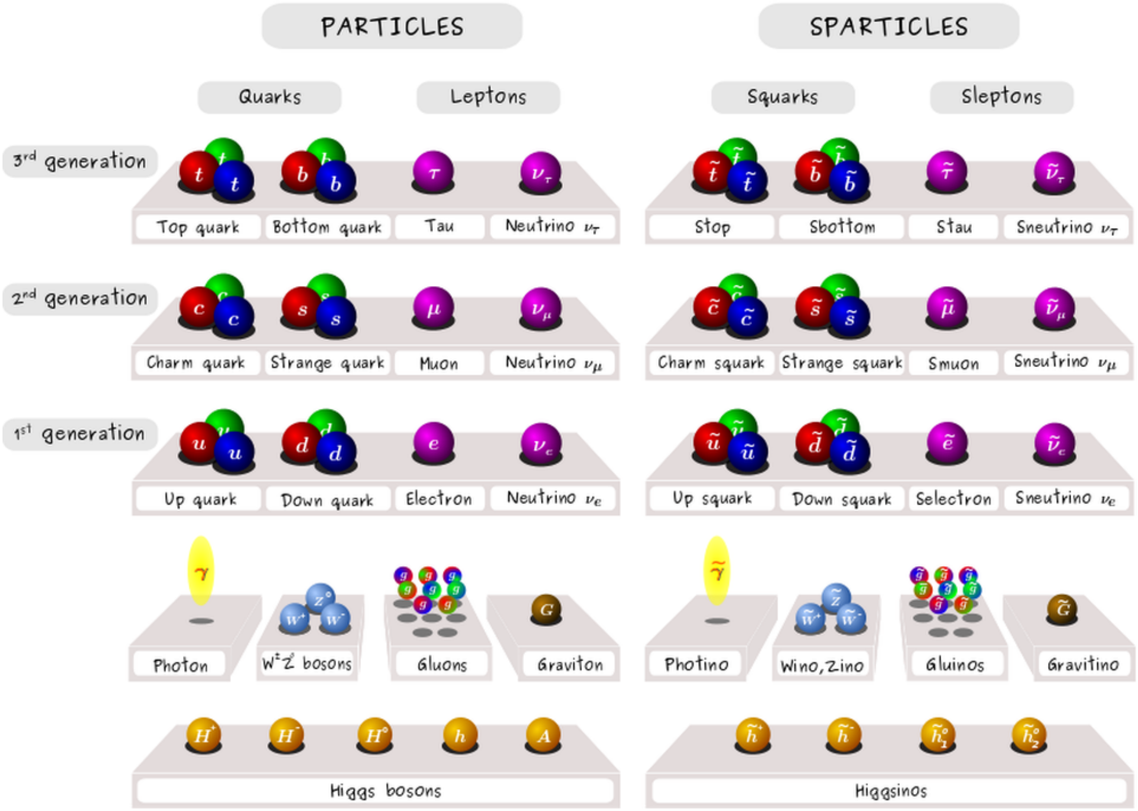

Figure 2.1: Spectra of SUSY particles along with SM particles.

SUSY is an essential theory to solve the hierarchy problem, to unify all the four interactions into a single framework called Grand Unified Theory (GUT) [7]. By including gravitational force with the other three forces in one framework, SUSY becomes local and supergravity [8] comes into existence. Below is the detailed description of how the SUSY model overcomes the shortcomings of SM.

- **Fixing of Hierarchy Problem:** As described in the last Chapter regarding hierarchy problem that m_H^2 is proportional to Λ_{UV} and receives large quantum corrections which appear due to virtual loops of all the particles that get coupled to the Higgs field. The fermions get coupled to the Higgs field through Yukawa coupling, y_f which is proportional to the fermion mass, hence the larger contribution is from the top quark. The Λ scale causes quadratic divergence and fine-tuning in Higgs mass. Hence to avoid such divergences, a scalar version of an SM fermion, basically a boson of mass m_s, that couples to the Higgs field is added to Higgs mass as shown in Equation 2.3.

  $$\Delta m_H^2 = \frac{\lambda_s}{16\pi^2}[\Lambda_{UV}^2 - 2m_s^2 ln(\Lambda_{UV}/m_s) + ...] \tag{2.3}$$

  This way the contribution of two scalar bosons just cancels the fermion contribution if the coupling strength of the scalar $\lambda_s = |y_f|^2$ and the hierarchy problem is resolved [9].

- **Unification of Coupling Constants:** The coupling constants of three forces (electromagnetic, weak and strong) do not merge at one point because they depend on energy (Q^2) and vary for each force. So the energy scale decides which coupling is observed due to the contribution of virtual particles, known as “Running Coupling” [10] which is measured in QFT as:

  $$\beta(g) = \frac{\partial g}{\partial ln\mu} \tag{2.4}$$

Here, μ represents the energy scale and g stands for the coupling parameter. The beta function increases with an increase in energy and is positive for QED. At low energies, the electromagnetic coupling constant α is $\approx 1/137$ but increases to 1/127 at the Z boson mass scale. Earlier it was said that α becomes infinite at higher finite energy called "Landau Pole" [11] but indeed it is false as now its performance is known at large energies. However, in QCD (non-abelian gauge theory), β can be negative and α becomes nearly zero at higher energy giving rise to a phenomenon called "Asymptotic Freedom". The behaviour of coupling constants in SM is shown in the left plot of Figure 2.2, however, rather than three different coupling constants, it is speculated that these couplings can converge to the one value at some energy scale called GUT scale $\sim 10^{16}$ GeV as shown in the right plot of Figure 2.2.

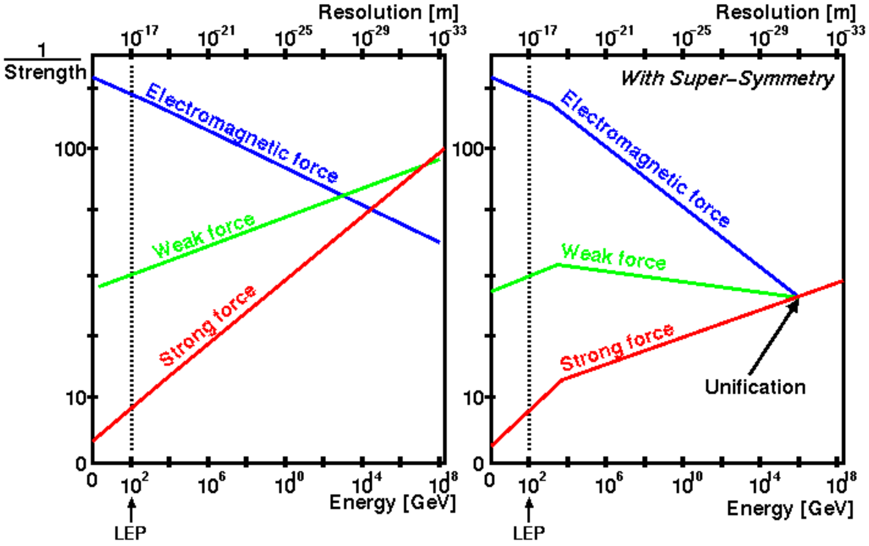

Figure 2.2: Left: Behaviour of coupling constant in SM parameteric space, Right: Coupling constants converge at some energy scale (GUT scale) in SUSY parameteric space.

SUSY provides a solution to the unification of coupling constants by considering SUSY particles (sparticles) masses of $\mathcal{O}(1)$TeV that solve the hierarchy problem. Some kinks and changes in the slopes can be seen in the right plot at TeV scale, this range is expected to be SUSY breaking scale and below this everything falls under SM.

- **Dark Matter Candidate:** SUSY has some kind of particles like sneutrinos, neutralinos, and gravitinos that can serve as potential candidates for dark matter search. They are known as "Lightest Supersymmetric Particles" (LSPs) and are stable. However, sneutrinos are excluded between the mass range 55 GeV to 2.3 TeV because of data collected by direct galactic dark matter searches based on the sneutrino-nucleon cross section values [12]. The other SUSY particle i.e. gravitino (supersymmetric partner of graviton with spin 3/2) is weakly interacting which makes it hard to detect experimentally. So the remaining particle, neutralino is the favored dark matter candidate which is formed by the combination of W, Z and Higgs bosons. The neutralino is expected to be in the mass range of 37-500 GeV. The analysis presented in this Thesis excludes the mass of neutralino up to 112 GeV in the compressed mass scenario having $\Delta m = 1$ GeV as described in detail in Chapter 6.

2.2 Minimal Supersymmetric Standard Model (MSSM)

As the name suggests, the Minimal Supersymmetric Standard Model (MSSM) [13] is the simplest extension of SM with the same gauge symmetries and have minimum new particles as it only doubles the SM particles by providing its superpartners. The supersymmetric fermions are scalars having spin-0 (i.e.bosons) are denoted with prefix "s" before the names of their SM partners and called as scalar-fermions or *sfermions*. They have the same symbol as of SM particles in addition to tilde on top ($\tilde{e}, \tilde{\mu}$ and $\tilde{\tau}$). The superpartners of leptons and quarks are called *sleptons* and *squarks* respectively. Due to the parity-violating nature of the weak interaction, left- and right-handed fermions have individual superpartners and are called left-and right-handed sfermions ($\tilde{e}_L, \tilde{e}_R$). The SM neutrinos are left-handed so is their superpartners *sneutrinos* ($\tilde{\nu}$) are left-handed. Like fermions, sfermions (sleptons and squarks) also come under the category of "chiral/scalar" supermultiplet and boson and their superpartners are in "vector/gauge" supermultiplet. Similarly, the superpartners of SM gauge bosons are fermions (spin-1/2) and have suffix *"ino"* to the name of SM boson. For example, W, B gauge boson of SM are called *wino*, *bino* and gluons are called *gluinos*. In MSSM, there are two Higgs supermultiplets (H_u, H_d) that carry hypercharge $\mathrm{Y} = \pm 1/2$ and provide mass to up and down-quarks respectively. Naturally, Y=1/2 Higgs supermultiplet has the Yukawa couplings for 2e/3 charge up quarks and Y= -1/2 for -e/3 down charge quarks. H_u field has two components corresponding to electric charge 1, 0 and weak isospin components $T_3 =$ (1/2, -1/2) named as (H_u^+, H_u^0) and for H_d as (H_d^0, H_d^-). The fermionic superpartners of SM Higgs boson are called *Higgsino* and are written as $\tilde{H}_u^+, \tilde{H}_u^0, \tilde{H}_d^0$ and $\tilde{H}_d^-$. The mixing of neutral gauginos ($\tilde{W}^0, \tilde{B}^0$) with neutral higgsinos ($\tilde{H}_u^0, \tilde{H}_d^0$) form four neutral mass eigenstates, known as *neutralinos*, $\tilde{\chi}_i^0$ with i = 1,2,3,4 whereas mixing of charged gauginos ($\tilde{W}^+, \tilde{W}^-$) with charged higgsinos ($\tilde{H}_u^+, \tilde{H}_d^-$) form two charged mass eigenstates, called as *charginos* $\tilde{\chi}_i^\pm$ with i = 1,2. All the superpartners of SM are listed in Table 2.1.

It has been said that the superpartners of the SM have the same mass as of SM particles but experimentally they have not been discovered yet which indicates SUSY is a "broken" symmetry in the vacuum state. However, this fact will not change the coupling dependence which is responsible for solving the hierarchy problem by canceling the divergent quadratic terms that give a large quantum correction to Higgs mass. This leads to the state of "soft" SUSY breaking. The MSSM Lagrangian is divided into two parts as: $\mathcal{L}_{MSSM} = \mathcal{L}_{SUSY} + \mathcal{L}_{soft}$. $\mathcal{L}_{SUSY}$ contains all the Yukawa and gauge interactions while $\mathcal{L}_{soft}$ has positive mass and coupling parameters. The mass term from $\mathcal{L}_{soft}$ is the largest mass scale, and when it approaches 0, the other

Particle	Supermultiplet	Spin-0	Spin-1/2	SU(3)$_C$	SU(2)$_L$	U(1)$_Y$
Quarks and Squarks	Q	$(\tilde{u}_{iL}, \tilde{d}_{iL})$	(u_{iL}, d_{iL})	3	2	+1/6
	$\bar{u}$	$\tilde{u}^*_{iR}$	$u^\dagger_{iR}$	3	1	-2/3
	$\bar{d}$	$\tilde{d}^*_{iR}$	$d^\dagger_{iR}$	3	1	+1/3
Lepton and Slepton	L	$(\tilde{e}_{iL}, \tilde{\nu}_{iL})$	(e_{iL}, ν_{iL})	1	2	-1/2
	$\bar{e}$	$\tilde{e}^*_{iL}$	$e^\dagger_{iR}$	1	1	+1
Higss, Higgsino	H_u	(H_u^+, H_u^0)	$(\tilde{H}_u^+, \tilde{H}_u^-)$	1	2	+1/2
	H_d	(H_d^+, H_d^0)	$(\tilde{H}_d^+, \tilde{H}_d^-)$	1	2	-1/2
gluino, gluon	G	$\tilde{g}$	g	8	1	0
wino, W boson	W	$\tilde{W}^{\pm}, \tilde{W}^0$	$W^{\pm}, W^0$	1	3	0
bino, B boson	B	$\tilde{B}^0$	B^0	1	1	0

Table 2.1: Supersymmetric particles in MSSM with their quantum numbers [6].

non-SUSY corrections must disappear to remove the proportionality to Δ^2_{UV}. The correction to the Higgs mass that depends on m_{soft} is given as:

$$\Delta m_H^2 = m_{soft}^2 \left[\frac{\lambda}{16\pi^2} ln \left(\frac{\Lambda_{UV}}{m_{soft}} \right) + ... \right] \tag{2.5}$$

If m_{soft} becomes very large, it can spoil the solution to the hierarchy problem. With the reasonable value of m_{soft} i.e. by using $\lambda \sim 1$ and $\Lambda_{UV} \sim M_P$ (Planck's Mass scale) in Equation 2.5, SUSY particle masses around $\sim$ 1 TeV are still possible at LHC energy. L_{SUSY} contains mass terms ($m^2|\phi|^2$) for *sfermions, gauginos* and *higgsinos* which are allowed by gauge invariance and because of this, SUSY particles are rather heavy than SM particles.

As SUSY contains chiral and gauge supermultiplets. The interaction of the superfields may be parameterized with the superpotential. The MSSM superpotential is given as [6]:

$$W_{MSSM} = \bar{u} y_u Q H_u - \bar{d} y_d Q H_d - \bar{e} y_e L H_d + \mu H_u H_d \tag{2.6}$$

where, y_u, y_d and y_e are 3×3 Yukawa matrices, μ is the Higgsino mass and $H_u, H_d, Q, L, \bar{u}, \bar{d}, \bar{e}$ represents the chiral superfields.

2.2.1 R-Parity

SM conserves the lepton and baryon number [14]. However, the MSSM superpotential defined in Equation 2.6 can permit some interaction that violates baryon and lepton number conservation which is not observed in nature yet. The terms that can violate the conservations are given as:

$$W_{\Delta L=1} = \frac{1}{2}\lambda^{ijk} L_i L_j \bar{e}_k + \lambda'^{ijk} L_i Q_j \bar{d}_k + \mu'^{i} L_i H_u \tag{2.7}$$

$$W_{\Delta B=1} = \frac{1}{2}\lambda'^{ijk} \bar{u}_i \bar{d}_j \bar{d}_k \tag{2.8}$$

These violation terms can lead to proton decay which is not observed. Proton has a long lifetime of 10^{33} years. Hence, such lepton or baryon number violating terms are unnaturally very much suppressed. To prevent lepton and baryon number violation, a new quantum number named "R-parity" [15] is introduced and is given as:

$$R = (-1)^{3(B-L)+2S} \tag{2.9}$$

where, B , L, and S refer to baryon number, lepton number, and spin of the particle. The value of R=1 corresponds to all SM particles and R= -1 is for SUSY particles. In the case of R-parity conservation (RPC), all coefficients defined in Equation 2.8 are set to zero. However, when R-parity is violated (RPV) [16], the terms will contribute to the superpotential making all SUSY particles unstable and allow them to decay to SM particles. In this Thesis, R-parity-conserving MSSM models are considered. Some of the requirements of R-parity conservation are given below:

- SUSY particles are always produced in pairs.

- SUSY particles must decay to another SUSY particle and a SM particle if it is allowed kinematically. Otherwise, it will decay to the Lightest Supersymmetric Particle (LSP) which is stable and least interacting with a mass of the order ∼100 GeV. The LSP is, therefore, a perfect candidate for Dark Matter.

2.3 SUSY Breaking Mechanism

As discussed in Section 2.2, the MSSM Lagrangian consists of $\mathcal{L}_{SUSY}$ and $\mathcal{L}_{soft}$, which means it has both SUSY conserving and breaking terms. $\mathcal{L}_{SUSY}$ [17] conserves the supersymmetric interactions while soft SUSY ($\mathcal{L}_{soft}$) breaks symmetry because of mass terms of superpartners allowed by gauge invariance which are given as [6]:

$$\begin{aligned}\mathcal{L}_{soft} = & -\frac{1}{2}(M_3\tilde{g}\tilde{g} + M_2\tilde{W}\tilde{W} + M_1\tilde{B}\tilde{B} + c.c.) \\ & - (\bar{u}a_uQH_u - \bar{d}a_dQH_d - \bar{e}a_eLH_d + c.c.) \\ & - Q^\dagger m_Q^2 Q - L^\dagger m_L^2 L - \bar{u}m_{\bar{u}}^2\bar{u}^\dagger - \bar{d}m_{\bar{d}}^2\bar{d}^\dagger - \bar{e}m_{\bar{e}}^2\bar{e}^\dagger \\ & - m_{H_u}^2 H_u^* H_u - m_{H_d}^2 H_d^* H_d - (bH_uH_d + c.c.)\end{aligned} \tag{2.10}$$

The tilde is not applied on Q, L, $\bar{u}, \bar{d}, \bar{e}, \bar{u}^\dagger, \bar{d}^\dagger$, and $\bar{e}^\dagger$ to not create mess. The M_1, M_2 and M_3 are the masses for *bino, wino* and *gluino*, respectively. The second line corresponds to the trilinear couplings between sfermions and the Higgs boson, while the third line refers to sfermions mass terms. Mass and bilinear terms for Higgs boson are represented by the fourth line.

These soft SUSY breaking terms introduce ∼ 105 extra parameters, as compared to SM, which means it is experimentally difficult to study MSSM. But there are two different approaches that can be helpful in reduction of these parameters. One approach to decrease the number of parameters is, by proposing some SUSY breaking mechanism and the other is, by creating Simplified Model Spectra (SMS).

In MSSM, SUSY breaking is introduced explicitly. Spontaneous SUSY breaking leads to the non-zero value of VEV which means the vacuum is not invariant under SUSY transformation. The above description indicates that SUSY breaking occurs in a “hidden sector” that has no or rare direct couplings to the “visible sector”. But if these two sectors are supposed to share some flavor-blind interactions, then what are the mediators between hidden and visible sectors. Hence, there are two models: The first one is based on gravity as a mediator i.e. gravity-mediated supersymmetry breaking - mSUGRA (minimal SUperGRAvity theory) [18] within the N=1 supergravity framework. The mSUGRA model reduces the number of parameters to a great extent. The second model is based on gauge interaction i.e. gauge-mediated supersymmetry breaking - GMSB [19]. The next Section contains a detailed description of reference model used for the study presented in this Thesis.

2.4 Simplified Models

Being the simplest extension of SM, the MSSM has 105 parameters in addition to 19 SM parameters. These large number of parameters leads to a broad spectrum of SUSY scenarios with various production and decay modes and makes it difficult for SUSY searches on such a large parameteric scale. So all these problems can be solved by a model called *Simplified Model Spectra* (SMS) [20, 21] which significantly reduces the number of parameters of interest for a given analysis. A simplified model contains a few numbers of parameters that are directly associated with collider physics observables, such as the mass, production cross section and branching fraction of the BSM particles. Another thing about SMS is that they are not complete model-independent, but allows the reinterpretation of the results in terms of a quite different theory, for which the final state should be the same as SMS.

In this Thesis, only the production processes of primary particles are considered in simplified models. The primary particle will experience either cascade decay or a direct decay by an intermediate particle but the final state will always end with the Lightest Supersymmetric Particle (LSP) as shown in Figure 2.3. The mass of LSP and parent particle will be considered as free parameters.

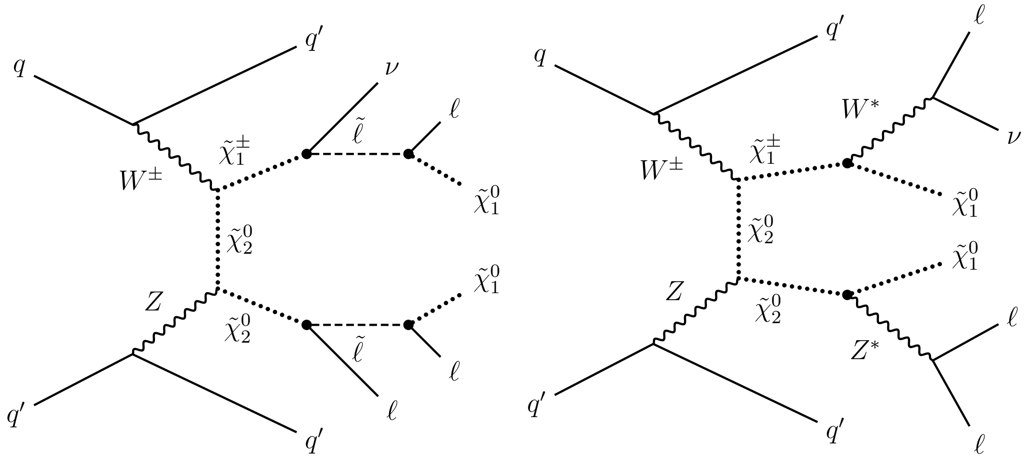

Figure 2.3: Feynman diagrams for the simplified models studied in this paper. Left: the "light slepton" model where $\tilde{l}$ is the next-to-lightest SUSY particle, Right: the "WZ" model where parent particles decay via W^* and Z^*.

This Thesis presents the study with two scenarios: 1.) the "light slepton" model where $\tilde{l}$ is the next-to-lightest SUSY particle, 2.) the "WZ" model where $\tilde{\chi}_1^\pm$ and $\tilde{\chi}_2^0$ decay via W^* and Z^*. These models differ in terms of branching ratio of $\tilde{\chi}_1^\pm$ and $\tilde{\chi}_2^0$ to leptonic final states. For the sleptonic decay model, the mass of intermediate particles is calculated in terms of variable $x_{\tilde{l}}$ as:

$$m_{\tilde{l}} = m_{\tilde{\chi}_1^0/LSP} + x_{\tilde{l}}(m_{\tilde{\chi}_1^\pm} - m_{\tilde{\chi}_1^0}) \tag{2.11}$$

where $0 < x_{\tilde{l}} < 1$. Here $x_{\tilde{l}}$ is taken 0.5 because three sleptons $(m_{\tilde{e}}, m_{\tilde{\mu}}, m_{\tilde{\tau}})$ are light.

2.4.1 Compressed SUSY Scenarios

Compressed SUSY scenarios refer [22] to a situation where the mass-splitting between next-to-SUSY and SUSY particles are very small i.e.mass between pair produced parent superparticle (in our case stau ($\tilde{\tau}$)) and the LSP ($\tilde{\chi}_1^0$) is very small. The pictorial comparison between the compressed mass scenario and normal scenario is shown in Figure 2.4.

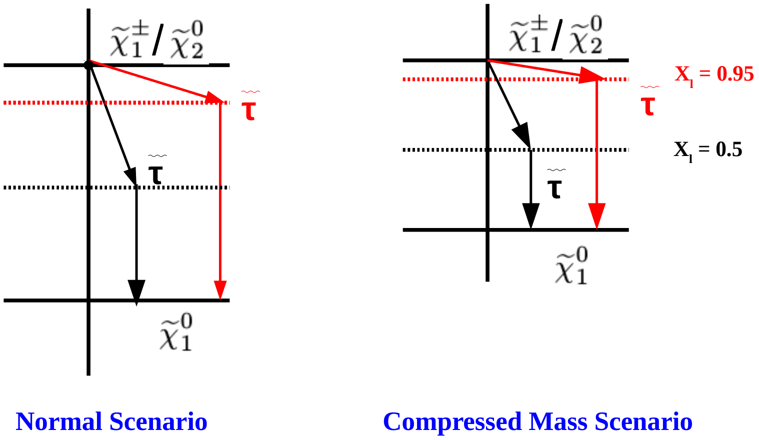

Figure 2.4: Comparison between Normal and Compressed mass scenarios. The black lines (dotted) represents the scenario where mass of stau is the average of mass of chargino and LSP (x=0.5) and a red dotted line represents the scenario where the mass of stau is closer to chargino mass (i.e. x =0.95).

These scenarios are experimentally challenging as the final state particle (LSP) is too soft to detect and also the variables used to distinguish between signal and background, based on large transverse momentum and missing transverse energy are less efficient. Various analysis techniques are developed to probe compressed mass scenarios. The analysis presented in this Thesis focuses on the electroweak SUSY sector using the Vector Boson Fusion (VBF) topology to look for these scenarios which is also helpful in reducing SM backgrounds to a great extent. Compressed scenarios involving electroweakinos are common in SUSY searches. In this Thesis, we have considered $\Delta m = m_{\tilde{\chi}_1^\pm/\tilde{\chi}_2^0} - m_{\tilde{\chi}_1^0} = 1, 10, 30, 50$ GeV.

2.5 SUSY Searches at LHC

SUSY searches can be done from direct as well as indirect measurements. The study presented in this Thesis corresponds to direct measurements of SUSY particles. SUSY searches have been already begun before the LHC era, by Large Electron Proton (LEP) colliders and Tevatron colliders, etc. These colliders have earlier established some exclusion limits on charginos and other sleptons production but later updated by LHC results. The LHC presented the first study on SUSY searches with 8 TeV data excluding gluino masses below 700 GeV at 95% confidence level [23]. LHC is a proton-proton collider, so the production of gluon-gluon and quark-gluon (strongly interacting particles) is larger than electroweakinos ($\alpha_W^2 \sim \alpha_s^2/250$) [24] as seen in Figure 2.5. The production of gluinos dominates because of their colored nature followed by squark and anti-squark ($q\bar{q}$) productions. Electroweakinos production is several order of magnitude smaller than gluinos and squarks production, but these processes become more interesting with larger data sets that counterbalance the low production cross section. The electroweakinos are followed by sleptons production which are suppressed due to the presence of s-channel [25] diagrams in their productions. As already stated, SUSY particles are always produced in pairs (one sparticle + one SM) and have LSP in the final state, conserving R-parity. LSP being in the final state creates momentum imbalance so most of the LHC SUSY

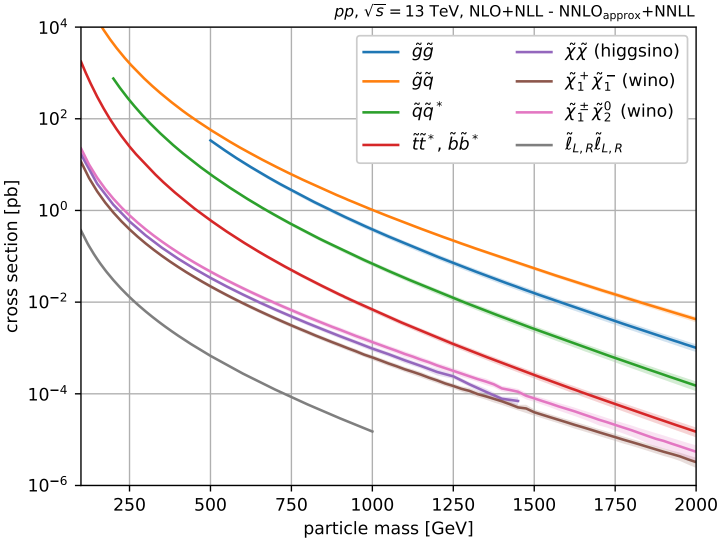

Figure 2.5: Production cross section of various SUSY processes at 13 TeV.

searches consist of missing transverse energy, jets, and leptons depending on mass spectra and sparticles involved.

2.5.1 SUSY Searches for Squarks and Gluinos

The gluinos and squarks decay usually results in a large number of secondary particles. If $m_{\tilde{q}} > m_{\tilde{g}}$ squarks will decay to a quark and a gluino ($\tilde{q} \to q\tilde{g}$) and if $m_{\tilde{q}} < m_{\tilde{g}}$, it will decay to neutralino/chargino ($\tilde{\chi}^0_2/\tilde{\chi}^{\pm}_1$) along with one SM quark. The decay to LSP with one SM quark is kinematically favored. On the other hand, gluinos can only decay to squarks either on-shell or virtual. If $m_{\tilde{g}} > m_{\tilde{q}}$, it will decay to $q\tilde{q}$ and if $m_{\tilde{g}} < m_{\tilde{q}}$, it will decay to neutralino/chargino ($\tilde{\chi}^0_2/\tilde{\chi}^{\pm}_1$) along with two SM quarks. The main decay modes of superpartners produced by colored SUSY particles (together with their signatures at detector level) are presented in Table 2.2.

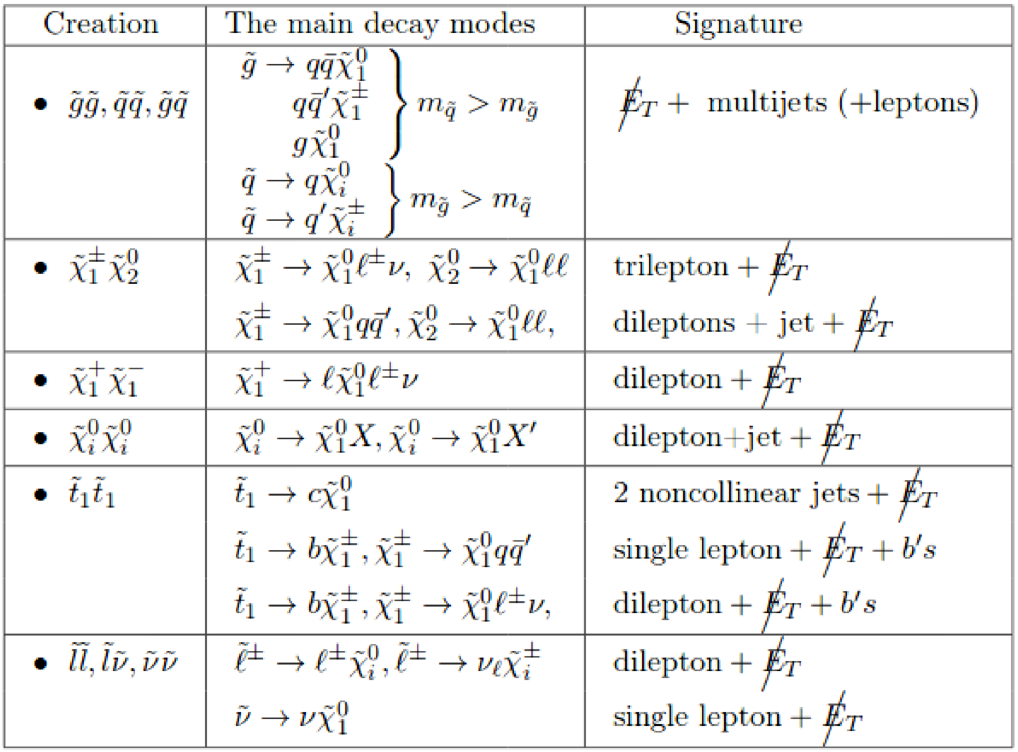

Creation	The main decay modes	Signature
• $\tilde{g}\tilde{g}, \tilde{q}\tilde{q}, \tilde{g}\tilde{q}$	$\left.\begin{array}{l}\tilde{g} \to q\bar{q}\tilde{\chi}^0_1 \\ \quad q\bar{q}'\tilde{\chi}^{\pm}_1 \\ \quad g\tilde{\chi}^0_1\end{array}\right\\} m_{\tilde{q}} > m_{\tilde{g}}$ $\left.\begin{array}{l}\tilde{q} \to q\tilde{\chi}^0_i \\ \tilde{q} \to q'\tilde{\chi}^{\pm}_i\end{array}\right\\} m_{\tilde{g}} > m_{\tilde{q}}$	$\not\!\!E_T +$ multijets (+leptons)
• $\tilde{\chi}^{\pm}_1\tilde{\chi}^0_2$	$\tilde{\chi}^{\pm}_1 \to \tilde{\chi}^0_1\ell^{\pm}\nu,\ \tilde{\chi}^0_2 \to \tilde{\chi}^0_1\ell\ell$ $\tilde{\chi}^{\pm}_1 \to \tilde{\chi}^0_1 q\bar{q}', \tilde{\chi}^0_2 \to \tilde{\chi}^0_1\ell\ell,$	trilepton + $\not\!\!E_T$ dileptons + jet + $\not\!\!E_T$
• $\tilde{\chi}^{+}_1\tilde{\chi}^{-}_1$	$\tilde{\chi}^{+}_1 \to \ell\tilde{\chi}^0_1\ell^{\pm}\nu$	dilepton + $\not\!\!E_T$
• $\tilde{\chi}^0_i\tilde{\chi}^0_i$	$\tilde{\chi}^0_i \to \tilde{\chi}^0_1 X, \tilde{\chi}^0_i \to \tilde{\chi}^0_1 X'$	dilepton+jet + $\not\!\!E_T$
• $\tilde{t}_1\tilde{t}_1$	$\tilde{t}_1 \to c\tilde{\chi}^0_1$ $\tilde{t}_1 \to b\tilde{\chi}^{\pm}_1, \tilde{\chi}^{\pm}_1 \to \tilde{\chi}^0_1 q\bar{q}'$ $\tilde{t}_1 \to b\tilde{\chi}^{\pm}_1, \tilde{\chi}^{\pm}_1 \to \tilde{\chi}^0_1\ell^{\pm}\nu,$	2 noncollinear jets + $\not\!\!E_T$ single lepton + $\not\!\!E_T + b's$ dilepton + $\not\!\!E_T + b's$
• $\tilde{l}\tilde{l}, \tilde{l}\tilde{\nu}, \tilde{\nu}\tilde{\nu}$	$\tilde{\ell}^{\pm} \to \ell^{\pm}\tilde{\chi}^0_i, \tilde{\ell}^{\pm} \to \nu_{\ell}\tilde{\chi}^{\pm}_i$ $\tilde{\nu} \to \nu\tilde{\chi}^0_1$	dilepton + $\not\!\!E_T$ single lepton + $\not\!\!E_T$

Table 2.2: Creation of superpartners in several channels with their main decay modes and detector signatures [26].

For the search of SUSY, a large number of physics analysis has been performed with CMS and ATLAS detectors at 8 TeV [8, 9] and 13 TeV [29] center-of-mass energies. Figure 2.6 (left) shows the limits on gluinos mass established at 95% confidence level (CL) by CMS detector at 13 TeV, where gluino decays to a pair of top-antitop quark and the LSP [29]. Gluinos with masses around ~ 2.1 GeV are excluded at 95% CL [29]. Figure 2.6 (right) [29] shows the upper limits at 95% CL where stop quarks is decaying to top quark and LSP. Depending on scenarios, stop quarks are excluded having a mass around 1.2 GeV.

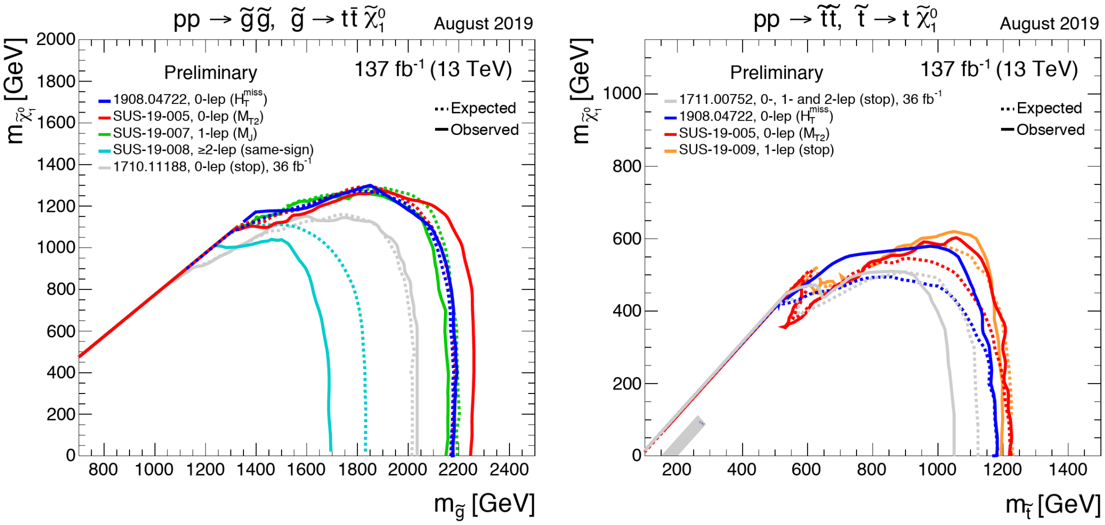

Figure 2.6: Left: 95% CL upper limit on the mass of the gluinos with Run-II data where gluino is decaying into a pair of top-antitop quark. Right: Exclusion limit at 95% CL on stop quark mass where stop quark is decaying to top quark and LSP, leading to a final state with two bottom quarks, two W bosons and two LSPs.

2.5.2 Electroweak SUSY Searches

The production of electroweak (EW) SUSY particles (electroweakinos - $\tilde{\chi}_1^{\pm}$, $\tilde{\chi}_2^0$ and $\tilde{\chi}_1^0$) are allowed directly as they are lighter than colored sparticles. They are produced along with leptons, jets and missing transverse energy in the final state which means that the decay chains of these channels are less complex than those of the colored sector making the searches simpler from the experimental point of view.

Since the electroweak particles suffer from smaller production cross section at LHC, the exclusion limits on this sector are less constrained as compared to the colored sector. Figure 2.7 shows the exclusion limit for different masses of $\tilde{\chi}_1^0$ as a function of $m_{\tilde{\chi}_1^\pm/\tilde{\chi}_2^0}$ obtained by CMS collaboration for the production of $\tilde{\chi}_1^\pm/\tilde{\chi}_2^0$ pair from different decay modes (via sleptons and W/Z/H). The two gauginos are assumed to have

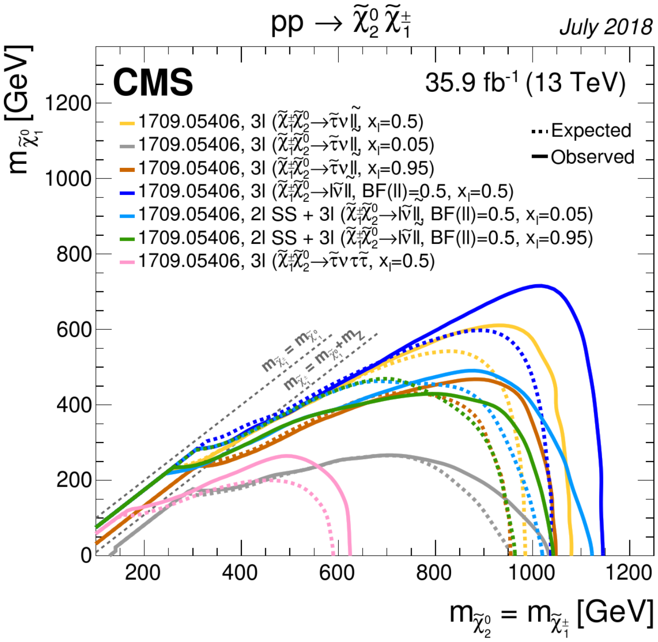

Figure 2.7: Expected (dashed lines) and observed (solid lines) upper limits at 95% CL on masses of chargino/neutralino and LSP at $\sqrt{s} = 13$ TeV [29].

the same mass as they belong to the same gauge group. The chargino/neutralino masses are excluded up to ∼ 1.1 TeV at 95% CL. But for compressed mass scenarios (where the mass difference between parent and daughter sparticles is very small) the limits are weaker as the particles in the final states have very low transverse momentum which makes it difficult to differentiate them from their corresponding SM backgrounds. Hence, electroweak SUSY searches through compressed mass spectra is a good way to probe SUSY particles.

The complete picture of the different SUSY searches (gluinos, squarks and electroweak) done by CMS Collaboration at $\sqrt{s}$= 13 TeV is shown in Figure 2.8.

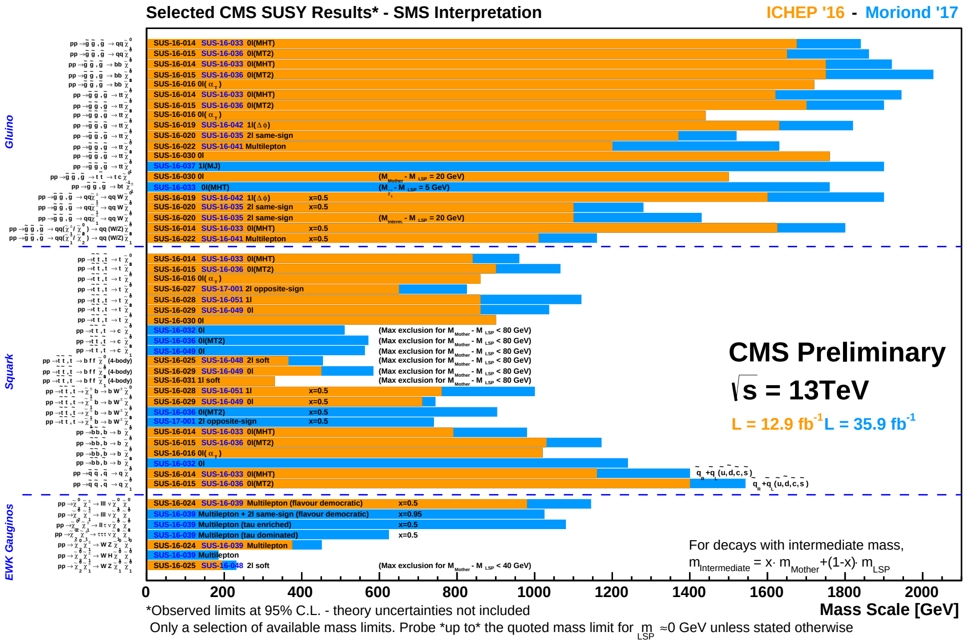

Figure 2.8: Different SUSY searches performed by CMS Collaboration at $\sqrt{s} = 13TeV$ in SMS framework. The orange colored searches are done with 12.9 fb^{-1} and same search is carried out with full 2016 data i.e. 35.9 fb^{-1} represented in blue color.

2.6 Electroweakinos Searches through VBF Topology

As already explained in the Subsection 2.5.1, gluinos and squarks are excluded up to the high mass range which indicates they are too heavy to be produced at LHC. As a consequence, electroweak SUSY production can be a possible way to probe new physics. One powerful tool for electroweak searches is through vector boson fusion processes that are appropriate for compressed mass scenarios [30]. VBF processes are used especially to observe a phenomenon where the signal rates are small. VBF processes occur in t-channel [31], in which incoming quarks radiate vector bosons that undergo fusion giving the particle under study (i.e. $W^{\pm}$, Z, higgs or other sparticles like $\tilde{\chi}_1^{\pm}/\tilde{\chi}_2^0$) as shown in Figure 2.9. The jets produced are highly boosted (energetic) and are in the forward area of the detector having large dijet

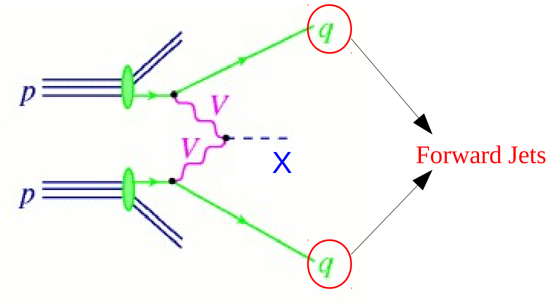

Figure 2.9: Vector Boson fusing together giving a particle (SM or SUSY) and two forward jets.

invariant mass with a large pseudorapidity gap in the opposite hemispheres of the detector. Other decay particles produced are usually in the central region of the detector. VBF processes are useful in reducing SM background to a good extent as the forward jets help to differentiate the QCD background. Also these high p_{T} jets permit the analysis to apply triggers designed to select events with this type of signature. These processes have small production cross section at higher mass, but benefits from less contamination which means great sensitivity at high mass regions. The VBF processes have been earlier used for Higgs boson searches in high mass region [32] but now they are used for VBF production of single gauge boson and extended to study the production of diboson. Various theoretical and experimental searches [30, 33] have been done with compressed mass scenarios where the staus and charginos are having almost same mass and provides correct dark matter relic density estimated by cosmology [34]. The VBF topology has also been utilized to study the new physics where the Higgs is decaying to invisible particles in different models like decay to neutralinos in SUSY models or graviscalars in models with extra dimensions [35, 36].

Coming back to present scenarios as seen in Figure 2.7, the charginos and neutralinos are excluded up to masses of around 1.1 TeV but the limits get weaker as the things approach compressed mass scenarios. Since the staus ($\tilde{\tau}$) mass is lighter than first and second-generation squarks i.e. $\tilde{\mu}$ and $\tilde{e}$ for large tanβ (tanβ

is the ratio of non-zero VEV (v_u/v_d) attained by H_u^0 and H_d^0), so the searches with stau are motivated in MSSM due to the enhancement of the $h \rightarrow \gamma\gamma$ channel [37]. Consequently, it is necessary to search for the SUSY particles in the final state consisting of low p_{T} leptons, especially taus. But staus in the final state are difficult to reconstruct in the compressed mass scenario because of large jet $\rightarrow \tau$ fake rate. The VBF topology is a complementary tool to investigate electroweak searches where classic searches have no experimental reach. The first-ever SUSY search utilizing the VBF dijet topology to look for $\tilde{\chi}_1^{\pm}/\tilde{\chi}_2^0$ using proton-proton collision data at $\sqrt{s}$ = 8 TeV having 19.7 fb^{-1} integrated luminosity is summarized in [38]. Although, no excess of data is found over SM backgrounds but an upper limit of 170 GeV is set on the mass of $\tilde{\chi}_1^{\pm}/\tilde{\chi}_2^0$ having 50 GeV mass gap between $\tilde{\chi}_1^0$ and $\tilde{\chi}_1^{\pm}/\tilde{\chi}_2^0$. Earlier, these scenarios with 50 GeV mass gap and light staus were not excluded by any other CMS electroweak SUSY searches.

In this thesis, we report about the SUSY search through VBF topology using proton-proton collision data collected with the CMS detector corresponding to an integrated luminosity of 35.87 fb^{-1}. The complete details of the analysis are presented in Chapter 6.

This Chapter briefly describes the Supersymmetry and the solutions to solve the shortcoming of the Standard Model. The MSSM model, which is the motivation for the study presented in this Thesis is also discussed in detail. An overview of SUSY breaking scenarios and motivation to study electroweak SUSY searches through VBF topology is also presented. In the next Chapter, the experimental details of LHC, its parameters and CMS detector are described.

Bibliography

[1] H. P. Nilles, “Supersymmetry, supergravity and particle physics”, *Phys. Rept.*, vol. 110 (1984), https://doi.org/10.1016/0370-1573(84)90008-5.

[2] P. Ramond, “Dual theory for free fermions”, *Phys. Rev. D*, vol. 3 (1971), https://doi.org/10.1103/PhysRevD.3.2415.

[3] S. Ferrara and B. Zumino, “Supergauge invariant Yang-Mills theories”, *Nucl. Phys. B*, vol. 79 (1974), https://doi.org/10.1016/0550-3213(74)90559-8.

[4] A. Salam and J. Strathdee, “Super-symmetry and non-Abelian gauges”, *Phys. Lett. B*, vol. 51 (1974), https://doi.org/10.1016/0370-2693(74)90226-3.

[5] L. J. Hall, J.D. Lykken and S. Weinberg, “Supergravity as the messenger of supersymmetry breaking”, *Phys. Rev. D*, vol. 27 (1983), https://doi.org/10.1103/PhysRevD.27.2359.

[6] S. P. Martin, “A Supersymmetry primer”, *Adv. Ser.Direct. High Energy Phys.*, vol. 18 (1998), https://doi.org/10.1142/9789812839657_0001.

[7] W. de Boer, “Grand unified theories and supersymmetry in particle physics and cosmology”, *Progress in Particle and Nucl. Phys.*, vol. 33 (1994), https://doi.org/10.1016/0146-6410(94)90045-0.

[8] P. Nath and R. Arnowitt, “Generalized super-gauge symmetry as a new framework for unified gauge theories”, *Phys. Lett. B*, vol. 56 (1975), https://doi.org/10.1016/0370-2693(75)90297-X.

[9] L. Pape and D. Treille, “Supersymmetry facing experiment: Much ado (already) about nothing (yet)”, *Rept. Prog. Phys.*, vol. 69 (2006), https://doi.org/10.1088/0034-4885/69/11/R01.

[10] G. M. Prosperi, M. Raciti and C. Simolo, “On the running coupling constant in QCD”, *Progress in Particle and Nucl. Phys.*, vol. 58 (2007), https://doi.org/10.1016/j.ppnp.2006.09.001.

[11] M. Göckeler, R. Horsley, V. Linke, P.E.L. Rakow, G. Schierholz, and H. Stüben, “Is there a Landau pole problem in QED?”, *Phys. rev. Lett.*, vol. 80 (1998), https://doi.org/10.1103/PhysRevLett.80.4119.

[12] K. A. Olive *et al.*, “Review of Particle Physics”, *Chinese. Phys. C*, vol. 40 (2016), https://doi.org/10.1088/1674-1137/40/10/100001.

[13] S. Dimopoulos and D.W Sutter, “The Supersymmetric flavor problem”, *Nucl. Phys. B*, vol. 452 (1995), https://doi.org/10.1016/0550-3213(95)00421-N.

[14] J. A. Bagger, “Weak-Scale Supersymmetry: Theory and Practice”, *High Energy Phys. - Phen.*, (1996), `arXiv:hep-ph/9604232v2`.

[15] A. Djouadi *et al.*, “The Minimal Supersymmetric Standard Model: Group Summary Report”, *High Energy Phys. - Phen.*, (1999), `arXiv:hep-ph/9901246v1`.

[16] R. Barbier *et al.*, “R-parity violating supersymmetry”, *Phys. Rept.*, vol. 420 (2005), https://doi.org/10.1016/j.physrep.2005.08.006.

[17] D. J. H. Chung, L. L. Everett, G. L. Kane, S. F. King, J. D. Lykken, and L.-T. Wang, “The Soft supersymmetry breaking La-

grangian: Theory and applications", *Phys. Rept.*, vol 407 (2005), https://doi.org/10.1016/j.physrep.2004.08.032.

[18] A. H. Chamseddine, R. L. Arnowitt, and P. Nath, "Locally Supersymmetric Grand Unification", *Phys. Rev. Lett.*, vol. 49 (1982), https://doi.org/10.1103/PhysRevLett.49.970.

[19] C. F. Kolda, "Gauge mediated supersymmetry breaking: Introduction, review and update", *Nucl. Phys. B - Proc. Supp.*, vol. 62 (1998), https://doi.org/10.1016/S0920-5632(97)00667-1.

[20] D. Alves *et al.*, "Simplified Models for LHC New Physics Searches", *J. Phys. G: Nucl. and Part. Phys.*, vol. 39 (2012), https://doi.org/10.1088/0954-3899/39/10/105005.

[21] The CMS Collaboration, "Interpretation of Searches for Supersymmetry with simplified Models", *Phys. Rev. D*, vol. 88 (2013), https://doi.org/10.1103/PhysRevD.88.052017.

[22] A. Nelson, P. Tanedo, and D. Whiteson, "Limiting SUSY compressed spectra scenarios", *Phys. Rev. D*, vol. 93 (2016), https://doi.org/10.1103/PhysRevD.93.115029.

[23] The ATLAS Collaboration, "Search for supersymmetry using final states with one lepton, jets, and missing transverse momentum with the ATLAS detector in $\sqrt{s}$ = 7 TeV pp", *Phys. Rev. Lett.*, vol. 106 (2011), https://doi.org/10.1103/PhysRevLett.106.131802.

[24] P. Bechtle, T. Plehn, and C. Sander,"Supersymmetry", *The Large Hadron Collider : Harvest of Run 1*(T. Schrner-Sadenius, ed.), (2015).

[25] D. H. Perkins, "Introduction to high energy physics", *Addison-Wesley*, (1982).

[26] A. V. Gladyshev and D. I. Kazakov, “Supersymmetry and LHC”, *Phys. of Atomic Nuclei*, vol. 70 (2007), https://doi.org/10.1134/S1063778807090104.

[27] “8 and 13 TeV Analysis from the ATLAS Supersymmetry physics group”, `https://twiki.cern.ch/twiki/bin/view/AtlasPublic/SupersymmetryPublicResults`.

[28] “8 TeV Analysis from the CMS Supersymmetry physics group”, `https://twiki.cern.ch/twiki/bin/view/CMSPublic/SUSYSMSSummaryPlots8TeV`.

[29] “ 13 TeV Analysis from the CMS Supersymmetry physics group” `https://twiki.cern.ch/twiki/bin/view/CMSPublic/PhysicsResultsSUS`.

[30] B. Dutta, A. Gurrola, W. Johns, T. Kamon, P. Sheldon, and S. Kuver, “Vector Boson Fusion Processes as a Probe of Supersymmetric Electroweak Sectors at the LHC”, *Phys. Rev. D*, vol. 87 (2013), https://doi.org/10.1103/PhysRevD.87.035029.

[31] F. Halzen and Alan D. Martin, “Quarks and Leptons: An Introductory Course in Modern Particle Physics”, *New York, USA: Wiley*, (1984), `http://inspirehep.net/record/205394?ln=en`.

[32] The CMS Collaboration, “Search for a standard-model-like Higgs boson with a mass in the range 145 to 1000 GeV at the LHC”, *Eur. Phys. J. C*, vol. 73 (2013), https://doi.org/10.1140/epjc/s10052-013-2469-8.

[33] M. Carena, S. Gori, N.R. Shah, C.E. Wagner, and L.-T. Wang, “Light Stau Phenomenologyand the Higgs $\gamma\gamma$ Rate”, *JHEP*, vol. 1207 (2012), https://doi.org/10.1007/JHEP07(2012)175.

[34] K. Griest and D. Seckel, “Three exceptions in the calculation of relic abundances”, *Phys. rev. D*, vol. 43 (1991), https://doi.org/10.1103/PhysRevD.43.3191.

[35] The CMS Collaboration, “Search for invisible decays of Higgs bosons in the vector boson fusion and associated ZH production modes”, *Eur. Phys. J. C*, vol. 74 (2014), https://doi.org/10.1140/epjc/s10052-014-2980-6.

[36] The ATLAS Collaboration, “Search for invisible decays of a Higgs boson using vector-boson fusion in pp collisions at $\sqrt{s} = 8$ TeV with the ATLAS detector”, *JHEP*, vol. 01 (2016), https://doi.org/10.1007/JHEP01(2016)172.

[37] M. Carena, S. Gori, N.R. Shah, C.E. Wagner, “A 125 GeV SM-like Higgs in the MSSM and the $\gamma\gamma$ Rate”, *JHEP*, vol. 3 (2012), https://doi.org/10.1007/JHEP03(2012)014.

[38] The CMS Collaboration, “Search for supersymmetry in the vector-boson fusion topology in proton-proton collisions at $\sqrt{s} = 8$ TeV”, *JHEP*, vol. 11 (2015), https://doi.org/10.1007/JHEP11(2015)189.

Chapter 3

Experimental Setup

This Chapter describes the experimental setup employed to collect the data used for the work presented in this Thesis. The first half explains the Large Hadron Collider (LHC) machine layout, how it is operated to bring out particle collisions and the current data-taking environment. The other half is completely dedicated to Compact Muon Solenoid (CMS) detector and its subdetectors which has been used for data taking.

3.1 CERN - The Largest Particle Physics Laboratory

The establishment of CERN - European Organization for Nuclear Research was approved on 29 September, 1954 by 12 countries in Europe. As the name suggests, this lab was initially assigned to study atomic nuclei, but then soon extended to high-energy physics to probe the interactions among subatomic particles. Nowadays CERN is considered as the most prestigious particle physics research laboratory world-wide. The main purpose of CERN is to facilitate the use of particle accelerators and other infrastructure required for high-energy physics research. CERN has some monumental discoveries in the field of particle physics. The discovery of weak

neutral currents in 1973 inside Gargamelle bubble chamber, W and Z bosons in 1983 by colliding protons and anti-protons, producing the antimatter inside a laboratory in 1995 and Charge-Parity (CP) violation in 1999 are some of the tremendous findings of CERN before the Large Hadron Collider (LHC) [1] era started. However the most significant physics harvest at CERN is the discovery of the final piece of Standard Model (SM), the Higgs Boson with a mass around 125 GeV/c^2 on 4 July, 2012 by LHC experiments. This led to the award of Noble Prize in Physics in year 2013 to theoreticians Peter Higgs and Francois Englert who among others, predicted theoretically the existence of Higgs Boson [2–4].
The exact description of the LHC machine as well as its detectors is addressed in the next segments.

3.2 The Large Hadron Collider

The LHC at CERN is currently the world's most powerful circular hadron accelerator ever built in the existing tunnel of Large Electron-Positron (LEP) [5] collider which ended its operation in the year 2000. The LHC is buried about 100 meters deep underground in between Geneva lake (Switzerland), the Jura Mountains and Cessy (France) spanning 27 km in circumference. The LHC is designed to accelerate two circular beams of protons coming from opposite directions up to a center-of-mass energy $\sqrt{s} = 14$ TeV with a peak instantaneous luminosity of 10^{34} cm^{-2} s^{-1}. Besides this, it also offers to collide lead-lead (Pb-Pb), proton-lead (p-Pb) and Xenon-Xenon (Xe-Xe) nuclei for the study of heavy-ion collisions at the center-of-mass energy $\sqrt{s}=$ 5.02, 8.16 and 5.44 TeV, respectively.

The LHC injected its first beam on 10th September, 2008, but due to some faulty electrical connection between the superconducting magnets it was stopped. Eventually after a year on 20th November, 2009 it gave us first proton-proton (pp) collisions at 900 GeV center-of-mass energy. Subsequently, on 30th March, 2010 the energy of proton beams was increased to 3.5 TeV leading to a center-of-mass energy $\sqrt{s} = 7$ TeV. The second period of data collection at $\sqrt{s} = 8$ TeV started on 5^{th} April, 2012 till 6^{th} February, 2013. This collision time-period (2010-2013) is known as **"Run I"** of the LHC. After a two-year-long shutdown (LS1) for upgrades, the LHC started its operation again in 2015 known as **"Run II"** with each proton beam of energy 6.5 TeV giving center-of-mass energy $\sqrt{s} = 13$ TeV. On 3^{rd} December, 2018 Run II ended after furnishing a large amount of data and LHC entered a second long shutdown (LS2) period. After LS2, LHC **"Run III"** is scheduled at $\sqrt{s} = 14$ TeV between 2021-2024 with an expected integrated luminosity of 300 fb^{-1}. Further, accelerator infrastructure will be improved in long shutdown (LS3) period in order to achieve unprecedented instantaneous luminosity of 5.0 to 7.5 $\times$ 10^{34} cm^{-2} s^{-1} resulting in a total of 3000 to 4000 fb^{-1} of data for the full accelerator lifetime. The project is titled HL-LHC for High-luminosity LHC. Figure 3.1 illustrates the detailed timeline of LHC run operations. Before being injected into the LHC machine, protons are accelerated by a series of accelerators and each accelerator stage raises the energy of the protons plus transfers them to the next stage. The accelerator complex for the LHC is presented in the next Section.

Figure 3.1: Overview of the timeline for the HL-LHC upgrade [6].

3.2.1 The CERN Accelerator Complex

The LHC has two main injection lines, one optimized for protons and the other one for lead ions. Figure 3.2 shows the detailed diagram of LHC injection. Protons are extracted from a small canister of ionized hydrogen gas by applying a large electric field, and then initially accelerated to an energy of 50 MeV with radio-frequency (RF) cavities in the Linear Accelerator 2 (LINAC-2). Afterward, accelerated protons are sent to the Proton Synchrotron Booster (PSB), which is made up of four superimposed synchrotron rings that assemble the protons into bunches and accelerate them to 1.4 GeV. Six proton bunches are sequentially supplied to Proton Synchrotron (PS), where they are accelerated up to 25 GeV and then resolved into

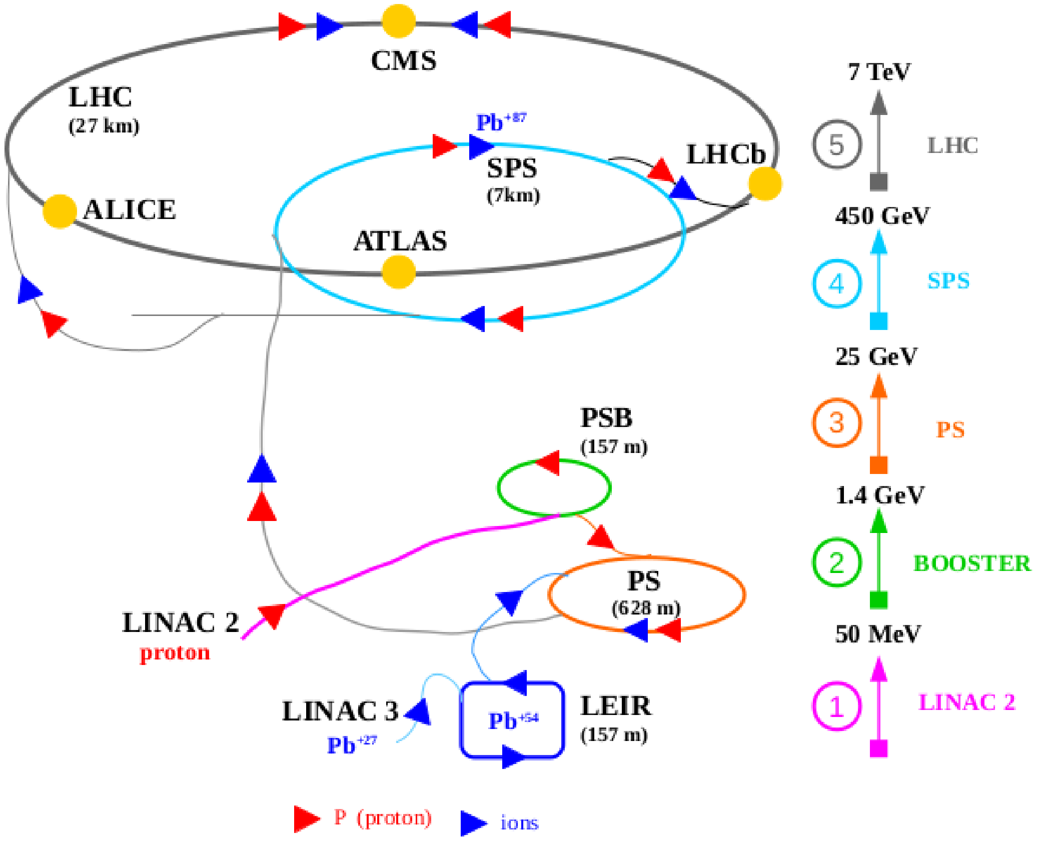

Figure 3.2: Detailed diagram of the LHC injection series for protons and Pb nuclei. The proton and lead ion trajectories are indicated with red and blue arrows respectively. The Position of four interaction points is also included.

72 bunches divided in time by 25 ns. From the PS, the separated proton bunches are accelerated in the Super Proton Synchrotron (SPS) to an energy of 450 GeV. The SPS divides the single beam into two counter-rotating ones and injects them in the LHC beam pipes. Common electromagnets are used to keep the particles circulating in the PSB, PS and SPS accelerators. Protons beams are accelerated for many hours to attain maximum energy of 7 TeV per beam within LHC. For Run I, the beam energy was 3.5 TeV & 4 TeV and increased to 6.5 TeV during Run II. In a planned year of running, LHC collides beams of protons for 6 to 7 months and one month is dedicated to heavy-ion collisions.

The LHC has eight direct sections called insertion regions (IR), connected by eight arc sections as shown in Figure 3.3. Series of superconducting magnets are used to control the size of bunch and trajectory of the particles. Superconductivity in the magnet is attained by a closed circuit of superfluid helium, which keeps the

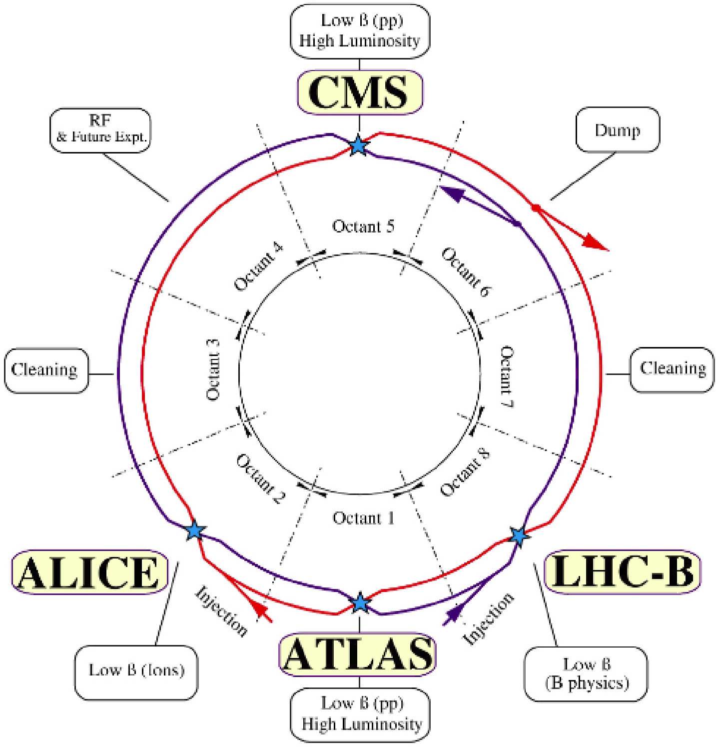

Figure 3.3: LHC schematic and the four main Interaction Points [7].

temperature to 1.9°K. Dipole magnets are employed to bend the trajectory of the particles, while quadrupole magnets are used for focusing the beam. The main four insertion regions house each of the four LHC detectors, where the beams are made to collide at the center of each detector as described below:

- **A Toroidal LHC ApparatuS (ATLAS)**: It is a general-purpose particle detector located at interaction points (IP) 1 or IP1, designed to cover an extensive range of precise measurements of the possible physics processes such as electroweak and strong physics [8]. The detector is formulated especially to provide the best possible sensitivity to Higgs boson and *New Physics* such as Supersymmetry (SUSY), dark matter, extra dimensions, etc.
- **Compact Muon Solenoid (CMS)**: It is a general-purpose particle detector located at IP5, having the identical design as an ATLAS detector covering the same physics goals [9].
- **A Large Ion Collider Experiment (ALICE)**: It is a particle detector located at IP2, dedicated to the measurements of the properties of nuclear matter at high energy densities [10]. The focus of the ALICE detector is the study of Quark-Gluon Plasma (QGP) [11] and different features of heavy-ion physics such as proton-lead and lead-lead collisions.
- **Large Hadron Collider beauty (LHCb)**: It is a single-sided spectrometer located at IP8, builds to study matter-antimatter asymmetry puzzle and to measure CP-violation parameters [12]. It aims to study physics with hadrons originating from b quarks. *The biggest discovery of LHCb Collaboration at CERN is the observation of a phenomenon, the matter-antimatter asymmetry known as CP violation in the decays of a particle known as* D^0 *meson for the first time* [13,14].

India contributes mainly to CMS and ALICE experiments at LHC.

3.2.2 LHC Parameters and Performance

The LHC is a two-ring superconducting proton accelerator and collider designed to explore TeV energy scale. The design of LHC depends on very basic principles associated with the latest technology. The main components of LHC are explained:

- **The LHC Magnets**: Within the LHC ring, to keep the energetic protons beams circulating throughout, 1232 dipole magnets with a central field in the range of 0.54 T (for 450 GeV proton energy) to 8.33 T (for 7 TeV proton energy) are used. In addition to dipole magnets, LHC uses around 850 quadrupole magnets out of which 392 lattice quadrupoles turn out much stronger as they aim to keep the proton beams confine along the four LHC collision points, to increase the probability of bunch interactions. Octupole and Sextuple magnets are also used for correcting the size and position of the beam. The LHC magnets are made up of niobium-titanium (NbTi) and are cooled down to 1.9°K using $\sim$ 96 tonnes of superfluid helium in the cryogenic system to create a strong magnetic field that is needed at the LHC. As the protons are charged particles, it is important to focus the beam and retain it in the ultrahigh vacuum chamber.

- **Center-of-mass Energy**: The center-of-mass energy ($\sqrt{s}$) of a system of particles, is the energy measured in the center-of-mass reference frame (E_{COM}) given as:

  $$E_{COM} = \sqrt{s} = \sqrt{(E_1 + E_2)^2 - (\vec{p_1} + \vec{p_2})^2} \tag{3.1}$$

  where E is the energy and $\vec{p}$ represents the momentum of the two initial-state particles. For the collider experiments, where head-on collisions of two particles take place, the center-of-mass energy is given by:

  $$\sqrt{s} = 2E_{beam} \qquad if \quad E_{beam} >> m_i \tag{3.2}$$

where E_{beam} is the energy of two incoming beams and m_i is the mass of interacting particles.

3.2.3 Beam Luminosity Measurements at the LHC

The performance of the LHC can be characterized on the basis of luminosity delivered. Higher the luminosity of the collider, more is the occurrence of particle interactions when the beams collide. The number of events produced for a specific process varies linearly with cross section defined as:

$$L = \frac{N_{events}}{\sigma_{process}} \tag{3.3}$$

where N_{event} represents the number of events that occur in cross section, $\sigma_{process}$. The instantaneous luminosity $\mathcal{L}$ is given by:

$$\mathcal{L} = \frac{1}{\sigma}\frac{dN}{dt} \tag{3.4}$$

In the case of circular beam profiles, the instantaneous luminosity depends upon various beam parameters:

$$\mathcal{L}_{inst} = \frac{\gamma f k_B N_p^2}{4\pi\epsilon_n\beta^*}F \tag{3.5}$$

The terms *f*, γ, k_B, N_p, β^*, ϵ_n and F in Equation 3.5 represents the revolution frequency at the LHC, relativistic Lorentz factor, number of bunches, number of particles per bunch, Betatron function defined at IP, transverse beam emittance and geometric reduction factor due to the angle at which beams collide, respectively. The integrated luminosity is derived by integrating the instantaneous luminosity over a given period of time. The integral is taken over the sensitive time, i.e., excluding the possible dead time of the LHC.

$$\mathcal{L}_{int} = \int_{t_0}^{t_1} L_{inst} dt \tag{3.6}$$

The $\mathcal{L}_{int}$ has dimensions of $\frac{1}{area}$, so the number of events produced per sec for a process of σ_p in LHC collisions are given as N = $\mathcal{L}_{int} \times \sigma p$. The left plot of Figure 3.4 shows the cumulative luminosity delivered to the CMS experiment in every year of data taking during Run I (2010-2012) and Run II (2015-2018). The analysis presented in this Thesis is based on the data collected by CMS detector at $\sqrt{s} = 13$ TeV during 2016 corresponding to an integrated luminosity of 35.9 fb^{-1}, as shown in the right plot of Figure 3.4. Total luminosity delivered by the LHC is 40.8 fb^{-1}, CMS recorded a total of 37.8 fb^{-1} but certified 35.9 fb^{-1} to be used for physics analyses. In CMS, the luminosity measurements are performed using signals from its two subdetectors: (a) the Forward Hadron Calorimeter (HF), and (b) the silicon pixel detector. The online measurement of luminosity is performed using HF which is capable of estimating the luminosity per bunch, whereas the offline measurement is done using a silicon pixel detector which is characterized by very low occupancy

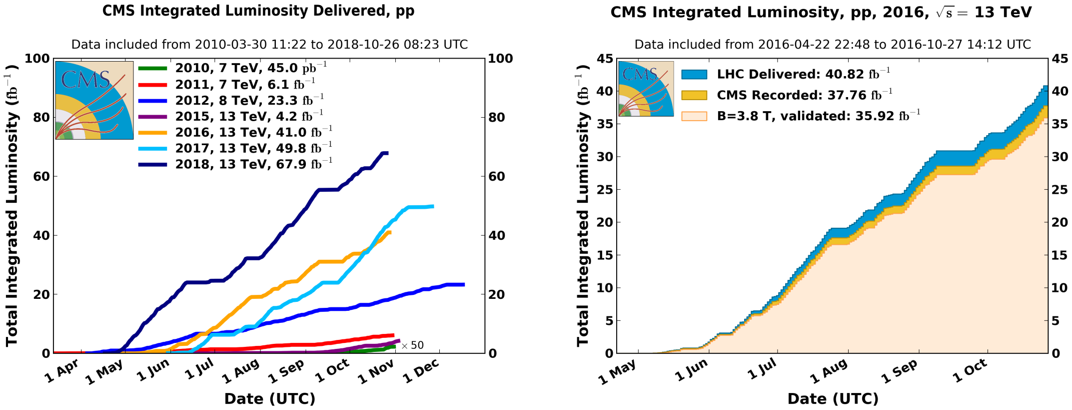

Figure 3.4: Left: Total integrated luminosity delivered by the LHC to the CMS for proton-proton collisions during Run I (from 2010 to 2012) and Run II (from 2015 to 2018) [15] Right: Total integrated luminosity delivered by the LHC to the CMS, and the total recorded versus validated luminosity by the CMS in 2016 for proton-proton collisions at 13 TeV [16].

and excellent stability over time.

3.2.4 Proton-Proton Collisions at LHC

At the LHC, accelerated protons moving in the opposite direction are made to collide head-on and undergoes various types of collisions processes.

Hard Scattering Processes:

Each proton consists of three valence quarks (uud) and a sea of $q\bar{q}$ pairs (sea quarks) which are held together by gluons that interact with them and exchange the color charge. Inner constituents of a proton are known as **"partons"**. Due to proton-proton interactions, many processes occur at the LHC. But the main process of interest is the **"Hard Scattering Process"**, which involves a high momentum transfer due to interactions between two partons. Figure 3.5 depicts the hard scattering proton-proton collision. The interactions between the rest of proton constituents that were not involved in hard scattering lead to the **"Underlying Events"** (UE). These partons may undergo soft scattering amongst themselves (Multiple Parton Scattering), may also radiate another gauge boson before and after they collide with each other known as **"Initial State Radiation"** (ISR) and **"Final State**

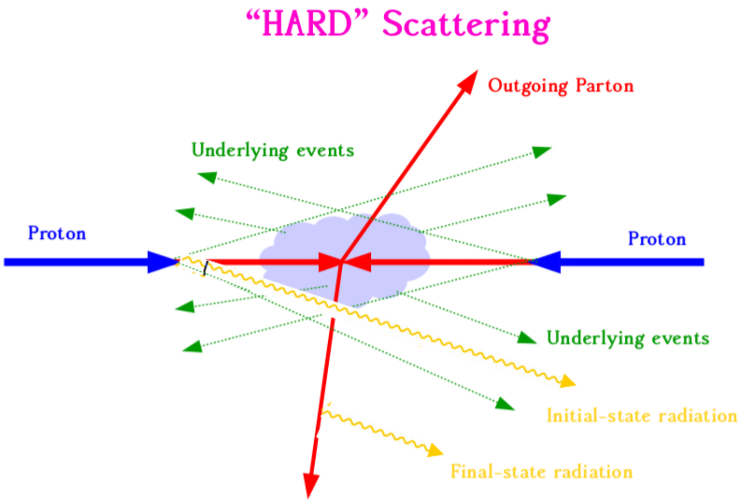

Figure 3.5: Schematic of a hard scattering proton-proton collision.

Radiation" (FSR) respectively.

Pileup Process: The LHC collides bunches and each bunch contains $\approx 10^{11}$ protons. This results in an increased chance of multiple proton-proton collisions in the same bunch crossing. On average $\backsim$ 23 collisions occur between different pairs of protons in every bunch crossing which leads to low p_T events called Pileup events. Figure 3.6 shows the mean number of interactions per bunch crossing in 2016 [15]. Table 3.1 represents some of the basic parameters designed and achieved during the year 2016 run.

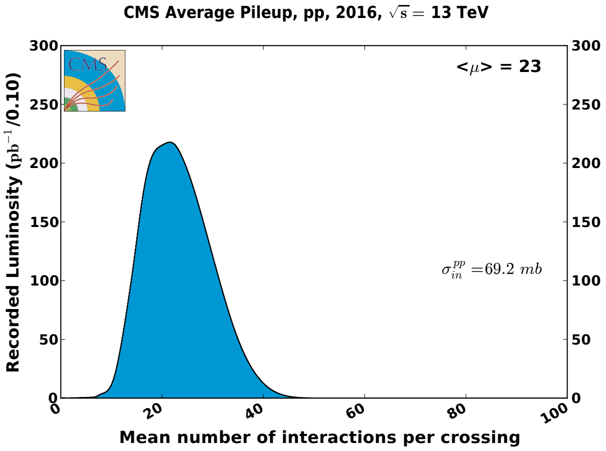

Figure 3.6: Mean number of interactions per bunch crossing at 13 TeV.

Parameters	Units	LHC Design	2016 LHC Operations
Center of Mass Energy	[TeV]	14	13
Proton Energy per beam	[TeV]	7	6.5
Bunch Spacing	[ns]	25	25
Peak Luminosity	[cm^{-2}s^{-1}]	1×10^{34}	1.45×10^{34}
β^*	[m]	0.55	0.4
Number of Bunches	N/A	2808	$\approx$ 2200
Proton per Bunch	N/A	1.15×10^{11}	1.1×10^{11}

Table 3.1: The designed LHC beam parameters and achieved for 2016 data.

3.3 The CMS Detector

The CMS detector is one of the two general-purpose detectors at the LHC, covering almost 4π and an entire range of physics opportunities provided by the proton-proton and heavy-ion collisions to measure SM processes precisely and to search for physics beyond the SM (BSM).The CMS detector is located in the underground hall, about 100 meters below at the IP5 of the LHC in the Cessy village of France. It is like a giant filter with onion structure, where each layer constitutes a subdetector designed to stop, track or measure different types of particle emerging from proton-proton or heavy-ion collisions as illustrated in Figure 3.7. Every layer takes a cylindrical shape and the subdetector components parallel to the beamline are referred to as the barrel regions while the ones closing the detector in the ±z direction are termed as endcap regions. The information from different layers about the energy, charge and momentum of a particle helps to build up its identity.

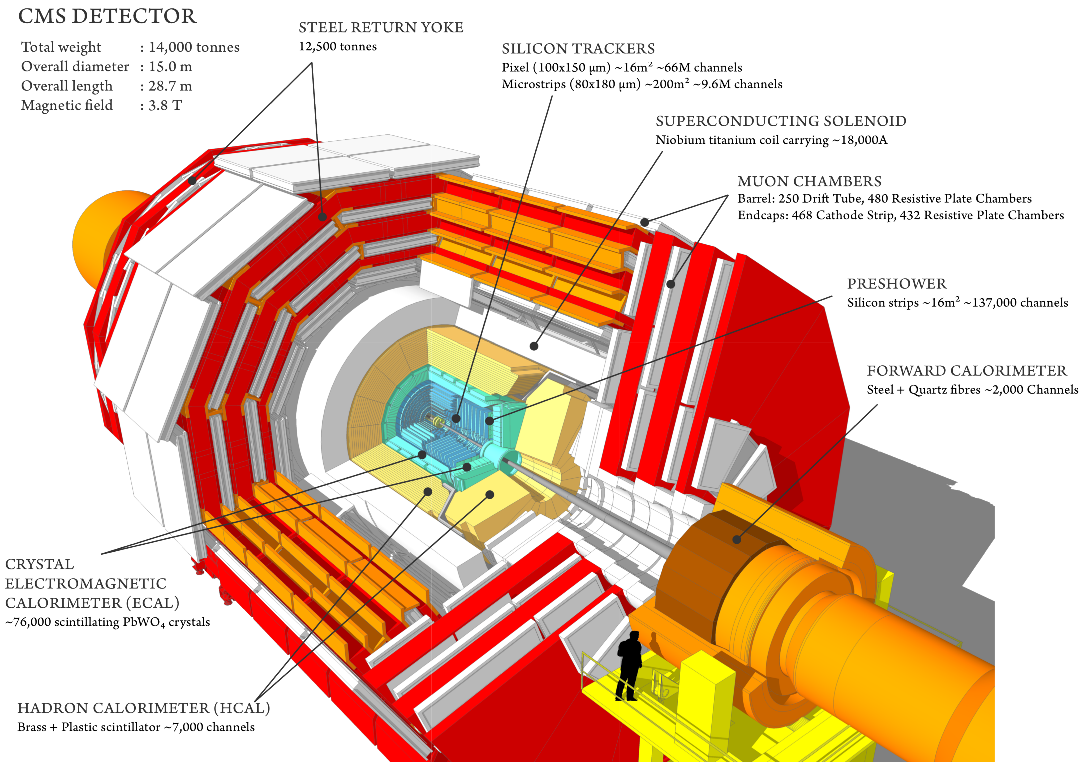

Figure 3.7: A perspective view of CMS detector and its subdetectors.

The heart of CMS detector i.e. superconducting solenoid provides a magnetic field of 3.8 T. The tracks of charged particles that are coming from the collisions are detected by the tracker system. Calorimeters (Electromagnetic and Hadron Calorimeter) that are placed outside the tracker, meant to stop the particles and measure their energy. The tracker and both the calorimeters are placed inside the coil of the magnet making it very compact. The iron return yoke with the return field of the solenoid around 2 T is located within the muon system. All the subdetectors of CMS are discussed in more detail in the coming Sections. Figure 3.8 shows the kind of signatures left by the passage of different types of the particles through the onion-like structure of the CMS detector.

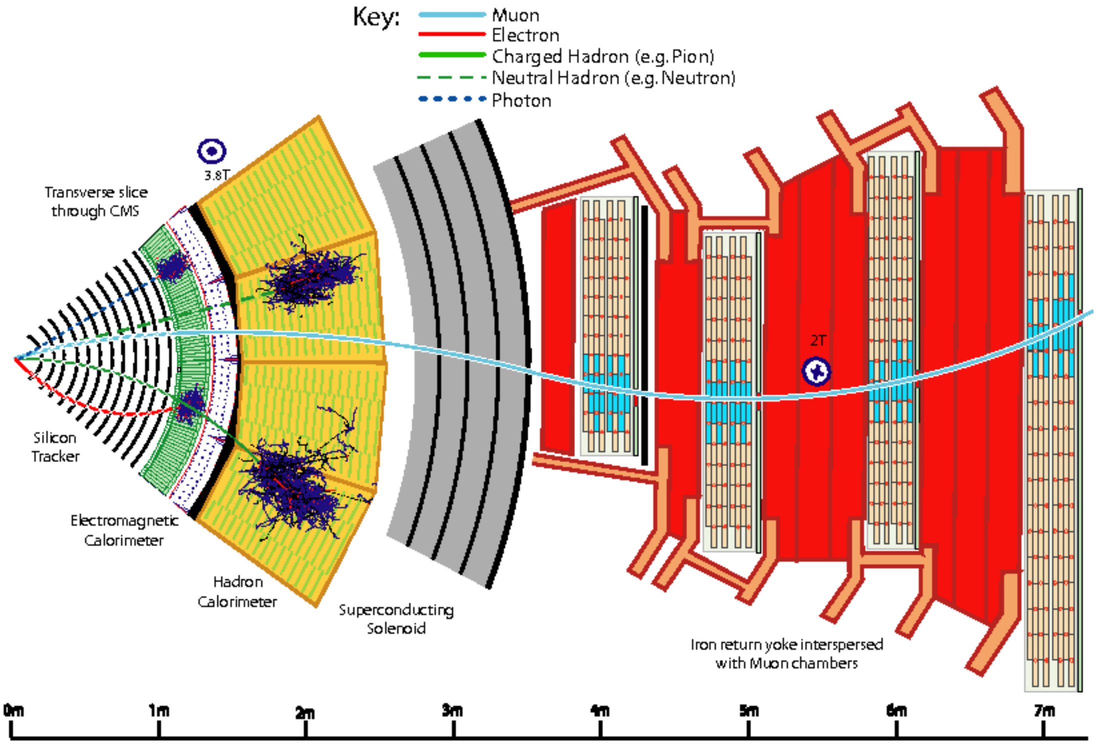

Figure 3.8: Schematic view of a transverse slice of the CMS detector, illustrating the specific signatures of different types of detected particles.

Before describing the CMS detector and its subdetectors in detail, understanding the Cartesian coordinate system used in CMS is necessary.

3.3.1 The CMS Coordinate System

A Cartesian coordinate system with its origin at the nominal interaction point in the CMS detector, the z-axis is collinear along the beam and the x-axis pointing radially toward the center of the LHC ring is chosen as the reference frame for the measurement of the physical quantities at the CMS detector. The y-axis is perpendicular to the x-z plane and points upward. An illustration of the CMS coordinate system is given in Figure 3.9. The azimuthal angle, ϕ, is measured in the transverse x-y plane and with respect to the z-axis. The radial distance r and the polar angle θ are measured from the z-axis. Instead of θ, a more useful angular variable is the pseudorapidity η, which is a good approximation of the rapidity to avoid energy dependence. Rapidity which is a Lorentz-invariant quantity is defined by:

$$y = \frac{1}{2} log \left(\frac{E + p_z}{E - p_z} \right) \tag{3.7}$$

where E is the energy of the particle, and p_z is the longitudinal component of its momentum.

Pseudorapidity is defined as:

$$\eta = -ln \left(tan(\frac{\theta}{2}) \right) \tag{3.8}$$

Smaller (larger) values of η represent the particles lying in a direction perpendicular (parallel) to the beam axis. The detector elements lying in a geometrical region defined by $|\eta| < 2.5$ are referred to as central detectors, while the ones in $|\eta| > 2.5$ regions are termed as forward detectors. The rapidity and pseudorapidity converges for the massless particles.

Second commonly used angular variable is ΔR which measures the distance between

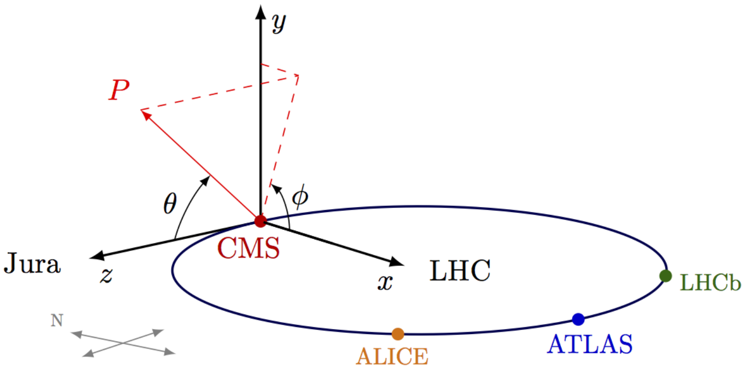

Figure 3.9: Schematic diagram of the coordinate system used in CMS experiment.

two particles in the $\eta - \phi$ plane and is defined as:

$$\Delta R = \sqrt{\Delta\eta^2 + \Delta\phi^2} \tag{3.9}$$

Due to the complex partonic structure of hadrons in proton-proton collisions, the initial p_z of the colliding partons is not known. Another useful variable is the transverse component of the momentum, $\vec{p_T} = \vec{p_x} + \vec{p_y}$. The transverse momentum is particularly useful because it can be assumed that p_T of the incoming parton is close to zero. The conservation of momentum can then be used to quantify an imbalance in the energies of the outgoing particles. The following Subsections will briefly review each subdetector and its properties.

3.3.2 Inner Tracking System

Being the closest subdetector to the IP and to the beamline of the CMS detector, the tracking system receives a high amount of radiation. The tracking system has been built to survive and operate in a high flux environment with around thousand of particles traversing through it in every bunch crossing. It measures the trajectories of the charged particles with transverse momentum greater than 1 GeV emerging from the proton-proton collisions. The tracker also allows for precise measurement of secondary vertices arising from the decay of heavy flavored hadrons which are produced in many physics channels. The full volume of the tracker which has a length of 5.8 m and a diameter of 2.5 m sits within the homogeneous magnetic field of 3.8 T and can provide tracking coverage for particles with $|\eta| < 2.5$. The challenging conditions created by the collisions at the LHC demand advanced technologies with high granularity and fast response in order to reliably measure the tracks and disentangle tracks from overlapping bunch crossings. The intense particle flux from the proton-proton interactions necessitates the use of radiation hard components in the detector, which leads to the all-silicon design of the CMS tracker system with a total active area of about 200 m^2. The tracker consists of two subsystems: the pixel tracker and the strip tracker. A schematic cross section of the CMS tracker is presented in Figure 3.10.

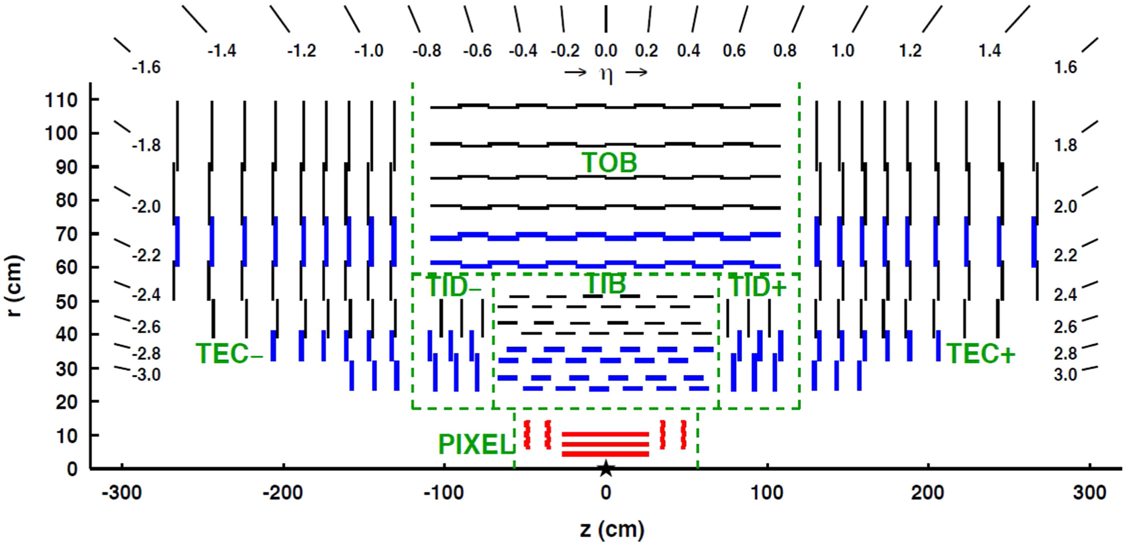

Figure 3.10: A slice through the CMS tracker detector in the *r*-*z* plane. The separate subsystem regions have been highlighted and are classified as the Tracker Inner Barrel and Disks (TIB and TIDs), the Tracker Outer Barrel (TOB) and the Tracker Endcaps (TECs). The Pixel subsystem is highlighted in red. Back-to-back stereo strip modules are highlighted in blue [17].

3.3.2.1 Pixel Detector

Pixel detector is the innermost layer of the CMS tracker and has large particle flux near the collision point, so a small-scale pixel geometry is constructed to achieve complete track reconstruction and precise vertex determination. Secondary vertices are produced by the particles having a relatively long lifetime, such as b and c quarks which arise from primary vertex but decay after traveling small distances. The pixel detector is meant to distinguish these secondary vertices from the primary collision points. The pixel detector is made of 1440 pixel modules and covers the pseudorapidity range of $|\eta| < 2.5$ with three Barrel Pixel (BPix) layers and two Forward Pixel (FPix) disks. The design of the pixel detector modules in the barrel (forward) region provides the full tracker coverage, three tracking hits per track and a position resolution of 15-20 (15) μm in the z-coordinate which is more than sufficient for track reconstruction and identification of primary and secondary vertices. However, over the time, the pixel detector will suffer from increased fake rates and the resolution can be degraded due to radiation damage. So in order to maintain its performance, "Phase Pixel Upgrade" [18, 19] was performed during the technical stop at the end of 2016. Figure 3.11 illustrates the layout of the pixel detector having barrel layers and endcap disks. The upgraded pixel detector constitutes 4 barrel layers and a turbine-like module arrangement for endcap disks.

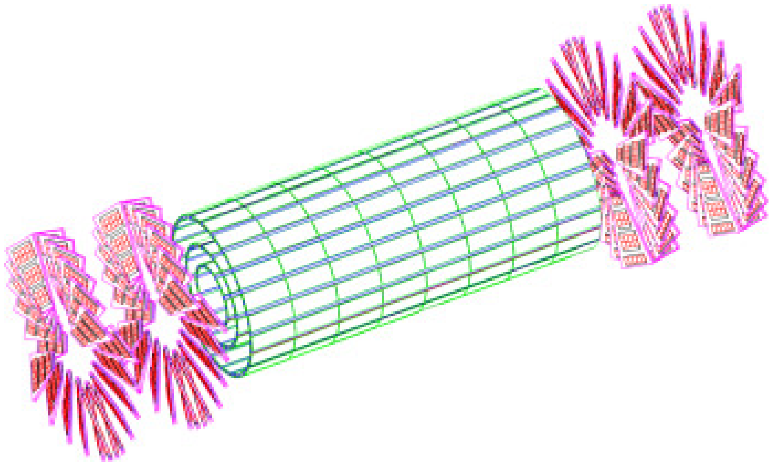

Figure 3.11: Layout of the pixel detector: barrel layers and endcap disks. The magenta wedges on the endcap disks are carbon-fiber blades, which hold plaquettes-rectangular arrangements of pixel sensors that come in five different sizes. The black rectangles in the barrel layers are the barrel modules-2 × 8 rectangular arrangements of pixel sensors, mounted on rectangular carbon-fibre blades.

3.3.2.2 Silicon Strip Detector

The strip tracker consists of silicon microstrips and is divided into an inner region having 4 barrel layers (Tracker Inner Barrel, TIB) and 3 endcap layers (Tracker Inner Disks, TID), and an outer region having 6 barrel layers (Tracker Outer Barrel, TOB) and 9 endcap disks (Tracker Endcaps, TEC) respectively. The distance covered by the TIB and TOB from the IP is up to $|z| < 65$ cm and $|z| < 110$ cm respectively, whereas TID and TEC covers $120 < |z| < 280$ cm.

The transverse momentum resolution of the tracker varies in the range from 0.7 % at 1GeV to 1.5 % at 100GeV. Tracks reconstructed in the pixel and strip detectors can then be used in vertex reconstruction, particle identification, charge identification and charged particle momenta measurements. The reconstruction of tracks and vertices is discussed in Chapter 5.

3.3.3 Electromagnetic Calorimeter

Calorimeters are used to measure the energy of different types of particles by slowing down and finally by stopping them, however it cannot stop muons and neutrinos. The incident particles interact with the material in the calorimeter and produce showers of the secondary particles of lower energies until the energy of the incident particle fall below critical energy not to further ionize/excite the material. The neutrinos weekly interact and penetrate the whole detector, thus their energy is referred to as missing transverse energy (MET) (more details in Section 5.4.6). For neutral Higgs bosons, with masses below ~ 140 GeV, the decay into two photons offers one of the cleanest channels for discovery. This has led to the choice of a high-resolution electromagnetic calorimeter (ECAL) [20] for CMS, sited within the 3.8T solenoid and hadron calorimeter, with a target energy resolution of 0.5% for electrons and photons above 100 GeV.

The CMS ECAL is hermetic homogeneous calorimeter consisting of 75848

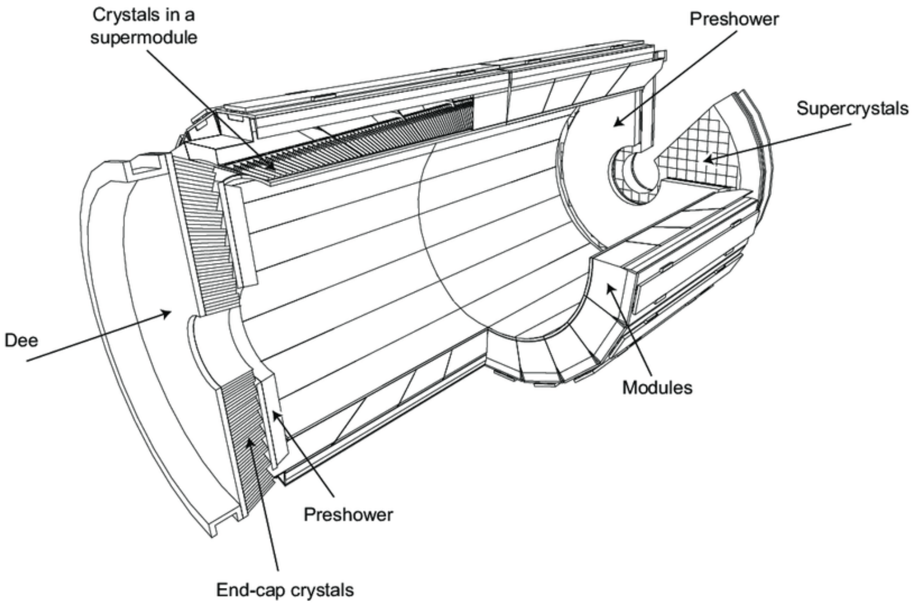

Figure 3.12: Geometric view and mechanical structure of the CMS ECAL. Crystals are grouped into modules and super-modules for the barrel and two half-disks or *dees* are in the endcap. The preshower detector covers most of the endcap surface.

lead-tungstate ($PbWO_4$) scintillating crystals (61200 in barrel and 14648 in endcap) and designed to fully absorb the energy of electromagnetically interacting particles, mainly photons and electrons. The reason to choose $PbWO_4$ material is due to its high density (8.28 g/cm^3), small Moliére length of 0.89 cm and a short radiation length of 2.2 cm which results in high granularity and high energy resolution of ECAL. The total thickness of ECAL is greater than 25 radiation lengths (X_0). Figure 3.12 and 3.13 represents the layout of ECAL.

For energy above 2 MeV, photons interact mostly through pair production and for below 1 MeV through the Compton scattering and photoelectric effect. On the other hand, electrons mainly interact via Bremsstrahlung for energies > 10 MeV and through ionization and excitation for energies below it. This process continues until the particles' energies are below critical energy at which point ionization becomes the dominant source of energy loss of electrons. The ionized atoms in the $PbWO_4$ crystal induces the blue scintillating light ($\lambda \approx 420$ nm), which is then measured in the photodetectors. The total amount of scintillating light produced is proportional

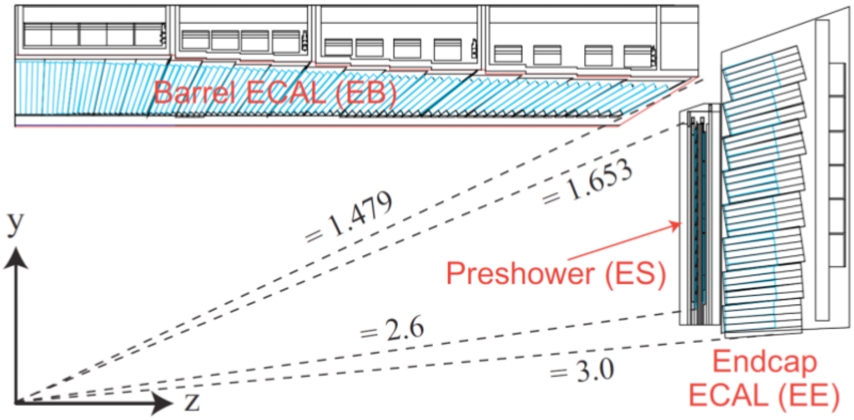

Figure 3.13: Longitudinal view of an ECAL quadrant. The pseudorapidity coverage of the barrel, endcap and preshower systems are indicated.

to the energy deposited in the crystals by the electrons and photons. Due to different radiations exposures and different orientations in the magnetic field, silicon Avalanche PhotoDiodes (APD) and Vacuum PhotoTriodes (VPT) were chosen as photodiodes in the barrel and endcap regions respectively.

3.3.3.1 ECAL Barrel

The ECAL Barrel (EB) extends from an inner radius of 1.29 m to an outer radius of 1.77 m covering the $|\eta| < 1.479$ with a granularity of 2×85-fold in η and 360-fold in ϕ. APD's are mounted in pairs on the back face of each crystal and measure the scintillating light produced in the EB. Each APD is operated, with a high-voltage power supply system, at a gain of 50 and a voltage between 340-430 V. The granularity of crystal in $\eta - \phi$ plane is 0.0174×0.0174.

3.3.3.2 ECAL Endcap

The ECAL Endcap (EE) covers the ECAL up to $|\eta| < 3.0$. The 220 mm long crystal are grouped in 5×5 units to form SuperCrystals (SCs). Each EE ring is divided into two halves known as "dees" and each dee contains 156 SCs. Scintillating photons are measured in single-stage photomultiplier called VPT, which are attached to the back face of each EE crystal. The crystals are aligned at angles ranging from 2 to 8 degrees with respect to the z-axis.

3.3.3.3 ECAL Preshower Detector

The ECAL preshower (ECAL PS) detector is a sampling calorimeter of 20 cm thickness installed between EB and EE, used to identify prompt photons and photons from neutral pion decay in the pseudorapidity range $1.65 < |\eta| < 2.6$. It is also used to identify electrons against the background of minimum ionizing particles (MIP) and improve the position resolution of electrons and photons in the ECAL. It is composed of two layers of lead absorbers that start the electromagnetic showers from incident photons and electrons. The energy deposited in the absorbers and the transverse profile of the shower is measured in the silicon strips. The lead planes are arranged in two "Dees" and the thickness of silicon sensors is 320 μm with an active area of 63×63 mm^2. The total thickness of the preshower silicon detector is 20 cm (3X_0 long).

3.3.3.4 ECAL Resolution

The energy resolution of the ECAL is affected by several sources, such as fluctuations in the lateral shower development, the energy released in the preshower detector, crystal non-uniformities, calibration errors and electric noise in the photodetectors. The relative energy resolution of the ECAL [21] is parameterized as a function of the measured energy E via:

$$\left(\frac{\sigma_E}{E}\right)^2 = \left(\frac{2.8\%}{\sqrt{E}}\right)^2 + \left(\frac{12\%}{E}\right)^2 + (0.3\%) \tag{3.10}$$

The energy (E) here is in the GeV scale and the result is in good agreement with the design-goal performance expected for a perfectly calibrated calorimeter.

3.3.4 Hadron Calorimeter

The CMS Hadron Calorimeter (HCAL) [22] is a hermetic sampling calorimeter sitting behind ECAL and is designed to measure the energy and position of hadronic jets. The reconstruction of jets and MET is crucial for many analyses which involves neutrinos and neutralinos as these particles do not interact much with the detector. HCAL covers the spatial region up to $|\eta| < 5$ which is essential for accurate measurements of the imbalance in MET. It consists of 70,000 plastic scintillator tiles and alternating layers of the brass absorber. Brass was chosen as absorber due to its non-magnetic behavior and short nuclear interaction length (16.24 cm). As the hadrons hit the absorber plate, they interact strongly with the brass nuclei, resulting in a cascade of new secondary particles referred to as *hadronic shower*. The particles in the shower enter the plastic layer, where their energy is measured from the emitted light by the scintillator at a peak wavelength of $\sim$ 440 nm.

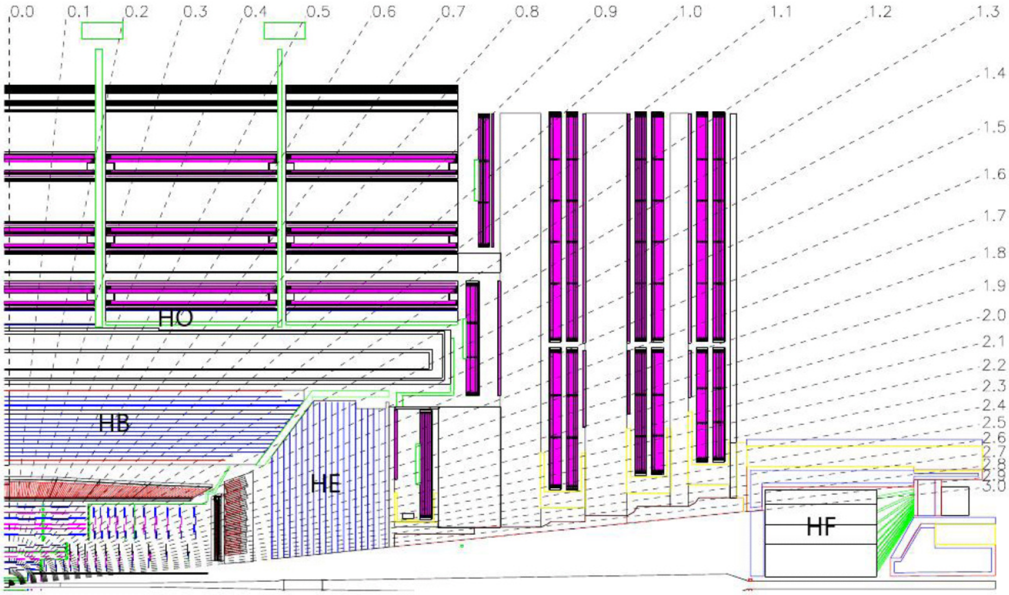

Figure 3.14: Longitudinal view of a CMS HCAL subdetectors.

HCAL is divided into four sub-parts into the different regions as shown in Figure 3.14: in the central region, the HCAL barrel (HB) and the HCAL outer (HO) and in the endcap region, the HCAL endcap (HE) and HCAL forward (HF).

3.3.4.1 Hadron Barrel Region

The HB covers the pseudorapidity range $|\eta| < 1.3$ and separated in two half-barrel sections (HB+ and HB-) each covering 18 identical azimuthal wedges. The total thickness of brass absorber is 5.82 interaction lengths (λ_I) at $90°$ and goes with θ up to 10.6 λ_I at $|\eta| = 1.3$ as $1/\sin(\theta)$ variation. The active medium, plastic scintillator tiles are split into 16 $\eta-$parts by giving a $\Delta\eta \times \Delta\phi$ segmentation of $0.087{\times}0.087$. The scintillator's light is read through optical fibers by photosensors. The HB photosensors consist of Hybrid PhotoDiode (HPD) transducers because of the wider range of wavelengths that they can detect and their low sensitivity to magnetic fields; those used in the HB and HE have a gain of roughly 2000.

3.3.4.2 Hadron Endcap Region

The coverage of the HCAL is extended in the forward region to $|\eta| = 3$ with the HE, which is located on endcap rings, lies under the impact of the 3.8 T magnetic field. The total length of the calorimeter is about 10 λ_I including the ECAL crystals. The HE contains 20916 plastic tiles and has $\Delta\eta \times \Delta\phi$ granularity of $0.17{\times}0.17$ for $|\eta| \geq 1.6$. The HE also use HPDs to measure the scintillator light due to their low sensitivity to the high magnetic field environment.

3.3.4.3 Hadron Outer Region

The HO is located outside the solenoid coil as an additional absorber confirming the sufficient sampling depth for $|\eta| < 1.3$. It is used to measure the energy of the tail of the particle shower deposited after the HB which increases the total depth of calorimeter to a minimum of 11.8 λ_I except at the boundary of barrel and endcap. The HO layers are mounted within the magnetic field returning iron yoke and are the first sensitive layers in each of the five rings of the yoke. In HO, the HPD's have been replaced by Silicon Photomultipliers (SiPM) due to their sensitivity to not well known magnetic field in the return yoke. By including the HO in the HCAL, a study has been performed on pion energy measurement which shows that hadronic shower energy leakage is significantly recovered, thus improving the energy resolution as shown in Figure 3.15 [23]. Improvement in accuracy of missing transverse energy measurement has been observed by including HO.

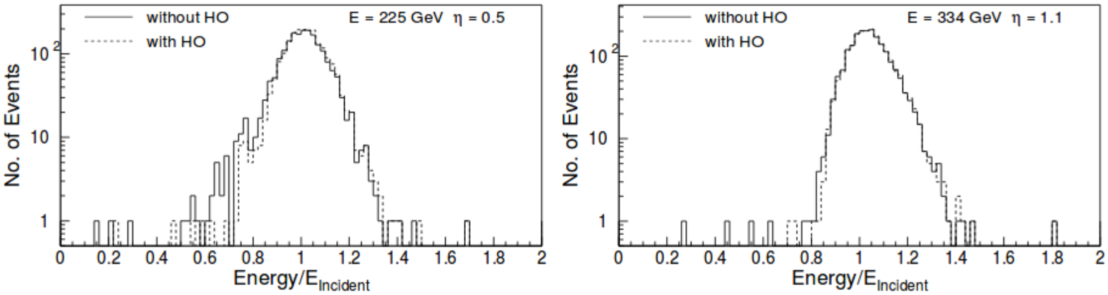

Figure 3.15: Distribution of measured energy scaled to incident energy for pions at incident E_T of 200 GeV at η values of 0.5(pointing towards the middle of muon ring 1) (left) and 1.1 (pointing towards the middle of muon ring2) (right). The solid and dashed histograms are measurements without and with HO.

3.3.4.4 Hadron Forward Region

The HCAL coverage reaches up to $|\eta| = 5.2$ with the two HF calorimeters. Since the HF experience a large energy deposit from the beam collisions, its design has been optimized to handle high levels of radiation. The HF made of stainless steel absorbers and radiation hard quartz fibers that collect Cherenkov light. The Cherenkov light is measured by multi-anode PhotoMultiplier Tubes (PMT) shielded behind 40 cm of steel.

3.3.4.5 HCAL Resolution

Muons and neutrinos produced in the nuclear interactions go unregistered in the HCAL except for a small muon MIP energy loss. The statistical fluctuations in the sampling and the leakage degrade the performance of the HCAL in comparison to the ECAL. The energy resolution of the HCAL and the HF subdetector, measured using test beam studies [24] is given as:

$$\frac{\sigma(E)}{E} = \frac{84.7\%}{\sqrt{E}} \oplus 7.4\% \qquad (HCAL) \tag{3.11}$$

$$\frac{\sigma(E)}{E} = \frac{198\%}{\sqrt{E}} \oplus 9\% \qquad (HF) \tag{3.12}$$

The electron energy resolution is less than 1% for all the energies above 20 GeV and goes below 0.4% for higher energies. For HCAL, at lower values of energy ($\sim$ 30 GeV), the resolution is $\sim$ 30% but this value goes down up to 10% for higher energy values which means resolution improves with an increase in energy.

3.3.5 The Solenoid Magnet

One of the most powerful superconducting solenoid magnet [25] of the CMS experiment has an internal diameter of 6 m and length 12.5 m which is designed to reach a magnetic field flux density of 4 T. However, it has been decided by the CMS collaboration to keep the operating magnetic field at 3.8 T in order to maximize the lifetime of the solenoid. The magnetic field created is approximately 100,000 times stronger than the earth's magnetic field. Stronger is the magnetic field, highly curved will be the particle's trajectory which favors good momentum measurement of charged particles up to $|\eta| < 2.4$ and do not allow low p_T particles i.e. $p_T \leq 0.75$ GeV to reach the surface of ECAL and hence contributes to the reduction of pileup. A 10,000-tonnes iron yoke is used to contain the magnetic field within the detector volume which is capable of stopping almost all particles (except muons and neutrinos). The iron yoke, enclosing all subdetectors, has a diameter of 14.6 m and extends to 21.6 m in length.

3.3.6 CMS Muon Spectrometer

For the discovery of new and interesting physics processes over the high background rate with high luminosity, a muon detection is a powerful tool. Some SUSY models also feature the discovery potential of muon final states and is a necessity for wide angular coverage for muon detection. Muon identification, muon measurements, and triggering are the main function of muon spectrometer. Muon system [26] aimed to have the potential to reconstruct the momentum and charge of muons over entire energy of the LHC. It is the outer most layer of CMS detector and has cylindrical barrel and endcap region as shown in Figure 3.16. Like neutrinos, muon also escapes the tracker and layers of calorimeters without interacting, but loose small energy fractions in the form of minimum ionization loss and gets trapped in muon system.

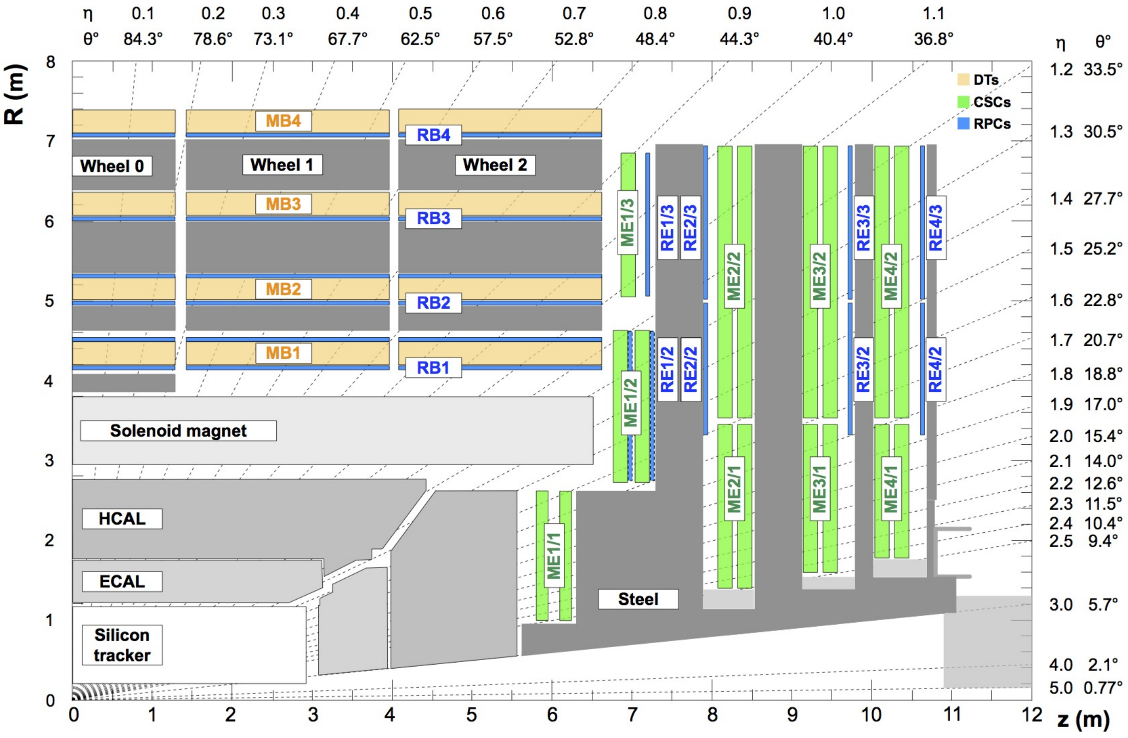

Figure 3.16: Schematic view of CMS Muon spectrometer.

Currently, Muon system consists of three types of gaseous detector namely, Drift Tubes (DT) in the barrel part, Cathode Strip Chamber (CSC) in the endcap and Resistive Plate Chamber (RPC) in both barrel and endcap regions.

DTs [27] covers pseudorapidity region up to $|\eta| < 1.2$ and has four stations named MB1, MB2, MB3 and MB4, alternated with the segmented return yoke. In this region, the occupancy of muon rates is low and the magnetic field is well contained in the iron plates of the magnet return yoke, which allows the usage of DTs being relatively cheap and easy to handle. The basic constituent of a DT chamber is a drift cell: a gas-filled tube with a rectangular cross section of 42×13 mm^2. A cell is surrounded by two parallel aluminium planes and by I-shaped aluminium beams serving as cathodes. A drift tube has one wire in the center, acting as the anode and the working principle is based on the ionization of charged particles. When a charged particle ionizes the gas, the electrons drift to the wire and induce a fast signal on the wire. Gas mixture used for DTs is Ar/CO_2 (85/15) which is good for quenching and provides a saturated drift velocity of about 5.6 $cm/\mu s$. A single cell has an efficiency of about 99.8% and a resolution of 180 μm.

CSCs [28] covers the endcap region from $0.9 < |\eta| < 2.4$ where we have the large muon rate and non-uniform magnetic field. CSCs chambers have four stations namely ME1, ME2, ME3, and ME4. CSCs are multi-wire proportional counters having a trapezoidal shape and consist of cathode plane divided into strips, running along the ϕ direction and orthogonal to the cathode strips. When muons pass through CSC, they ionize the gas atoms, the electron drift towards anode wires forming an avalanche of electrons. Positive ions move away from the wire and towards the copper cathode, also inducing a charge pulse in the strips. Due to good spatial and timing resolution, CSCs are used in endcap regions. The CSCs have a fast response time and more radiation-resistant than the DTs. The gas mixture used for CSC chambers is 40% Ar, 50% CO_2 and 10% CF_4 with a spatial resolution of 80 μm. The CF_4 is included to prevent polymerization on the wires.

RPCs [29] A redundant system covering both barrel (along with DTs) and endcap (along with CSCs) is provided by the resistive plate chambers (RPCs), who mainly contribute to the muon trigger. A total of 1056 RPC detectors are present in CMS muon system covering $|\eta| < 1.9$. Five wheels are placed in the barrel region and eight disks (4 for the positive side and 4 for the negative side from the IP) are placed in the endcap region. RPCs are parallel plate gaseous detectors made up of two gas gaps, with a strip readout plane in between, providing an extra coordinate along the ϕ direction. The working principle is based on ionization. The RPCs have an excellent time resolution of the order of 1-2 ns, making them suitable for muon triggering. Gas mixture used for RPC is 95.2% $C_2H_2F_4$ (tetrafluoroethane - Freon), 4.5% $i - C_4H_10$ (isobutane) and 0.3% SF_6 (sulphur hexafluoride). In the next Chapter, the RPCs detectors are discussed in more detail.

3.3.7 Upgrade of CMS Muon Spectrometer

The present muon system is performing well at the designed luminosity of LHC, but to assure the performance of muon triggering and tracking also during HL-LHC, it is necessary to upgrade each subsystem [18].

CSCs upgrade will focus on electronics. At HL-LHC, L1 trigger latency and the rate will increase, so to cope with it, replacement of cathode front-end boards (CFEB) on inner chambers is needed. **DTs** modifications are also based on electronics because DT has a low tolerance for radiation, so this improvement in electronics increases the trigger rate capability, performance and enhances maintainability. **RPCs** are installed in the fourth RPC endcap station (RE-4) in the η region up to $|\eta| = 1.6$ during LS1. For the muon trigger, the important goal is to deliver the good enough resolution to identify high p_T tracks. With the installation of the fourth layer in the endcap region, it gave the finer timing and resolution to the corresponding CSC station and maintained a low p_T threshold. For the upgrade on the present RPC system, the link system must be replaced and few improved RPC (iRPC) detectors will be installed in high-η regions as shown in Figure 3.17.

A new station will be installed in the innermost region of the CMS forward muon

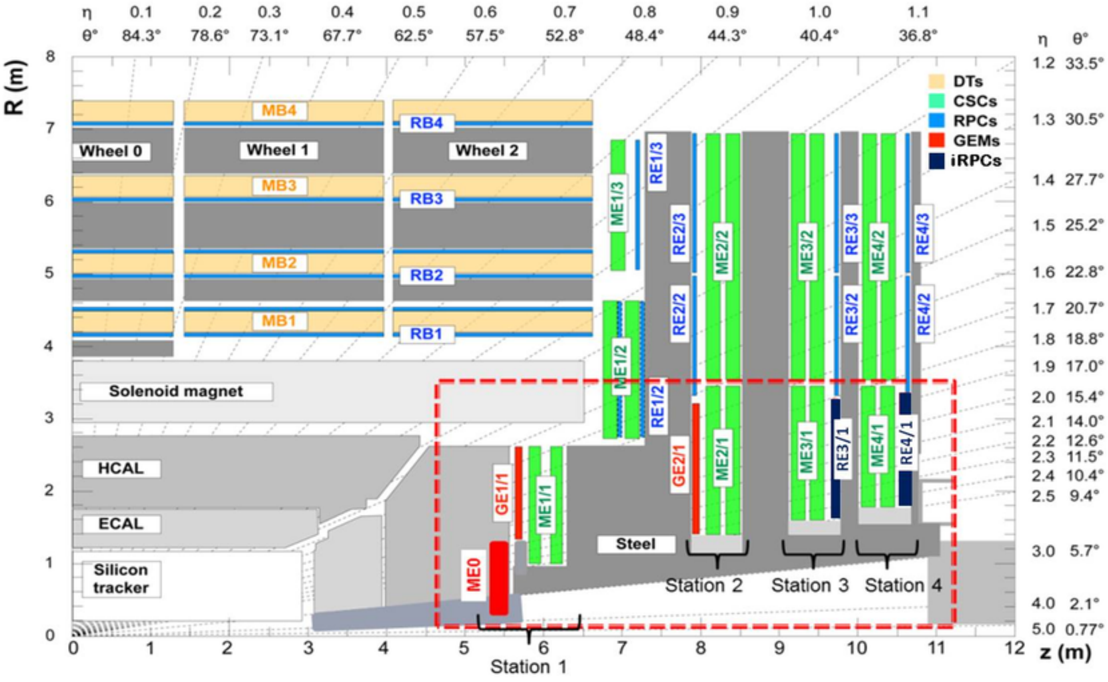

Figure 3.17: A quadrant of the CMS Muon Spectrometer, showing DT chambers (yellow), RPC (light blue), and CSC (green). The locations of new forward muon detectors for HL-LHC phase are contained within the dashed box and indicated in red for GEM stations (ME0, GE1/1, and GE2/1) and violet for improved RPC stations (RE3/1 and RE4/1).

spectrometer in the region $1.5 < |\eta| < 2.4$. In this η region, currently, only 4 stations of CSCs are placed and because of that less redundancy is a challenge for muons in terms of background and momentum resolution. To maintain good L1 muon trigger acceptance in this region it is therefore proposed to enhance these four stations with additional chambers that make use of new detector technologies with a higher rate capability. Triple Gas Electron Multiplier (**GEM**) [31] detectors are going to be installed in two forward regions at $1.5 < |\eta| < 2.4$, namely GE1/1 and GE2/1 during LS2 and LS3 respectively. GEMs are gaseous detectors having various properties: 1.) to detect efficiency more than 98% even for rate exceeding a few MHz/cm^2 2.) high spatial resolution of order ~ 100 μm and good time resolution of order ~ 8 and ~ 5 ns at the efficiency plateau for Ar/CO_2 (70/30) and $Ar/CO_2/CF_4$ (45/15/40) gas mixtures, respectively.

Panjab University is one of the production sites for the production of GEM chambers. We have already assembled 8 GE1/1 detectors to be successfully installed in CMS detector at CERN and preparing for the assembly of GE2/1.

3.4 The CMS Event Trigger and Data Acquisition

The LHC is designed in such a way that the two beams collide at each IP every 25 ns (40 MHz) corresponding to $\sim 10^9$ interactions per second. Data collected for each interaction would require 40 TB of storage per second which is not feasible for CERN main computing farm, called as Tier-0 as its processing is limited by CPU performance and storage capacity. Most of the events are from soft interaction between the protons and known as *minimum bias* events. In order to remove the unwanted data and to save the interesting information, CMS has developed a Trigger system and Data Acquisition (DAQ) [32, 33] system to transfer the data to Tier-0 and for further processing. The CMS trigger system checks each event recorded and store the data from the event only if it passes some criteria for being called as an event of interest. In this way, it reduces the event rate from 40 $\times 10^6$ Hz to 1 $\times 10^6$ Hz by implementing a two-level trigger system, the Level-1 (L1) Trigger and High-Level Trigger (HLT).

3.4.1 Level-1 Trigger

L1 Trigger [34] leans on highly programmable custom-designed electronics and acquire the event rate from the initial 40 MHz to 100 kHz with the latency of 3.2 μs. L1 Trigger uses the raw information from two parts: Calorimetry and Muon system. The L1 trigger search for key signatures of interesting events: leptons, photons, hadronic jets, and p_T^{miss}, known as trigger objects. These trigger objects, also called as trigger primitives (TPs) are produced based on the energy deposit in the calorimeters, and track segments or hit patterns in the muon chambers. The

L1 trigger from muon and calorimeter are then combined in the L1 Global Trigger (GT) which decides whether to pass or reject the event. The data is temporarily stored in pipelines of processing elements while waiting for the L1 decision. The events which pass the requirements of at least one of the L1 seeds that form the L1 triggers are selected and passed on to the HLT. Figure 3.18 shows the schematics of the L1 trigger system.

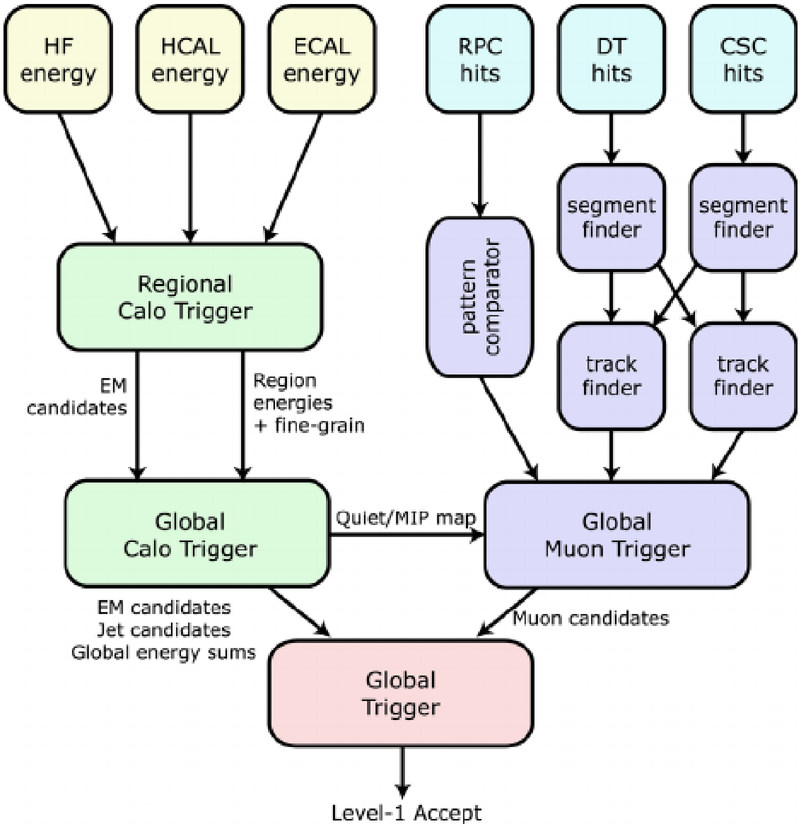

Figure 3.18: Flow diagram of the L1 Trigger system of CMS.

3.4.2 High Level Trigger

The High Level Trigger (HLT) [35] uses advanced software with a processor farm consisting of an array of multi-core computers, designed to reduce the event rate from 100 kHz to 1 kHz with a processing delay time of about 100 ms. The HLT can be used to reconstruct basic physics objects like jets and leptons etc. To pass the

HLT, event needs to satisfy the requirements of at least one of its paths, which are in the HLT menu, the same procedure as in the L1 trigger. The events which passed the HLT are recorded permanently on the disk by the data acquisition (DAQ) system for further physics analysis and transferred to CERN Tier0 (T0) storage system in one or more data streams. Data quality monitoring (DQM) checks the quality of recorded data using histograms and graphs especially designed to identify problems. Depending on this, datasets can then be labeled in the database either good or bad and conveyed to the subdetector experts. At the end of the DQM chain, a list of datasets certified to be used for physics analysis is produced. Figure 3.19 shows the CMS data flow starting from the HLT up to the datasets that are used for physics analysis.

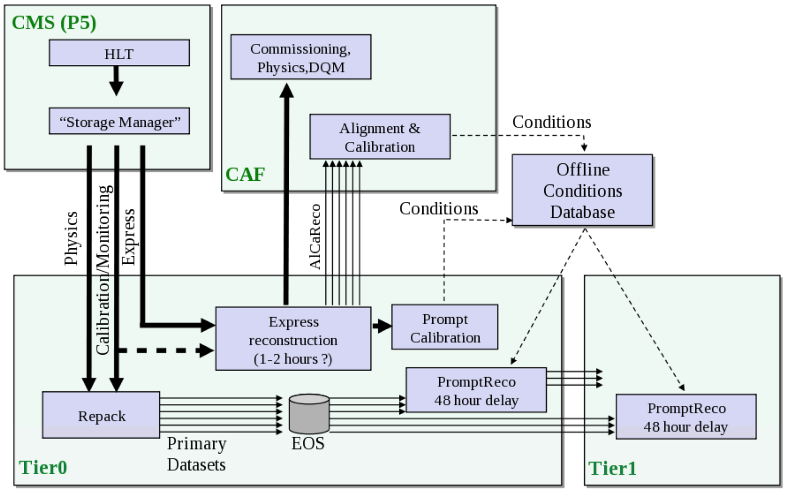

Figure 3.19: CMS Data flow from HLT to physics datasets.

To summarize, this Chapter describes the LHC machine and the CMS detector. The design and working of each subdetector of the CMS detector have been discussed briefly. CMS detector uses a two-level trigger to shortlist the events to be stored for physics analysis. Different algorithms employed at the CMS detector for particle reconstructions and event flow descriptions will be discussed in the coming Chapter.

Bibliography

[1] Lyndon Evans and Philip Bryant, “LHC Machine”, *JINST*, vol. 3, S08001 (2008).

[2] The CMS Collaboration, “Evidence for the direct decay of the 125 GeV Higgs boson to fermions”, *Nature Phys.*, vol. 10, Jan (2014).

[3] The CMS Collaboration, “Observation of a new boson at amass of 125 GeV with the CMS experiment at the LHC”, *Phys. Lett. B*,vol. 716, (2012), https://dx.doi.org/10.1016/j.physletb.2012.08.021.

[4] The ATLAS Collaboration, “Observation of a new particle in the search for the Standard Model Higgs boson with the ATLAS detector at the LHC”, *Phys. Lett. B*, vol. 716, (2012), https://dx.doi.org/10.1016/j.physletb.2012.08.020.

[5] C. O’Luanaigh, “The Large Electron-Positron Collider”, Jul (2012).

[6] The HL-LHC Project, https://hilumilhc.web.cern.ch/about/hl-lhc-project.

[7] https://cds.cern.ch/record/841573/files/lhc-pho-1997-060.jpg.

[8] The ATLAS Collaboration, G.Aad *et al.*, “The ATLAS Experiment at the CERN Large Hadron Collider”, *JINST*, vol. 3, S08003 (2008).

[9] The CMS Collaboration, “The CMS experiment at the CERN LHC”, *JINST*, vol. 3, S08004 (2008).

[10] The ALICE Collaboration, K. Aamodt *et al.*, "The ALICE experiment at the CERN LHC", *JINST*, vol. 3, S08002 (2008).

[11] R. S. Bhalerao and R. V. Gavai, "Heavy Ions at LHC: A Quest for Quark-Gluon Plasma", (2009), https://dx.doi.org/10.1007/978-81-8489-295-6_8.

[12] The LHCb Collaboration, A. Augusto *et al.*, "The LHCb Detector at the LHC", *JINST*, vol. 3, S08005 (2008).

[13] The LHCb Collaboration, "Observation of *CP* violation in charm decays", http://cds.cern.ch/record/2668357.

[14] http://moriond.in2p3.fr/2019/EW/slides/5_Thursday/1_morning/4_betti_federico_v4.pdf.

[15] "Public CMS Luminosity Information", `https://twiki.cern.ch/twiki/bin/view/CMSPublic/LumiPublicResults`.

[16] "Public CMS Data Quality Information", `https://twiki.cern.ch/twiki/bin/viewauth/CMSPublic/DataQuality`.

[17] The CMS Collaboration, "Description and performance of track and primary-vertex reconstruction with the CMS tracker", *JINST*, vol. 9, (2014), https://dx.doi.org/10.1088/1748-0221/9/10/p10009, arXiv:1405.6569v2

[18] The CMS Collaboration, "CMS Technical Design Report for the Pixel Detector Upgrade", Techincal Design Report CMS CERN Geneva, (2012).

[19] The CMS Collaboration, "Upgrade of the CMS tracker", *JINST*, vol. 9, C03041 (2014), https://dx.doi.org/10.1088/1748-0221/9/03/C03041.

[20] The CMS Collaboration, "The CMS electromagnetic calorimeter project: Technical Design Report", *CMS-TDR-4*, CERN/LHCC 97-033, (1997).

[21] The CMS Collaboration, “Energy Calibration and Resolution of the CMS Electromagnetic Calorimeter in pp Collisions at $\sqrt{s} = 7$ TeV”, *JINST*, vol. 8 (2013), http://dx.doi.org/10.1088/1748-0221/8/09/P09009.

[22] The CMS Collaboration, “The CMS hadron calorimeter project: Technical Design Report”, *CMS-TDR-2*, CERN/LHCC 97-031, (1997).

[23] S. Banerjee, “Performance of Hadron Calorimeter with and without HO”, Tech. Rep. CMS-NOTE-1999-063, CERN, Geneva, Nov (1999).

[24] The CMS Collaboration, “The CMS experiment at the CERN LHC”, *JINST*, vol. 3 (2008), http://dx.doi.org/10.1088/1748-0221/3/08/S08004.

[25] The CMS Collaboration, “The CMS Magnet Project”, (1997), https://cds.cern.ch/record/331056.

[26] The CMS Collaboration, “The CMS muon project: Technical Design Report”, *Technical Design Report CMS CERN*, (1997).

[27] The CMS Collaboration, “Performance of the CMS drift tube chambers with cosmic rays”, *Journal of Instrumentation*, vol. 5, T03015, (2010).

[28] The CMS Collaboration, “Performance of the CMS cathode strip chambers with cosmic rays”, *Journal of Instrumentation*, vol. 5, T03018, (2010).

[29] G. Pugliese, The CMS Muon Collaboration,“The RPC system for the CMS experiment”, *2006 IEEE NSS Conference Record N24-3*, (2007).

[30] The CMS Collaboration, “The Phase-2 Upgrade of the CMS Muon Detectors”, *CMS-TDR-016*, CERN/LHCC 2017-12, (2017).

[31] The CMS Collaboration, “CMS Technical Design Report for the Muon Endcap GEM Upgrade”, *CMS-TDR-013*, CERN/LHCC (2015).

[32] Vardan Khachatryan *et al.*, “The CMS trigger system”, *JINST 12*, P01020 (2017).

[33] Andrea Perrotta, “Performance of the CMS High Level Trigger”, *Journal of Physics: Conference Series 664*, 082044, (2015).

[34] CMS Trigger and Data Acquisition Group, “The CMS high level trigger”, *Eur. Phys. J.C*, vol. 46, (2006), https://dx.doi.org/10/1140/epjc/s2006-02495-8.

[35] The CMS Collaboration, “CMS The TriDAS Project:Technical Design Report”. https://cds.cern.ch/record/578006.

Chapter 4

Aging Study of Resistive Plate Chambers (RPC) for HL-LHC

This Chapter gives a sketch about the gaseous detectors and mainly Resistive Plate Chambers. The first segment of the Chapter explains the working principle, design, and configuration of RPC inside the CMS experiment, while the second part is dedicated to the aging study being performed on RPC detectors which are currently used in CMS. For the aging study, chambers are under continuous gamma radiation at CERN Gamma Irradiation Facility (GIF+++) to monitor the detector parameters. The detector performance is also tested from time to time with the muon beam.

4.1 Gaseous Particle Detectors

As mentioned in the previous Chapter 3 (Section 3.3.6), Gaseous detectors [1] are the basic detectors that have been used to detect and observe particles in High Energy Physics (HEP) since the advent of the detector development phase for particle physics. The layout and configuration have emerged throughout the time from the single-wire proportional counters to a wide range of fine resolution, fast and efficient detectors. But the basic principle is the same despite the varieties i.e. the ionization created by a charged particle as it crosses through matter. On the passage of a charged particle through a gas, free electrons and positive ions are generated along the trajectory of the particle. When the external electric field is applied, these free electrons and ions get accelerated and gain sufficient energy to produce secondary ionization and thus cause an avalanche. These charges induce a signal on the read-out electrodes, which depending on the detector design and electronics can provide good spatial and time resolution on the particle's path.

The next Section will define the special types of gaseous detectors known as RPCs detectors which are used in the muon subsystem of CMS because of its extremely good time resolution ($\sim$ 1 ns). Scintillators are replaced by RPCs in all the experiments where large detection areas are involved because of their low cost. The RPC characteristics depend on the mode of their operations in the detector system that are discussed in the coming Sections.

4.2 Resistive Plate Chambers

RPCs [2] are parallel plate gaseous detectors with simple geometry, low cost, exceptional time and spatial resolution. RPC consists of two electrodes, a positively-charged anode, and a negatively-charged cathode, both made out of a very high resistive material having bulk resistivity of 10^{10}-10^{12} $\Omega - cm$ and separated by a gas gap of 2 mm [3]. RPCs used in the CMS detector are made up of bakelite material which is highly resistive (1-6$\times 10^{10} \Omega - cm$). Poly Vinyl Chloride (PVC) spacers (button shape) are used to maintain the constant distance among them, thus assuring electrical and mechanical stability. The electrodes are connected to an HV supply in order to form a uniform and intense electric field (about 5 kV/mm) in the gap between them. The outer surface of the high resistive electrodes is coated with a thin conductive layer of graphite ($\rho_{surface} \sim 1\ M\Omega/A$, thickness $\sim 100\ \mu$m) to allow uniform application of the high voltage. The CMS-RPC detector readout is based

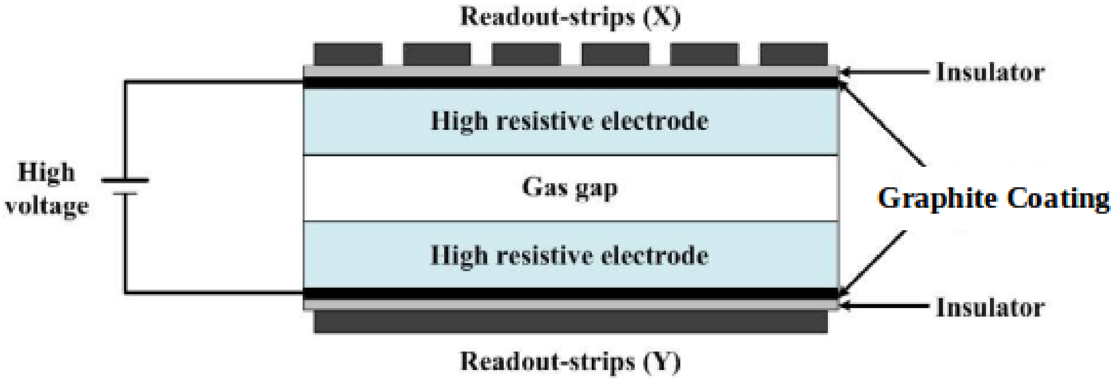

Figure 4.1: Illustration of an RPC.

on the charge induced on the copper strips running in horizontal (vertical) direction, and thus providing one (two) dimensional position measurements. These readout strips are separated from the graphite coating using insulating film (generally, mylar sheets). A schematic design of an RPC is shown in figure 4.1.

4.2.1 RPC Working Principle

Like other gaseous detectors, RPC working principle is also based on gas ionization, in which when a charged particle passes through the gas, it ionizes the gas and results into the production of electron-ion pairs. The electrons produced during the ionization are grouped into clusters. An external electric field is applied to accelerate the number of electrons in a cluster (n_0) which triggers further ionization in the gas, hence leading to the formation of an avalanche of electrons in the gaseous medium as shown in Figure 4.2.

This process of multiplication is characterized by a parameter, α, which represents the number of ionizations per unit length and another parameter, β, which is the attachment coefficient defined as the number of electrons captured by the gas per unit length. For the gas mixture made up of electronegative gases (the gases having a high tendency to absorb free electrons to form an ion), β becomes a crucial

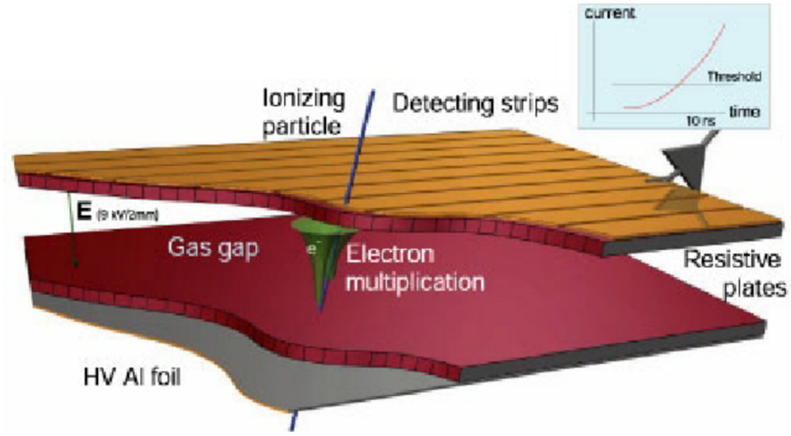

Figure 4.2: Working principle of RPC.

parameter. Due to the high bulk resistivity of the electrodes, the spread of electric charge is limited to a very small region around the point of initial ionization. The signal produced by discharge is collected using the readout strips and transmitted for further processing through the readout electronics. If "x" is the distance between the anode and the point where the cluster is placed, the number of electrons reaching the anode will be given by:

$$n = n_0 e^{\eta x} \tag{4.1}$$

where $\eta = \alpha - \beta$. The gain factor (M) is defined in terms of the cluster size per ionization as:

$$M = \frac{n}{n_0} \tag{4.2}$$

"M" decides the working mode of the RPC detector. The RPCs can be operated either in the avalanche mode or in the streamer mode [4]. The value of M $\approx \mathcal{O}(10^8)$ or higher corresponds to the streamer mode, whereas the avalanche mode is recognized by lower values of gain factor ($M < 10^6$). In the avalanche mode of operation, a simple charge multiplication phenomenon occurs with a lower formation probability of additional secondary avalanches and therefore leading to a limited amount of charge build-up. The counting rate capability of the avalanche mode could be improved by using the electronegative gas in the gas mixture, which restrains the growth of streamers. To obtain the best detection results, i.e. to maximize the strength of output signal and to attain the maximum detection efficiency, the gas gain should be as high as possible. The electron-ion pairs produced in the ionizations influence the electric field in the gas gap, which are spread across a wider region in a streamer mode as compared to that in the avalanche mode. At large values of the gas gain, photons (produced in the secondary ionizations) start to participate in the avalanche production and lead to streamers. The signal strength, in this case, is quite large as compared to the one in avalanche mode. The rate capability of an RPC operating in the streamer mode is limited to a few hundreds of Hz/cm^2, hence these are more suitable for low count rate neutrino experiments.

The bulk resistivity and quality of the electrodes of an RPC determine its count rate capability. The high rate count capability of RPC ($\sim$ 1 kHz/cm^2), detection efficiency and radiation hardness make them an excellent choice for triggering of particles produced in collider based experiments [5–13]. The roughness on the surface of electrodes can produce spontaneous discharge which can significantly diminish the rate capability of an RPC. The width of the gas gap between the electrodes determines the timing characteristics which is $\sim$ 1 ns for CMS-RPC.

In the CMS detector, Double-gap bakelite RPCs are being used for muon detection which provides fast timing signals in coincidence with the LHC bunch crossing rate. The double-gap geometry improves the detection efficiency (over 95%), time resolution ($\sim$ 1 ns), and allows a safer operation at higher threshold voltage. Trigger signals coming from DTs, CSCs, and RPCs proceed in parallel to reach the level of the global trigger logic. This provides a redundancy while calculating the detection efficiencies, and results in better detection efficiency and higher rate capabilities. The RPC system of CMS detector is contributing to the trigger, reconstruction and identification of muons.

4.2.2 Standard Gas Mixture for RPC

The selection of gases for an RPC is based on various factors such as the working voltage of the detector, good proportionality, and high background rate capability. For the purpose, where expected background rates are high, the detectors should be operated in avalanche mode in order to keep the total produced charge low to avoid aging and rate capability. To achieve this, the suitable gas mixture is used that prevents the shift from avalanche to streamer modes keeping the detection efficiency above 90%. The use of Fluorine (F)-based gases, usually used in refrigerants, have shown so far to give the best performance [14]. For an RPC, the primary component of the gas mixture consists of a gas that acts as a target for ionizing particles. The quenching gas which absorbs the photons and restricts the formation of secondary avalanches, electronegative gas like SF_6, are also used to improve the gas gain by limiting the amount of free charge in the gas. So, the CMS-RPC gas mixture is composed of 95.2% $C_2H_2F_4$ which is the charge carrier gas and has to be ionized by the charged particles, 4.5% iC_4H_{10} acting as a quencher gas to absorb UV photons from molecule de-excitation and 0.3% SF_6 the electronegative gas preventing the excess of electrons which will result in streamer mode.

Though this gas mixture is widely used, $C_2H_2F_4$ and SF_6 are not eco-friendly gases because of their large Global Warmth Potential (GWP) [15]. So, global efforts are going on to look for good substitutes and to test various eco-friendly gases.

4.2.3 RPC Detector Layout

As muons are less interactive, the main reason behind the detector layout of the CMS RPC system is the need to trigger on the transverse momentum of passing muons. To determine the p_T of the muons, it should cross at least 3 out of 4 layers in the muon system and can be measured with the bending of the muon in the CMS magnetic field. These layers are interleaved with the steel return yokes ensuring a maximum muon track bending between them.

At present, there are 1056 RPCs installed in the barrel and endcap region which are designed to provide muon identification, excellent triggering, timing, and momentum measurements at the LHC at the nominal luminosity of 1×10^{34} cm^{-2}s^{-1}. The RPCs are organized in 4 stations called RB1 to RB4 covering a pseudorapidity range of $|\eta| < 1.2$ in the Barrel region, and RE1 to RE4 in the Endcap region covering $0.9 < |\eta| < 1.9$ in the Endcap. It has more than 110000 electronic channels and covers a sensitive area of 3500 m^2.

Barrel RPCs: A total of 480 RPCs are installed in the barrel part of CMS muon system and divided equally among 5 wheels along the beam pipe named Wheel 0, Wheel ± 1 and Wheel ± 2 as represented in Figure 4.3. Each wheel consists of 4 muon stations (RB1, RB2, RB3 and RB4) at the increasing radius (R) and is divided into 12 sectors (S01-S12) in ϕ. The inner two stations consist of 2 layers of RPCs (RB1in, RB1out, RB2in and RB2out) with a DT in the center and the

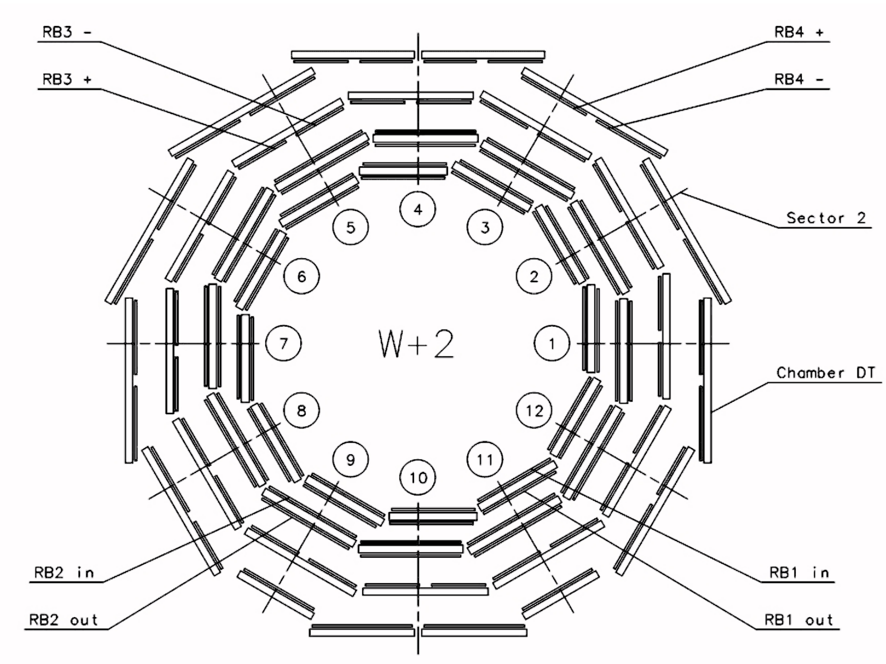

Figure 4.3: Schematic layout of RPC Barrel Geometry with one of the 5 wheels.

outer two station consists of a single layer of RB3 and RB4 and one layer of DTs. RPCs in RB3 and RB4 are divided in + and - along ϕ for mechanical reasons in all sectors apart from sectors S04, S09, S11 in RB4. RB4/S09 and RB4/S11 are in the feet of the barrel wheel and they consist of a single RPC chamber. RB4/S04 is divided into 4 chambers: $++$, $+$, $-$ and $--$. For trigger requirements, RPC barrel chambers are divided along the beam axis into 2 $|\eta|$ partitions: forward and backward rolls [16].and only two chambers are divided into 3 $|\eta|$ partitions (forward, middle and backward) i.e. RB2in in Wheels -1, 0, 1 and RB2out in Wheel -2, +2.

Endcap RPCs: Their design is very much similar to the barrel RPCs except some difference in the geometry and the fine segmentation which is essential for higher multiplicity forward regions. A total of 576 RPCs are installed in the endcap and distributed along 8 disks (4 disks per each endcap, positive and negative) named RE±1, RE±2, RE±3 and RE±4 as given in Figure 4.4. Run I data have been taken with only 3 stations i.e. (RE±1-3) and the two disks for the fourth stations both positive and negative were installed with 144 RPC detectors during the LS1 (2013-2014). Each disk is divided into 36 sectors along ϕ and has two concentric rings: ring 2 (R2) and ring 3 (R3). Each ring is made up of 36 trapezoidal chambers spanning 10° which are further split into three rolls, identified A, B and C concerning increasing η. The strip pitch of the endcap chambers is between 1.8-3.8 cm. Due to the partitioning of the read-out strips into three rolls, the TOP layer gap is divided into two gaps: Top Narrow (TN) and Top Wide (TW) but Bottom (BOT) layer consist of one gap. During the LHC Run I and Run II data taking the performance of the muon systems was outstanding [17]. In the second phase of the LHC physics program, HL-LHC, the instantaneous luminosity will reach 5×10^{34} cm^{-2}s^{-1} (factor five more than the nominal LHC luminosity), providing to CMS an additional integrated luminosity of about 3000 fb^{-1} over 10 years of operation, starting in 2026. The expected conditions in terms of background, pile-up and the probable aging of the present detectors will make the muon identification and correct p_T assignment

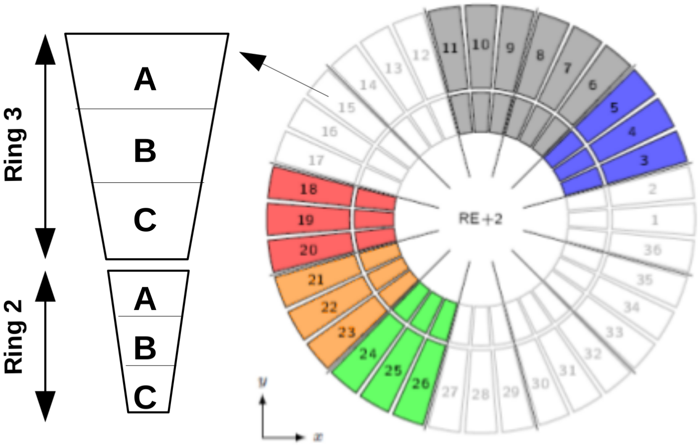

Figure 4.4: Schematic design of one of the Endcap disks (RE+2) showing the assembly of chambers into sectors.

a challenge for the muon system. To ensure redundancy also under the HL-LHC conditions, two upgrades [18] are planned on the RPC system: the consolidation of the present system and the extension of the muon coverage at the $|\eta| < 2.4$. In this Chapter, we will discuss only the consolidation of the present RPC system.

4.3 RPC Aging Studies for the Present System

The existing RPC system has been endorsed for 10 years of LHC operation, at a maximum background rate of 300 Hz/cm^2 and a total integrated charge of 50 mC/cm^2 [19]. Based on Run II data and assuming a linear dependence of background rates as a function of the instantaneous luminosity, the expected background rates and integrated charge at HL-LHC will be $\approx$ 600 Hz/cm^2 and $\approx$ 840 mC/cm^2 respectively, (including a safety factor of three) [18]. Hence, HL-LHC will be a challenge for the current RPC system since new operating conditions are much harsher with respect to those for which the detectors had been designed, and could induce non-recoverable aging effects that can alter the detector properties and performance.

To estimate the impact of the HL-LHC conditions up to an integrated charge equivalent to the integrated luminosity of 3000 fb^{-1} and in order to confirm that the present RPC system will survive to the expected HL-LHC conditions, aging/longevity analysis is required. Longevity studies will identify possible aging effects by monitoring the main detector parameters and performance as a function of the integrated charge. A dedicated longevity study was set up at the CERN Gamma Irradiation Facility (GIF++) where it is possible to test real size detectors. GIF++ is discussed in more detail in the next Section.

As a part of CMS-RPC group, we are working on RPC aging study in the GIF++ since June 2018 along with other RPC group members. The GIF++ RPC data is analyzed every week to monitor the parameters of the detector. Also, to check detector performance, muon test beam happen from time to time and the results are presented in Section 4.3.4.

4.3.1 Gamma Irradiation Facility (GIF++)

GIF++ was designed and built at the CERN SPS North Area 1 during the Long Shutdown1 (LS1) period which offers two separated irradiation areas and has been operational since spring 2015. It focuses on the characterization and testing of the long-term performance of large gas-based particle detectors. The facility is equipped with a 13 TBq ^{137}Cs gamma source and a system of movable filters that allows to variate the gamma irradiation conditions, providing a fairly realistic simulation of the HL-LHC background conditions. A 100 GeV/c muon beam from the secondary SPS beamline H4 provides excellent probes for detector performance studies, and complements the source [20]. Preference is given to ^{137}Cs isotope rather than ^{60}Co due to its long half-life of 30.08 years and also a small decrease in the photon rate over the expected lifetime of this facility. The design of the GIF++ facility and its coordinate system are shown in Figure 4.5 [21].

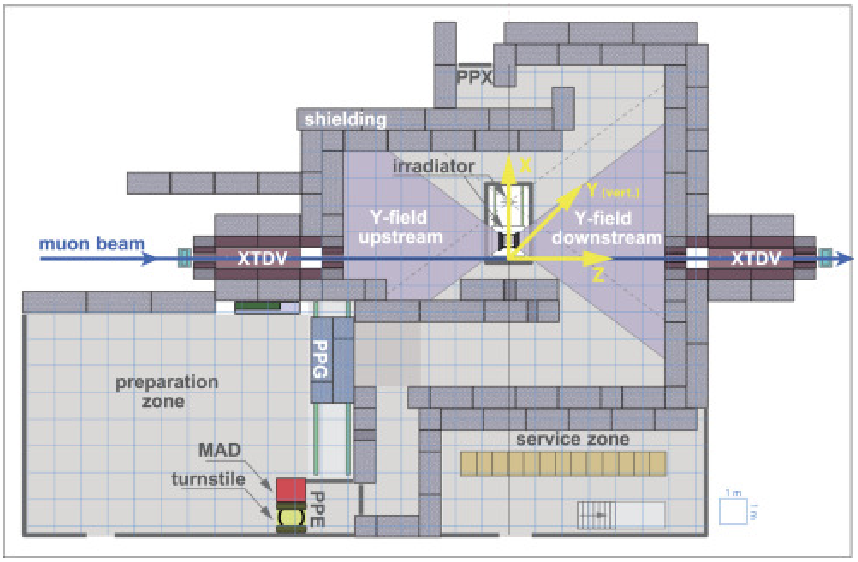

Figure 4.5: Schematic diagram of GIF++.

4.3.2 Setup and Test Procedure

Since the maximum background rate is expected in the endcap region, so four spare endcap chambers: two RE2/2 and two RE4/2 are placed under the irradiation test at GIF++. Two different types of chambers have been used because the endcap RPC production has been completed in two periods: in 2005 for all RPCs in the endcap system, except RE4/2 and RE4/3 chambers, which were made in 2013 (during LS1).

In order to study the detector's longevity, two chambers out of the four (one RE2/2 and one RE4/2), are continuously operated under gamma irradiation, while the remaining two chambers are turned on only from time to time and used as a reference as shown in Figure 4.6. The main detector parameters are monitored and periodically compared with those of the reference chambers (currents and counting rates at several background conditions, noise and dark current, etc). Moreover, when the muon beam at GIF++ is available, the detector performance is studied at different irradiation conditions. The method for the analysis is described in reference [3]. All measurements are performed under controlled environmental and gas conditions. The irradiated chambers are getting operated with three gas volumes

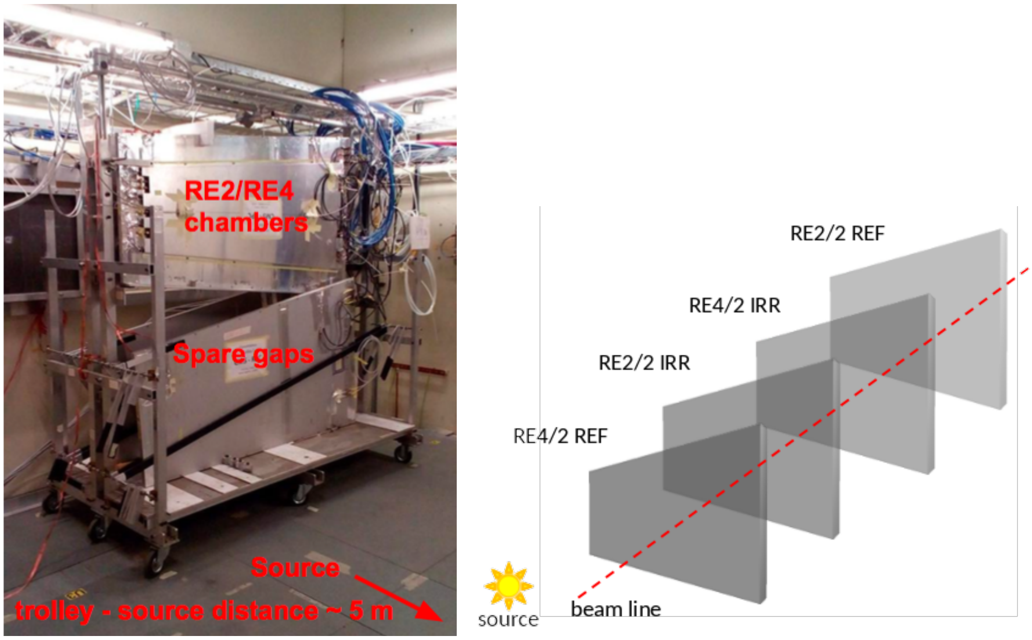

Figure 4.6: Left: Position of the trolley inside the GIF++ bunker at a distance of 5m from ^{137}Cs source, Right: Schematic diagram of the chambers placed inside trolley.

change per hour and one for the reference chambers, and with a relative gas humidity of ∼40%. The integrated charge versus time from day one of irradiation up to now is shown in Figure 4.7. At the time of this thesis writing, about 650 mC/cm^2 and 362 mC/cm^2 integrated charge has been accumulated for RE2/2 and RE4/2 irradiated detectors, which correspond at around 77% and 43% respectively of the expected integrated charge at HL-LHC (840 mC/cm^2).

4.3.3 Detector Parameters Monitoring

To spot the possible degradations on the surface of the electrodes due to the irradiation, the detector noise rate and dark current are periodically measured. Figure 4.8 shows the current (left) and noise rate (right) at the working point as a function of the integrated charge for the RE2/2 irradiated and reference chambers. From the distribution, it is clear that no significant variations have been observed so far.

The variations of current and rate with background radiation are periodically

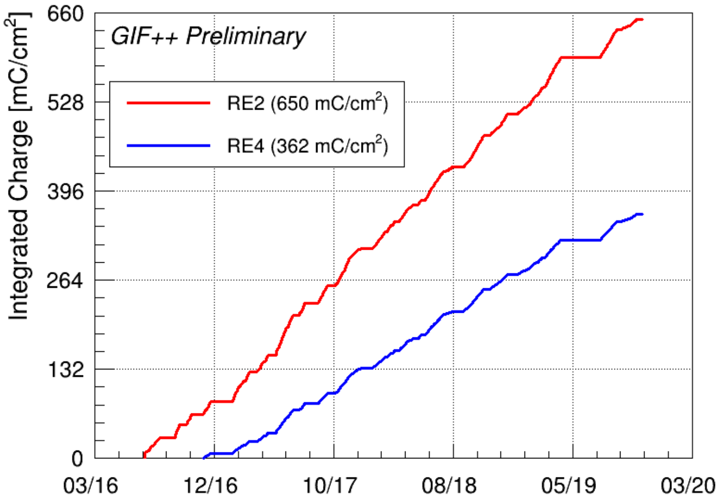

Figure 4.7: Integrated charge versus time, accumulated during the longevity test at GIF++ for RE2/2 (red) and RE4/2 (blue) chambers. The RE4/2 chamber has been turned on a few months later because of total gas flow limitations. Different slopes account for different irradiation conditions during data taking.

measured as well. To eliminate the dependence on the external parameters such as different setup, gas humidity and temperature, the ratios of the irradiated and the reference chambers is measured as a function of the integrated charge. Figure 4.9 left shows the RE2/2 current and rate ratio. The measurements show a decreasing trend at the beginning of the irradiation period, up to ≈ 300 mC/cm^2, when the operating conditions, in terms of gas flow rate and relative gas humidity were too low with respect to the high gamma background rate. These operating conditions lead to the electrodes resistivity increase, which caused the observed rate and current decrease. The argon gas is used to measure the resistivity. The electrodes resistivity increase is confirmed by the measurements performed by operating the RPCs filled with argon gas. Figure 4.9 right shows the coherent correlation between the RE2/2 currents ratio (red) and the resistivity variation (blue). The resistivity variation allows us to cancel out the dependence on the environmental conditions and is defined as:

$$\rho_{var} = \frac{\rho_{irr} - \rho_{ref}}{\rho_{irr}} \tag{4.3}$$

These plots also show that the resistivity increase is a recoverable effect, because

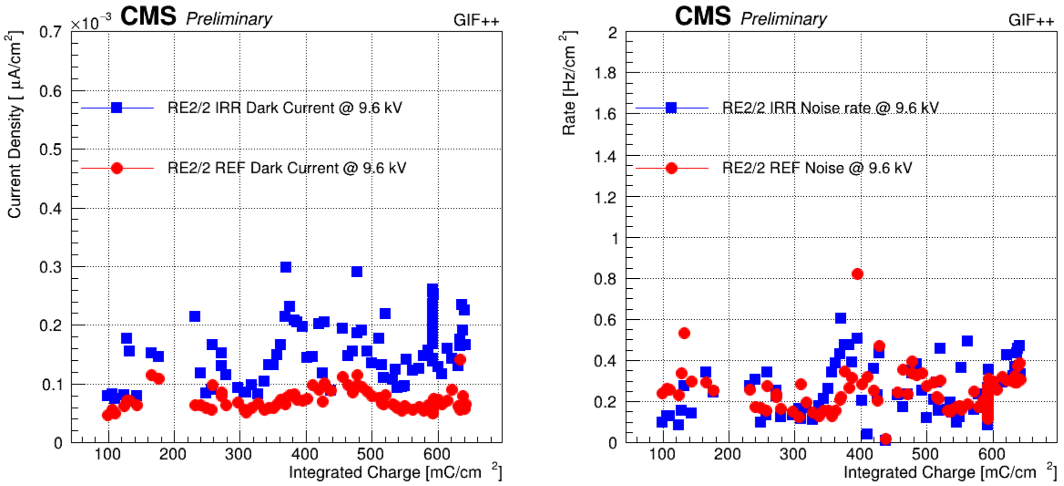

Figure 4.8: Dark current (left) and noise rate (right) versus the integrated charge, for RE2/2 irradiated (blues) and reference (red) chamber, at the working point voltage.

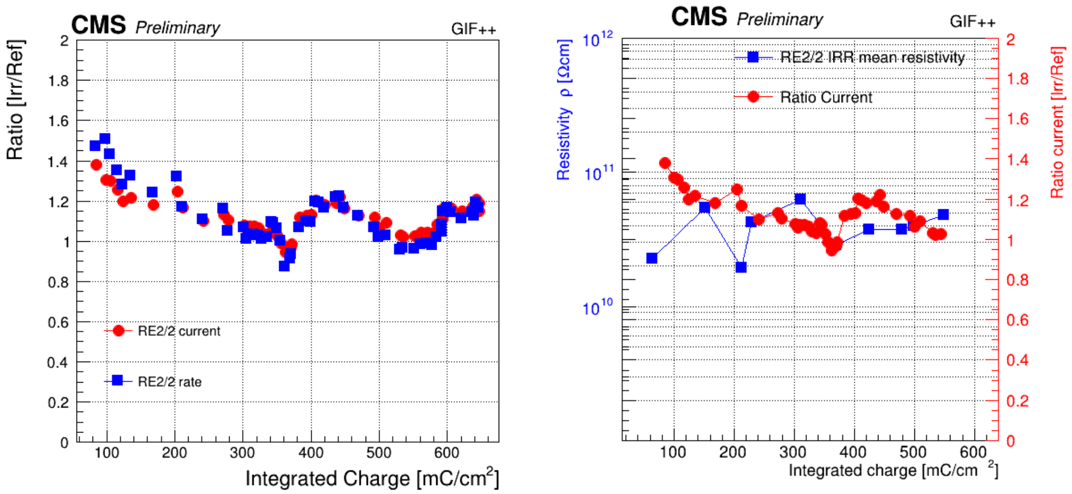

Figure 4.9: Left: RE2/2 current (red) and rate (blues) ratio between irradiated and reference chamber as a function of the integrated charge. Right: RE2/2 current ratio (red) and resistivity variation (blue).

on increasing the gas flow and gas relative humidity (around 352 mC/cm^2), the resistivity starts to decrease, and the current and rate begin to increase.

4.3.4 Detector Performance Monitoring

The detector performance has been tested using the muon beam, before starting the longevity test and repeated after different irradiation periods at GIF++. Up to now 51% of the expected integrated charge has been collected. Figure 4.10 shows the RE2/2 irradiated chamber efficiency as a function of the effective High Voltage (voltage normalized at the standard temperature and pressure), without irradiation (left), and with a gamma background rate of $\approx$ 600 Hz/cm^2 (right).

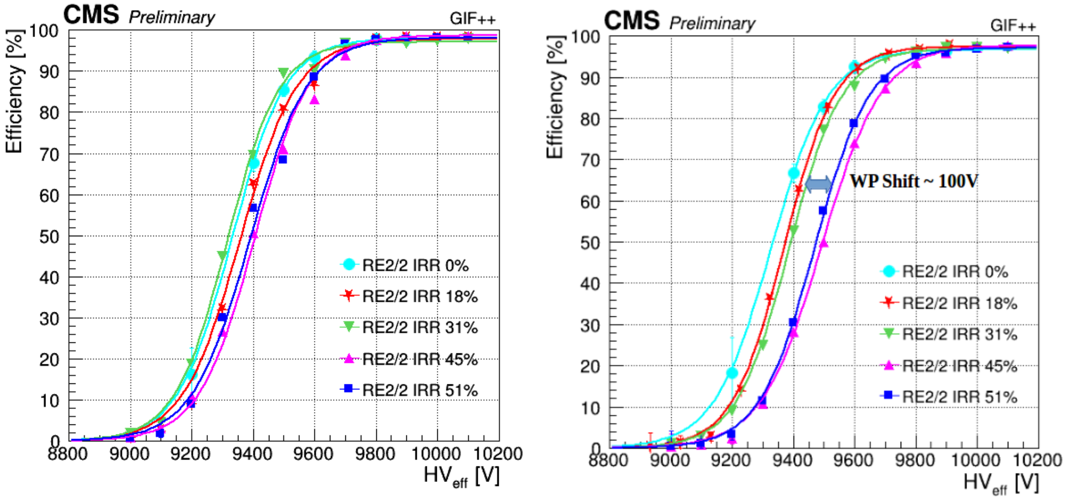

Figure 4.10: RE2/2 irradiated chamber efficiency as a function of the effective HV, taken with no irradiation (left) and under a gamma background rate of about 600 Hz/cm^2 (right). The efficiency is measured during different Test Beams (TB) corresponding to different fractions of the target charge to integrate.

The performance without background rate is stable in time and we didn't witness any efficiency degradation or working point shift. With a background rate of $\approx$ 600 Hz/cm^2, the efficiency remains stable at the working point but observed 100V shift starting from 45% of the expected integrated charge. The working point shift is related to the electrodes resistivity increase since the effective voltage applied to the electrodes (HV) is reduced by the voltage drop across the electrodes, which is proportional to the current (I) produced by the ionizing particles and to the bakelite resistance (R) [22]. The effective voltage applied to the gas (HV_{gas}) is therefore defined as:

$$HV_{gas} = HV - RI \tag{4.4}$$

The detector operation regime is invariant with respect to HV_{gas}, therefore the efficiency as a function of HV_{gas} does not depend any longer on the background radiation and the bakelite resistance. Figure 4.11 left represent the RE2/2 irradiated chamber efficiency curves at different background radiation (up to $\approx$ 600 Hz/cm^2) and at a different integrated charge. All the efficiency curves overlap and no working point shift observed since the electrodes resistivity increase effect has been removed. The RE2/2 irradiated chamber efficiency at the working point as a function of the background rate is shown in Figure 4.11 right. The efficiency is stable in time with a 2% decrease at the highest expected background rate, 600 Hz/cm^2.

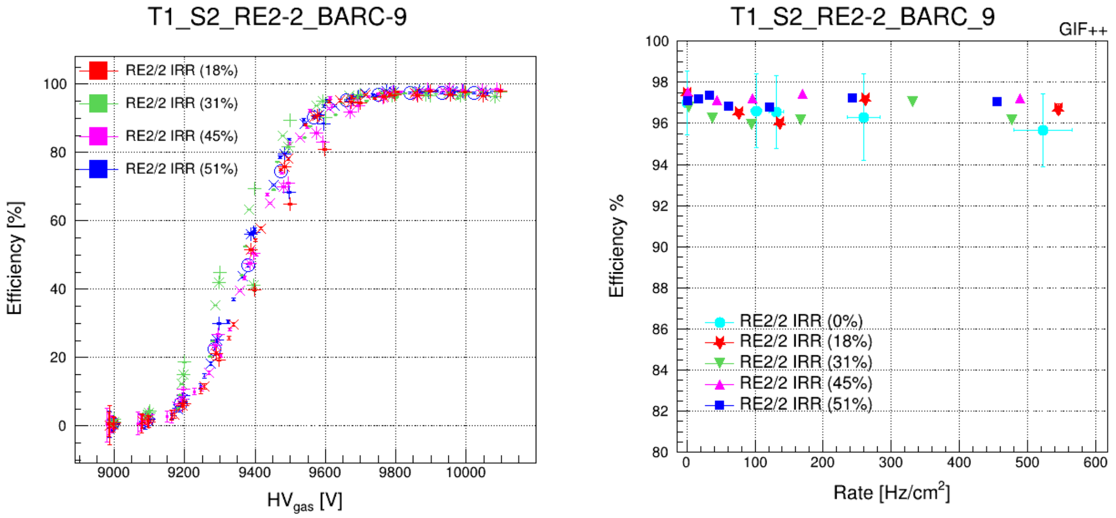

Figure 4.11: Left: RE2/2 irradiated chamber efficiency as a function of the HV gas, at different background irradiations and at different integrated charge values. Right: RE2/2 irradiated chamber efficiency at working point as a function of the background rate at different integrated charge values.

This Chapter summarizes the RPC detectors, their working principle, and design. The RPC detectors are tested in GIF++ and main parameters like current and rate get studied. From preliminary results, no evidence of any aging effect has been observed so far in the RPC detectors. The main detector parameters are stable, other than minor variations like the resistivity of electrodes, that did not affect the performance remains stable up to 51% of the expected integrated charge. Further investigations are needed to get closer to the final integrated charge of 840 mC/cm^2. In the next Chapter, simulation and reconstruction of events will be discussed.

Bibliography

[1] M. Titov, “Gaseous Detectors”, *Handbook of Part. Det. and Imaging, Springer*, vol. 2 (2012), https://doi.org/10.1007/978-3-642-13271-1_11

[2] R. Santonico and R. Cardarelli, “Development of Resistive Plate Counters”, *Nucl. Instrum. Meth.*, vol. 187, (1981), https://doi.org/10.1016/0029-554X(81)90363-3.

[3] M. Abbrescia *et al.*, “Cosmic ray tests of double-gap resistive plate chambers for the CMS experiment”, *Nucl. instrum. Meth. A*, vol. 550, (2005), https://doi.org/10.1016/j.nima.2005.06.074.

[4] R. Cardarelli, and others, “Avalanche and Streamer mode operation of resistive plate chambers”, *Nucl. instrum. Meth. A*, vol. 382, (1996), https://doi.org/10.1016/S0168-9002(96)00811-X.

[5] The CMS Collaboration, “The CMS experiment at the CERN LHC”, *JINST*, vol. 3, S08004 (2008), http://dx.doi.org/10.1088/1748-0221/3/08/S08004.

[6] The ATLAS Collaboration, G.Aad *et al.*, “The ATLAS Experiment at the CERN Large Hadron Collider”, *JINST*, vol. 3, S08003 (2008), http://dx.doi.org/10.1088/1748-0221/3/08/S08003.

[7] INO Collaboration, “India-based Neutrino Observatory: Project Report”, vol. 1, (2006), http://www.imsc.res.in/ ino/OpenReports/INOReport.pdf.

[8] A. Abashian *et al.*, “The Belle Detector”, *Nucl. instrum. Meth. A*, vol. 479, (2002), http://dx.doi.org/10.1016/S0168-9002(01)02013-7.

[9] Belle-II Collaboration, “Belle II Technical Design Report”, (2010), https://arxiv.org/abs/1011.0352.

[10] ILC Collaboration, “ILC Reference Design Report volume 4 - Detectors”, (2007), https://cds.cern.ch/record/1075831.

[11] BaBar Collaboration, “BaBar Technical Design Report EPAC Meeting Stanford, California, March 17-18, 1995”, (1995), http://www.slac.stanford.edu/BFROOT/doc/TDR.

[12] The ALICE Collaboration, “Performance of the RPC-based ALICE muon trigger system at the LHC”, *JINST*, vol. 7, (2012), http://dx.doi.org/10.1088/1748-0221/7/12/T12002.

[13] The ATLAS Collaboration, “ATLAS: Detector and physics performance technical design report”, (1999), https://cds.cern.ch/record/391176.

[14] M. Abbrescia *et al.*, “Eco-friendly gas mixtures for Resistive Plate Chambers based on tetrafluoropropene and Helium”, *JINST*, vol. 11, P08019 (2016), https://doi.org/10.1088/1748-0221/11/08/p08019.

[15] R. Guida, B. Mandelli and G. Riogoletti, “Performance studies of RPC detectors with new environmentally friendly gas mixtures in presence of LHC-like radiation background”, *Nucl. Instr. Meth.*, (2019), https://doi.org/10.1016/j.nima.2019.04.027.

[16] The CMS Collaboration, https://twiki.cern.ch/twiki/bin/view/CMSPublic/RPCDPGResultsforVenice.

[17] A. M. Sirunyan *et al.*, "Performance of the CMS muon detector and muon reconstruction with proton-proton collisions at $\sqrt{s} = 13$ TeV", *JINST*, vol. 13, P06015 (2018), https://doi.org/10.1088/1748-0221/13/06/P06015.

[18] The CMS Collaboration, "The Phase-2 Upgrade of the CMS Muon Detectors", *CMS-TDR-016*, CERN/LHCC 2017-012, (2017).

[19] G. Pugliese et al., "Long-term performance of double gap resistive plate chambers under gamma irradiation", *Nucl. Instr. Meth. A*, vol. 477 (2002), https://doi.org/10.1016/S0168-9002(01)01860-5.

[20] R. Guida, EN and EP and AIDA GIF++ Collaborations, "A new CERN Irradiation Facility to test large-area detectors for the HL-LHC program", *PoS ICHEP*, vol. 2016, (2016), https://doi.org/10.22323/1.282.0260.

[21] D. Pfeiffer *et al.*, "The radiation field in the Gamma Irradiation Facility GIF++ at CERN", *Nucl. instrum. Meth. A*, vol. 866, (2017), https://doi.org/10.1016/j.nima.2017.05.045.

[22] G. Pugliese *et al.*, "Aging study for resistive plate chambers of the CMS muon trigger detector", *Nucl. instrum. Meth. A*, vol. 515, (2003), https://doi.org/10.1016/j.nima.2003.09.021.

Chapter 5

Event Generators, Simulation and Physics Objects Reconstruction

This Chapter provides the description of event generation, simulation study and the reconstruction of physics objects. All the particles leave their signature in various parts of the CMS detector and by combining the information from each subdetector, the reconstruction and identification of leptons, jets and missing transverse energy are performed. Different algorithms and reconstruction procedures for various physics objects used in the CMS experiment are explained in this Chapter.

Before designing any particle detector, one needs to know the physics goals and how it will work according to physics requirements. For this purpose, detector simulation plays a significant role. From the very beginning of detector design, up to the final data-taking period and even after that, event simulation study helps to check its development, performance, and calibration of several components. The simulation study helps to strategize the analysis as one could determine the nature of SM backgrounds for a particular physics process. The comparison of real data with the outcome from simulation helps in refining the event generators, check for the modeling of a detector in simulation, identification of particles and calculation of reconstruction efficiencies. There is no solution for theoretical predictions that can fake our signal/physics process in the study because of the insufficient knowledge of non-perturbative QCD processes such as hadronization and effect of the partonic substructure of incoming hadrons on particle production [1]. Quantum Field Theory (QFT) helps to calculate differential and integral cross sections of multiple processes. However, these cross sections cannot be compared directly with the detector output because the hadronization processes are too difficult to compute analytically and nonlinear response of particle detector brings a considerable change in the shape of the final state particle kinematic distributions. Hence, to get final kinematic distributions, simulated events are generated by a stochastic way called Monte Carlo (MC) simulations [2,3].

Monte Carlo technique makes use of "random" numbers to solve difficult physical or mathematical systems (like complex integration) which cannot be explained analytically. High Energy Physics (HEP) experiments involve a large number of variables/parameters that are difficult to estimate, so the MC technique is used to make complex integration on these variables. Figure 5.1 [4] represents one of proton-proton collision event generation along with other major contributing processes using MC generators.

5.1 Anatomy of an Event

The generation of events is the preliminary step of the simulation process which uses the MC technique to simulate events that should be as genuine as from real experiments. At LHC, a proton-proton collision takes place at very high energy and the interesting physics process takes place through hard scattering. However, MC event generators simulate the events in various steps starting from the hard scattering followed by parton shower evolution, hadronization, and hadronic decays [5] as shown in Figure 5.1. The Perturbation theory can calculate the matrix elements (ME), (the sum of Feynman diagrams contributing to scattering amplitude) from

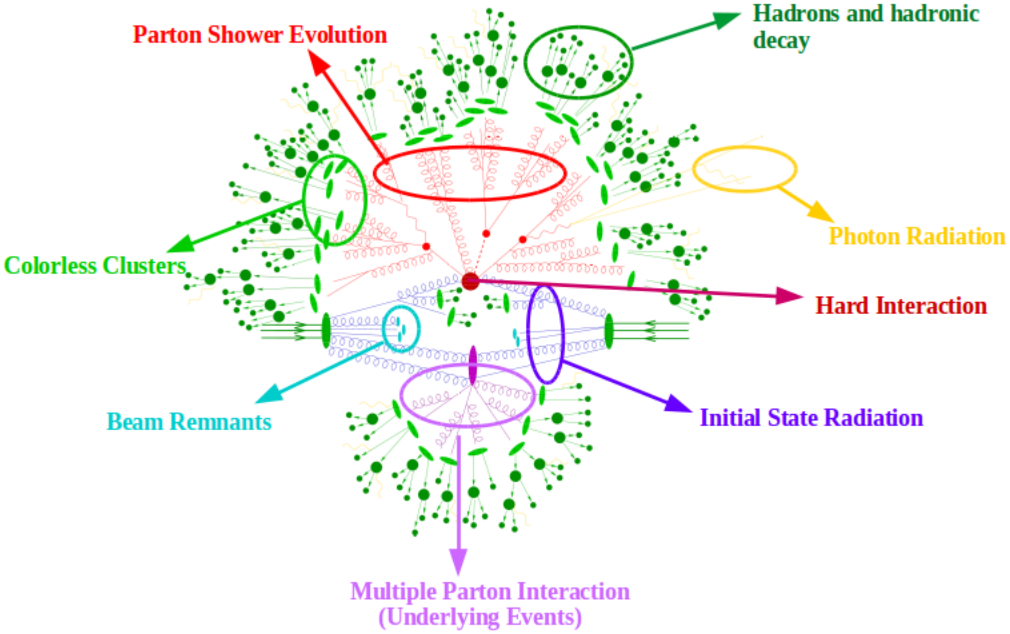

Figure 5.1: Figure representing hadron-hadron collision as simulated by a Monte-Carlo event generator. Each circle represents its corresponding meaning during the process of event generation. Red color bob represents the hard scattering, dark green corresponds to hadrons, purple bob is for Multiple Parton Interaction and Underlying Events and cyan color represent beam remnants.

the hard scattering to the final stable particles observed in a detector while the ones at lower momentum scales require non-perturbative approaches. Below are the steps that add to the event generation:

- **Hard Scattering Processes:** Hard processes take place due to interaction between constituents of two colliding protons called “partons” having high momentum exchange between them. The cross section for the hard scatterings can be easily calculated up to leading order (LO) with a perturbative approach using ME as a series in the expansion of strong coupling constant (α_s). However, this accuracy is process dependent and does not provide information about the whole data, like for next-to-leading order (NLO) processes which contain more Feynman diagrams or an extra power of α_s, extra radiation. Also, it does not provide a prediction of the normalization and shape of the kinematic distributions.

- **Parton Showering:** The incoming and outgoing partons of the hard scattering process further emit initial and final-state radiations, creating Parton Showers (PS). Parton showering is employed after hard processes to include higher-order QCD effects. PS continues with a backward evolution, beginning from the hard processes or initial interacting partons up to lower momentum scales ($\sim$ 1 GeV) where non-perturbative effects start coming into the picture. The extensively used algorithm for PS is the Sudakov form factor approach [6] which defines the probability for a parton that it does not split into other partons when evolving from a high scale to a smaller scale. The PS algorithm stops when QCD (or α_s) coupling becomes large enough to begin non-perturbative interactions. Since the strong forces prevent asymptotic freedom, the partons (gluons and hadrons) cannot exist in a free state and they need to be confined into color-neutral hadrons.

- **Hadronization:** Hadronization is the process of combining colorless hadrons out of quarks and gluons. This occurs when the partons reach the hadronization scale having very low energy of $\sim$ 1 GeV and at this scale, a perturbative QFT approach cannot be utilized. Hence, there are two models which are used to simulate the hadronization of partons in the event generators, are explained below:

  - ***Cluster Hadronization Model***: According to this model [7], gluons undergo a non-perturbative splitting into $q\bar{q}$ pairs and quarks are clustered into colorless groups. Clusters are made from the momentum space neighbouring $q\bar{q}$ pairs, possess high invariant mass and are further decayed to smaller mass scales suitable to form hadrons.

  - ***Lund String Model***: This hadronization model [8] is the process of transforming partons into hadrons and is build on the string analogy that when the two quarks (q and $\bar{q}$) try to move apart from their production vertex, the QCD potential starts growing linearly. On stretching the string, the potential energy stored in the string rises and kinetic energy decreases which break the string into two parts, creating additional color-singlet $q\bar{q}$ pairs, till energy left to create another such pair, is less. The remaining partons can be identified with hadrons.

Apart from hard processes and hadronization etc, some other steps are necessary to simulate as they help in building the event's anatomy.

- The Initial State Radiation (ISR) are the radiations emitted by incoming partons before hard interaction takes place and result in the creation of jets close to the direction of incoming hadrons. Similarly, the Final State Radiation (FSR) is emitted by final state partons and they help in building the structure of jets. Also, the decay of unstable hadron particles can produce many other particles. During the collisions, many interactions take place in addition to hard scattering which undergoes soft scatterings among themselves, known as Multiple Parton Interactions (MPI) and contribute to Underlying Events (UE). Also, the leftover partons (not involved in hard scattering) known as Beam Remnant can interact with each other and should be taken into account for UE to get the correct balance of momentum and charge.

5.2 MC Event Generators

The CMS Collaboration is using a variety of event generators for different purposes. The MC event generators used to generate physics processes studied in this Thesis are described below:

- PYTHIA: This general-purpose generator has two versions: PYTHIA6 [9] and PYTHIA8 [10] which are based on Fortran and C++ respectively. They are used to generate events in proton-proton, electron-electron and electron-proton collisions. The MC samples used in this Thesis are based on PYTHIA8 version. PYTHIA is used to simulate mostly 2 → 2 processes (ME) at LO and have tools like p_T-ordered ISR, FSR, MPI, and many other processes. In addition, Pythia has an interface to other MC generators and tools, for instance, to use NLO generated events. The CMS collaboration widely uses Pythia for the hadronization and showering in the majority of the SM and SUSY physics.

- Madgraph: Madgraph [11] is the most frequently used event generator in CMS as it can calculate the cross section up to higher-order corrections. This generator is a 2 → n ME generator where "n" is the number of partons in the final state and goes maximum up to 8. However, it needs to be interfaced with other generators such as Pythia or Powheg to compute parton showering, hadronization and UE, etc. Also, one package, Madgraph with MC@NLO or we can say Madgraph5_MC@NLO is used to perform the parton shower calculation having less uncertainty in the cross section.

- Powheg: As the name, Powheg stands for Positive Weight Hardest Emission Generator, it generates events only with positive weights at NLO precision and is 2 → 2 ME generator. It also has to be interfaced with a general-purpose generators like Pythia to perform parton and hadronization steps. The processes including the production of the Higgs boson through vector boson fusion topology have been generated using Powheg generator.

- TAUOLA: TAUOLA [12] is the dedicated package to simulate τ leptons and it has to be interfaced with other generators like Pythia, Madgraph for correct modeling of τ lepton production and decay. The TAUOLA package takes into account the relative QED corrections and spin correlations. Taking generator level information from Pythia, it calculates the form factors for tau decays. TAUOLA requires a general-purpose MC generator, which produces stable τ-leptons.

5.3 Detector Simulation

After the MC event generation, the last step is to pass the final state particles through the CMS detector for the reconstruction of an event, to have some idea about the physics interaction involved and detector signal as is the case of real collision data. The data and simulation could then use the same reconstruction methods, permitting a direct comparison of objects at the detector level. The detector simulation is based on a full description of the CMS detector geometry which is implemented in the GEANT4 (GEometry ANd Tracking) [13] simulation toolkit that contains many C++ libraries and is widely used in High Energy Physics detectors. The modeling of the full geometry and information regarding the tracking of the particles from each sub-parts of the detector is also provided by GEANT4. This software is also capable to handle the magnetic field and particle interaction, their energy losses across each subdetector as they pass through them. For each subdetector, the response is precisely simulated giving an output signal in an equivalent way as the output available in actual data. The simulated signals are stored and processed similarly as real detector signals in subsequent event reconstruction steps. All the data and MC simulated samples are analyzed by the CMS software (CMSSW) framework that is flexible with modular software structure, having a large collection of C++ classes (related to various detector subsystems, processing steps and analysis elements), and python scripts. The CMSSW is also interfaced with the ROOT software package [14] which helps in the statistical analysis of data and graphical illustration of physics results.

5.4 Physics Object Reconstruction

During proton-proton collision at LHC, a large number of particles get produced but it is not easy to identify them without any knowledge about its signatures in the detector. Each particle interacts differently and leaves their signatures in different parts of the detector. The electrons and photons deposit their energy in the ECAL, but electrons also have tracks in the tracker (refer Section 3.3.2) which helps to differentiate between electron and photon. The neutral and charged hadrons deposit their energy in HCAL, neutral hadrons have no associated tracks in the tracker but charged hadrons have hits in the tracker. Muons and neutrinos are weakly interacting particles, but muons cross all the layers of the detector, deposit little energy in the calorimeters, have tracks in the tracker and muon detectors, which is enough to reconstruct and identify muons. However, neutrinos leave unidentified that cause the momentum imbalance. In the next Section, the reconstruction of physics objects which are used in the present Thesis are explained. Figure 5.2 shows one of the event display in the CMS detector where Higgs is decaying to four leptons: 2 electrons (green) and 2 muons (red).

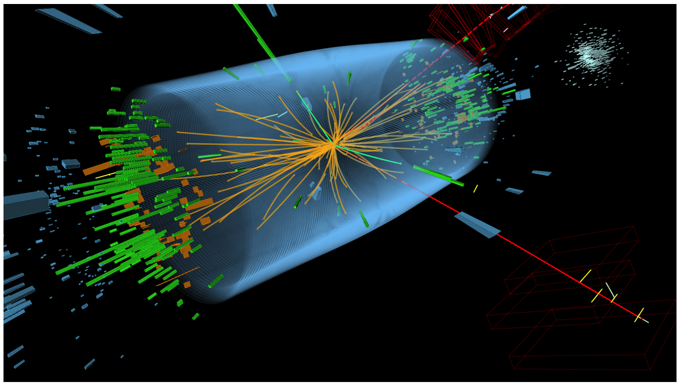

Figure 5.2: Figure depicting the event visualization of Higgs boson decaying to four leptons i.e. 2 electrons (green) and 2 muons (red).

Once the information about the signatures of the particles is known, the CMS software takes information from each subdetector and provides a set of reconstructed objects at the output. For the tracker and muon detectors, the information is available in terms of position coordinates while for the calorimeters, this is available in energy clusters. Up to now, this is called local reconstruction. These reconstructed hits are employed to reconstruct electrons from the charged particle tracks, and photons and jets from the calorimeter clusters, etc. and this step is called global reconstruction. After combining all the objects from each subdetector, the high-level objects like E_{T}^{miss}, τ and b-jets, etc. are reconstructed by using particle-flow (PF) event reconstruction algorithm [15] to present a complete and final explanation of an event resulting in a more accurate measurement of the momentum of charged particles. The reconstruction algorithm steps are illustrated in Figure 5.3.

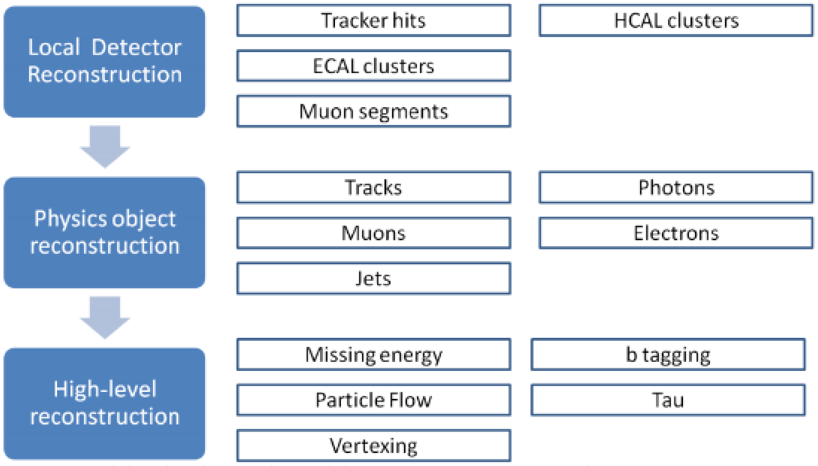

Figure 5.3: Reconstruction algorithm for physics objects in CMS.

5.4.1 Particle Flow Clustering - Particle Reconstruction

The particle flow (PF) event reconstruction algorithm developed by the CMS experiment is used to reconstruct and identify the particles by taking input from all the subdetectors in various forms: charged particle tracks reconstructed in the tracking system, energy cluster deposits in the calorimeters (ECAL and HCAL), and muon tracks in the muon spectrometer. The PF algorithm combines necessary information from all subdetectors in several forms (described above) to detect and identify the stable physics objects (particles) like muon, electron, photons, charged and neutral hadrons, etc. Pictorial view of the PF algorithm is shown in Figure 5.4. Tracker subdetector has high resolution and granularity, so measurement of charge, position and momentum of the charged particles is made in tracker instead of calorimeters. Extrapolation of charged particle tracks is done through calorimeters and if tracks

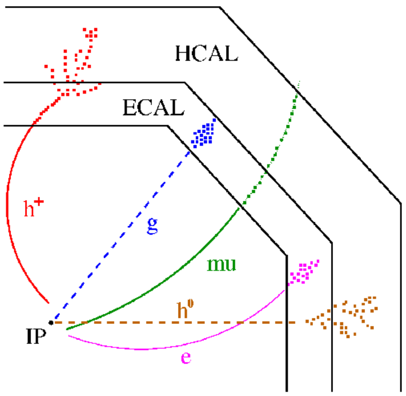

Figure 5.4: Particle flow Reconstruction algorithm for physics objects in CMS.

fall in the close proximity of the energy cluster, the tracks get associated with that energy cluster. This association of tracks and energy cluster constitutes the charged hadron and the building blocks are not considered anymore in the rest of the algorithm. The muons are identified and reconstructed prior to charged hadrons to avoid the overlay between them. The PF muon is constructed if the global fit of the tracker and muon tracks results in a combined momentum that is within three standard deviations from the momentum of the track from the inner tracker. If the tracks pass the criteria for PF muon, the link is excluded from further considerations. The electrons have to be reconstructed carefully as they can count on the frequent photon emissions during Bremsstrahlung. Thus a special way, like calorimeter clustering is helpful for good reconstruction and identification of electrons against Bremsstrahlung photons. Once muons and electrons get reconstructed, their associated tracks and clusters associated are removed from the block. If all deposits get associated with the particles, the leftover cluster in the ECAL gets assigned to photons and similarly to the neutral hadrons in the HCAL. Since tau lepton has a short lifetime and it decays immediately (leptonically and hadronically) after being produced, hence, it can be reconstructed by combining its decay product information. The information from energy deposits in the calorimeters and tracking information is used to reconstruct its decay products. The four momentum of the particles are calculated by combining the information from all subdetectors.

5.4.2 Tracks and Primary Vertex Reconstruction

To begin with the reconstruction of the physics objects in the CMS detector, the first move is to reconstruct charged particle tracks. When the collisions take place, energy deposits, called "hits" are recorded by pixel, strip tracker and muon spectrometer. The CMS has got a tracking software package designed in such a way to achieve efficient track reconstruction across a wide p_T range (100 MeV to 1 TeV) as well as to keep a low misidentification rate from unrelated hits. The standard algorithm employed for the reconstruction of tracks is Combinatorial Track Finder (CTF) based on Kalman Filtering (KF) [16].

The reconstructed tracks which satisfy the quality flags like the number of hits, vertex compatibility and normalized chi-square (χ^2) value are kept for further physics analysis. The tight quality cuts imposed on the reconstructed tracks increase the purity of real track but decrease the efficiency while loose quality cuts result in low purity but high efficiency. Hence, with the global combinatorial track finder, the efficiency to reconstruct real tracks is around 80% - 90% for the charged pions and goes to 99% for isolated muons with $\sim$ 1.5% fake rate.

***Primary Vertex Reconstruction*:** The reconstructed tracks go as input to reconstruct all the true vertices in a collision, Primary Vertex (PV) (from hard scattering) along with the pileup vertices (from pileup interactions-soft scatter collisions). The PV refers to the exact point where the hard scattering or proton-proton collisions happen and the vertex with the largest quadratic sum of the p_T of associated physics objects. Secondary vertices arise because of the decay of long-lived particles that originated from PV such as b-jets.

The Deterministic Annealing (DA) clustering method [17] is employed to reconstruct offline primary vertex which is done in two steps. The first step is to adjust the tracks in clusters according to the z coordinate of the track point near to the beamline. Second, each track in the cluster has to be fitted with a three-dimensional vertex fit that uses the full track information from the tracking system. The fit decides whether to accept or to reject the reconstructed vertex. If the vertex gets accepted, it should have four degrees of freedom (n_{dof}). This results in multiple primary vertices reconstruction and all of them get stored. Further, the primary vertex must satisfy two conditions that are described below:

1.) Its z position should be within 24 cm of the nominal detector center.
2.) Radial position within 2 cm from the beam spot.

After having a set of elected/feasible primary vertices, the one vertex which has the maximum sum of the square of the transverse momentum of the tracks associated with it, is chosen as hard scattering vertex. The primary vertex is then used to measure the location and the associated uncertainty of proton-proton interactions in each event. Once the PV gets reconstructed, the next task is to reconstruct leptons and high-levels objects.

5.4.3 Tau Lepton Reconstruction and Identification

Among the lepton family, Tau (τ) lepton is the heaviest, having mass 1.76 GeV (1776.82 ± 0.12 MeV/c^2) and lifetime 2.9×10^{-13}s ($c\tau = 87$ μm). Because of high mass and small lifetime, it decays close to the primary vertex into leptons and hadrons. Table 5.1 shows the decay modes and their branching fractions. Tau decays 2/3 (65%) hadronically into either one or three charged hadrons "h" (basically pions and kaons) and 35% leptonically (electrons and muons). Figure 5.5 shows the leptonic decay of tau lepton and Figure 5.6 shows all the hadronic tau (τ_h) decay into charged pions ($\pi^\pm$) with up to two neutral pions (π^0), which further decay to two γ's each ($\pi^0 \rightarrow \gamma\gamma$). Hadronic tau lepton is the most challenging to reconstruct and identify because of its separation from quark and gluon jets as the QCD multijet production at LHC is in abundance than the production of hadronic Taus. However,

Decay Mode	Resonance (mass)	Branching Ratio (%)	Name
$\tau^- \rightarrow e^- \nu_\tau \bar{\nu}_e$	-	17.8	Leptonic
$\tau^- \rightarrow \mu^- \nu_\tau \bar{\nu}_\mu$	-	17.4	Leptonic
$\tau^- \rightarrow h^- \nu_\tau$	-	11.5	1-Prong
$\tau^- \rightarrow h^- \pi^0 \nu_\tau$	ρ^- (770)	26.0	1-Prong + π^0
$\tau^- \rightarrow h^- \pi^0 \pi^0 \nu_\tau$	a_1 (1260)	9.5	1-Prong + π^0
$\tau^- \rightarrow h^- h^+ h^- \nu_\tau$	a_1 (1260)	9.8	3-Prong
$\tau^- \rightarrow h^- h^+ h^- \pi^0 \nu_\tau$	-	4.8	3-Prong + π^0
other modes with hadrons	-	3.2	-

Table 5.1: Tau lepton Decay mode and their branching fraction.

taus are well collimated and isolated, so they are well identified. *Hadron Plus Strip (HPS)* algorithm is used to reconstruct and identify the hadronic τ decays in the study described in this Thesis. The τ leptons are expected to play a significant role in exploring new physics phenomena at the LHC. They appear in the final state of many SM and beyond SM (BSM) scenarios.

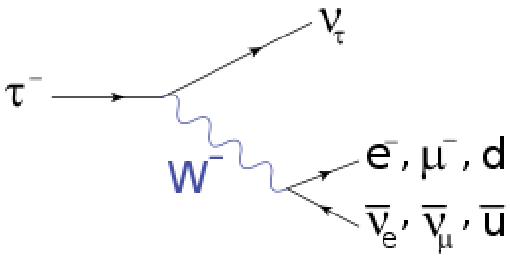

Figure 5.5: Leptonic decay of tau into electron or muon with tau neutrino.

5.4.3.1 Hadron Plus Strip Algorithm

The HPS [19] algorithm is the most promising, in terms of energy resolution and fake physics objects (the reconstructed objects that can mimic the physics objects) rejection. This is often used in CMS to reconstruct τ_h's in the final state which decays into charged pions and neutral pions that subsequently decay to pair of two photons or electron-positron pairs. Figure 5.7 shows the decay mode of hadronic tau into hadron plus one strip or two strips. The PF jets reconstructed using an anti-k_T

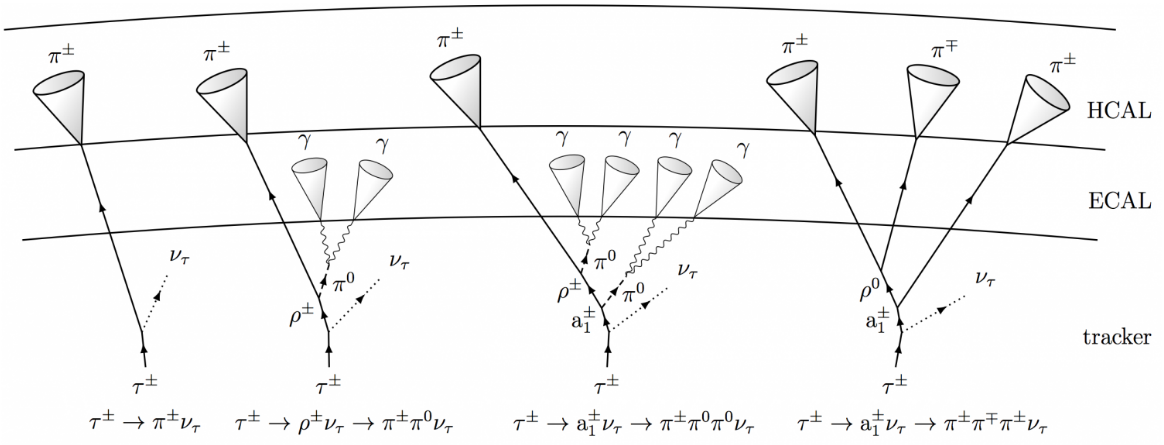

Figure 5.6: Tau lepton decay hadronically into one or three charged pions with maximum two neutral pions each of which further decays into two γ's [18].

(AK) algorithm (more details in Section 5.10) with a distance parameter $\Delta R = 0.4$ goes as an input seed to the HPS algorithm.

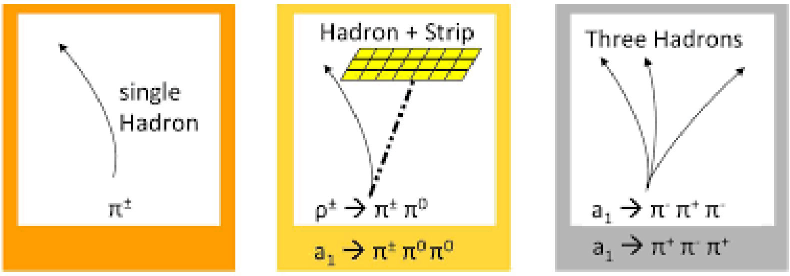

Figure 5.7: HPS algorithm showing the one or three hadrons plus strips decay.

To begin with, the reconstruction of π^0 is done and then combined with charged hadrons to reconstruct the τ_h decay modes and measurement of the tau four-momentum and isolation quantities is done. Photons coming from the decay of neutral pions get converted within the tracking system of the detector, and the energy deposited by them is accounted by clustering the electron and photon constituents of the jet seeding the τ_h reconstruction into "strips" in $\eta - \phi$ plane. The strip size is restricted to $0.05 < \Delta\eta < 0.15$, $0.05 < \Delta\phi < 0.3$ in $\eta - \phi$ plane, which is magnified in ϕ-direction because of the bending of e^-/e^+ pairs under the influence of CMS magnetic field. The electron or photon with the highest p_T which is not yet involved in the strip is used to compose a new strip. The new strip position is determined by its η and ϕ candidates. And then it again searches for the next highest energetic electromagnetic particles within the strip size window. As soon as the particle is found, it is merged with the strip and the new strip position is re-computed as the energy-weighted average of the electron/photon constituents in the strip. This procedure is repeated until there are no more electrons or photons with $p_T > 0.5$ GeV within the strip window. If no particle is found in the proximity, a new strip centered around the next highest energetic particle is created which is not associated with any strip. The total transverse momentum (p_T) of the strip should be > 2.5 GeV to be considered as π^0 and then it is combined with the charged hadrons to reconstruct individual hadronic tau decay modes as shown in Figure 5.6. Following are the decay modes of τ_h:

- **Single hadron/prong plus no strip/π^0:** Only one charged particle and no strip ($h^{\pm}$) is produced or neutral pion decay to particles having very small energy to be reconstructed as strips.

- **One hadron plus one strip:** One charged particle with two photons coming from π^0 decay within proximity of calorimeter surface to be included in single strip size ($h^{\pm}\pi^0$) and having a mass window of $0.3 < m_{\tau_h} < 1.3 \times \sqrt{p_T/100}$ GeV. For tau candidates with $p_T < 100$ GeV and $p_T > 1044$ GeV, the mass window upper limit is 1.3 and 4.2 GeV, respectively.

- **One hadron plus two strips:** One charged particle with two photons coming from π^0 decay and are well separated in the calorimeter surface resulting in the formation of two strips ($h^{\pm}\pi^0\pi^0$). The mass window of this combination is $0.4 < m_{\tau_h} < 1.2 \times \sqrt{p_T/100}$ GeV. For tau candidates with $p_T < 100$ GeV and $p_T > 1044$ GeV, the mass window upper limit is 1.2 and 4.0 GeV, respectively.

- **Three hadrons:** Three charged particles ($h^{\pm}h^{\mp}h^{\pm}$) having total charge one within a mass window of $0.3 < m_{\tau_h} < 1.5$ GeV. The tracks are required to originate within $\Delta z < 0.4$ cm of the same vertex.

- **Two hadrons plus one or two strips:** This category is to reconstruct three charged hadrons from τ_h decay, but one of the tracks escapes detection or get merged with another one. This is useful to recover efficiency losses for high-p_T taus.

However, two charged hadrons result in large jet backgrounds as they fake the τ_h, so they are not considered in the analysis presented in this Thesis. The τ_h candidates having charge other than ±1 and any charged hadrons or strips not falling between signal cone size of $\Delta R = 3.0/p_T$ GeV centered on tau direction are rejected, where the p_T depends on tau hadronic system. The cone size in the range 0.05-0.1 is used for the cases with $\Delta R <0.05$ and $\Delta R > 0.1$. After having multiple combinations passing these window selections, only τ_h candidate with the highest p_T is selected resulting in a single τ_h per jet and others are discarded.

For the SUSY search, the present analysis emphasizes only on compressed mass spectra scenario with soft leptons, with the "old decay mode finding" algorithm, as per the official recommendation by the tau Physics Object Group (tauPOG). This discriminator combines the tau isolation and lifetime information to well discriminate between real τ_h candidates and hadronic jets.

Once the τ_h candidates get reconstructed, it is necessary to discriminate it against muons, electrons, quark and gluon jets. To discriminate between τ_h and other physics objects, multivariate analysis (MVA) and Cut-isolation based discriminators are employed which are discussed in details below:

- **Discrimination of τ_h Against Electrons:** Isolated electrons can easily fake the τ_h with one prong/hadron ($h^{\pm}$). The Bremsstrahlung photons emitted by electrons can easily be reconstructed in $h^{\pm}\pi^0$ decay mode and have a high probability to pass the isolation discriminators. For the analysis presented in this Thesis, MVA [19] based anti-electron discriminator developed by CMS TauPOG has been applied because of better fake rate rejection and high selection efficiency for real τ_h decays over wide p_T range.

  - **MVA-based Electron Discriminators:** The discriminator based on boosted decision tree (BDT) takes some input variables like energy deposited by charged particles and photons in ECAL and HCAL, p_T, η and mass of the τ_h candidate, etc. [20] along with some photon-related variables like energy fraction of τ_h carried by photons, the number of photons in any of the strips associated with the τ_h candidate, for training to differentiate τ_h against electrons. By cutting on the output BDT variable, the "Loose" working point has been used in the current analysis because of high identification efficiency.

- **Discrimination of τ_h Against Muons:** Muons can easily fake τ_h with one prong ($h^{\pm}$) decay mode. The discriminators (Cut-based and MVA-based) developed to reduce $\mu \rightarrow \tau_h$ misidentification rate are based on the fact that τ_h candidate is rejected if the signal is found in the muon system close to τ_h direction [20]. For the analysis presented in this Thesis, the "Tight" working point is used because of high fake muon rejection capability.

- **Discrimination of τ_h Against Jets:** The PF jet constituents are the main input seed for the reconstruction of τ_h candidates, so there is a large probability for $jet \rightarrow \tau_h$ fake rate from quark and gluons jets. Since taus have low particle multiplicity, they are isolated from other particles. Cut-based or isolation sum and MVA-based isolation discriminators are defined below to differentiate between tau jet and other jets [20].

  - **Cut-based Isolation Discriminator:** This discriminator determines the isolation of hadronic taus by summing the scalar p_T of charged particles ($\sum p_T^{charged}$) passing some quality cuts and photons with $p_T > 0.5$ GeV ($\sum p_T^{\gamma}$) reconstructed utilizing the PF algorithm within the isolation cone of size $\Delta R = 0.5$ centered around tau direction. The charged hadrons ($h^{\pm}$) and strips/photons used to reconstruct the tau signal cone are discarded while calculating the isolation sum [20] which is given as:

$$I_{\tau_h} = \sum p_T^{charged}(d_Z < 0.2cm) + max(0, \sum p_T^{\gamma} - \Delta\beta \sum p_T^{charged}(d_Z < 0.2cm)) \tag{5.1}$$

$\Delta\beta$ corrections are applied to correct the effect of the pileup on photon isolation. These corrections are achieved by summing the p_T of the charged particles within a cone of size $\Delta R = 0.8$ away from tau production vertex with a distance in z-direction greater than 0.2 cm. Earlier, 0.46 was used as the $\Delta\beta$ empirical factor but PU contribution to isolation in 2015 and 2016 data was overestimated, so a new $\Delta\beta$ factor of 0.2 is elected. The isolation sum is multiplied by 0.2 to make identification insensitive to the PU. This discriminator has three working points: loose, medium and tight requiring I_{τ_h} to be less than 2.5, 1.5, or 0.8 GeV, respectively. These thresholds are chosen such that the resulting efficiencies for the three working points cover the range required for the analyses.

- **MVA-based Isolation Discriminator:** The MVA-based τ_h identification discriminator sums up the isolation and other differential variables that are sensitive to the lifetime of τ_h, by well differentiating the τ_h decays and quark or gluon jets. This is based on boosted decision tree (BDT) and on employing, it provides a reduction in the $jet \rightarrow \tau_h$ misidentification probability. The BDT takes the input variables like energy deposited by charged and neutral particles isolation sums, p_T, η and mass of the τ_h candidate, the ratio of transverse impact parameters and its uncertainty, etc. along with some new variables like the multiplicity of photon and electron candidates with $p_T > 0.5$ GeV in the signal and isolation cones which are discussed in more detail in Ref. [19]. By cutting the output on BDT variable, the tight working point is used in our analysis to create a balance between real τ_h efficiency ($\sim 50\%$) and hadron jet rejection rate ($> 99\%$ for jets with $p_T > 20$ GeV).

5.4.4 Tau Energy Scale and Resolution

The tau resolution and scale of mass reconstruction depends on how well the τ_h is reconstructed. The tau response is defined as the relative difference between the transverse momentum of a reconstructed τ_h (after passing all discriminators) and transverse momentum of a generated τ_h matched within $\Delta R < 0.2$ to the reconstructed tau. The tau response is shown in Figure 5.8. Clearly, we have the significant narrow Gaussian-like component with a long tail (in contrast to electron and muon), but at high p_T the Gaussian peak gets broaden and tails become less substantial.

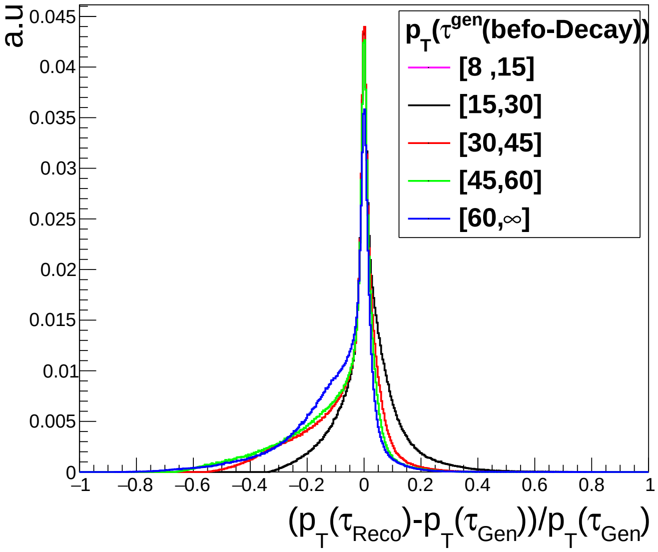

Figure 5.8: Relative p_t resolution of reconstructed τ_h candidates.

5.4.5 Jets Reconstruction

Quarks and gluons (called partons) are the mainly produced particles after the proton-proton collision occurs. But due to quark confinement, they cannot move freely through the detector. However, they get combined with the other partons that are created in the QCD vacuum to produce colorless particles as explained in Section 5.1. A bunch of collimated hadrons is called a jet [21] and deposit most of their energy in HCAL. Jets can be reconstructed [22] from various methods depending upon the information available from different parts/subdetectors of CMS detector as shown in Figure 5.9.

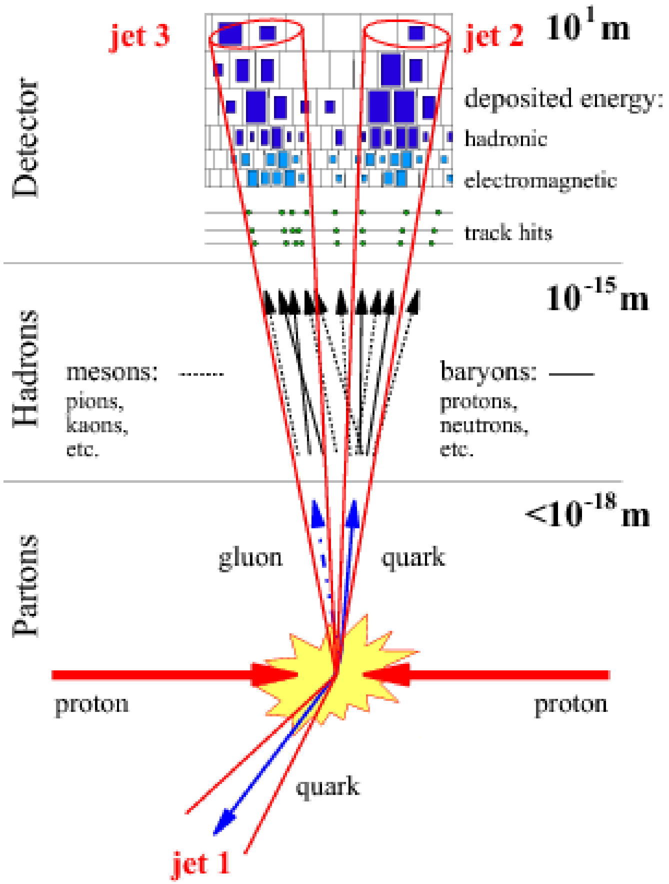

Figure 5.9: Illustration of a jet to which bundles of partons, hadrons, or detector measurements are grouped together [23].

- **Calorimeter Jets (CaloJets):** As in the name, these CaloJets are reconstructed by crystal information in the ECAL subdetector and from the calorimeter tower in the HCAL subdetector [24]. The energy of the calorimeter towers is the combination of the energy of ECAL and HCAL readout cells. Certain energy thresholds are added to cope with noise from the detector readout electronics and jets arising from the pileup. CaloJets have a relatively poor resolution because of the compact size of HCAL.

- **Jet-plus-track (JPT) Jets:** These jets are reconstructed using the information from tracker and calorimeters [25] and rely on a high-quality tracking system. The charged particle tracks are associated with the CaloJets which are bent out of the cone used in the reconstruction of CaloJets. With the additional tracks, the energy and direction of CaloJets are improved.

- **Particle Flow (PF) Jets:** The PF jets are reconstructed using the PF event reconstruction algorithm discussed in Section 5.4.1. In the present study, PF jets are employed which are reconstructed by combining the information from all the subdetector systems i.e. the tracks of the charged particles in the tracker, energy deposited in ECAL and HCAL, signals in the preshower and muon spectrometer. PF jets are considered the best in terms of momentum and spatial resolution.

The charged hadrons take 65% of the jet energy in the tracker detector region, 25% is taken by photons while neutral hadrons carry 10% of jet energy. So to conclude, PF can reconstruct about 90% of the jet energy with good accuracy, and remaining 10% of jet energy is affected by the insufficient resolution of the HCAL.

5.4.5.1 Jet Clustering Algorithm and Jet Identification

In the CMS collaboration, jets are clustered using the anti-k_T algorithm. Anti-k_T algorithm combines the PF objects to cluster into jets and calculates the distance between 1.) beamline and particle (objects) d_{iB} 2.) between two particles d_{ij} (i.e. pseudo-jets, particles) i and j as shown below:

$$d_{iB} = k_{T,i}^{2p} \tag{5.2}$$

$$d_{ij} = min(k_{T,i}^{2p}, k_{T,j}^{2p})\frac{\Delta R_{ij}^2}{R^2} \tag{5.3}$$

where $\Delta R_{ij}^2 = (y_i - y_j)^2 + (\phi_i - \phi_j)^2$ is the $(\eta - \phi)$ space distance between the two particles and R is the radius parameter that determines the final size of the jet and is usually between 0.4 - 0.7. In the present study, cone size of $\Delta R = 0.4$ is used, as this provides a good agreement between the energy of jet itself and external energy coming from overlap with other jets, PU interactions, ISR or FSR, etc. Variable "p" is added to govern the relative power of energy vs geometrical scales to differentiate the three algorithms i.e. if p = 0 it corresponds to Cambridge/Aachen algorithm [26], p = 1 and p = -1 corresponds to k_T [27] and anti-k_T [28] algorithms respectively. The algorithm proceeds by finding the smallest of the two distance d_{ij} and d_{iB}. If d_{ij} is the smallest, combine i and j to have one particle (ij) using summation of four-vectors after which i and j are removed from the list of particles. If d_{iB} is the minimum, call i a final jet and remove it from the list of particles. The distances are recalculated and the process is repeated until either all particles are part of a jet with the distance between the jet axis $R_{ij} >$ R, which is inclusive clustering or until a desired amount of jets have been found, this is exclusive clustering.

The anti-k_T algorithm is dominated by high-p_{T} and hence it favors to cluster high particles first as shown in Figure 5.10. This algorithm is less susceptible to soft radiation i.e. UE and PU, and also independent of the distributions of energy in the collinear particles which refers to infrared safety and collinear safety respectively.

The fake jets namely the jets coming from detector noise or bad reconstruction are rejected by PF criteria. In the present study, jets are required to have $p_T > 60$ GeV, $|\eta| < 5.0$ and identified using "loose" PF ID. The jet reconstruction and ID

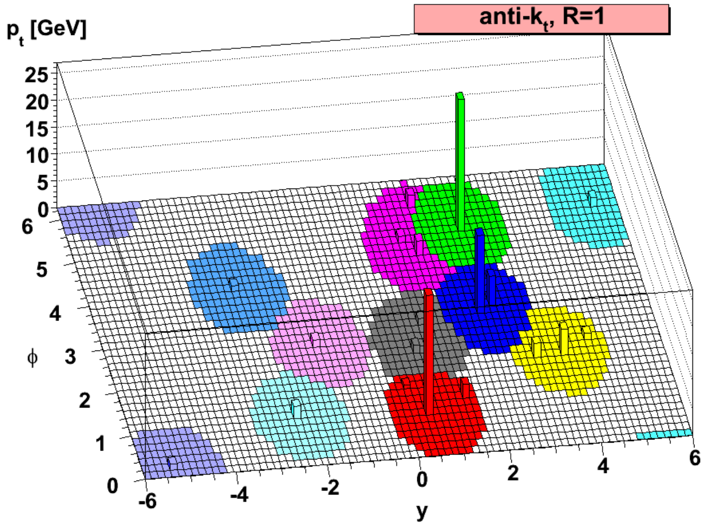

Figure 5.10: Parton level jets clustered with cone size R=1 using anti-k_T jet algorithm [28].

efficiency in simulation is $>$ 99% for the entire η and p_T range.

5.4.5.2 Jet Energy Corrections (JEC)

The PF jet energy is usually different than that of the corresponding particle because of detector non-linear response and also due to soft interactions. So, jets require some energy corrections obtained using simulated events that are generated with PYTHIA, processed through a detector simulation based on GEANT4, and confirmed with in situ measurements of the p_T balance. The overall JEC depends on the η and p_T values of jets. Each level of correction is independent of the other and deals with a different effect. The JEC are applied by Level 1 (L1) FastJet, Level 2 (L2) Relative, and Level 3 (L3) Absolute corrections. L1 FastJet corrections are used to remove the extra energy in jets from the underlying event (UE) and pileup (PU), using the event-by-event UE/PU densities. The L2 and L3 corrections use jet balancing and photon+jet events to improve the non-uniformity of the detector and non-uniformity of the calorimeters as a function of jet η and p_{T} respectively. These corrections also provide better energy response and are applied in the same sequence to both the simulations and data. For data, additional residual corrections are applied to account for remaining small discrepancies between the data and simulations.

5.4.5.3 b-jet Tagging

B-jet tagging implies to tag jets arising from the hadronization of bottom quarks. B-jets can be easily distinguished from any other quark jets (u, d, s, etc.) because of a long lifetime of around 10^{-12} s ($c\tau = 450$ μm) and a decay length of 3-5 mm away from the primary vertex as shown in Figure 5.11. In the present study, b-jets are required to have $p_T > 30$ GeV, $|\eta| < 2.4$ and are identified using Combined Secondary Vertex v2 (CSVv2) algorithm [29]. This algorithm combines reconstructed secondary vertex and track-based lifetime information to build an MVA-based discriminator to distinguish between jets from b-quarks and those from charm or light quarks and gluons. This algorithm has three working points: loose, medium, and tight. Their efficiencies with corresponding misidentification probabilities are shown in Table 5.2. The "Medium" operating point is used in the presented study because of the large efficiency and small fake rate. The b-tagged jets are used to obtain $t\bar{t}$ enriched

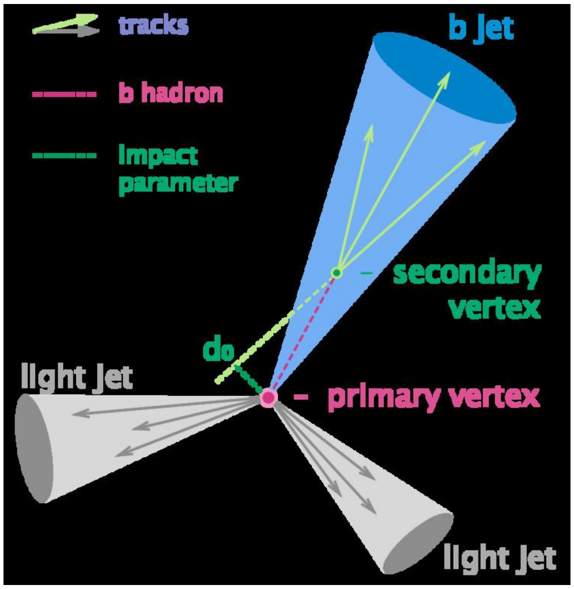

Figure 5.11: b-jet hadronization.

Working Point	CSVv2 Discriminator	b-tagging Efficiency	fake rate
Loose	≥ 0.5426	$\approx 84\%$	10%
Medium	≥ 0.8484	$\approx 69\%$	1%
Tight	≥ 0.9535	$\approx 49\%$	0.5%

Table 5.2: b-tagging efficiency and misidentification probability for the three different working points of the CSVv2 discriminator.

control samples to estimate the $t\bar{t}$ rate in the signal region.

5.4.6 Missing Transverse Energy

Missing Transverse Energy (MET or E_{T}^{miss}) [30] is the large transverse momentum imbalance in the plane orthogonal to the beam axis (transverse plane) and is defined as the magnitude of the negative vector sum of the transverse momentum of visible/reconstructed particles in an event.

$$E_{\mathrm{T}}^{miss} = | - \sum_{i} \overrightarrow{p_T^i}| \tag{5.4}$$

where the index i runs over all particle flow candidates. The non-zero value of E_{T}^{miss} could be strong evidence of new physics such as SUSY due to the presence of heavy weakly interacting particles such as the LSP in the present case, which escape from the detector without producing any direct response. E_{T}^{miss} is also one of the most important observables for discriminating the signal events from background events that do not contain neutrinos, such as QCD multijet and $Z/\gamma^* \rightarrow ee/\mu\mu$ events. In addition to the imperfect resolution of all detectable and reconstructed physics objects, E_{T}^{miss} is also sensitive to overlapping detector signals from the additional pileup interactions as well as detector malfunctions. Many factors may cause spurious E_T^{miss}, hence comprehensive studies of E_T^{miss} measured using the CMS detector are performed. The standard and recommended, "MET Filters" are utilized in the reconstruction of E_{T}^{miss}. Events with $E_T^{miss} > 250$ GeV are chosen for this study.

5.4.7 Muon Reconstruction and Identification

Muon reconstruction [31] is a multistep process that begins with the information gathered from the muon subdetector. In the standard CMS muon reconstruction, the charged particle tracks are first reconstructed independently in the tracking system (tracker-track) and in the muon system (standalone-muon track). The reconstruction of tracks in the muon system starts with the determination of hit positions in the DT, CSC, and RPC subdetector systems. These hits are geometrically matched within DTs and CSCs to form muon track segments. These track segments are collected and matched with each other to generate seeds for the actual track fit corresponding to all the hits registered in the muon system. The standalone muon trajectory is reconstructed by extrapolating from the innermost muon station to the outer tracker surface. Below are some of the approaches used to reconstruct muon.

- **Tracker Muon Reconstruction (inside-out):** In this approach, all tracker tracks having transverse momentum greater than 0.5 GeV and total momentum greater than 2.5 GeV are identified as the possible muon candidates. These tracks are then extrapolated to the muon system considering the energy losses and also uncertainty coming from multiple scattering. If at least one muon segment made up of DT or CSC hits is matched, the track is qualified as tracker muon track. This method has a better energy resolution for low momentum muons having $p_{\mathrm{T}} < 5$ GeV.

- **Global Muon Reconstruction (outside-in):** This algorithm starts from a standalone-muon track which is matched to an inner track in the tracking system. The hits from both the inner track and the standalone-muon track are combined into a global-muon track using the KF technique. The global-muon fit provides a better resolution for large values of $p_T > 200$ GeV, as compared to the tracker muon reconstruction.

CMS detector has good track reconstruction efficiency so most of the muons are reconstructed with both above said approaches (i.e. sharing the same tracker-track), and are combined into one single muon candidate. CMS detector reconstructs about 99% of the muons produced in proton-proton collisions with $p_{\mathrm{T}} > 5$ GeV. Muon misidentification rate is small as they are the only detectable particles at the LHC which are capable of reaching the muon chambers of the CMS detector. Reconstructed muon has to be identified so isolated muons are required to have minimal energy from PF neutral and charged candidates in a cone of $\Delta R = 0.4$ around the lepton trajectory. The PF-based combined relative isolation < 0.25 is used to correct pileup with $\Delta\beta$ corrections. In this analysis, the "Tight" identification working point is utilized which means muon candidate must be reconstructed with global and PF muon with a track χ^2/d.o.f. < 10 and at least one muon chamber hit included in global-muon track fit.

5.4.8 Electron Reconstruction and Identification

Electrons are reconstructed using information from the tracker and ECAL detector. When electrons pass through the silicon tracker material it loses energy due to Bremsstrahlung radiation and ionization. The radiated photon spreads its energy on various crystals of the ECAL detector along the electron trajectory, mostly in the ϕ direction (the magnetic field is in the z-direction). The energy of photons and electrons [32] are measured by two algorithms based on energy clustering, "Hybrid" for the barrel and "multi-5×5" for the endcaps. Electron tracks are reconstructed by matching trajectories in the silicon strip tracker to seed hits in the pixel detector. A pixel seed is composed of two-pixel hits compatible with the beam spot. A Gaussian Sum Filter (GSF) is used for the reconstruction of trajectories in the silicon strips. In order to minimize the many possible trajectories due to different combinations of hits, the track that best matches an energy supercluster in the ECAL is chosen to be the reconstructed track. The preselection of primary electron candidates requires good geometrical matching and good agreement between the momentum of the track and the energy of the ECAL supercluster. Two quantities used to estimate the geometrical matching are $\Delta\eta_{inSeed}$ and $\Delta\phi_{in}$. The η_{sc} and ϕ_{sc} coordinates correspond to the supercluster position and are measured using an energy weighted algorithm. The η_{vertex}^{Track} and ϕ_{vertex}^{Track} coordinates are the position of the track at the interaction vertex extrapolated, as a perfect helix, to the ECAL detector. The good energy-momentum matching is measured by taking the ratio between the corrected energy E_{corr} in the ECAL supercluster and the momentum of the track P_{in} measured in the inner layers of the tracker.

Electron selections have two main components, electron identification and electron isolation. The PF-based combined relative isolation< 0.25 is used to correct pileup with $\Delta\beta$ corrections. "Medium" identification working point of the cut based ID is used in the present study and also "safe" impact parameter cuts suggested by the POG are applied. In addition, electrons which arise from photon conversions are removed by requiring that the track associated with the electron to have hits in the inner layers of the pixel detector.

To summarize this Chapter, starting from the first Section, it explains the generation, simulation of events and also the reconstruction of all physics objects used in the presented study. All kinds of processes emerging from proton-proton collisions are discussed in detailed. Reconstructed objects are identified using an identification algorithm to reject fakes. This Chapter in association with the previous Chapters cover all the relevant information required to carry out the physics analysis reported in Chapter 6.

Bibliography

[1] T. Gleisberg, S. Höche, F. Krauss, A. Schälicke, S. Schumann, and J.-C. Winter, "Sherpa 1.α, a proof-of-concept version", *JHEP*, vol. 2 (2004), https://doi.org/10.1088/1126-6708/2004/02/056.

[2] M. Dobbs *et al.*, "Les Houches guidebook to Monte Carlo generators for hadron collider physics", arxiv.org/abs/hep-ph/0403045.

[3] C. P. Robert, "Monte Carlo Methods", `https://onlinelibrary.wiley.com/doi/abs/10.1002/9781118445112.stat03876.pub2`.

[4] S. Höche, "Introduction to Parton-Shower Event Generators", https://doi.org/10.1142/97898146787664_0005.

[5] Buckley, Andy *et al.*, "General-purpose event generators for LHC physics", *Phys. Rept.*, vol. 504 (2011), https://doi.org/10.1016/j.physrep.2011.03.005.

[6] V. V. Sudakov, "Vertex parts at very high-energies in quantum electrodynamics", *Sov. Phys. JETP*, vol. 3 (1956), [Zh. Eksp. Teor. Fiz.30,87(1956)].

[7] B. R. Webber, "A QCD Model for Jet Fragmentation Including Soft Gluon Interference", *Nucl. Phys. B*, vol. 238 (1984), https://doi.org/10.1016/0550-3213(84)90333-X.

[8] Andersson, B. and Gustafson, G. and Ingelman, G. and Sjöstrans, T., "Parton Fragmentation and String Dynamics", *Phys. Rept.*, vol. 97 (1983), https://doi.org/10.1016/0370-1573(83)90080-7.

[9] Sjöstrand, Torbjörn and Mrenna, Stephen and Skands, Peter, "PYTHIA 6.4 physics and manual", *JHEP*, vol. 5 (2006), http://dx.doi.org/10.1088/1126-6708/2006/05/026.

[10] Sjöstrand, Torbjörn and Mrenna, Stephen and Skands, Peter, "A brief introduction to PYTHIA 8.1", *Comp. Phys. Comm.*, vol. 178 (2008), http://dx.doi.org/10.1016/j.cpc.2008.01.036.

[11] Alwall, J. and Frederix, R. and Frixione, S. and Hirschi, V. and Maltoni, F. and Mattelaer, O. and Shao, H.-S. and Stelzer, T. and Torrielli, P. and Zaro, M., "The automated computation of tree-level and next-to-leading order differential cross sections, and their matching to parton shower simulations", *JHEP*, vol. 7 (2014), http://dx.doi.org/10.1007/JHEP07(2014)079.

[12] Z. Was, "TAUOLA for simulation of tau decay and production: perspectives for precision low energy and LHC applications", *Nucl. Phys. B*, vol. 218 (2011), https://doi.org/10.1016/j.nuclphysbps.2011.06.040.

[13] S. Agostinelli *et al.*, "GEANT4- simulation toolkit", *Nucl. Instum. Meth. A*, vol. 506 (2003), https://doi.org/10.1016/S0168-9002(03)01368-8.

[14] R. Brun and F. Rademakers, "ROOT: An object oriented data analysis framework", *Nucl. Instum. Meth. A*, vol. 389 (1997), https://cds.cern.ch/record/491486.

[15] The CMS Collaboration, "Particle-flow reconstruction and global event description with the CMS detector", *JINST*, vol. 12 (2017), https://doi.org/10.1088/1748-0221/12/10/P10003.

[16] R. Fruhwirth, "Application of Kalman filtering to track and vertex fitting", *Nucl. Instum. Meth. A*, vol. 262 (1987), https://doi.org/10.1016/0168-9002(87)90887-4.

[17] The CMS Collaboration, "Description and performance of track and primary-vertex reconstruction with the CMS tracker", *JINST*, vol. 9 (2014), https://doi.org/10.1088/1748-0221/9/10/P10009.

[18] CMS Wiki Pages, https://wiki.physik.uzh.ch/cms/latex:tikz:tau_decay_signatures.

[19] The CMS Collaboration, "Performance of reconstruction and identification of τ leptons decaying to hadrons and μ_τ in pp collisions at $\sqrt{s} = 13$ TeV", *JINST*, vol. 13 (2018), https://doi.org/10.1088/1748-0221/13/10/P10005.

[20] The CMS Collaboration, "Reconstruction and identification of τ lepton decays to hadrons and μ_τ at CMS", *JINST*, vol. 11 (2016), https://doi.org/10.1088/1748-0221/11/01/P01019.

[21] G. P. Salam, "Towards Jetography" *Eur. Phys. J.*, vol. 67 (2010), https://arxiv.org/abs/0906.1833v2.

[22] The CMS Collaboration, "Determination of Jet Energy Calibration and Transverse Momentum Resolution in CMS", *JINST*, vol. 6 (2011), https://doi.org/10.1088/1748-0221/6/11/P11002.

[23] T. Carli, K. Rabbertz, S. Schumann, "Studies of Quantum Chromodynamics at the LHC", *The Large Hadron Collider. Springer, Cham*, https://doi.org/10.1007/978-3-319-15001-7_5.

[24] The CMS Collaboration, "Jet Performance in pp collisions at $\sqrt{s} = 7$ TeV", *CMS-PAS-JME-10-03*, (2010), https://cds.cern.ch/record/1279362.

[25] The CMS Collaboration, “Jet Plus Tracks Algorithm for Calorimeter Jet EnergyCorrections in CMS”, *CMS-PAS-JME-09-002*, (2009), https://cds.cern.ch/record/1190234.

[26] The CMS Collaboration, “A Cambridge-Aachen (C-A) based Jet Algorithm forboosted top-jet tagging” *Tech. Report CMS-PAS-JME-09-001*, CERN, Geneva (2009), https://cds.cern.ch/record/1194489.

[27] S. Catani *et al.*, “Longitudinally invariant K_t clustering algorithms for hadron hadron collisions”, *Nucl. Phys. B*, vol. 406 (1993), https://doi.org/10.1016/0550-3213(93)90166-M.

[28] Matteo Cacciari, Gavin P. Salam, Gregory Soyez, “The anti-k_t jet clustering algorithm”, *JHEP*, vol. 4 (2008), https://doi.org/10.1088/1126-6708/2008/04/063.

[29] The CMS Collaboration, “Identification of b-quark jets with the CMS experiment”, *JINST*, vol. 8 (2013), https://doi.org/10.1088/1748-0221/8/04/P04013.

[30] The CMS Collaboration, “Missing transverse energy performance of the CMS detector”, *JINST*, vol. 6 (2011), https://doi.org/10.1088/1748-0221/6/09/P09001.

[31] The CMS Collaboration, “ Performance of CMS muon reconstruction in pp collision events at $\sqrt{s} = 7$ TeV”, *JINST*, vol. 7 (2012), https://doi.org/10.1088/1748-0221/7/10/P10002.

[32] The CMS Collaboration, “Performance of Electron Reconstruction and Selection with the CMS Detector in Proton-Proton Collisions at $\sqrt{s} = 8$ TeV”, *JINST*, vol. 10 (2015), https://doi.org/10.1088/1748-0221/10/06/P06005.

Chapter 6

Electroweak SUSY Searches through VBF Processes

Supersymmetry (SUSY) searches through the Electroweakino production modes are performed in this Thesis. In this Chapter, we present the study to look for SUSY signal through vector boson fusion (VBF) topology in single hadronic tau final state along with two forward jets and missing transverse energy. The signal, background processes and the analysis techniques adopted for the search presented in this Thesis, are discussed briefly in the coming Sections.

6.1 Introduction to SUSY Searches

SUSY prevails as one of the best extensions of the Standard Model (SM) which explains SM limitations such as the gauge hierarchy problem and can provide a suitable dark matter candidate. SUSY predicts a large number of particles on the top of SM particles but these SUSY particles are not discovered yet experimentally. Nevertheless, for all of its appealing features, there is no experimental evidence of its existence. The mass of gluinos ($\tilde{g}$) as well as the squarks ($\tilde{q}$) of the first and second generations, have been ruled out to $\sim$ 1.9 TeV in certain scenarios (Section 2.5.1) [1]. In contrast, the limits on the electroweak sector i.e. charginos and neutralinos masses are less stringent, as may be expected in a hadron collider where these particles suffer from smaller production cross section. The chargino-neutralino system plays a significant role in the dark matter (DM) connection to SUSY models. The lightest neutralino $\tilde{\chi}_1^0$, known as the Lightest Supersymmetric Particle (LSP), is the canonical dark matter candidate in R-parity conserving SUSY extensions of the SM [2].

The exclusion limits for chargino mass is $<$ 720 GeV for the scenarios where LSP is massless as detailed in references [3,4] but get weaker to $\approx$ 100 GeV for compressed-mass spectrum scenarios (Δm = $m_{\tilde{\chi}_1^\pm}$ - $m_{\tilde{\chi}_1^0}$ = 2 GeV), assuming decays of the $\tilde{\chi}_1^\pm$ and $\tilde{\chi}_2^0$ to leptonic final states proceed through the mediation of virtual W and Z boson [5,6]. These searches become difficult as the mass difference between SUSY particles decreases because the momentum available to the co-produced SM particles is small, resulting in "soft" products having low transverse momentum. Nonetheless,

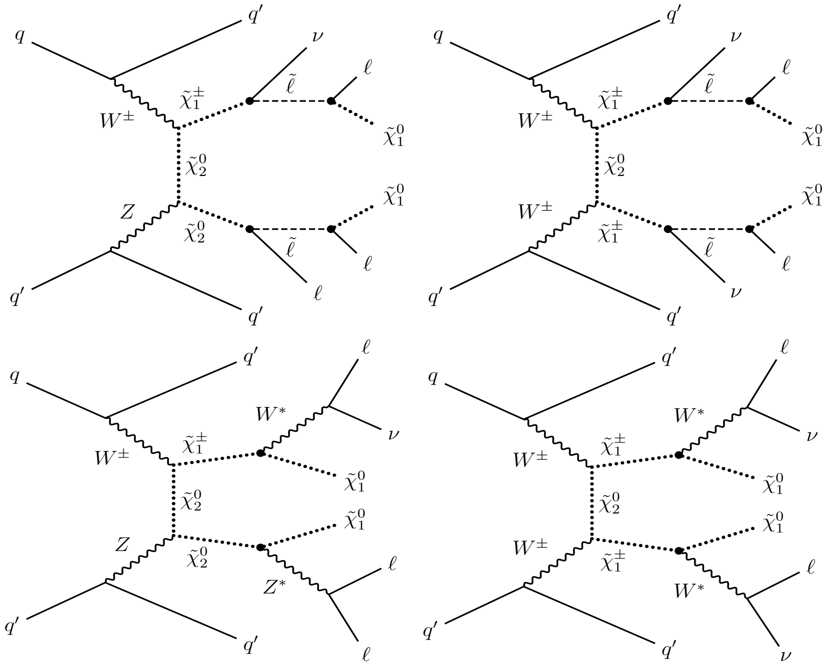

Figure 6.1: Feynman diagrams for the pair-production of chargino-neutralino (left) and chargino-chargino (right) through VBF topology, followed by their decay to leptons and $\tilde{\chi}_1^0$ via light sleptons (top row) or a W^*/Z^* (bottom row).

chargino and neutralino production via VBF processes of order α_{EW}^4 is very useful in background reduction and tackling some of these interesting compressed SUSY scenarios [7]. In VBF processes, electroweak SUSY particles are pair-produced in association with two high-p$_T$ oppositely-directed jets close to the beam axis (forward), resulting in a large dijet invariant mass (m_{jj}). Figure 6.1 shows the Feynman diagrams for two of the possible VBF production processes: chargino–neutralino (left) and chargino–chargino (right) production.

6.2 Electroweak Signal Processes through VBF Tagging

The signal processes involve the production of chargino and neutralino pairs ($\tilde{\chi}_1^{\pm}\tilde{\chi}_1^{\pm}$, $\tilde{\chi}_1^{\pm}\tilde{\chi}_2^0$, $\tilde{\chi}_1^{\pm}\tilde{\chi}_1^{\mp}$, $\tilde{\chi}_2^{\pm}\tilde{\chi}_2^0$) from the fusion of two vector bosons radiated by incoming partons of the colliding protons at the LHC. The charginos and neutralinos are produced along with two high-p_{T} forward jets, in the opposite hemisphere of a detector having large dijet invariant mass and pseudorapidity separation. Due to the presence of two high-p_T VBF jets in the event, this topology suppresses the SM backgrounds to a greater extent on the order of $10^2 - 10^4$. The decay chain of $\tilde{\chi}_1^{\pm}$ ($\tilde{\chi}_2^0$) goes as: $\tilde{\chi}_1^{\pm} \rightarrow \tilde{l}^{\pm}\nu_l \rightarrow l^{\pm}\nu_l\tilde{\chi}_1^0$ ($\tilde{\chi}_2^0 \rightarrow \tilde{l}^{\pm}l^{\mp} \rightarrow l^{\pm}l^{\mp}\tilde{\chi}_1^0$) as indicated in Figure 6.1. It provides outstanding sensitivity for electroweak SUSY searches in the compressed mass spectra scenarios than any other analysis techniques accessible at the moment. The evidence of this aspect is the first SUSY search for electroweakinos through VBF dijet topology in the Minimal Supersymmetric Standard Model (MSSM), with proton-proton collision data collected with CMS detector at $\sqrt{s} = 8$ TeV [8] having integrated luminosity of 19.7 fb^{-1}. An interesting case with $\tilde{\tau}$ (lightest third-generation slepton) dominating scenario and an assumption of $m(\tilde{\tau}) < m(\tilde{\chi}_1^{\pm})$ has been considered for 8 TeV analysis and an upper limit of 170

GeV for the nearly mass-degenerate $\tilde{\chi}_1^{\pm}/\tilde{\chi}_2^0$ was established for compressed mass spectrum scenario where the mass difference between $\tilde{\chi}_1^{\pm}/\tilde{\chi}_2^0$ and LSP is 50 GeV.

VBF topology has shown its potential by enhancing the sensitivity of electroweak searches because no other CMS methods have excluded a mass gap (Δm = $m_{\tilde{\chi}_1^{\pm}}$ - $m_{\tilde{\chi}_1^0}$) of 50 GeV with light $\tilde{\tau}$. Compressed mass spectra scenario referred to as when the mass of parent and daughter particles are very close to each other such that daughter particles are generated with low-lying kinetic energy/soft p$_T$ spectrum and hence the leptons produced in the final state are difficult to reconstruct and identify in the CMS detector. VBF processes have two or three leptons in the final state, but due to low p$_T$ or low reconstruction efficiency, it is easy to reconstruct one lepton naturally which will enhance the signal sensitivity of VBF SUSY searches. The present search has been done with VBF topology at $\sqrt{s} = 13$ TeV using CMS data in 4 final states: e, μ, τ and invisible channel. We will focus on single hadronic tau final state along with two forward jets and missing transverse energy due to LSP and neutrinos. The other decay channels (muon, electron) are covered by other team members. The final outcomes are interpreted under the R-parity conserving MSSM as detailed in Section 2.2.1, focusing on compressed slepton democratic scenario (where all three sleptons are light and with similar mass) and from W^* and Z^* decay model. Starting from 1 GeV mass difference between $\tilde{\chi}_1^{\pm}/\tilde{\chi}_2^0$ and $\tilde{\chi}_1^0$ up to 50 GeV, all the VBF SUSY signal cases have been examined and results are compared with data and SM backgrounds which are discussed in detail in the next Section.

6.3 Background Processes

Background (BG) events correspond to the outcomes that can mimic the characteristics of the signal which we are searching but are not the real signal events. So, all the SM processes that may give the same signature (like jets, leptons, and p_t^{miss}) in the detector as the SUSY signal process with the VBF topology are acknowledged as a possible source of background events and their aspects are discussed below.

- **QCD Multijet Background:** The major background for the final state considered in this analysis is QCD multijet background and it is hard to control the contribution of QCD at the hadron colliders as it can fake the signal process easily. The scenario is more severe in the final states consisting of hadronically decaying tau leptons as this signature is easily copied by the quark and gluon jets. The production cross section of these events is several orders of magnitude higher as compared to the SUSY signal. The left picture of Figure 6.2 represents the QCD process where one jet can fake as hadronic tau and two additional jets are faking the VBF jets. Data-driven estimation of QCD background is performed and explained in Section 6.7.5.

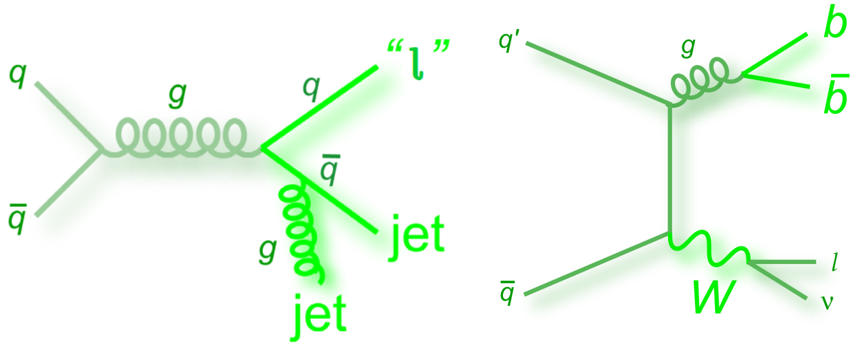

Figure 6.2: Left: Feynman Diagram for QCD+jets production process, Right: W+Jets process featuring jets and lepton.

- **W+Jets Background:** The second highest background for this analysis is the W+Jets background which can simply imitate the signal process. The leptonic decay of W boson can fake hadronic tau and two other jets can be either hadronic taus or VBF jets as depicted in right picture of Figure 6.2. Tau discriminators and identification criteria are applied to reduce the fakes.

- **t$\bar{\text{t}}$ and Single Top Background Production:** We can generate the $t\bar{t}$ background either by $q\bar{q}$ annihilation or by gluon fusion. The top (anti-top) quark decays into a W boson and a bottom (anti-bottom) quark as shown in the left picture of Figure 6.3. The further decay of W boson into leptons or hadrons can give the same signature as the signal τ_h and the b-jet can fake as the signal jet.

Single top quark processes also play an important role where b-jets are present in the search. These processes can happen by three different modes viz. t-channel, s-channel and tW-channel as shown in Figure 6.4. As discussed in Section 5.4.5.3, b-jets discriminator and b-jet veto are applied to reduce the background contribution.

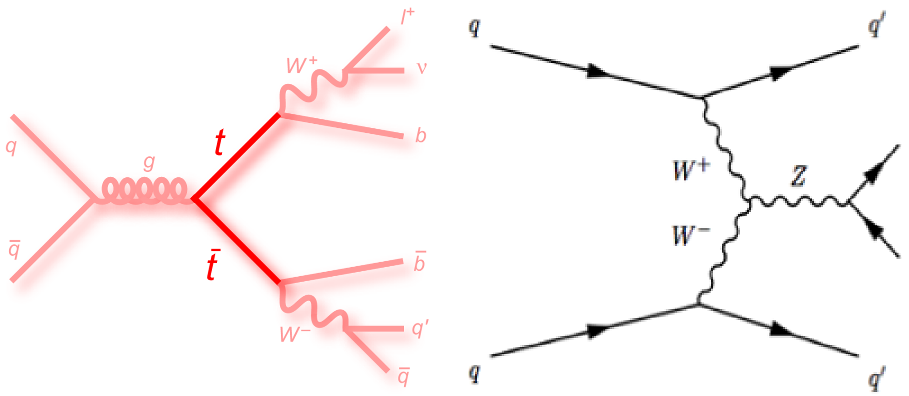

Figure 6.3: Left: Production mechanism for $t\bar{t}$ by quark annihilation and its decay, Right: Feynman diagram for Z+Jets background production.

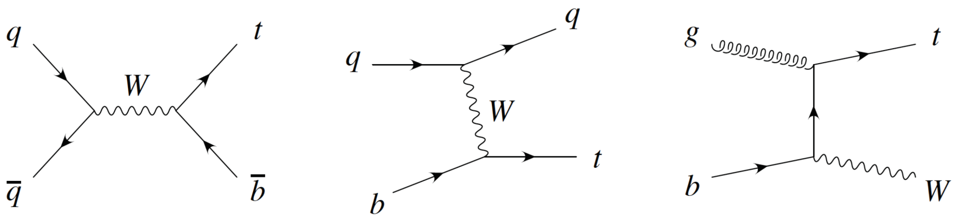

Figure 6.4: Feynman diagram portraying the single top quark production.

- **Z+Jets (DY+Jets) Background:** The production of single Z boson is followed by the production of quark, which then hadronizes to a jet. The hadronic tau produced from Z boson can fake the signal τ_h and there is little probability that muons and electrons can also be misidentified as hadronic taus. Additionally, the two forward jets can fake as VBF jets. The right picture of Figure 6.3 shows one of the possible processes that can mimic the signal.

- **Diboson (WW, WZ and ZZ) Processes:** The decay of the diboson background results in a final state with more than two leptons. The contribution from this background is small in this analysis because of the single lepton requirement. However, the signal τ_h can be easily mimicked from the decay of vector bosons (ZZ, WZ, WW) and VBF jets can be faked by associated jets as presented in Figure 6.5. The leptons or hadronic taus from the decay of Z can also fake the signal taus.

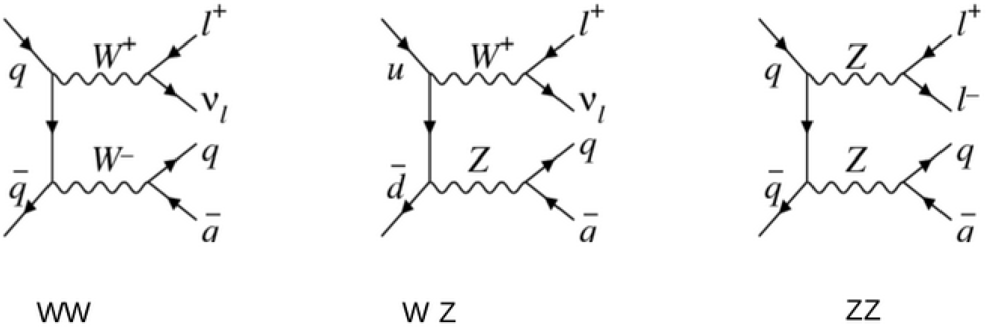

WW

W Z

ZZ

Figure 6.5: Feynman Diagram illustrating the diboson background production.

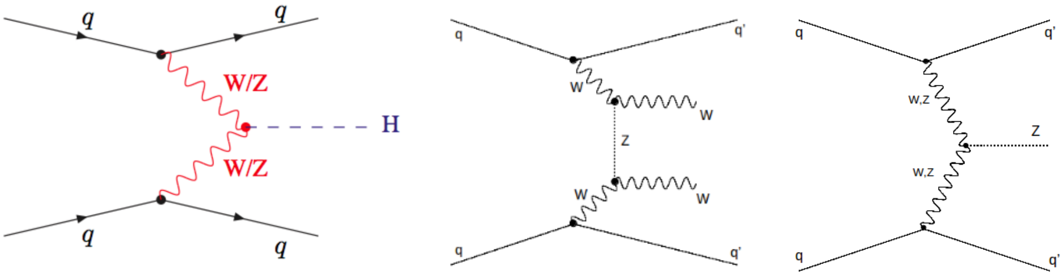

Figure 6.6: Generation of VBF Higgs process (left) and SM electroweak process WWjj (middle) and Zjj (right).

- **VBF Higgs and SM Electroweak Processes:** The processes in which the production of Higgs boson is accompanied by two forward jets can usually imitate the signal processes as shown in Figure 6.6 (left). Nevertheless, the forward jets in this process are less boosted as compared to signal jets because mass of the SM Higgs boson is notably less than the masses of charginos and neutralinos under study. The pure SM electroweak processes with forward jets can easily fake the signal process as shown in Figure 6.6 (right). The leptonic decay of W or Z boson, accompanying with VBF jets, can easily mimic the signal process.

6.4 Experimental Data and Simulation Samples

6.4.1 Dataset - 2016

As the search presented in this Thesis corresponds to the final state with large missing transverse energy (MET), naturally the MET stream of 2016 proton-proton collision dataset of 13 TeV is used for the main search region. Following many data-quality checks on data collected in 2016, the dataset corresponding to 35.87 fb^{-1} have been considered good for this physics analysis. Additionally, the muon dataset is used in several cases like trigger study and some control regions to estimate the background prediction. The MET dataset is defined by filtering events based on only the MET requirement to avoid any bias on the p_T of the lepton. Table 6.1 shows the official datasets used to carry out this analysis.

6.4.2 Signal and Background Samples

Different Monte Carlo (MC) event generators like Pythia8 [9] and Madgraph are used to simulate the signal and background processes. These event generators are part of central production by the CMS Collaboration. The signal samples used for the present analysis are of leading order (LO) precision, generated with the Madgraph5_MC@NLO v2.3.3 generator [10] and with the requirement of pure

Physics Sample	Official CMS Datasets
Run 2016B SingleMu Run2016B-03Feb2017	*/SingleMuon/Run2016B-03Feb2017_ver2-v2/MINIAOD*
Run 2016C SingleMu Run2016C-03Feb2017	*/SingleMuon/Run2016C-03Feb2017-v1/MINIAOD*
Run 2016D SingleMu Run2016D-03Feb2017	*/SingleMuon/Run2016D-03Feb2017-v1/MINIAOD*
Run 2016E SingleMu Run2016E-03Feb2017	*/SingleMuon/Run2016E-03Feb2017-v1/MINIAOD*
Run 2016F SingleMu Run2016F-03Feb2017	*/SingleMuon/Run2016F-03Feb2017-v1/MINIAOD*
Run 2016G SingleMu Run2016G-03Feb2017	*/SingleMuon/Run2016G-03Feb2017-v1/MINIAOD*
Run 2016Hv2 SingleMu Run2016H-03Feb2017	*/SingleMuon/Run2016H-03Feb2017_ver2-v1/MINIAOD*
Run 2016Hv3 SingleMu Run2016H-03Feb2017	*/SingleMuon/Run2016H-03Feb2017_ver3-v1/MINIAOD*
Run 2016B Met Run2016B-03Feb2017	*/Met/Run2016B-03Feb2017-v3/MINIAOD*
Run 2016C Met Run2016C-03Feb2017	*/Met/Run2016C-03Feb2017-v1/MINIAOD*
Run 2016D Met Run2016D-03Feb2017	*/Met/Run2016D-03Feb2017-v1/MINIAOD*
Run 2016E Met Run2016E-03Feb2017	*/Met/Run2016E-03Feb2017-v1/MINIAOD*
Run 2016F Met Run2016F-03Feb2017	*/Met/Run2016F-03Feb2017-v1/MINIAOD*
Run 2016G Met Run2016G-03Feb2017	*/Met/Run2016G-03Feb2017-v1/MINIAOD*
Run 2016Hv2 Met Run2016H-03Feb2017	*/Met/Run2016H-03Feb2017_ver2-v1/MINIAOD*
Run 2016Hv3 Met Run2016H-03Feb2017	*/Met/Run2016H-03Feb2017_ver3-v1/MINIAOD*

JSON: Cert_271036-284044_13TeV_03Feb2017ReReco_Collisions16_JSON.txt

Table 6.1: Collision Data Samples along with the JSON file.

electroweak pair production (i.e. QCD = 0 in generation command to remove the QCD vertices) of $\tilde{\chi}_1^\pm$ and $\tilde{\chi}_2^0$ gauginos with two associated partons. There are no VBF filters implemented in the central production of signal samples in order to remain unbiased in our offline selections. However, at the time of generation, few conditions are imposed on the signal events, like $p_T > 30$ GeV for each parton and pseudorapidity gap $|\Delta\eta| > 3.5$ between two partons for having no bias with respect to the final requirement on the reconstructed dijet pseudorapidity gap. Table 6.2 shows all the signal mass points and their respective cross sections used for the analysis presented in this Thesis.

The predicted background yields are simulated using next-to-leading (NLO) or next-to-next-to-leading order (NNLO) cross sections except for single top and diboson which are simulated at LO but their contribution is less. The LO cross sections are used to normalize simulated signal events, while NLO cross sections are used for simulated backgrounds [11–13]. Table 6.3 presents the list of background samples and their corresponding production cross sections. The weight factor (w) calculated from production cross section of the MC samples (σ) and luminosity (L)

Process- VBF-C1N2-leptonic-($m_{\tilde{\chi}_1^\pm}, m_{\tilde{\chi}_1^0}$)	xs [fb]	Process- VBF-C1N2-WZ-($m_{\tilde{\chi}_1^\pm}, m_{\tilde{\chi}_1^0}$)	xs [fb]	Process- VBF-C1N2-leptonic-($m_{\tilde{\chi}_1^\pm}, m_{\tilde{\chi}_1^0}$)	xs [fb]	Process- VBF-C1N2-WZ-($m_{\tilde{\chi}_1^\pm}, m_{\tilde{\chi}_1^0}$)	xs [fb]	Process- VBF-C1N2-leptonic-($m_{\tilde{\chi}_1^\pm}, m_{\tilde{\chi}_1^0}$)	xs [fb]	Process- VBF-C1N2-WZ-($m_{\tilde{\chi}_1^\pm}, m_{\tilde{\chi}_1^0}$)	xs [fb]
100 50	286.306	100 50	287.8	250 200	15.993	250 200	15.9	400 350	3.119	400 350	3.13
100 55		100 55		250 205		250 205		400 355		400 355	
100 60		100 60		250 210		250 210		400 360		400 360	
100 65		100 65		250 215		250 215		400 365		400 365	
100 70		100 70		250 220		250 220		400 370		400 370	
100 75		100 75		250 225		250 225		400 375		400 375	
100 80		100 80		250 230		250 230		400 380		400 380	
100 85		100 85		250 235		250 235		400 385		400 385	
100 90		100 90		250 240		250 240		400 390		400 390	
100 95		100 95		250 245		250 245		400 395		400 395	
100 98		100 98		250 248		250 248		400 398		400 398	
100 99		100 99		250 249		250 249		400 399		400 399	
150 100	80.538	150 100	80.5	300 250	8.660	300 250	8.59	450 400	2.033	450 400	2.04
150 105		150 105		300 255		300 255		450 405		450 405	
150 110		150 110		300 260		300 260		450 410		450 410	
150 115		150 115		300 265		300 265		450 415		450 415	
150 120		150 120		300 270		300 270		450 420		450 420	
150 125		150 125		300 275		300 275		450 425		450 425	
150 130		150 130		300 280		300 280		450 430		450 430	
150 135		150 135		300 285		300 285		450 435		450 435	
150 140		150 140		300 290		300 290		450 440		450 440	
150 145		150 145		300 295		300 295		450 445		450 445	
150 148		150 148		300 298		300 298		450 448		450 448	
150 149		150 149		300 299		300 299		450 449		450 449	
200 150	32.609	200 150	32.6	350 300	5.050	350 300	5.01	500 450	1.358	500 450	1.37
200 155		200 155		350 305		350 305		500 455		500 455	
200 160		200 160		350 310		350 310		500 460		500 460	
200 165		200 165		350 315		350 315		500 465		500 465	
200 170		200 170		350 320		350 320		500 470		500 470	
200 175		200 175		350 325		350 325		500 475		500 475	
200 180		200 180		350 330		350 330		500 480		500 480	
200 185		200 185		350 335		350 335		500 485		500 485	
200 190		200 190		350 340		350 340		500 490		500 490	
200 195		200 195		350 345		350 345		500 495		500 495	
200 198		200 198		350 348		350 348		500 498		500 498	
200 199		200 199		350 349		350 349		500 499		500 499	

Table 6.2: Signal mass points and their cross sections.

is applied to normalize the event yield for MC simulated samples and is given as:

$$w = \frac{\sigma \cdot L}{N} \tag{6.1}$$

where N represents the total number of MC simulated events for the corresponding process. We know that the pileup for the MC simulated samples is different than the pileup for data and so is the difference in pileup distribution for data and MC. Hence to match the pileup distribution of data and MC, each bin of the MC pileup distribution needs to be re-weighted properly. The weight factor that has to be applied to MC events is the ratio of probabilities to obtain "n" true interactions in data (P$_{data}$(n)) and MC (P$_{MC}$(n)), and is given as:

$$w_{PU}(n) = \frac{P_{data}(n)}{P_{MC}(n)} \tag{6.2}$$

The primary vertices distribution after applying the pileup weight on the MC events is shown in Figure 6.7.

Process	cross section [pb]	Official CMS Datasets (MINIAODSIM)
$Z \to ll$ HT binned LO	4895 × 1.17781 (NNLO)	/DYJetsToLL_M-50_HT-0to70_TuneCUETP8M1_13TeV-madgraphMLM-pythia8/RunIISummer16MiniAODv2-PUMoriond17_80X_mcRun2_asymptotic_2016_TrancheIV_v6_ext1-v2/MINIAODSIM
	175.3 × 1.17781 (NNLO)	/DYJetsToLL_M-50_HT-70to100_TuneCUETP8M1_13TeV-madgraphMLM-pythia8/RunIISummer16MiniAODv2-PUMoriond17_80X_mcRun2_asymptotic_2016_TrancheIV_v6-v1/MINIAODSIM
	147.4 × 1.17781 (NNLO)	/DYJetsToLL_M-50_HT-100to200_TuneCUETP8M1_13TeV-madgraphMLM-pythia8/RunIISummer16MiniAODv2-PUMoriond17_80X_mcRun2_asymptotic_2016_TrancheIV_v6-v1/MINIAODSIM
	147.4 × 1.17781 (NNLO)	/DYJetsToLL_M-50_HT-100to200_TuneCUETP8M1_13TeV-madgraphMLM-pythia8/RunIISummer16MiniAODv2-PUMoriond17_80X_mcRun2_asymptotic_2016_TrancheIV_v6_ext1-v1/MINIAODSIM
	40.99 × 1.17781 (NNLO)	/DYJetsToLL_M-50_HT-200to400_TuneCUETP8M1_13TeV-madgraphMLM-pythia8/RunIISummer16MiniAODv2-PUMoriond17_80X_mcRun2_asymptotic_2016_TrancheIV_v6-v1/MINIAODSIM
	40.99 × 1.17781 (NNLO)	/DYJetsToLL_M-50_HT-200to400_TuneCUETP8M1_13TeV-madgraphMLM-pythia8/RunIISummer16MiniAODv2-PUMoriond17_80X_mcRun2_asymptotic_2016_TrancheIV_v6_ext1-v1/MINIAODSIM
	5.678 × 1.17781 (NNLO)	/DYJetsToLL_M-50_HT-400to600_TuneCUETP8M1_13TeV-madgraphMLM-pythia8/RunIISummer16MiniAODv2-PUMoriond17_80X_mcRun2_asymptotic_2016_TrancheIV_v6-v1/MINIAODSIM
	5.678 × 1.17781 (NNLO)	/DYJetsToLL_M-50_HT-400to600_TuneCUETP8M1_13TeV-madgraphMLM-pythia8/RunIISummer16MiniAODv2-PUMoriond17_80X_mcRun2_asymptotic_2016_TrancheIV_v6_ext1-v1/MINIAODSIM
	1.363 × 1.17781 (NNLO)	/DYJetsToLL_M-50_HT-600to800_TuneCUETP8M1_13TeV-madgraphMLM-pythia8/RunIISummer16MiniAODv2-PUMoriond17_80X_mcRun2_asymptotic_2016_TrancheIV_v6-v2/MINIAODSIM
	0.6759 × 1.17781 (NNLO)	/DYJetsToLL_M-50_HT-800to1200_TuneCUETP8M1_13TeV-madgraphMLM-pythia8/RunIISummer16MiniAODv2-PUMoriond17_80X_mcRun2_asymptotic_2016_TrancheIV_v6-v1/MINIAODSIM
	0.116 × 1.17781 (NNLO)	/DYJetsToLL_M-50_HT-1200to2500_TuneCUETP8M1_13TeV-madgraphMLM-pythia8/RunIISummer16MiniAODv2-PUMoriond17_80X_mcRun2_asymptotic_2016_TrancheIV_v6-v1/MINIAODSIM
	0.002592 × 1.17781 (NNLO)	/DYJetsToLL_M-50_HT-2500toInf_TuneCUETP8M1_13TeV-madgraphMLM-pythia8/RunIISummer16MiniAODv2-PUMoriond17_80X_mcRun2_asymptotic_2016_TrancheIV_v6-v1/MINIAODSIM
EWK $Z \to ll$	3.998 (LO)	/EWKZ2Jets_ZToLL_M-50_13TeV-madgraph-pythia8/RunIISummer16MiniAODv2-PUMoriond17_80X_mcRun2_asymptotic_2016_TrancheIV_v6_ext2-v1/MINIAODSIM
W+jets HT binned LO	50260.0×1.21378 (NNLO)	/WJetsToLNu_TuneCUETP8M1_13TeV-madgraphMLM-pythia8/RunIISummer16MiniAODv2-PUMoriond17_80X_mcRun2_asymptotic_2016_TrancheIV_v6-v1/MINIAODSIM
	1319×1.21378 (NNLO)	/WJetsToLNu_HT-70To100_TuneCUETP8M1_13TeV-madgraphMLM-pythia8/RunIISummer16MiniAODv2-PUMoriond17_80X_mcRun2_asymptotic_2016_TrancheIV_v6-v1/MINIAODSIM
	1345×1.21378 (NNLO)	/WJetsToLNu_HT-100To200_TuneCUETP8M1_13TeV-madgraphMLM-pythia8/RunIISummer16MiniAODv2-PUMoriond17_80X_mcRun2_asymptotic_2016_TrancheIV_v6-v1/MINIAODSIM
	1345×1.21378 (NNLO)	/WJetsToLNu_HT-100To200_TuneCUETP8M1_13TeV-madgraphMLM-pythia8/RunIISummer16MiniAODv2-PUMoriond17_80X_mcRun2_asymptotic_2016_TrancheIV_v6_ext1-v1/MINIAODSIM
	359.7×1.21378 (NNLO)	/WJetsToLNu_HT-200To400_TuneCUETP8M1_13TeV-madgraphMLM-pythia8/RunIISummer16MiniAODv2-PUMoriond17_80X_mcRun2_asymptotic_2016_TrancheIV_v6-v1/MINIAODSIM
	359.7×1.21378 (NNLO)	/WJetsToLNu_HT-200To400_TuneCUETP8M1_13TeV-madgraphMLM-pythia8/RunIISummer16MiniAODv2-PUMoriond17_80X_mcRun2_asymptotic_2016_TrancheIV_v6_ext1-v1/MINIAODSIM
	48.91×1.21378 (NNLO)	/WJetsToLNu_HT-400To600_TuneCUETP8M1_13TeV-madgraphMLM-pythia8/RunIISummer16MiniAODv2-PUMoriond17_80X_mcRun2_asymptotic_2016_TrancheIV_v6-v1/MINIAODSIM
	48.91×1.21378 (NNLO)	/WJetsToLNu_HT-400To600_TuneCUETP8M1_13TeV-madgraphMLM-pythia8/RunIISummer16MiniAODv2-PUMoriond17_80X_mcRun2_asymptotic_2016_TrancheIV_v6_ext1-v1/MINIAODSIM
	12.05×1.21378 (NNLO)	/WJetsToLNu_HT-600To800_TuneCUETP8M1_13TeV-madgraphMLM-pythia8/RunIISummer16MiniAODv2-PUMoriond17_80X_mcRun2_asymptotic_2016_TrancheIV_v6-v1/MINIAODSIM
	12.05×1.21378 (NNLO)	/WJetsToLNu_HT-600To800_TuneCUETP8M1_13TeV-madgraphMLM-pythia8/RunIISummer16MiniAODv2-PUMoriond17_80X_mcRun2_asymptotic_2016_TrancheIV_v6_ext1-v1/MINIAODSIM
	5.501×1.21378 (NNLO)	/WJetsToLNu_HT-800To1200_TuneCUETP8M1_13TeV-madgraphMLM-pythia8/RunIISummer16MiniAODv2-PUMoriond17_80X_mcRun2_asymptotic_2016_TrancheIV_v6-v1/MINIAODSIM
	5.501×1.21378 (NNLO)	/WJetsToLNu_HT-800To1200_TuneCUETP8M1_13TeV-madgraphMLM-pythia8/RunIISummer16MiniAODv2-PUMoriond17_80X_mcRun2_asymptotic_2016_TrancheIV_v6_ext1-v1/MINIAODSIM
	1.329×1.21378 (NNLO)	/WJetsToLNu_HT-1200To2500_TuneCUETP8M1_13TeV-madgraphMLM-pythia8/RunIISummer16MiniAODv2-PUMoriond17_80X_mcRun2_asymptotic_2016_TrancheIV_v6-v1/MINIAODSIM
	1.329×1.21378 (NNLO)	/WJetsToLNu_HT-1200To2500_TuneCUETP8M1_13TeV-madgraphMLM-pythia8/RunIISummer16MiniAODv2-PUMoriond17_80X_mcRun2_asymptotic_2016_TrancheIV_v6_ext1-v1/MINIAODSIM
	0.03216×1.21378 (NNLO)	/WJetsToLNu_HT-2500ToInf_TuneCUETP8M1_13TeV-madgraphMLM-pythia8/RunIISummer16MiniAODv2-PUMoriond17_80X_mcRun2_asymptotic_2016_TrancheIV_v6-v1/MINIAODSIM
	0.03216×1.21378 (NNLO)	/WJetsToLNu_HT-2500ToInf_TuneCUETP8M1_13TeV-madgraphMLM-pythia8/RunIISummer16MiniAODv2-PUMoriond17_80X_mcRun2_asymptotic_2016_TrancheIV_v6_ext1-v1/MINIAODSIM
EWK W+jets	25.81 (LO)	/EWKWPlus2Jets_WToLNu_M-50_13TeV-madgraph-pythia8/RunIISummer16MiniAODv2-PUMoriond17_80X_mcRun2_asymptotic_2016_TrancheancheIV_v6_ext2-v1/MINIAODSIM
	20.35 (LO)	/EWKWMinus2Jets_WToLNu_M-50_13TeV-madgraph-pythia8/RunIISummer16MiniAODv2-PUMoriond17_80X_mcRun2_asymptotic_2016_TrancheIV_v6_ext2-v1/MINIAODSIM
QCD	246700000 (LO)	/QCD_HT50To100_TuneCUETP8M1_13TeV-madgraphMLM-pythia8/RunIISummer16MiniAODv2-PUMoriond17_80X_mcRun2_asymptotic_2016_TrancheIV_v6-v1/MINIAODSIM
	28080000 (LO)	/QCD_HT100To200_TuneCUETP8M1_13TeV-madgraphMLM-pythia8/RunIISummer16MiniAODv2-PUMoriond17_80X_mcRun2_asymptotic_2016_TrancheIV_v6-v1/MINIAODSIM
	1712000 (LO)	/QCD_HT200To300_TuneCUETP8M1_13TeV-madgraphMLM-pythia8/RunIISummer16MiniAODv2-PUMoriond17_80X_mcRun2_asymptotic_2016_TrancheIV_v6-v1/MINIAODSIM
	347500 (LO)	/QCD_HT300To500_TuneCUETP8M1_13TeV-madgraphMLM-pythia8/RunIISummer16MiniAODv2-PUMoriond17_80X_mcRun2_asymptotic_2016_TrancheIV_v6-v1/MINIAODSIM
	32100 (LO)	/QCD_HT500To700_TuneCUETP8M1_13TeV-madgraphMLM-pythia8/RunIISummer16MiniAODv2-PUMoriond17_80X_mcRun2_asymptotic_2016_TrancheIV_v6-v1/MINIAODSIM
	6823 (LO)	/QCD_HT700To1000_TuneCUETP8M1_13TeV-madgraphMLM-pythia8/RunIISummer16MiniAODv2-PUMoriond17_80X_mcRun2_asymptotic_2016_TrancheIV_v6-v1/MINIAODSIM
	1208 (LO)	/QCD_HT1000To1500_TuneCUETP8M1_13TeV-madgraphMLM-pythia8/RunIISummer16MiniAODv2-PUMoriond17_80X_mcRun2_asymptotic_2016_TrancheIV_v6-v1/MINIAODSIM
	120 (LO)	/QCD_HT1500To2000_TuneCUETP8M1_13TeV-madgraphMLM-pythia8/RunIISummer16MiniAODv2-PUMoriond17_80X_mcRun2_asymptotic_2016_TrancheIV_v6-v1/MINIAODSIM
	25.26 (LO)	/QCD_HT2000ToInf_TuneCUETP8M1_13TeV-madgraphMLM-pythia8/RunIISummer16MiniAODv2-PUMoriond17_80X_mcRun2_asymptotic_2016_TrancheIV_v6-v1/MINIAODSIM
$Z \to \nu\nu$+jets HT binned LO	280.35 (LO)	/ZJetsToNuNu_HT-100To200_13TeV-madgraph/RunIISummer16MiniAODv2-PUMoriond17_80X_mcRun2_asymptotic_2016_TrancheIV_v6-v1/MINIAODSIM
	77.67 (LO)	/ZJetsToNuNu_HT-200To400_13TeV-madgraph/RunIISummer16MiniAODv2-PUMoriond17_80X_mcRun2_asymptotic_2016_TrancheIV_v6-v1/MINIAODSIM
	10.73 (LO)	/ZJetsToNuNu_HT-400To600_13TeV-madgraph/RunIISummer16MiniAODv2-PUMoriond17_80X_mcRun2_asymptotic_2016_TrancheIV_v6-v1/MINIAODSIM
	0.853 (LO)	/ZJetsToNuNu_HT-600To800_13TeV-madgraph/RunIISummer16MiniAODv2-PUMoriond17_80X_mcRun2_asymptotic_2016_TrancheIV_v6-v1/MINIAODSIM
	0.3942 (LO)	/ZJetsToNuNu_HT-800To1200_13TeV-madgraph/RunIISummer16MiniAODv2-PUMoriond17_80X_mcRun2_asymptotic_2016_TrancheIV_v6-v1/MINIAODSIM
	0.0974 (LO)	/ZJetsToNuNu_HT-1200To2500_13TeV-madgraph/RunIISummer16MiniAODv2-PUMoriond17_80X_mcRun2_asymptotic_2016_TrancheIV_v6-v1/MINIAODSIM
	0.002308 (LO)	/ZJetsToNuNu_HT-2500ToInf_13TeV-madgraph/RunIISummer16MiniAODv2-PUMoriond17_80X_mcRun2_asymptotic_2016_TrancheIV_v6-v1/MINIAODSIM
EWK $Z \to \nu\nu$	3.998 (LO)	/EWKZ2Jets_ZToNuNu_13TeV-madgraph-pythia8/RunIISummer16MiniAODv2-PUMoriond17_80X_mcRun2_asymptotic_2016_TrancheIV_v6-v1/MINIAODSIM
Top quark	831.76 (NNLO)	/TT_TuneCUETP8M2T4_13TeV-powheg-pythia8/RunIISummer16MiniAODv2-PUMoriond17_80X_mcRun2_asymptotic_2016_TrancheIV_v6-v1/MINIAODSIM
	35.6 (LO)	/ST_tW_antitop_5f_inclusiveDecays_13TeV-powheg-pythia8_TuneCUETP8M1/RunIISummer16MiniAODv2-PUMoriond17_80X_mcRun2_asymptotic_2016_TrancheIV_v6_ext1-v1
	35.6 (LO)	/ST_tW_top_5f_inclusiveDecays_13TeV-powheg-pythia8_TuneCUETP8M1/RunIISummer16MiniAODv2-PUMoriond17_80X_mcRun2_asymptotic_2016_TrancheIV_v6_ext1-v1
	136.02 (LO)	/ST_t-channel_top_4f_inclusiveDecays_13TeV-powhegV2-madspin-pythia8_TuneCUETP8M1/RunIISummer16MiniAODv2-PUMoriond17_80X_mcRun2_asymptotic_2016_TrancheIV_v6-v1
	80.95 (LO)	/ST_t-channel_antitop_4f_inclusiveDecays_13TeV-powhegV2-madspin-pythia8_TuneCUETP8M1/RunIISummer16MiniAODv2-PUMoriond17_80X_mcRun2_asymptotic_2016_TrancheIV_v6-v1
WW	63.21 (LO)	/WW_TuneCUETP8M1_13TeV-pythia8/RunIISummer16MiniAODv2-PUMoriond17_80X_mcRun2_asymptotic_2016_TrancheIV_v6-v1/MINIAODSIM
WZ	22.82 (LO)	/WZ_TuneCUETP8M1_13TeV-pythia8/RunIISummer16MiniAODv2-PUMoriond17_80X_mcRun2_asymptotic_2016_TrancheIV_v6-v1/MINIAODSIM
ZZ	10.32 (LO)	/ZZ_TuneCUETP8M1_13TeV-pythia8/RunIISummer16MiniAODv2-PUMoriond17_80X_mcRun2_asymptotic_2016_TrancheIV_v6-v1/MINIAODSIM
VBS		/WWJJToLNuLNu_EWK_13TeV-madgraph-pythia8/RunIISummer16MiniAODv2-PUMoriond17_80X_mcRun2_asymptotic_2016_TrancheIV_v6-v1/MINIAODSIM
		/WZJJ_EWK_13TeV-madgraph-pythia8/RunIISummer16MiniAODv2-PUMoriond17_80X_mcRun2_asymptotic_2016_TrancheIV_v6-v1/MINIAODSIM
		/ZZJJTo4L_EWK_13TeV-madgraph-pythia8/RunIISummer16MiniAODv2-PUMoriond17_80X_mcRun2_asymptotic_2016_TrancheIV_v6-v1/MINIAODSIM
VBF-SUSY		/VBF-C1N2_leptonicDecays_TuneCUETP8M1_13TeV-madgraphMLM-pythia8/RunIISummer16MiniAODv2-PUSummer16Fast_80X_mcRun2_asymptotic_2016_TrancheIV_v6-v1/MINIAODSIM
		/VBF-C1N2_WZ_TuneCUETP8M1_13TeV-madgraphMLM-pythia8/RunIISummer16MiniAODv2-PUSummer16Fast_80X_mcRun2_asymptotic_2016_TrancheIV_v6-v1/MINIAODSIM

Table 6.3: MC Samples with their cross sections.

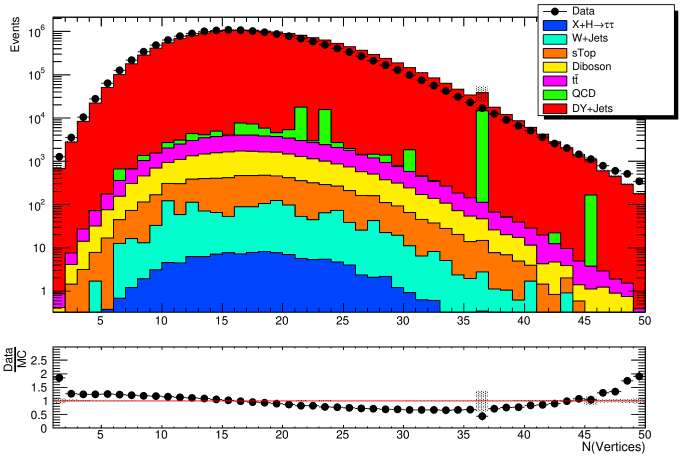

Figure 6.7: NVertices distribution after implementing the pileup weight.

6.5 Trigger Strategy

The collision data events which pass the "MET trigger" named HLT_PFMETNoMu120_ PFMHTNoMu120_IDTight are selected for this analysis.

To define the trigger used in present analysis, below is the explanation for each part.

- **HLT:** As described in Subsection 3.4.2, HLT means high level trigger which contains L1 seeds. There are many L1 seeds for this trigger and each seed has E_T^{miss} higher than a certain threshold.
    - L1_ETM"x", where x = 50,60,70,75,80,85,90,95,100,120.
    - L1_ETM75_Jet60_dPhi_Min0p4
    - L1_DoubleJetC60_ETM60
- **PFMETNoMu120:** This part implies that the selected events have to meet the requirement of $E_T^{miss} > 120$ GeV and during the E_T^{miss} reconstruction, all the muons have to be rejected due to the low deposition of energy left by muons in the detector.
- **PFMHTNoMu120:** As the name suggests, events with reconstructed jets with a condition of MHT $>$ 120 GeV are selected. Also, during the reconstruction of jets, all the events containing muon reconstructed with particle flow algorithm as part of jets, are removed.

An enriched/high purity sample of W+Jets is created to examine the "MET" trigger by applying the various conditions. Single muon dataset with single-muon trigger (HLT_IsoMu24_Eta2p1_v) is chosen to get events with a muon produced by the W decay (W $\rightarrow \mu\nu$) and this trigger will be used to determine the denominator for understanding the MET trigger as shown in Equation 6.3. To get well-reconstructed muon, the requirement of tight ID, $p_T > 30$ GeV and $\eta > 2.1$ has to be applied. Also, the same VBF selections used in our final search region for the jets are implemented to study events that have signal-like topology. At last, $E_T^{miss} > 50$ GeV cut is applied to study the trigger turn on curve as a function of E_T^{miss}. Once the enriched sample is obtained after imposing all the above requirements, the numerator has to be defined with the MET trigger along with all the selection in the denominator part. The efficiency is defined as below:

$$\epsilon = \frac{\text{Denominator \& HLT\_PFMETNoMu120\_PFMHTNoMu120\_IDTight}}{\text{HLT\_IsoMu24\_Eta2p1\_v \& tight ID \& } p_{\mathrm{T}} > 30 \text{ \& } \eta < 2.1 \text{ \& } E_{\mathrm{T}}^{miss} > 50 \text{ \& VBF cuts}} \tag{6.3}$$

The meaning of '&' symbol in Equation 6.3 is AND operator. MET Trigger efficiency as a function of E_T^{miss} is shown in Figure 6.8. Left plot of Figure 6.8 shows where both

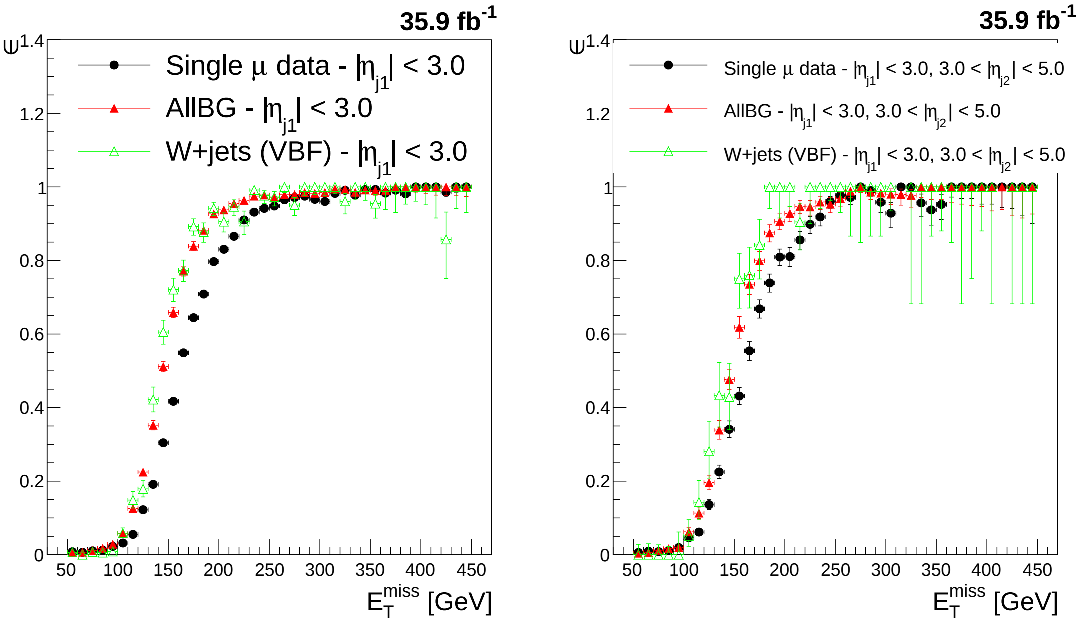

Figure 6.8: MET trigger efficiency as a function of E_T^{miss}. The left plot shows the efficiency where both the jets are "central" ($|\eta| < 3$) and right plot corresponds to the case where one jet is central and other is in the forward region ($3 < |\eta| < 5$).

the jets are "central" ($|\eta| < 3$), and the right distribution of Figure 6.8 corresponds to the case where one jet is central and other is in the forward region ($3 < |\eta| < 5$). The red curve corresponds to the case where all background are counted and the green curve belongs to the W+jets sample with initial state radiation (ISR) jets, both have the same trigger turn-on curve. The black curve corresponds to single muon data and is slightly different in turn-on curve. The efficiency is 100% for the values near to E_T^{miss} of 250 GeV for all three cases while for lower values of E_T^{miss}

the behavior of curves is different. This motivates us to choose the $E_T^{miss} > 250$ GeV for final states. In the present analysis, the trigger is applied only to the data because the trigger is not well modeled with MC samples but trigger weight which is very close to unity is applied to MC and we observed the negligible difference on applying either trigger weight or trigger on MC.

6.6 Event Selections

As already discussed in Subsection 6.4.2, Standard Model (SM) backgrounds can mimic the VBF signal signature, so one needs to be careful while making the event selection criteria to increase the signal events with a large rejection of background events. Event selection for selecting the events similar to VBF signal is divided into two parts: **Central selections** and **VBF selections**.

6.6.1 Central Selections

Central selections intend to select the events with identification of lepton i.e. single hadronic tau channel, b-jets and missing transverse energy. The selected final event is required to have well-reconstructed tau with $20 < p_T < 40$ GeV and $|\eta| > 2.1$ to ensure that both the tracks are inside tracker acceptance. The lower limit on p_T of τ_h is higher than muon and electron (8 and 10 GeV respectively) due to well-known fact that it is difficult to reconstruct low p_T τ's, because they do not provide a "pencil-like jet" in the detector and it becomes difficult to differentiate from gluon or quark jets. The upper limit on p_T is because of the signal point with a mass gap of $\Delta M = m(\tilde{\chi}_1^{\pm}) - m(\tilde{\chi}_1^0) = 10$ GeV has a higher signal significance between 20 to 40 GeV. Figure 6.9 shows the reason to chose an upper limit of 40 GeV in τ, e, and μ channel. Apart from p_T and η selection, the hadronic tau should be well isolated from other leptons like e or μ and from gluon or quark jets. So to reject the fakes and for good identification of taus, many discriminators are applied.

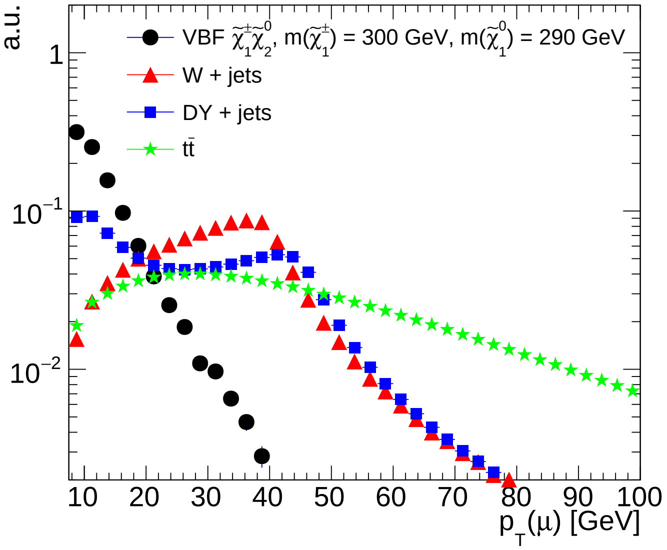

Figure 6.9: p_T distribution normalized to unity to check the upper cut on the lepton p_T.

- **Tau Decay Mode Reconstruction:** We are studying the compressed mass spectra with low p_T taus, so tau should pass "old" decay mode finding as per recommendation from tauPOG. We have also calculated the old decay mode finding efficiency with the requirement of reconstructed tau having $p_T > 20$ GeV and $|\eta| < 2.1$ GeV matched to generator level visible tau with $\Delta R(\tau_{reco}, \tau_{gen}) < 0.3$ to pass the decay mode finding discriminator. Visible taus here means the tau excluding the neutrinos coming from tau decays. Figure 6.10 shows the efficiency of taus to pass the old DMF reconstruction as a function of p_T which is greater than 95% depending on true visible tau p_T. The MVA based isolation discriminator which uses the lifetime information of taus, charge and neutral isolation sums, etc. with a "tight" working point gives the best possible discrimination handle between hadronic taus and quark or gluon jets. The tight working point has 50% efficiency and > 99% for rejection rate with $p_T > 20$ GeV.

- **Veto for Muons and Electrons:** Since muons and electrons can fake hadronic tau, so to reject muons and electrons, the tight working point of

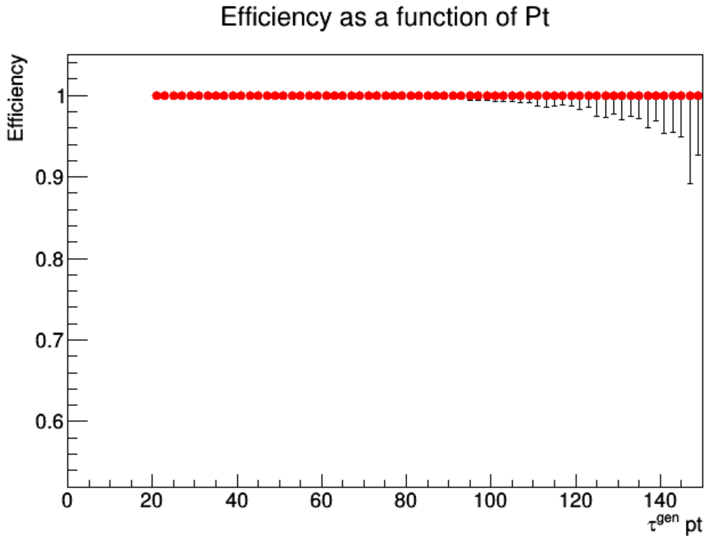

Figure 6.10: Old DMF reconstruction efficiency for taus as a function of the generator level taus (visible taus).

anti-muon discriminator named and loose working point of MVA based anti-electron discriminator is used. Electron discriminator uses a BDT technique based on the various properties of taus, photons, tracks, and electrons. Muon discriminator searches for hits in the muon system which are associated with the track of the tau candidate and then reject them.

- After all these cuts, tau should pass exactly one signal charged hadron i.e. one-prong decay. One-prong tau is selected instead of higher multiplicity taus, because of higher signal significance.

Aside from tau identification, we require to implement some usual cuts as defined further. To decrease $t\bar{t}$ background, the events are obliged to have no jets classified as b-quark jet (b-jet). The jets with $p_T > 30$ GeV, $|\eta| < 2.4$ and separated from the leptons by $\Delta R > 0.4$ are searched for b-jets and then rejected by medium working point of Combined Secondary Vertex (CSV) discriminator. The medium working point is chosen because of good discrimination and great efficiency. Similarly, to reduce the W+jets background, transverse mass cut between lepton (tau, electron or muon depending on the final state) and missing transverse energy $m_T(\tau, E_T^{miss}) >$

110 GeV is applied to avoid the jacobian peak of W boson mass. An example of $m_T(\mu, E_T^{miss})$ distribution is displayed in the top plot of Figure 6.11. Also $m_T > 110$ GeV gives the large-signal significance as shown in the bottom plot of Figure 6.11.

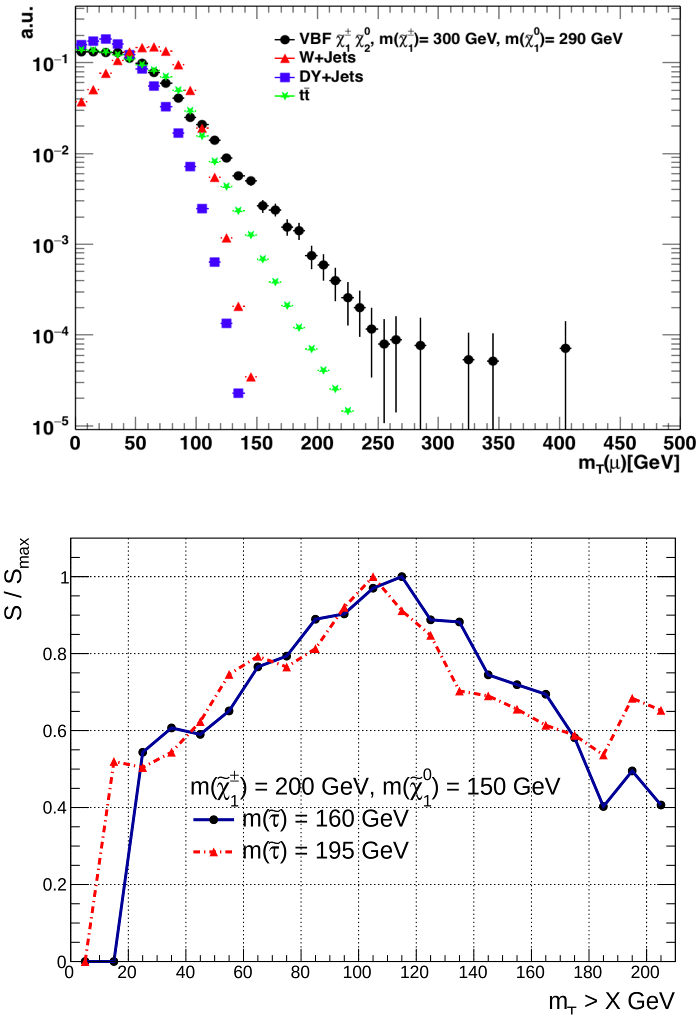

Figure 6.11: Top: $m_T(\mu, E_T^{miss})$ plot normalized to unity with all signal region cuts, except m$_T$ cut for various background and VBF signal sample $\tilde{\chi}_1^\pm \tilde{\chi}_2^0$ with mass points m($\tilde{\chi}_1^\pm$) = 300 GeV and m($\tilde{\chi}_1^0$) = 290 GeV. Bottom: Ratio of signal significance S and maximum significance S_{max} as a function of m_T cut values for two different VBF signal samples. Clearly, $m_T > 110$ GeV gives the best signal significance.

For the SUSY searches, computation of E_{T}^{miss} is significant since the LSP leaves the detector without any signature. In R-parity conserving models, SUSY particles are always produced in pairs and having cascade decay ending with the creation of an LSP, so there are two LSP's in our final state which gets counted through E_T^{miss}. Because of the presence of two LSP, we expect large E_T^{miss} in VBF signal rather than neutrinos which are produced by SM Backgrounds. The $E_T^{miss} > 250$ GeV is applied to suppress the DY $\rightarrow$ ll SM background and left with a great signal as shown in the top distribution of Figure 6.12. Moreover, it also gives the high signal significance as depicted in the bottom plot of Figure 6.12. We cannot go beyond 250 GeV E_T^{miss} cut as it will reduce the statistics. Signal significance is defined as:

$$S = \frac{s}{\sqrt{\sigma_s^2 + \sigma_B^2}} = \frac{s}{\sqrt{s + B}} \tag{6.4}$$

where σ_s and σ_B refers to the uncertainties in signal and background events, respectively. "s" is event yield from the signal and "B" is the sum of event yields of all SM backgrounds. In addition, efficiency as a function of E_T^{miss} is also plotted for both signal and background as shown in Figure 6.13. All the plots are produced with the "N-1" scenario which means all SR cuts are applied except the cut under consideration like in this plot all the cuts are applied except E_T^{miss} cut. With $E_T^{miss} > 250$ GeV cut, the *Central Selection* cuts are finished.

6.6.2 VBF Selections

As outlined earlier, VBF processes are characterized by the presence of two forward energetic jets in opposite hemispheres, with a large pseudorapidity gap and large invariant dijet mass. All the VBF cuts are optimized to give the best signal significance and reduce the SM background to enhance the signal yield. The events are required to have large p_T in VBF processes rather than SM backgrounds because the signal jets must have sufficient momentum to radiate the SM vector bosons and continue in the forward direction as shown in the left distribution of Figure 6.14. The right distribution shows the pseudorapidity (η) for all jets plotted with main backgrounds added together ($t\bar{t}$, W+jets and DY+jets) compared to one VBF SUSY

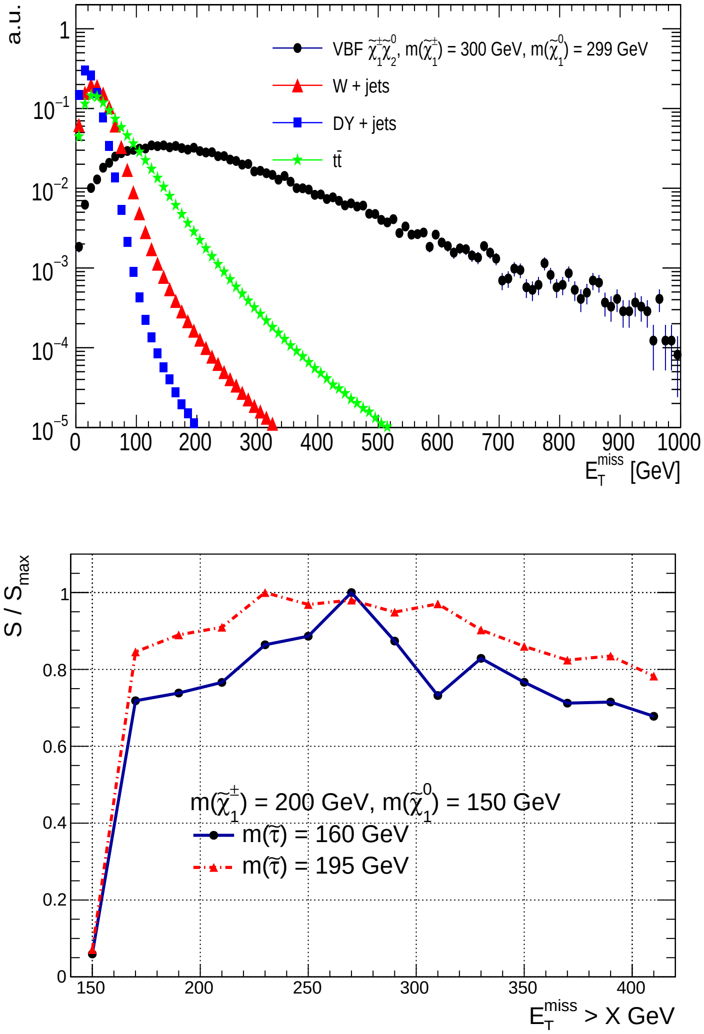

Figure 6.12: Top: Normalized to unity E_T^{miss} distribution for signal and background. Clearly, 250 GeV cut will suppress the background to a high extent specially DY + Jets. Bottom: Signal significance S divided by maximum significance S_{max} as a function of E_T^{miss}.

signal sample. Obviously, as stated earlier, signal jets have large momentum in the forward direction or they are non-central with large dijet invariant mass while SM backgrounds give central jets having less dijet mass. So from these plots, it is clear that VBF selection requires at least two jets with $p_T > 60$ GeV and $|\eta| < 5.0$ passing the loose jet identification criteria and separated from the leptons (e, μ and τ) by $\Delta R = \sqrt{\Delta\phi^2 + \Delta\eta^2} > 0.3$.

After passing the above-mentioned kinematics cuts, jets are required to pass

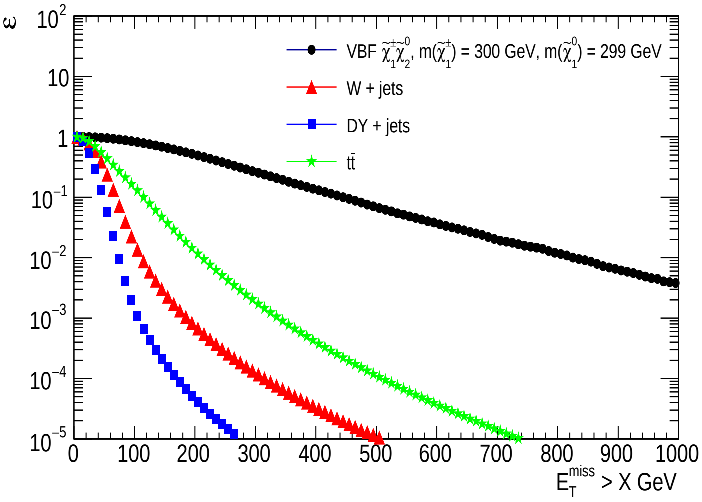

Figure 6.13: N-1 plot for signal and background efficiency as a function of E_T^{miss}.

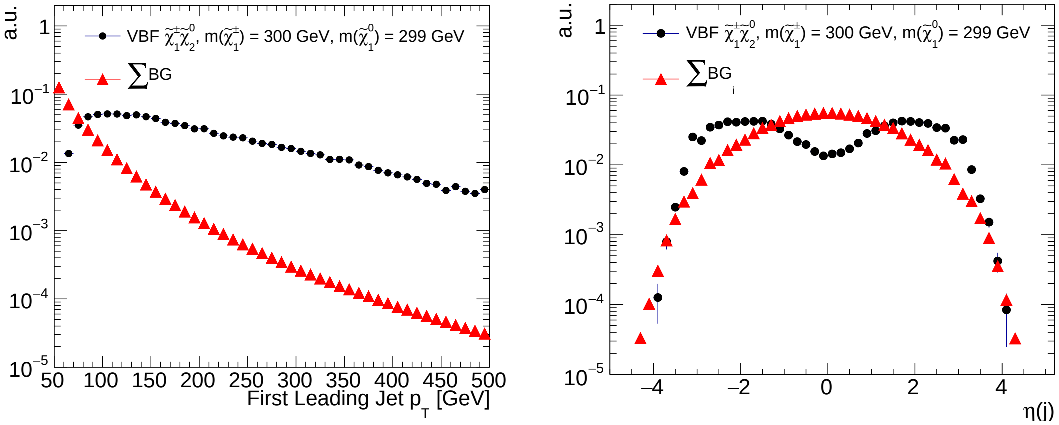

Figure 6.14: Leading jet p_T (left) and η_{jets} (right) distribution normalized to unity with all the SR cuts except m_{jj} and $\Delta\eta_{jj}$ cuts for backgrounds summed together (red) and the VBF signal sample (black).

$|\Delta\eta_{jj}| > 3.8$, $\eta_1 \cdot \eta_2 < 0$, and $m_{jj} > 1$ TeV to get dijet candidates. The high m_{jj} cut has been decided because of the fact that forward jets are boosted in energy and it also enhances the signal significance. The m_{jj} distribution comparing the SM backgrounds and VBF signal sample is shown in Figure 6.15. Once all these requirements are implemented, only $\sim 0.01\%$ of the events have more than one good dijet candidate. Out of them, a jet pair having highest dijet invariant mass is selected. The p_T, pseudorapidity gap ($|\Delta\eta_{jj}|$) and dijet mass (m_{jj}) of jets are

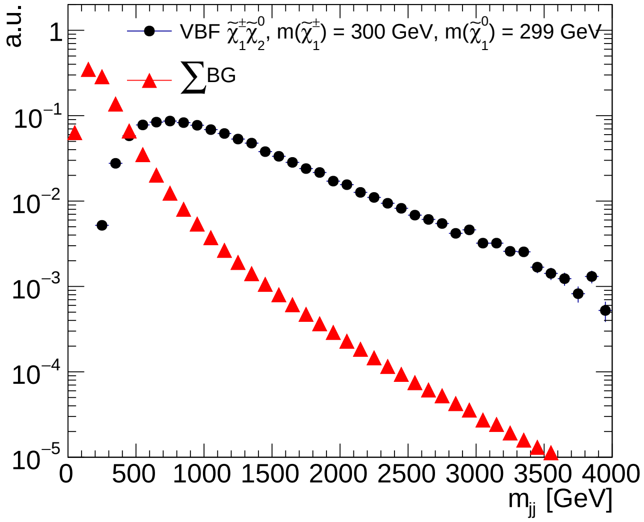

Figure 6.15: Dijet invariant mass distribution normalized to unity with all the SR cuts except m_{jj} and $\Delta\eta_{jj}$ requirements for backgrounds summed together (red) and VBF signal sample (black).

related to each other as $m_{j_1 j_2} \approx e^{\frac{\Delta\eta}{2}}\sqrt{2|p_T^{j1}||p_T^{j2}|}$ [14]. Figure 6.16 summarizes the signal region (SR) event selections and bins used to find the access of VBF signal over SM backgrounds for all three different channels (e, μ and τ_h).

		$e^{\pm}$ Channel	$\mu^{\pm}$ Channel	$\tau^{\pm}$ Channel
lepton flavor	$e^{\pm}$	Selected	Vetoed	Vetoed
	$\mu^{\pm}$	Vetoed	Selected	Vetoed
	$\tau^{\pm}$	Vetoed	Vetoed	Selected
lepton ID		Medium ID	Tight ID	Discrimination prong type 1 hps
lepton Iso		-	0.25	Tight Isolation MVA run2 v1 DB new DMwLT
lepton p_{T}	$e^{\pm}$	10-40 GeV	$>$ 10 GeV	$>$ 10 GeV
	$\mu^{\pm}$	$>$ 8 GeV	8-40 GeV	$>$ 8 GeV
	$\tau^{\pm}$	$>$ 20 GeV	$>$ 20 GeV	20-40 GeV
$m_{\mathrm{T}}(l, p_{\mathrm{T}}^{miss})$	$e^{\pm}$	$>$ 110 GeV	No Cut	No Cut
	$\mu^{\pm}$	No Cut	$>$ 110 GeV	No Cut
	$\tau^{\pm}$	No Cut	No Cut	$>$ 110 GeV
p_{T}^{miss}		$>$ 250 GeV		
Overlap Removal		Yes		
b-jet		$N_{bjet} = 0$, CSVv2M (Medium WP), $p_{\mathrm{T}} > 30$ GeV, $\lvert\eta\rvert < 2.4$		
VBF Selection		$N_{jets} \geq 2$ with $p_{\mathrm{T}}^{jet} > 60$ GeV, $\lvert\eta(j)\rvert < 5$ At least one set of jets (j_1, j_2) with $\eta(j_1) \times \eta(j_2) < 0$, $\Delta\eta(j_1, j_2) > 3.8$, $m_{jj} > 1$ TeV		
SR m_T Bins		[110-130], [130-150], [150-170], [170-190], [190-210], [210-∞]		

Figure 6.16: Signal region event selection for all three channels.

6.7 Strategy to Estimate SM Backgrounds

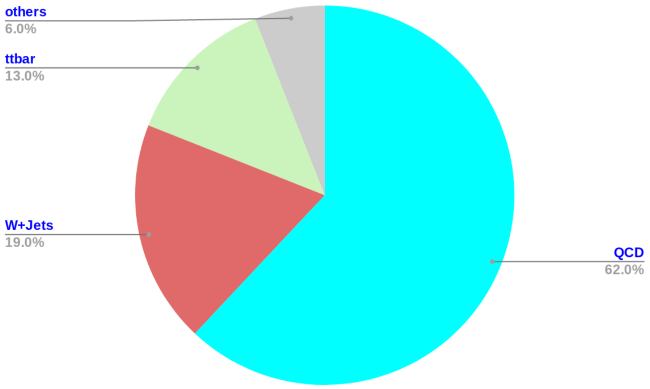

Figure 6.17: Pie chart representing the major backgrounds for the τ_h channel.

The event selections defined in Section 6.6 are for the signal region but the remaining MC yields in the SR has to be estimated. The major backgrounds for the single hadronic tau (τ_h) are QCD, followed by W+jets and then $t\bar{t}$ as shown in Figure 6.17. So to estimate these major backgrounds we obtain control regions (CR) with the selections orthogonal to the signal region selections. By choosing the CR selections, one could get a sample of real events from proton-proton collisions, with a dominating/enriched background that has to be estimated.

The two CR's, CR1 and CR2 are defined in order to extract data-to-MC correction factors for central selections and VBF efficiency respectively. CR2 is also used to extract the shapes of m$_{jj}$ and m$_T(l, E_T^{miss})$ from data. The CR's should have a negligible contribution from the signal (to avoid any signal contamination) to get high purity of the dominating background under study. The correction/scale factors (SF1 and SF2) obtained from the CR1 and CR2 are applied to MC yield to improve any mismodeling. Figure 6.18 shows the strategy followed to estimate the major backgrounds by choosing the CR's orthogonal to SR.

CR1 is defined by using the central selections and Inverted VBF cuts. By means of Inverted VBF cuts, the events are required to fail VBF cuts which can be

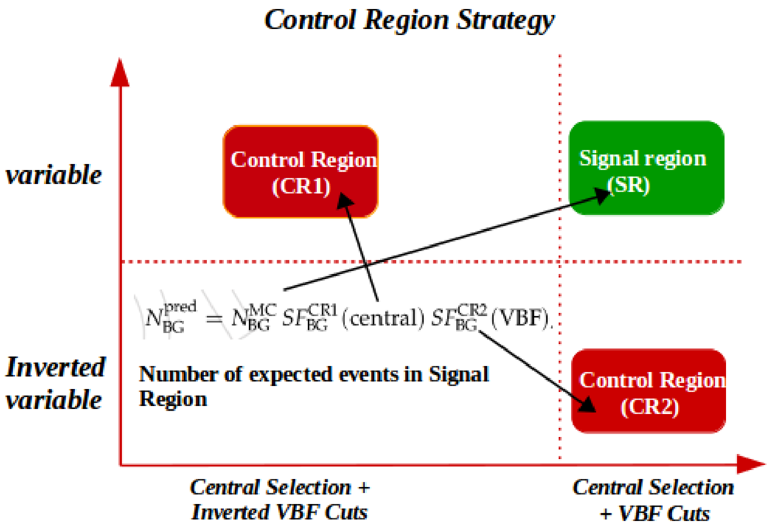

Figure 6.18: Strategy to define CR's and to obtain correction factors from central and VBF selections.

performed in different ways as explained below and shown in Figure 6.19.

- Jets fail to pass the kinematics cuts i.e. $p_T > 60$ GeV and $|\eta| < 5.0$.
- Jets passing the kinematics cuts but failed to pass either one or all VBF selection.

CR2 is used to extract VBF efficiency so it is defined by using the VBF selections in addition to some other selections that are orthogonal to CR1 and SR. This can be accomplished by selecting a "variable" which enriches the background sample and simultaneously the inverted cuts on that variable allows reaching near to the signal region. The expected number of background yield in the signal region is defined by Equation 6.5.

$$N_{BG}^{Data} = N_{BG}^{MC}\ (\text{SR cuts}) \cdot SF^{CR1}_{\text{w/o VBF cuts}} \cdot SF^{CR2}_{\text{with VBF cuts}} \tag{6.5}$$

where N_{BG}^{Data} is the predicted background rate in the signal region, N_{BG}^{MC} is the predicted rate by MC simulation with central selections only. $SF^{CR1}_{w/oVBFcuts}$ given in Equation 6.6 is the data-to-MC correction factor without VBF cuts i.e. with

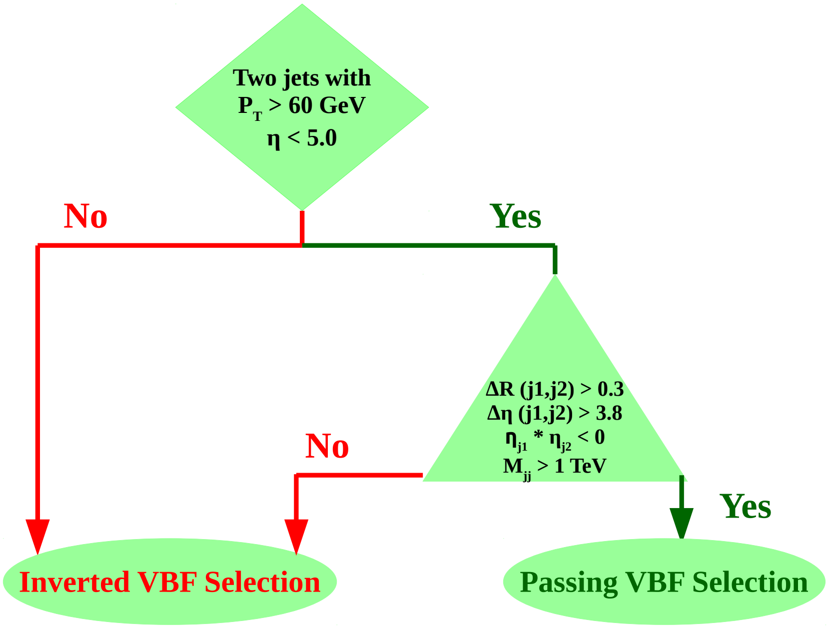

Figure 6.19: Diagram showing the criteria for Inverted VBF selections.

central selections only as obtained from background enriched control region (CR1) and it contains the correction for object identification, isolation, misidentification rates and MET requirement.

$$SF^{CR1}_{\text{w/o VBF Cuts}} = \frac{N^{CR1}\ (\text{Data}) - N^{CR1}\ (\text{sum of other backgrounds})}{N^{CR1}\ (\text{Background under consideration})} \tag{6.6}$$

Here, N^{CR1} (Data) represents the number of data events after passing CR1 selection, N^{CR1} (sum of other backgrounds) is the sum of number of events of other backgrounds different than background understudy and N^{CR1} (Background under consideration) is the number of events obtained for an enriched background. Similarly, $SF^{CR2}_{VBFcuts}$ is the data-to-MC correction factor with VBF cuts as obtained in a background enriched CR2 and given by the following equation :

$$SF^{CR2}_{\text{with VBF Cuts}} = \frac{N^{CR2}\ (\text{Data}) - N^{CR2}\ (\text{sum of other backgrounds})}{N^{CR2}\ (\text{Background under consideration}) \cdot SF^{CR1}_{\text{w/o VBF Cuts}}} \tag{6.7}$$

Likewise, N^{CR1} (Data) represents the number of data events after passing CR2 selection, N^{CR2} (sum of other backgrounds) is the sum of number of events of other backgrounds different than background understudy and N^{CR2} (Background under consideration) is the number of events obtained for an enriched background. In the next Section, we will discuss in detail how the control regions are obtained for different backgrounds.

6.7.1 $t\bar{t}$ Background Estimation

In the SR selection, no b-jets requirement is implemented to remove $t\bar{t}$ background but still, some part of $t\bar{t}$ events can mimic our final state. Therefore, to estimate $t\bar{t}$ background, we use the strategy defined in the previous Section 6.7. The $t\bar{t}$ background enriched control region is obtained by selecting the events with a requirement of 1 b-tagged jet with $p_T > 30$ GeV and $\eta < 2.4$ because top quark decays to the b-jet. Apart from getting the high purity sample, one should be careful about the contamination of signal i.e. event yield for the signal has to be negligible in the CR as compared to the SR and also about the biasing of kinematics so that SF's are not biased and could be used for correcting the MC yield in the SR. Figure 6.20 shows the comparison of m_{jj} and $\Delta\eta_{jj}$ distributions in the 1 b-jet (CR1) and 0 b-jet (SR) which clearly describes that there is no biasing in the VBF shapes after using the b-tagged jet for CR. Figure 6.21 shows the p_{T} and η plots in $t\bar{t}$ enriched CR and in SR. This also shows that choosing 1 b-tagged jet does not bias the lepton kinematics and hence the SFs are also not biased.

Further, we also need to check that composition of real τ_h in the CR and SR is same or not to avoid any bias in lepton kinematics. If the composition is different, the SF obtained from the CR will not reflect the proper corrections for event yield in SR. The difference between real and fake τ_h can be defined as: if generated level τ passes all the tau selection (kinematics and other discriminators) it is called as real τ_h and if any other gets reconstructed as τ_h but not identified at generation

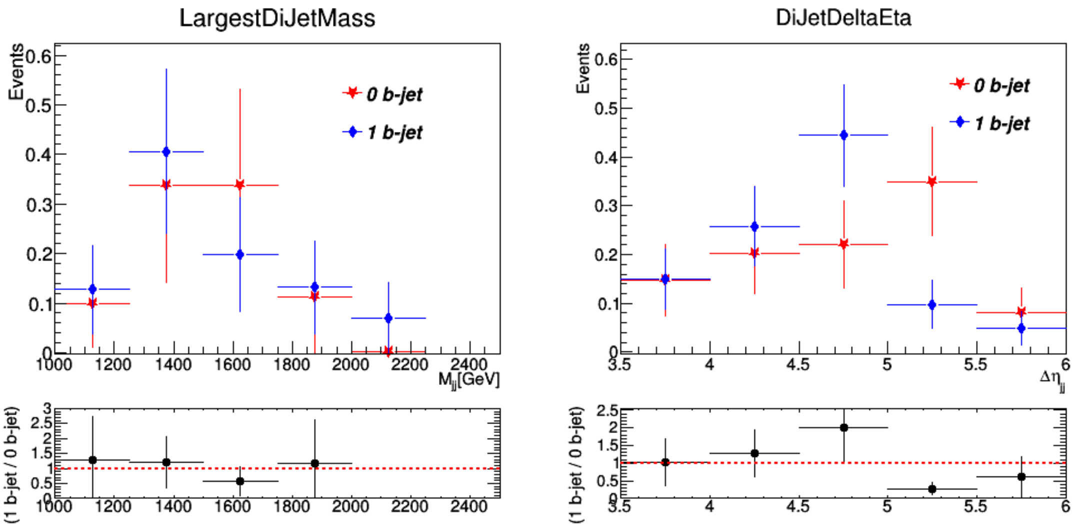

Figure 6.20: Comparison of 1 b-jet (CR) and 0 b-jet (SR) for m$_{jj}$ and $\Delta\eta_{jj}$ distribution .

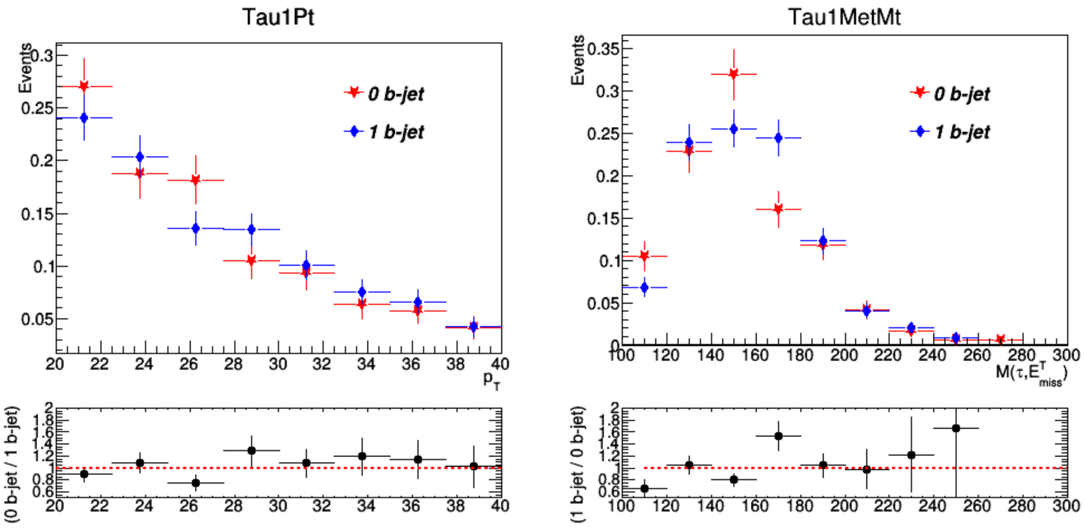

Figure 6.21: Comparison of 1 b-jet (CR) and 0 b-jet (SR) for p_{T} and $m_T(\tau, E_{\mathrm{T}}^{miss})$ distribution to be sure about the fact that 1 b-jet does not bias the lepton kinematics.

level as tau is termed as fake tau. The fraction of real and fake τ_h along with VBF efficiencies are measured in both 1 b-jet and 0 b-jet regions to check the difference. From Table 6.4 it is clear that the composition, as well as the VBF efficiency, are the same within statistical uncertainty for 1 b-jet and 0 b-jet regions. Following the preceding study about the composition and biasing of lepton kinematics, the

Composition of τ_h	0 b-jets (signal region)	1 b-jets (control region)
$\frac{\text{Real } \tau_h}{\text{Total} = \text{Real } \tau_h + \text{fakes } \tau_h}$	0.60 ± 0.04	0.62 ± 0.03
$\epsilon_{t\bar{t}}$(VBF cuts)	$5.51 \pm 1.74\%$	$4.60 \pm 1.33\%$

Table 6.4: Comparison of the composition of $t\bar{t}$ events in the signal and control region.

condition of 1 b-jet is suitable for $t\bar{t}$ enriched background sample. The strategy to define various CRs (CR1, CR2, VR1, VR2, and Signal Region (SR)) is described in Figure 6.22.

CR1 consists of 1 b-tagged jet, central selections, inverted VBF cuts and $m_T(\tau, E_{\mathrm{T}}^{miss}) > 110$ GeV. Figure 6.23 represents the E_{T}^{miss}, $m_T(\tau, E_{\mathrm{T}}^{miss})$, $\eta(\tau_h)$ and $p_{\mathrm{T}}(\tau_h)$ distributions from CR1 which clearly shows that Data/MC agrees well within statistical uncertainty (pink band in lower part of the plot) for the variables of our interest i.e. p_{T} and $m_T(\tau, E_{\mathrm{T}}^{miss})$. Note that, in these plots only statistical uncertainty is considered. Taking the benefit of the good agreement between data and MC, we can use the shapes of $t\bar{t}$ background directly from the simulation in the signal region.

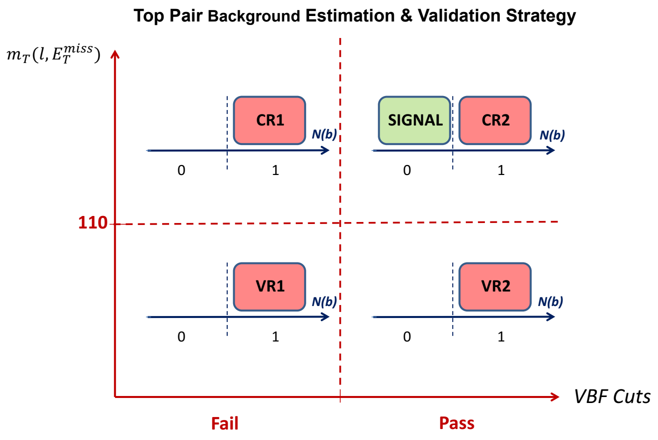

Figure 6.22: Diagram showing the strategy to estimate $t\bar{t}$ background.

The scale factor for CR1 is calculated from Equation 6.8 and measured to be

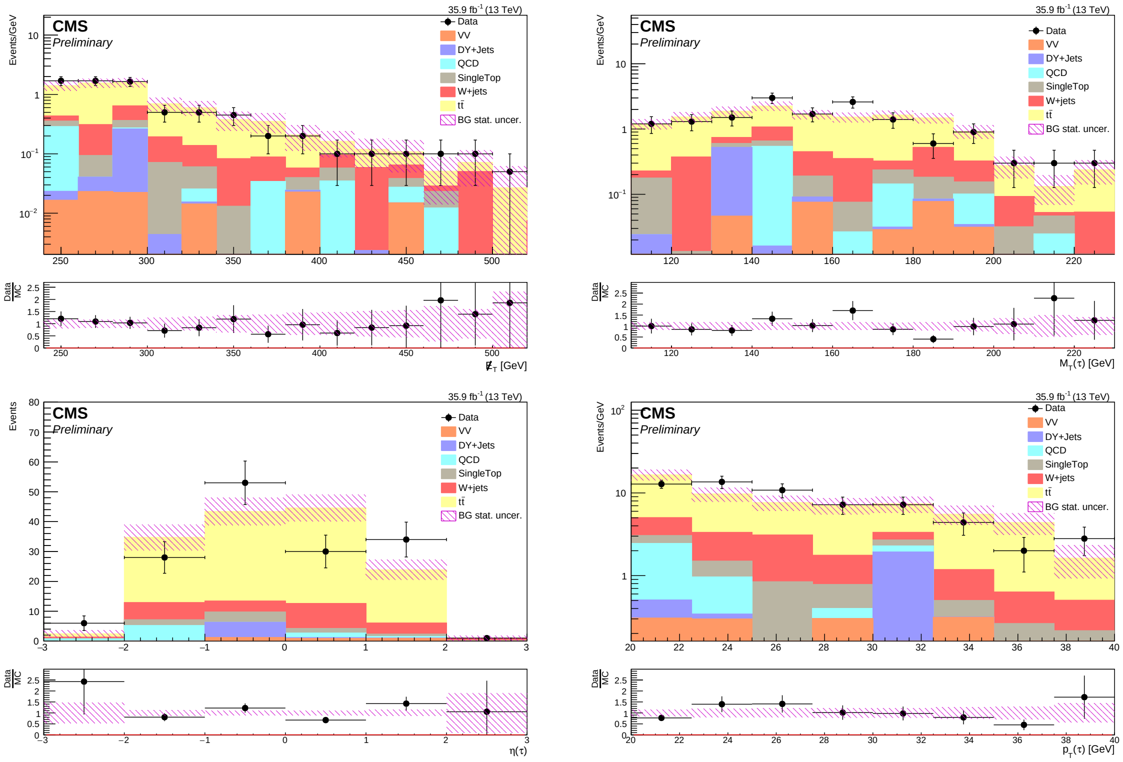

Figure 6.23: (a) E_{T}^{miss}, (b) $m_T(\tau_h, E_T^{miss})$, (c) $\eta(\tau_h)$, and (d) $p_T(\tau_h)$ distributions for the $t\bar{t}$ CR1.

1.06 ± 0.19 which is very close to unity. The plots shown in Figure 6.23 are already corrected with the SF measured from CR1. The contamination from the other backgrounds specially their statistical uncertainty will be taken care in the systematics uncertainty calculations.

$$SF^{CR1} = \frac{N^{CR1}\ (\text{Data})\ -\ N^{CR1}\ (\text{sum of other BGs})}{N^{CR1}\ (t\bar{t})} \tag{6.8}$$

The main cause for mismodeling between data and MC are the VBF selections as they are not well modeled with MC simulations. So to check the behavior of data and MC after applying VBF selections, we need to define CR2. This control region contains all the selection similar to CR1 with the requirement of VBF cuts. The scale factor for CR2 is calculated from Equation 6.9 and measured to be 1.30 ± 0.50. The reason for high uncertainty in SF^{CR2} is due to less statistics left after applying VBF selections.

$$SF^{CR2} = \frac{N^{CR2}\ (\text{Data}) - N^{CR2}\ (\text{sum of other BGs})}{N^{CR2}\ (t\bar{t}) \cdot SF^{CR1}} \tag{6.9}$$

The event yield obtained for data and MC in $t\bar{t}$ CR1 and CR2 is given in Table 6.5.

Sample	$t\bar{t}$ CR1$_{\tau_h}$ (No. of Events)	$t\bar{t}$ CR2$_{\tau_h}$ (No. of Events)
Diboson	3.3 ± 1.1	—
QCD	7.8 ± 4.6	0.08 ± 0.05
Single Top	8.4 ± 1.3	0.2 ± 0.1
W + jets	22.6 ± 3.4	0.4 ± 0.1
DY + jets	5.6 ± 4.6	—
$t\bar{t}$	98.0 ± 6.2	4.8 ± 1.4
Total MC yield	145.7 ± 9.8	5.5 ± 1.5
$m(\tilde{\chi}_1^{\pm}), m(\tilde{\ell}), m(\tilde{\chi}_1^0) = 100, 75, 50$ GeV	0.1 ± 0.1	0.1 ± 0.1
$m(\tilde{\chi}_1^{\pm}), m(\tilde{\ell}), m(\tilde{\chi}_1^0) = 100, 95, 90$ GeV	$0.0^{+0.1}_{-0.0}$	$0.0^{+0.1}_{-0.0}$
$m(\tilde{\chi}_1^{\pm}), m(\tilde{\ell}), m(\tilde{\chi}_1^0) = 400, 375, 350$ GeV	$0.0^{+0.1}_{-0.0}$	$0.0^{+0.1}_{-0.0}$
$m(\tilde{\chi}_1^{\pm}), m(\tilde{\ell}), m(\tilde{\chi}_1^0) = 400, 395, 390$ GeV	$0.0^{+0.1}_{-0.0}$	$0.0^{+0.1}_{-0.0}$
Purity	67.3%	87.3%
Data Events	152	7
Scale Factor	1.06 ± 0.19	1.3 ± 0.5

Table 6.5: Predicted and observed rates for the $t\bar{t}$ control regions for CR1 and CR2.

Finally, the expected event yield of $t\bar{t}$ in SR is given by Equation as:

$$N_{t\bar{t}}^{Expected} = N_{t\bar{t}}^{MC}\ (\text{SR cuts}) \cdot SF^{\text{CR1}} \cdot SF^{\text{CR2}} \tag{6.10}$$

where $N_{t\bar{t}}^{MC}$ (SR cuts) is the predicted yield in MC simulation in signal region (both central and VBF selections). SF^{CR1} and SF^{CR2} are the scale factors obtained from CR1 and CR2 respectively. So, the final $t\bar{t}$ yield obtained in SR for τ_h is 5.1 ± 2.7.

6.7.2 Validation of $t\bar{t}$ Scale Factors and VBF Shapes in low-$\mathbf{m}_T$ Region

As data/MC agrees well in the control region (CR1), the $t\bar{t}$ shapes are directly taken from simulation in the signal region. Since VBF efficiency obtained from data in CR2 is with less statistics due to passing VBF selections, so to get more confidence about the SF obtained from CR1 and CR2, we performed closure test with the Validation Regions (VR) based on selections that are orthogonal to CRs and SR as shown in Figure 6.22. The VRs should have high statistics and high purity of $t\bar{t}$ events. So, to validate the SF from CR1, a validation region with 1 b-jet, inverted VBF jets and $m_T(\tau, E_{\mathrm{T}}^{miss}) < 110$ GeV named "VR1" is defined. Data/MC agreement is studied in this region after applying the SF obtained from CR1 in order to correct the predicted yield from MC for central selections. Simulation study predicts $\sim 65\%$ $t\bar{t}$ events and SF^{VR1} is 1.01 ± 0.03 in VR1. Figure 6.24 shows the kinematics distribution obtained from VR1 having good agreement between data and MC which gave us more confidence about SF^{CR1} that it can be used to correct the $t\bar{t}$ background yield in the SR.

Similarly, to validate the VBF efficiencies obtained from data in CR2, validation

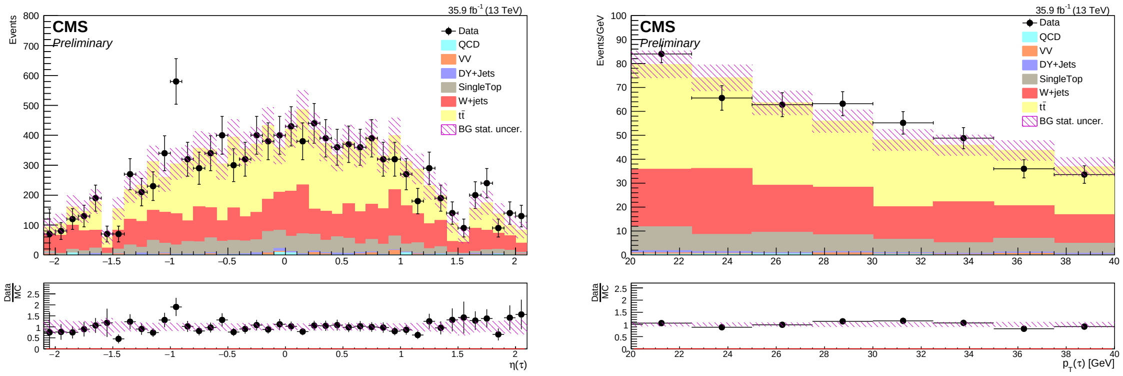

Figure 6.24: (a) $\eta(\tau_h)$ and (b) $p_T(\tau_h)$ distributions for the $t\bar{t}$ validation region VR1$_{\tau_h}$.

region with 1 b-jet, passing VBF jets and $m_T(\tau, E_{\mathrm{T}}^{miss}) < 110$ GeV named "VR2" is defined. Figure 6.25 shows the kinematics and VBF related distributions obtained from VR2. SF obtained from CR2 (SF^{CR2}) have been applied in VR2 to validate them and to check the agreement between data and MC. One can see that data/MC agrees well for m_{jj} and $m_T(\tau, E_{\mathrm{T}}^{miss})$ within statistical uncertainties which gives surity that shapes can be taken from simulation for $t\bar{t}$ in the signal region. Table 6.6 shows the predicted and expected rates for $t\bar{t}$ validation regions (VR1 and VR2).

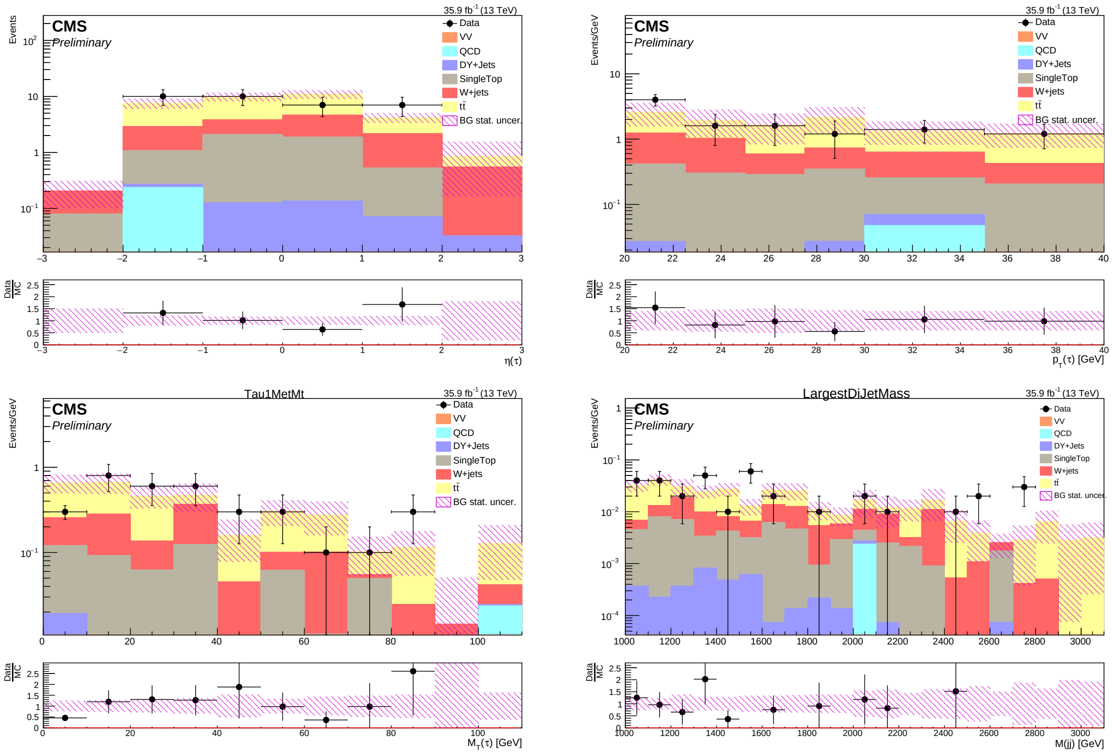

Figure 6.25: (a) $\eta(\tau_h)$, (b) $p_T(\tau_h)$, (c) $m_T(\tau_h, E_T^{miss})$, and (d) m_{jj} distributions for the $t\bar{t}$ validation region VR2$_{\tau_h}$.

6.7.3 Validation of $t\bar{t}$ Background Scale Factors with Dimuon Samples

To become even more confident concerning the fact that $t\bar{t}$ shapes can be directly taken from MC samples, we performed a study to check data/MC agreement with dimuon dataset to which single-muon trigger named “HLT_IsoMu24_Eta2p1_v” is applied. The $t\bar{t}$ enriched sample is achieved with $e\mu$ and $\mu\mu$ final state with muon $p_{\mathrm{T}} > 30$ GeV and a b-jet. After having these requirements, signal contamination is

Sample	$t\bar{t}$ VR1$_{\tau_h}$ (No. of Events)	$t\bar{t}$ VR2$_{\tau_h}$ (No. of Events)
Diboson	5.6 ± 1.2	—
QCD	2.6 ± 1.0	0.2 ± 0.2
Single Top	101.3 ± 3.6	3.9 ± 0.6
W + jets	282.1 ± 10.1	6.6 ± 1.1
DY + jets	9.1 ± 0.7	0.3 ± 0.1
$t\bar{t}$	627.2 ± 13.7	21.9 ± 2.6
Total MC yield	$1027.9\pm$	32.9 ± 2.7
Purity	66.6%	61.0%
Data Events	34	1123

Table 6.6: Predicted and observed rates for the $t\bar{t}$ validation regions, VR1 and VR2.

less because signal events do not have real b-jets and also, in our signal region, we do not require two leptons that have to pass p_T threshold of 30 GeV. Figure 6.26 shows the distributions of m_{jj} and $m_T(\tau, E_{\mathrm{T}}^{miss})$ for the $t\bar{t}$ MC and the data with the selections defined above. $SF_{t\bar{t}}^{CR1}$ and $SF_{t\bar{t}}^{CR2}$ are applied to all the distributions in Figure 6.26 to correct for the $t\bar{t}$ prediction from the MC. Since the m_{jj} and $m_T(\tau, E_{\mathrm{T}}^{miss})$ gives us good agreement for data and MC within statistical uncertainty, we are very sure about the decision to use the shapes for $t\bar{t}$ in the signal region directly from simulation.

6.7.4 W+jets Background Estimation

For τ_h channel, W+jets is the second major background as shown in Figure 6.17 which contains ∼ 19% of the total SM background rate. W+jets can easily mimic our VBF SUSY signal because of the decay of W into a lepton and E_{T}^{miss} and associated jets can fake the signal (VBF) jets as explained in Section 6.3. A similar strategy will be used to estimate W+jets background as we did for $t\bar{t}$ background. We expect the central selections efficiency to be well modeled by simulation, but with VBF selections one could see the mismodeling of W+jets event yield and shapes in the signal region. So to correct the central selections efficiency and VBF efficiency

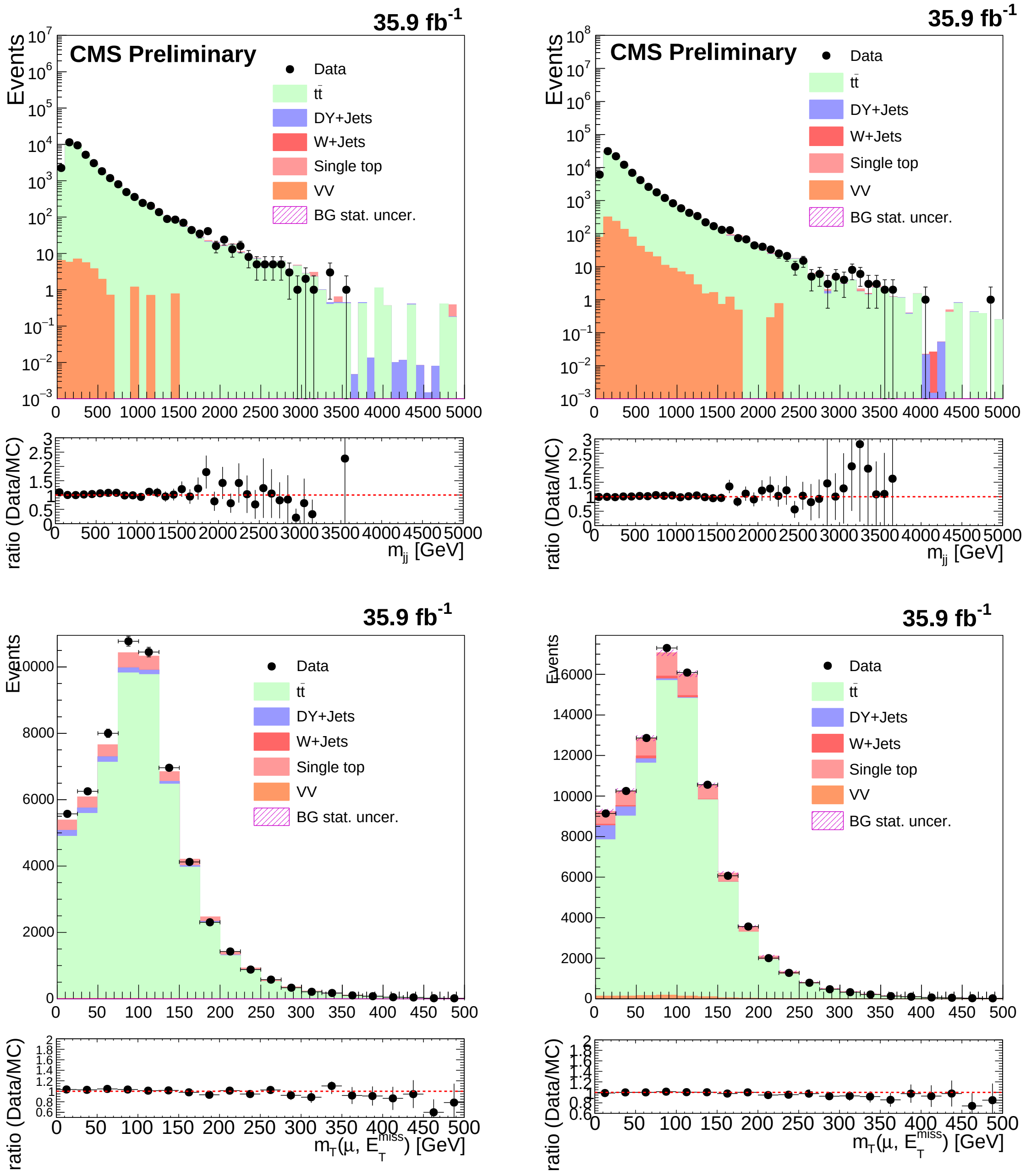

Figure 6.26: m_{jj} and m_T distributions for the $t\bar{t}$ $\mu\mu$ (top left and bottom left) and $e\mu$ (top right and bottom right) shape validation regions.

two CR has to be defined. The strategy to estimate W+jets background is shown in Figure 6.27. For the correct modeling of central selections and to get data-to-MC scale factor, we define CR1 with all the central selections and inverted VBF selections (Figure 6.19). By inverting the VBF selection, statistics of W+jets background increases by $\mathcal{O}(2)$ and reduce signal contamination to a good extent. After

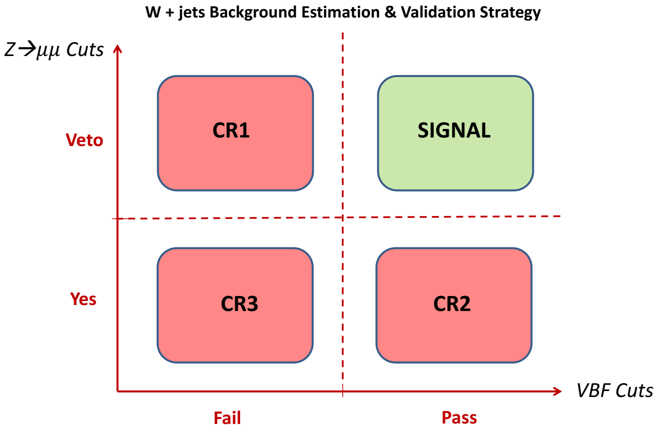

Figure 6.27: Strategy to estimate W+jets background.

implementing these requirements, W+jets enriched control sample with 63% purity is obtained. Figure 6.28 shows the $m_T(\tau, E_{\mathrm{T}}^{miss})$ and p_{T} distributions from W+jets CR1. However, there is a huge discrepancy between data and MC because of large jet → τ_h fake rate as compared to the misidentification rate for other leptons (e, μ). Because of this, QCD multijet background came into the picture as highest background for τ_h channel. It is clear from the plots that because of the large contribution of QCD background, it is difficult to perform data-driven estimation of W+jets background to the signal region. Nevertheless, we believe that modeling of W $(\rightarrow \tau\nu \rightarrow \tau_h\nu)$ + jets in simulation is same for W $(\rightarrow e\nu)$ / W $(\rightarrow \mu\nu)$ + jets and all of these have real E_{T}^{miss} from W boson decay to a neutrino and real leptons (not jets). It can be explained differently, the data-to-MC SF for e/μ channel should be similar to τ_h channel as also observed in $t\bar{t}$ control regions. So, SF used in single τ_h channel for W+jets CR1 is the average of SF from electron and muon channels which are calculated in the same way from Equation 6.8 (W+jets is main background here) and measured to be 0.97 ± 0.10 and 1.1 ± 0.10 for electron and muon channels respectively. The uncertainties presented here are purely statistical

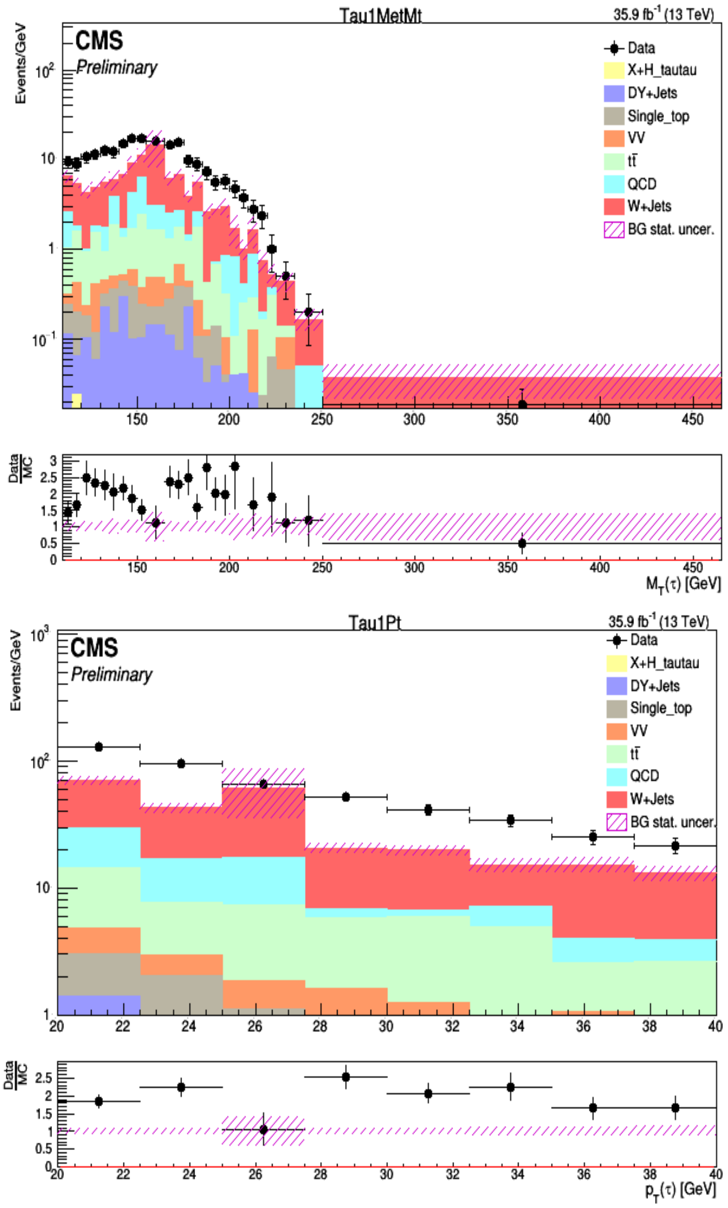

Figure 6.28: (a) $m_T(\tau_h, E_T^{miss})$ and (b) $p_T(\tau_h)$ distributions for W+jets CR1.

with less than 2% signal contamination. Remaining things like contamination from other backgrounds ($\sim 35\%$) and their uncertainties are considered during systematic study. The SF for τ_h is calculated as the average of SF_e^{CR1} and SF_μ^{CR1} i.e. $\frac{0.97+1.1}{2}$ = 1.04 and uncertainty is the absolute difference 1.1 - 0.97 = 0.13.

On the other hand, to measure the mismodeling for VBF selections, we apply our knowledge for a small difference between W and Z masses to get a control region (CR2) enriched with Z + jets events. Two muons with $p_{\mathrm{T}} > 30$ GeV and other central cuts are used to obtain CR2. Since muons are very clean and completely understood, any discrepancy observed between data and MC in Z+jets CR is used to measure or make a conclusion for the SF obtained for modeling of the VBF selection efficiency in W+jets events. But before CR2, usual "Z" control region named CR3 is constructed with two opposite-sign muons having $p_{\mathrm{T}} > 30$ GeV, $m_{\mu\mu}$ invariant mass between 60 and 120 GeV and inverted VBF selections. With these CR3 selections, a data sample with greater than 99% purity of $Z \to \mu\mu$ events (according to MC) is obtained where observed shapes and rates in data can be compared to expectations from MC in order to validate our expectation that $\sigma_Z \cdot L_{int} \cdot \epsilon(\mu\mu)$ is well-understood to $< 2\%$. The scale factor for CR3 can be calculated from Equation given below:

$$SF^{CR3} = \frac{N^{CR3}\ (\text{Data}) - N^{CR3}\ (\text{sum of other BGs})}{N^{CR3}(Z \to \mu\mu)} \tag{6.11}$$

Being the cleanest and standard Z control sample, here defined as CR3, the data-to MC correction factor obtained is 0.99 ± 0.001 as expected. The dimuon invariant mass ($m_{\mu\mu}$) and $p_{\mathrm{T}}(\mu)$ for CR3 is shown in Figure 6.29. The SF obtained from CR3 is used to correct MC in CR2. So, to study the VBF efficiency and to correct the

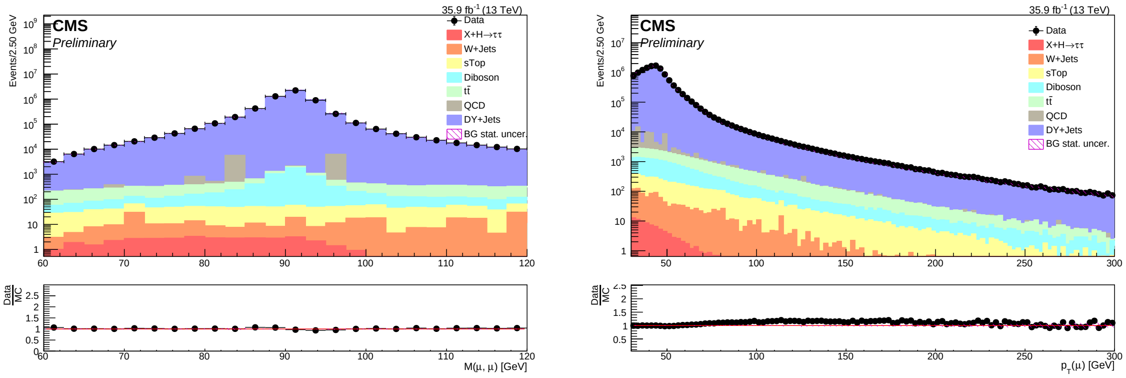

Figure 6.29: (a) $m_{\mu\mu}$ and (b) $p_T(\mu)$ distributions for Z+jets CR3.

mismodeling by VBF selection, we calculate the SF^{CR2} as:

$$SF^{CR2} = \frac{N^{CR2}\ (\mathrm{Data}) - N^{CR2}\ (\text{sum of other BGs})}{N^{CR2}(Z \to \mu\mu) \cdot SF^{CR3}} \tag{6.12}$$

which comes out to be 1.18 ± 0.09. Figure 6.30 shows the $m_{\mu\mu}$ and m_{jj} distribution having good agreement within statistical uncertainty for data and MC for CR2.

Finally, the expected event yield of W+jets MC in SR is given by Equation as:

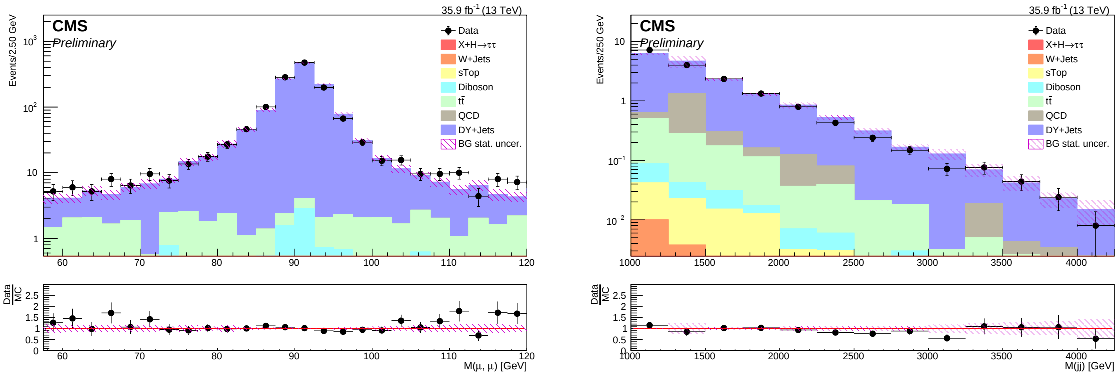

Figure 6.30: (a) $m_{\mu\mu}$ and (b) m_{jj} distributions for W/Z + jets CR2. The last bin of the m_{jj} distribution represents the overflow bin.

$$N^{Expected}_{W+jets} = N^{MC}_{W+jets}\ (\text{SR cuts}) \cdot SF^{\mathrm{CR1}} \cdot SF^{\mathrm{CR2}} \tag{6.13}$$

and obtained as $N^{Expected}_{W+jets} = 7.0 \pm 1.7$. Table 6.7 shows the predicted and observed rates for Z($\to \mu\mu$) + jets CR3 and CR2.

6.7.4.1 Validation of W+jets Background Scale Factors and VBF Shapes in low-m$_T$ Region

Similar to $t\bar{t}$ background estimation methodology, W+jets background is estimated by using two CRs: to measure data-to-MC correction factor for central selection efficiency and for VBF efficiency from W+jets events in Z($\to \mu\mu$) enriched control region. To validate the SF obtained from the CR1 and CR2, two validation regions

Sample	$Z(\rightarrow \mu\mu)$ + jets CR3 (No. of Events)	$Z(\rightarrow \mu\mu)$ + jets CR2 (No. of Events)
Diboson	18533.7 ± 78.1	25.0 ± 2.8
QCD	62412.8 ± 23860.0	373.3 ± 250.5
Single Top	5625.1 ± 32.9	20.3 ± 1.9
W + jets	1372.1 ± 100.9	3.0 ± 0.9
DY + jets	15795222.6 ± 7659.0	3100.7 ± 42.6
$t\bar{t}$	34336.6 ± 115.6	252.5 ± 9.9
Total MC yield	15917502.9 ± 25059.7	3774.8 ± 254.3
$m(\tilde{\chi}_1^{\pm}), m(\tilde{\ell}), m(\tilde{\chi}_1^0) = 100, 75, 50$ GeV	41.6 ± 2.1	5.7 ± 0.8
$m(\tilde{\chi}_1^{\pm}), m(\tilde{\ell}), m(\tilde{\chi}_1^0) = 100, 95, 90$ GeV	0.3 ± 0.2	$0.0^{+0.1}_{-0.0}$
$m(\tilde{\chi}_1^{\pm}), m(\tilde{\ell}), m(\tilde{\chi}_1^0) = 400, 375, 350$ GeV	0.7 ± 0.3	0.1 ± 0.1
$m(\tilde{\chi}_1^{\pm}), m(\tilde{\ell}), m(\tilde{\chi}_1^0) = 400, 395, 390$ GeV	$0.0^{+0.1}_{-0.0}$	$0.0^{+0.1}_{-0.0}$
Purity	99.2%	82.1%
Data Events	15715632	4174
Scale Factor	0.99 ± 0.001	1.13 ± 0.08

Table 6.7: Predicted and observed rates for Z($\rightarrow \mu\mu$) + jets CR3 and CR2. CR2 is used to obtain a scale factor for the VBF selection, SF^{CR2}. CR3 is used to obtain an scale factor for the central selections (SF^{CR3}) to correct the MC of Z($\rightarrow \mu\mu$) in CR2.

(VR) having high purity of W+jets is chosen. SF^{CR1} is validated by obtaining VR1 having $m_T(\tau, E_{\mathrm{T}}^{miss}) < 110$ GeV and inverted VBF cuts along with other central cuts and SF^{CR2} is validated with $m_T(\tau, E_{\mathrm{T}}^{miss}) < 110$ GeV and VBF selection called as VR2. Note that, SF^{CR1} and $SF^{CR2}$are also applied to VR1 and VR2 respectively for correcting the predictions from MC and VBF shapes. Since for single τ_h channel, SF is used from the average of SF obtained from electron and muon channels, it also becomes important to check whether those SF are appropriate to apply or not. Figure 6.31 shows the strategy for the validation region of W+jets. Table 6.8 shows the event yield obtained in data and MC for VR1 and VR2. Figures 6.32 and 6.33 shows the distributions $\eta(\tau_h)$ and $p_{\mathrm{T}}(\tau_h)$ for VR1, and $\eta(\tau_h)$, $p_{\mathrm{T}}(\tau_h)$, E_{T}^{miss} and m_{jj} for VR2, respectively.

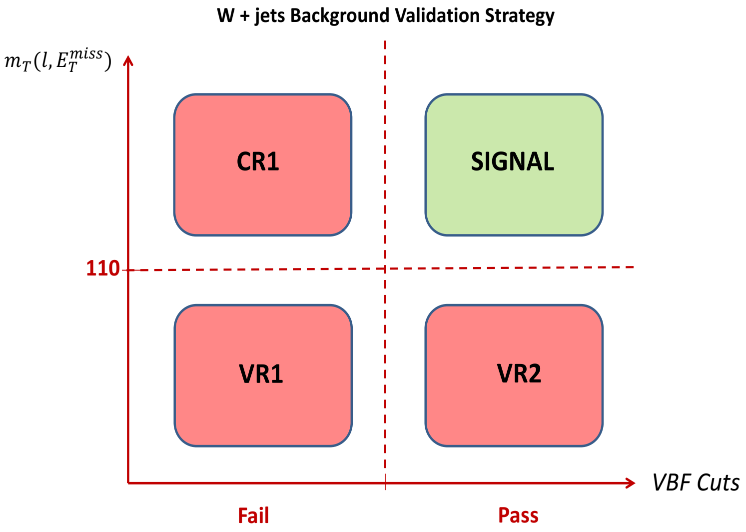

Figure 6.31: W+jets validation strategy.

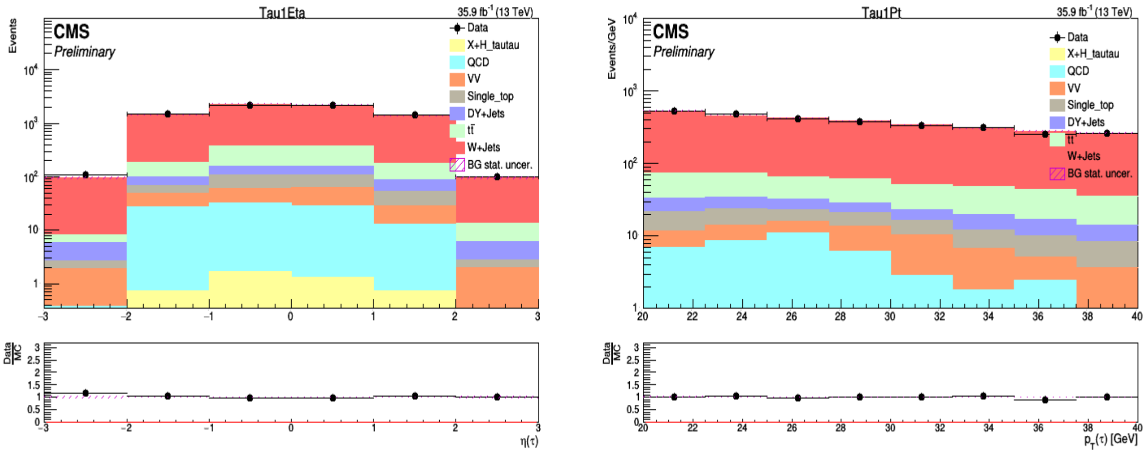

Figure 6.32: (a) $\eta(\tau_h)$ and (b) $p_T(\tau_h)$ distributions for the W+jets validation region VR1_{τ_h}.

6.7.5 QCD Multijet Background Estimation

The QCD multijet background plays a major role in the single τ_h channel and has significant contribution in SR as shown in Figure 6.17. To differentiate between QCD background and VBF SUSY signal, the main discriminating variables are VBF selec-

Sample	W+jets VR1$_{\tau_h}$ (No. of Events)	W+jets VR2$_{\tau_h}$ (No. of Events)
Diboson	103.4 ± 6.0	1.6 ± 0.7
QCD	97.1 ± 20.1	2.1 ± 0.9
Single Top	137.9 ± 4.7	6.0 ± 0.9
W + jets	6679.1 ± 1197.2	134.1 ± 8.6
DY + jets	165.7 ± 4.3	4.7 ± 1.0
$t\bar{t}$	627.4 ± 15.6	29.5 ± 3.4
Total MC yield	7810.6 ± 1197.5	178.0 ± 9.5
Purity	85.5%	75.3%
Data Events	7402.0	188
Scale Factor	0.94 ± 0.15	1.07 ± 0.16

Table 6.8: Predicted and observed rates for the W+jets validation region VR1 obtained with inverted m_T + and failing VBF selections.

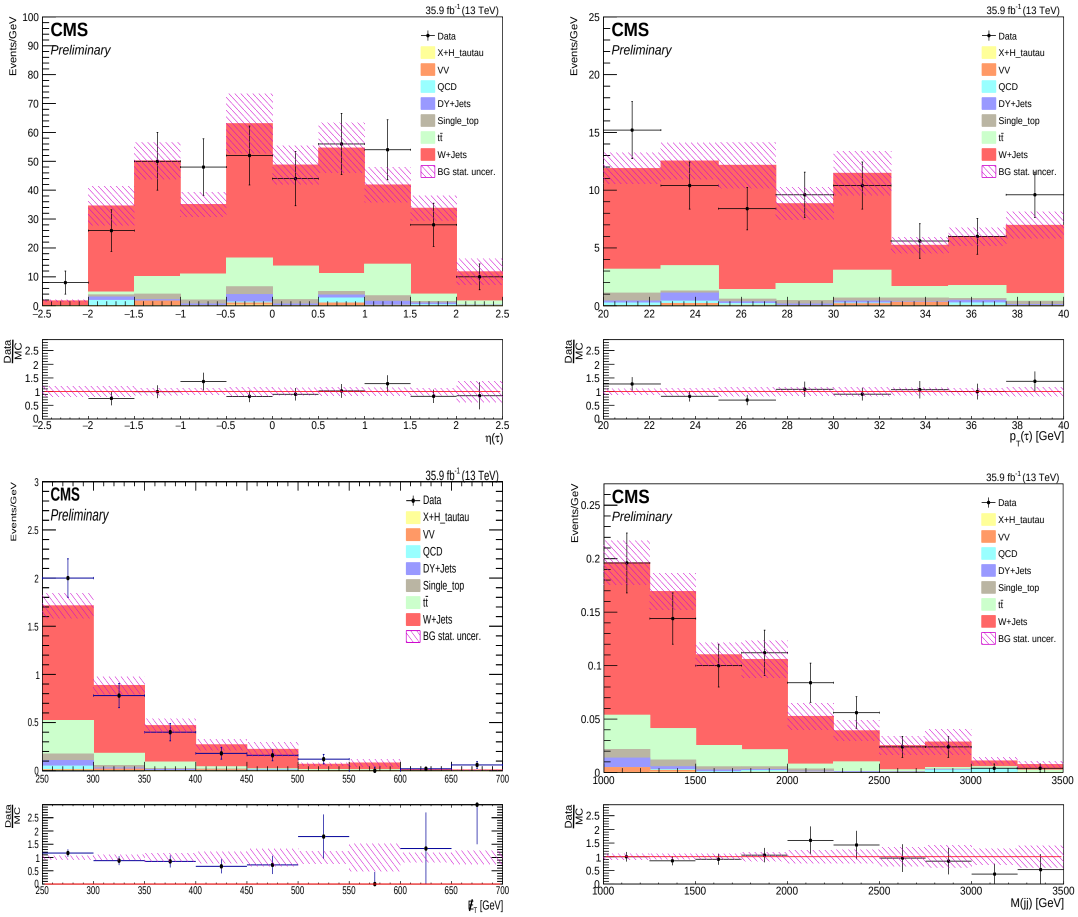

Figure 6.33: (a) $\eta(\tau_h)$, (b) $p_T(\tau_h)$, (c) E_{T}^{miss} and (d) m_{jj} distributions for the W+jets validation region VR2$_{\tau_h}$.

tions, the minimum separation between $\overrightarrow{E}_T^{miss}$ and any jet $|\Delta\phi_{\min}(\overrightarrow{E}_T^{miss}, j)|$, and τ_h isolation. Therefore, to estimate the QCD multijet background, CRs are constructed by inverting the above said requirements as shown in Figure 6.34. A complete data-driven approach has been used to estimate the QCD multijet background in the τ_h channel, which relies on the classic ("ABCD") method. The definition of each control region is defined as:

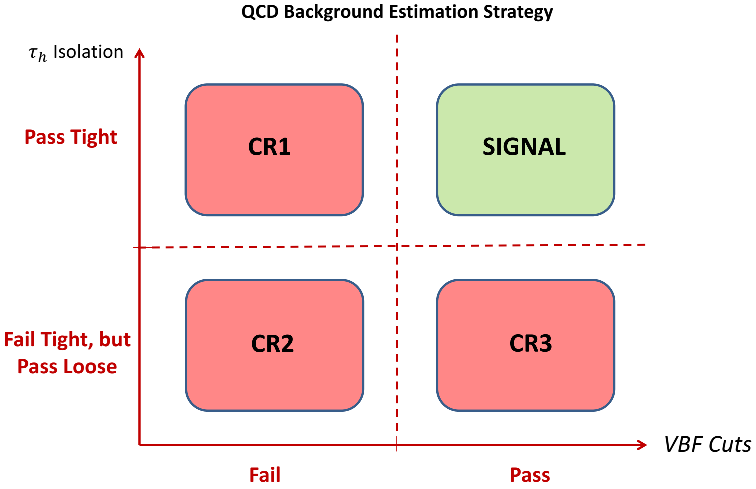

Figure 6.34: QCD estimation strategy.

- CR1: inverted VBF selection, pass the nominal (tight) τ_h isolation;
- CR2: inverted VBF selection, fail the nominal τ_h isolation but pass loose τ_h isolation;
- CR3: pass the VBF selection, fail the nominal τ_h isolation but pass loose τ_h isolation and;
- CR4/Signal region: pass the VBF selection, pass the nominal τ_h isolation.

The QCD background component N^{i}_{QCD} in regions $i = \text{CR1}, \text{CR2}, \text{CR3}$ is estimated by subtracting non-QCD backgrounds (predicted using simulation) from data ($N^{i}_{\text{QCD}} = N^{i}_{\text{Data}} - N^{i}_{\neq\text{QCD}}$). Finally, in the signal region i.e. CR4, QCD is estimated as $N^{SR}_{\text{QCD}} = N^{\text{CR1}}_{\text{QCD}} \frac{N^{\text{CR3}}_{\text{QCD}}}{N^{\text{CR2}}_{\text{QCD}}}$, where $\frac{N^{\text{CR3}}_{\text{QCD}}}{N^{\text{CR2}}_{\text{QCD}}}$ is referred to as the "Pass-to-Fail VBF" transfer factor (TF_{VBF}). In other words, the event yield of QCD in data is taken from passing inverted VBF selections and then extrapolated in the signal region by "Pass-to-fail" transfer factor (or called as "VBF efficiency"), which is calculated with QCD enriched data sample procured by inverting the τ_h isolation. Inverting τ_h isolation means that τ_h fail to pass nominal "tight" isolation but passes the "loose" isolation working point. The m_T distribution shape is obtained from CR2 (from the non-isolated τ_h plus inverted VBF control sample). This "ABCD" method relies on TF_{VBF} being unbiased by the τ_h isolation requirement. Closure test is also provided to validate this hypothesis and shown in Figure 6.35 (left). The distribution of m_{jj} which is normalized to unity for nominal τ_h isolation (red) and inverted τ_h isolation (blue) clearly shows that there is no biasing by using τ_h isolation sidebands to extract the "Pass-to-Fail VBF" transfer factor. The event yield for data and expected

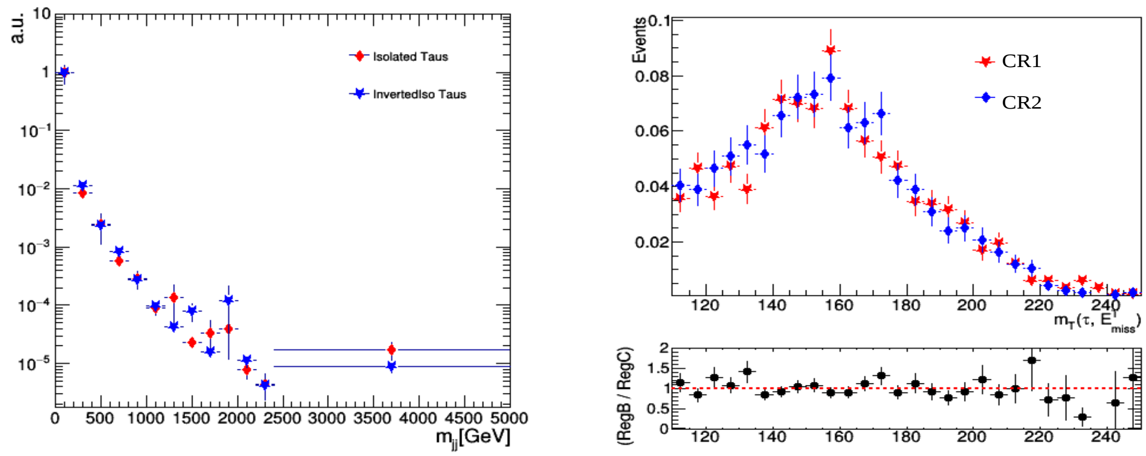

Figure 6.35: Left: QCD closure test with MC showing that the m_{jj} shapes and proving that "Pass-to-Fail VBF" transfer factor is unbiased by the use of the τ_h isolation sideband. Right: Closure test with data shows that the shape of m_T distribution remains unbiased by the use of the τ_h isolation sidebands.

MC from all control region of QCD is given in Table 6.9.

The purity of QCD background defined by formula: Data - $\sum_i BG_i$ is $\approx$ 53-77% with a signal contamination of $<$ 1% in all control regions. Figure 6.35 (right) shows the $m_T(\tau, E_{\mathrm{T}}^{miss})$ distribution from CR1 (isolated τ_h and inverted VBF). The QCD shape has been taken from data in CR2 after subtracting the non-QCD contributions. The expected QCD multijet yield in CR1 is calculated as $N_{\mathrm{QCD}}^{\mathrm{CR1}} = N_{\mathrm{Data}}^{\mathrm{CR1}} - N_{\neq\mathrm{QCD}}^{\mathrm{CR1}}$. Figure 6.36 shows the plot comparing the m_T shapes between CR1 (nominal isolation with inverted VBF cuts) and CR2 (inverted isolation with inverted VBF cuts). The good data/MC agreement indicates that m_T shape is not biased by inversion of τ_h isolation and QCD (m_T) shape with nominal VBF cuts can be extracted from non-isolated sideband (CR2).

Sample	QCD CR1$_{\tau_h}$ (No. of Events)	QCD CR2$_{\tau_h}$ (No. of Events)	QCD CR3$_{\tau_h}$ (No. of Events)
Diboson	13.8 ± 2.1	18.7 ± 2.5	—
Single Top	11.6 ± 1.4	13.1 ± 1.5	0.2 ± 0.2
W + jets	403.9 ± 41.9	404.1 ± 16.2	6.6 ± 1.1
DY + jets	21.6 ± 7.1	8.5 ± 0.9	0.2 ± 0.1
$t\bar{t}$	89.2 ± 5.9	81.0 ± 5.6	3.4 ± 1.2
Total MC yield	540.1 ± 43.0	525.4 ± 17.4	10.4 ± 1.6
$m(\tilde{\chi}_1^{\pm}), m(\tilde{\ell}), m(\tilde{\chi}_1^0) = 100, 75, 50$ GeV	2.4 ± 0.5	1.0 ± 0.3	$0.0^{+0.1}_{-0.0}$
$m(\tilde{\chi}_1^{\pm}), m(\tilde{\ell}), m(\tilde{\chi}_1^0) = 100, 95, 90$ GeV	1.0 ± 0.3	0.6 ± 0.3	$0.0^{+0.1}_{-0.0}$
$m(\tilde{\chi}_1^{\pm}), m(\tilde{\ell}), m(\tilde{\chi}_1^0) = 400, 375, 350$ GeV	0.2 ± 0.1	$0.0^{+0.1}_{-0.0}\pm$	$0.0^{+0.1}_{-0.0}$
$m(\tilde{\chi}_1^{\pm}), m(\tilde{\ell}), m(\tilde{\chi}_1^0) = 400, 395, 390$ GeV	$0.0^{+0.1}_{-0.0}$	$0.0^{+0.1}_{-0.0}\pm$	$0.0^{+0.1}_{-0.0}$
Purity	53.0%	64.5%	77.4%
Data Events	1160	1482	46
QCD Events = Data - MC	619.9 ± 52.6	956.6 ± 42.3	35.6 ± 7.0

Table 6.9: Predicted and observed rates for QCD MC sample in all control regions.

The method described in this section yields a QCD multijet background estimate of $N_{\mathrm{QCD}}^{SR} = N_{\mathrm{QCD}}^{\mathrm{CR1}} \cdot \frac{N_{\mathrm{QCD}}^{\mathrm{CR3}}}{N_{\mathrm{QCD}}^{\mathrm{CR2}}} = (619.9 \pm 52.6) \times \frac{(35.6 \pm 7.0)}{(956.6 \pm 42.3)} = 23.1 \pm 5.0$ in the VBF $jj + \tau_h + E_{\mathrm{T}}^{miss}$ search region. The uncertainty provided here is based on the statistics of the data and MC samples. We stress that this is the QCD predicted rate over the entire $m_T(\tau, E_{\mathrm{T}}^{miss})$ spectrum.

As discussed in Section 6.3, the other background processes like Diboson,

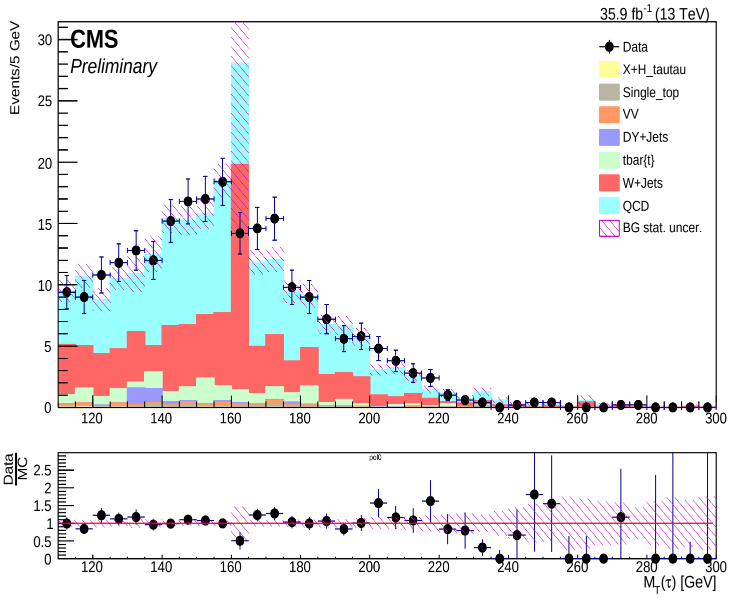

Figure 6.36: $m_T(\tau, E_{\mathrm{T}}^{miss})$ distribution in QCD CR1. The SFs calculated for W+jets and $t\bar{t}$ for CR1 have been used to correct the MC prediction corresponding to these processes. The QCD multijet normalization is determined as data minus non-QCD backgrounds. The m_T shape is extracted from QCD CR2.

DY+jets, and Single Top can also mimic our VBF SUSY signal but they contribute only 6% of the total background yield as shown in Figure 6.17. So the event yield for these processes is taken directly from the simulation in the signal region.

6.8 Data in Signal Region after Background Estimation

The event selection criteria for the signal region in case of a single τ_h channel is mentioned in Section 6.6. Depending on the modeling of central and VBF selections for different backgrounds and their contributions, estimation of backgrounds is done either by semi data-driven ($t\bar{t}$ and W+jets) or by full data-driven technique (QCD multijet). The remaining backgrounds with negligible/less contribution have been estimated directly from MC simulations in the signal region. Table 6.10 shows the number of observed events in data as well as the predicted background for single hadronic tau VBF + τ_h + jj channel. The uncertainties are purely statistical and

Sample	N_{BG}^{MC} (SR/CR) (No. of Events)	N_{BG}^{Data} (corrected) (No. of Events)
Diboson	0.5 ± 0.4	0.5 ± 0.4
QCD	619.9 ± 52.6	23.1 ± 5.0
Single Top	0.5 ± 0.2	0.5 ± 0.2
W + jets	5.7 ± 1.1	7.0 ± 1.7
DY + jets	0.1 ± 0.1	0.1 ± 0.1
$t\bar{t}$	3.7 ± 1.2	5.1 ± 2.7
SR background prediction	630.4 ± 52.6	36.3 ± 5.9
Data Events	–	38

Table 6.10: Predicted and observed event yield in the signal region without and with correction applied to W+jets, $t\bar{t}$ and QCD background.

also contains the statistical uncertainties from the CR and MC simulated event samples. Figure 6.37 shows the distributions for N_{jet}, p_{T}, E_{T}^{miss}, $m_T(\tau, E_{\mathrm{T}}^{miss})$, and m_{jj} for data and MC in the SR.

6.9 Systematics Uncertainties

Table 6.11 represents the systematics for all channels (e, μ, τ_h) that have been used for this analysis. The brief discussion is also given below.

Source	QCD	W	DY	$t\bar{t}$	VV	Signal
channel:	inv., e, μ, τ_h	inv., e, μ, τ_h	inv., e, μ, τ_h	inv., e, μ, τ_h	inv., e, μ, τ_h	inv., e, μ, τ_h
Lumi	L,L,L,L	L,L,L,L	L,L,L,L	L,L,L,L	L,L,L,L	L,L,L,L
μ ID	–,–,–,–	< 1,< 1,2,< 1	< 1,< 1,2,1	< 1,< 1,2,1	< 1,< 1,2,1	1,1,3,1
e ID	–,–,–,–	< 1,2,< 1,< 1	< 1,2,< 1,1	< 1,2,< 1,1	< 1,2,< 1,1	1,3,1,1
τ_h ID	–,–,–,–	1,1,1,6	1,1,1,8	1,1,1,9	1,1,1,9	2,2,2,9
Trigger	3,3,3,3	3,3,3,3	3,3,3,3	3,3,3,3	3,3,3,3	3,3,3,3
b ID	1,1,1,1	1,1,1,1	1,1,1,1	7,7,7,7	1,1,1,1	1,1,1,1
JES	s,s,s,s	s,s,s,s	s,s,s,s	s,s,s,s	s,s,s,s	s,s,s,s
TES	s,s,s,s	s,s,s,s	s,s,s,s	s,s,s,s	s,s,s,s	s,s,s,s
MMS	< 1,< 1,< 1,< 1	< 1,< 1,< 1,< 1	< 1,< 1,< 1,< 1	< 1,< 1,< 1,< 1	< 1,< 1,< 1,< 1	< 1,< 1,< 1,< 1
EES	< 1,< 1,< 1,< 1	< 1,< 1,< 1,< 1	< 1,< 1,< 1,< 1	< 1,< 1,< 1,< 1	< 1,< 1,< 1,< 1	< 1,< 1,< 1,< 1
pdf	–,–,–,–	4.8,4.8,4.8,4.8	4.2,4.2,4.2,4.2	4.2,4.2,4.2,4.2	3.5,3.5,3.5,3.5	6.5,6.5,6.5,6.5
scale	–,–,–,–	1,1,1,1	1,1,1,1	3.5,3.5,3.5,3.5	–,–,–,–	2,2,2,2
bin-by-bin stat.	s,s,s,s	s,s,s,s	s,s,s,s	s,s,s,s	s,s,s,s	s,s,s,s
Closure+Norm.	10,–,–,22	10,13,11,13	10,8,8,8	–,33,26,42	–,–,–,–	–,–,–,–

Table 6.11: Summary of systematic uncertainties. Values are given in percent. "s" indicates template variations ("shape" uncertainties). L = 2.5%.

- **Luminosity:** There is a 2.5% uncertainty on the measured CMS luminosity [15] which is examined 100% correlated across MC based backgrounds and

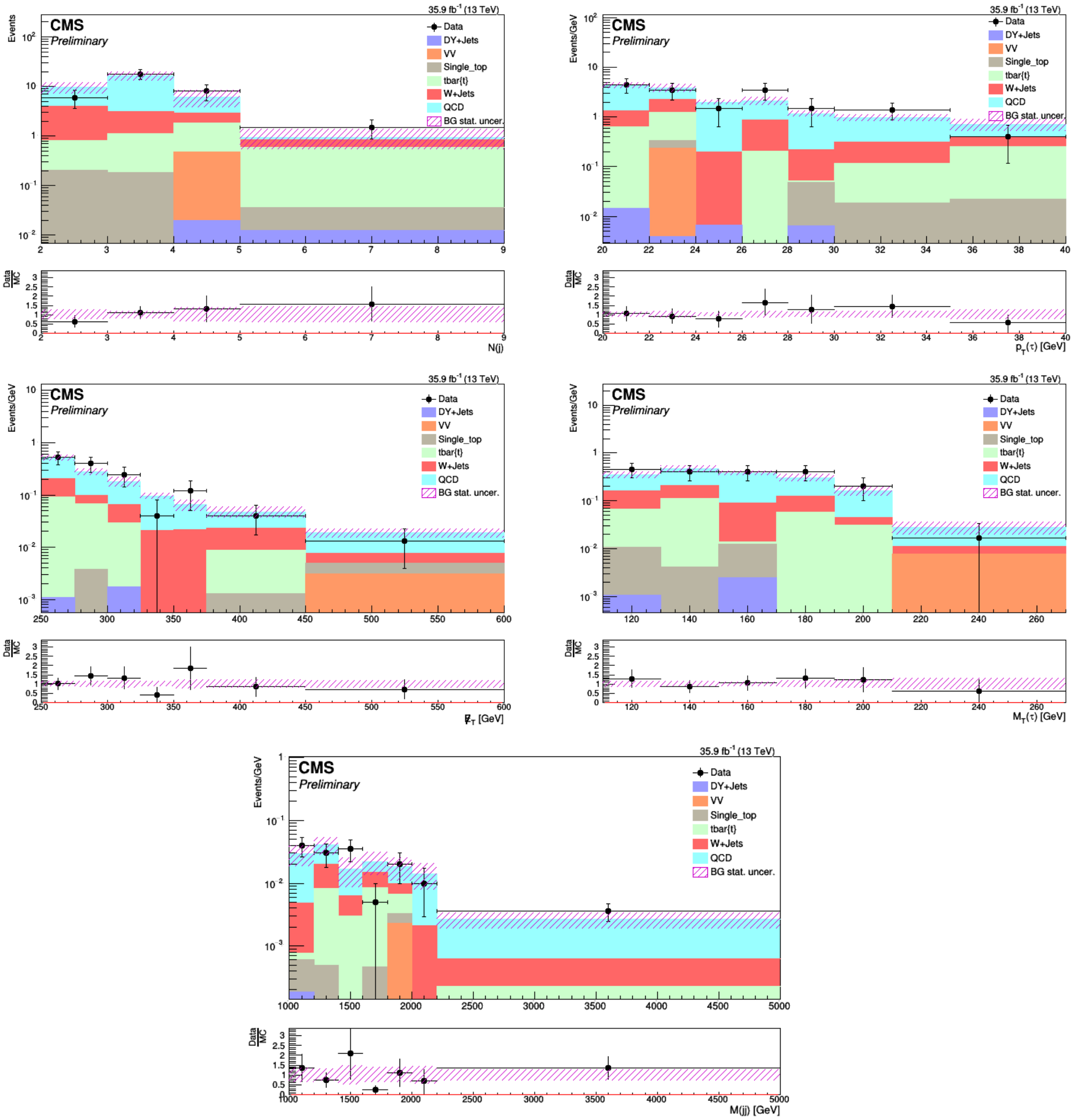

Figure 6.37: (a) N_{jet}, (b) pt, (c) E_{T}^{miss}, (d) $m_T(\tau, E_{\mathrm{T}}^{miss})$ (e) m_{jj} distributions in the SR. The SF obtained from the W+jets, $t\bar{t}$ and QCD are applied on respective backgrounds.

signal within a channel.

- **Parton Distribution Function:** We are also considering the uncertainty due to the variations in parton distribution functions [16] as shown in Table 6.11.
- **Trigger, Reconstruction, and Selection:** An overall 3% systematic uncertainty is applied on the trigger efficiency due to the uncertainty on the fit to the trigger turn-on curve at the plateau $E_T^{miss} > 250$ GeV. The trigger

uncertainty is considered 100% correlated across MC based estimates within a channel.

- ***b*-Tagging Efficiency:** We consider the uncertainty on the mis-tag rate as measured by the b-tagging POG [17,18] ($\approx 10\%$). For the case of our signal, the systematic uncertainty on the requirement of 0 jets mis-tagged as b-jets is determined by propagating the 10% uncertainty on the mis-tag rate through the following Equation (which represents the signal efficiency for requiring 0 jets mis-tagged as b-Jets):

$$\epsilon^{\mathrm{NBtag}<1} = 1 - \sum_{n=1} P(n) \cdot \sum_{m=1}^{n} C(n,m) \cdot f^{m} \cdot (1-f)^{n-m} \tag{6.14}$$

where $P(n)$ is the probability to obtain n additional jets (non-tau and non-lepton) in the event, $C(n,m)$ the combinatorial of n choose m and f the mis-tag rate. The probability to obtain at least one additional jet in the event is $\sim$ 10%. Therefore, based on the above equation, the mis-tag rate and uncertainty, and the probability to obtain at least one additional jet we calculate a systematic effect of $\sim$ 1% on our signal due to the mis-tag rate. The b-tagging/mis-tagging systematics are considered 100% correlated across MC based backgrounds with similar composition (e.g. W+jets and DY+jets where there are typically no real b-jets), but completely uncorrelated to backgrounds that have different composition (e.g. $t\bar{t}$ vs. DY+jets). We note the b-tagging uncertainties are evaluated on a per-event basis, following the POG recommendation and as referenced in the object reconstruction section.

- **Tau Identification:** The 6% uncertainty on the τ_h identification is taken into consideration as recommended by the tauPOG [19,20].

- **Tau Energy Scale (TES):** We consider the effect of the 5% tau energy scale uncertainty measured by the tau POG on the signal acceptance. For example, the tau four-momentum is scaled by a factor of $k = 1.05$ or 0.95 ($p_{smeared} = k \cdot p_{default}$) and variables are recalculated using $p_{smeared}$. We find that by using $p_{smeared}$ calculated with a factor of $k = \pm 1.05$ or 0.95, the signal and MC based backgrounds fluctuate by up to $\sim$ 8%. We note that since this is a shape based analysis of m_T, the bin-by-bin uncertainty (i.e. shape uncertainties) due to TES are considered in the limit calculations. This is represented by a "s" in the systematics table.

- **Jet Energy Scale (JES):** We consider the effect of a 3-5% jet energy scale uncertainty on the signal acceptance (depending on the η and p_T of the considered jet as prescribed by the JetMET *POG*) [25]. For example, for a 5% JES uncertainty, the jet four-momentum is scaled by a factor of $k = 1.05$ or 0.95 ($p_{smeared} = k \cdot p_{default}$) and variables are recalculated using $p_{smeared}$. We find that by using $p_{smeared}$ calculated with a factor of ranging from $k = \pm 1.05$ to 0.95 (i.e. 3-5% depending on η and p_T), the signal and MC based backgrounds fluctuate by up to $\sim$ 14%. We note that since this is a shape based analysis of m_T, the bin-by-bin uncertainty (i.e. shape uncertainties) due to JES are considered in the limit calculations. This is represented by a "s" in the systematics table.

- **MET:** The uncertainty on MET for our signal process is driven by the tau energy scale (TES), jet energy scale (non-tau jets) (JES), light lepton energy/momentum scale (LES), and unclustered energy (UCE) as per official recommendation. The systematic effect from MET due to TES, JES and LES is included in the JES, TES, LES systematic uncertainties described above. We find that 10% uncertainty on unclustered energy results in at most a 1.0% fluctuation on the signal acceptance and MC-based background predictions.

- **Pileup:** We have followed the recommendation for pileup corrections and used a 69.2 mb minbias cross section. We have considered the official recommendation to determine systematic uncertainty due to pileup. The official recommendation is to vary the minbias cross section by 5% and re-derive pileup weights. Using the new weights with ±5% in the minbias cross section results in at most a 2% change in the signal and MC-based background yields over the full mass range.

- **Background Estimates:** The uncertainty on the data-driven background estimations are driven by the statistics in data in the various control samples and the statistics in the MC samples as discussed in Section 6.7. In cases where MC based backgrounds must be subtracted off, the uncertainties in the MC backgrounds due to the above listed systematic uncertainties are propagated throughout the subtraction and used to assign a systematic uncertainty on the background prediction. For example, the cross section uncertainty on backgrounds (see "pdf" row of Table 6.11) that are subtracted off in the CRs is propagated throughout and contributes to the systematic uncertainty on the background prediction of interest. The "Closure+Norm" row represents the uncertainty in the background prediction due to the extracted data-to-MC SFs in control regions or the transfer factors used to derive full data-driven estimates. Since the W+jets and Z+jets background processes have similar VBF selection efficiency (as described in the background estimation section), the uncertainty on the W+jets SF is also used to assign "Closure+Norm" systematic uncertainty on the DY background. In summary, the systematic uncertainties range from 8-42%, depending on the background. The "bin-by-bin stat." row represents the uncertainty on the MC yield (which is corrected with data-driven scale factors). This stat uncertainty is treated as a bin-by-bin shape uncertainty in the combine tool.

- **Generator scale variations on signal acceptance:** These uncertainties are found to be small for both signal (2%) and backgrounds (1% for W/Z and 3.5% for $t\bar{t}$).

6.10 Comparison between τ_h, e, μ and 0-lepton (invisible) Channels

The author of this Thesis has analyzed the final state VBF $\tau_h + jj + E_{\mathrm{T}}^{miss}$, but CMS Collaboration decided to make a combined paper for publication with single 1-lepton channel and 0-lepton channel, so the same methodology (as of τ_h channel) have been followed for electron and muon channels which have been analyzed by other members of the group in CMS Collaboration. All the selections (central and VBF) for each channel are summarized in Table 6.16. Figure 6.38 shows the final plots from SR for all three leptonic (e, μ and τ_h) and invisible (0-lepton) channels. Invisible channel refers to the case where no produced leptons get reconstructed either because of very low p_{T} of the leptons or less energy to be reconstructed by the detector. For an invisible channel, variable to be used in the search region is m_{jj}, because of the unavailability of the reconstructed lepton to do a m_T based shape analysis. The invisible channel is expected to give a signal in compressed mass scenarios where the mass difference between chargino and neutralino (LSP) is very less ($\Delta m = m_{\tilde{\chi}_1^{\pm}} - m_{\tilde{\chi}_1^0} < 10$ GeV). Table 6.12 shows the selection criteria used for the invisible channel in SR.

The τ_h channel is different than e and μ channels because of domination of QCD multijet background as QCD is negligible for e and μ channel. QCD multijet background comes into existence because of jet → τ fake rate as τ is reconstructed from its hadronic tau. Unfortunately, we do not observe any excess of data over SM backgrounds in neither muon, electron, tau nor invisible channel. Thus, we set 95% CL exclusion limits with the analyzed data on the SUSY VBF signal which is

Basic selection	Muon veto	$p_T(\mu) > 8$ GeV $\vert\eta(\mu)\vert < 2.5$ Tight ID Isolation: $I < 0.25$
	Electron veto	$p_T(e) > 10$ GeV $\vert\eta(e)\vert < 2.5$ Medium ID
	Tau veto	$p_T(\tau_h) > 20$ GeV $\vert\eta(\tau_h)\vert < 2.5$ 1 prong $\Delta R(\tau_h, \mu\,\mathrm{or}\,e) > 0.3$
	Jets definition	$p_T(j) > 60$ GeV $\vert\eta(j)\vert < 5$ Loose ID $N(j) \geq 2$
	b-tagged jets veto $N(b) = 0$	$p_T(b) > 30$ GeV $\vert\eta(b)\vert < 2.4$ CSV Medium WP
p_T^{miss} criterion		$p_T^{\mathrm{miss}} > 250$ GeV
VBF		$\eta(j_1)\eta(j_2) < 0$ $\vert\Delta\eta(j_1, j_2)\vert > 3.8$ $M(j_1, j_2) > 1$ TeV
QCD rejection		$\vert\Delta\phi(p_T^{\mathrm{miss}}, j_2)\vert > 0.5$

Table 6.12: Signal region selection for invisible channel.

described briefly in the next Section. Table 6.13 summarizes the entire study for raw MC events, final expected background events and the SF from each estimated background to correct MC mismodeling of central selections and VBF selections.

6.11 Result and Interpretation

This analysis has been performed in the context of R-parity conserving Minimal Supersymmetric Standard Model (MSSM) for pure electroweak production of chargino and neutralino as discussed in Chapter 1. The analysis has been carried out as a shape-based analysis by fitting the data to the predicted $m_T(\tau, E_{\mathrm{T}}^{miss})$ or dijet mass spectrum for 1-lepton or 0-lepton channel, respectively. The $m_T(\tau, E_{\mathrm{T}}^{miss})$ distribution has been used as the discriminating variable for 1-lepton channel. As explained earlier, in Figure 6.38, the data is found to be consistent with the SM background predictions taking account of statistical and systematic uncertainties.

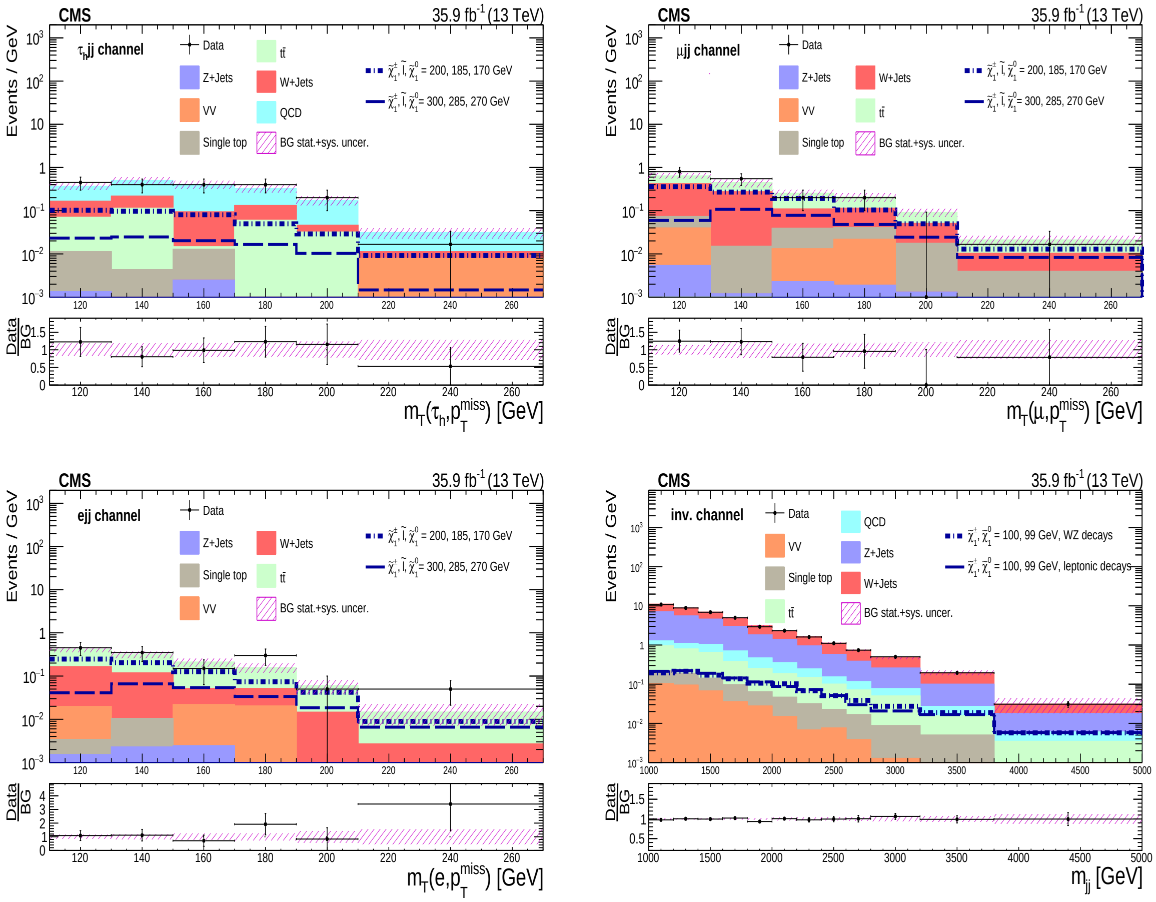

Figure 6.38: The observed m_T and m_{jj} distributions in the 1ℓjj (a–c) and 0ℓjj signal regions (d) compared with the SM background yields from the fit described in the text. The last bin in the m_T distributions of the 1ℓjj channels include all events with $m_T > 210$ GeV. The last bin of the m_{jj} distributions of the 0ℓjj channel include all events with $m_{jj} > 3800$ GeV.

So the upper limit using m_T/m_{jj} shapes has been set on the production cross section of chargino ($\tilde{\chi}_1^{\pm}$) and neutralino ($\tilde{\chi}_2^0$) pairs produced along with two forward jets. We have considered models with a bino-like $\tilde{\chi}_1^0$ (neutralino i.e. LSP), wino-like $\tilde{\chi}_2^0$ (second lightest neutralino) and $\tilde{\chi}_1^{\pm}$ (lightest chargino). Also, $\tilde{\chi}_1^{\pm}$ and $\tilde{\chi}_2^0$ are assumed as mass-degenerate because they belong to the same gauge group multiplet. Therefore, the final results are presented as a function of mass of these degenerate particles ($m_{\tilde{\chi}_1^{\pm}}$, $m_{\tilde{\chi}_2^0}$) and LSP mass ($m_{\tilde{\chi}_1^0}$). The final results have been evaluated in terms of two scenarios: (i) the "light slepton" model where $\widetilde{\ell}$ is the next-to-lightest

SUSY particle, (*ii*) the “WZ” model where sleptons are too heavy and thus $\widetilde{\chi}_1^{\pm}$ and $\widetilde{\chi}_2^0$ decays proceed via W^* and Z^*. The main difference between the two models is the branching ratio of $\widetilde{\chi}_1^{\pm}$ and $\widetilde{\chi}_2^0$ to leptonic final states. The top left of Figure 6.1 shows the model with democratic slepton decay where the mass $m_{\tilde{l}}$ of the intermediate slepton is parameterized in terms of a variable $x_{\tilde{l}}$ as:

$$m_{\tilde{\ell}} = m_{\tilde{\chi}_1^0} + x_{\tilde{\ell}}(m_{\tilde{\chi}_1^{\pm}} - m_{\tilde{\chi}_1^0}) \tag{6.15}$$

where $0 < x_{\tilde{\ell}} < 1$. The presented results are for $x_{\tilde{\ell}} = 0.5$ in the “$\tilde{\ell}$-democratic” model where all three sleptons ($m_{\tilde{\ell}} = m_{\tilde{e}} = m_{\tilde{\mu}} = m_{\tilde{\tau}_1}$) are light. The results are interpreted by considering the fact that $Br(\tilde{\chi}_2^0 \to \ell\tilde{\ell} \to \ell\ell\tilde{\chi}_1^0) = 100\%$, $Br(\tilde{\chi}_1^{\pm} \to \nu\tilde{\ell} \to \nu\ell\tilde{\chi}_1^0) = 100\%$. To highlight the evolution of the search sensitivity for compressed spectra with mass gap $\Delta m = m_{\tilde{\chi}_1^{\pm}} - m_{\tilde{\chi}_1^0}$, values between $\Delta m = 1$ and 50 GeV are studied.

The calculation of the exclusion limit is obtained by using the m_T or m_{jj} distribution in each channel (m_T in 1$l$jj and m_{jj} in 0$l$jj) to construct a combined profile likelihood ratio test statistics [26] in bins of m_T/m_{jj} and computing a 95% confidence level (CL) upper limit (UL) on the signal cross section using the asymptotic CL$_s$ criterion [27, 28]. Systematic uncertainties are taken into account as nuisance parameters, which are removed by profiling, assuming gamma function or log-normal priors for normalization parameters, and Gaussian priors for mass spectrum shape uncertainties. The combination of the four search channels require simultaneous analysis of the data from the individual channels, accounting for all statistical and systematic uncertainties and their correlations. Correlation among backgrounds, both within a channel and across channels, are taken into considerations for the limit calculation. For example, the uncertainty in the integrated luminosity is treated as fully correlated across channels. The uncertainties from the closure tests are treated as uncorrelated within and across the different final states. Figure 6.39 shows the expected and observed limits as well as the theoretical cross section as functions of $m_{\tilde{\chi}_1^\pm}$ for $\Delta m = 1$ and 50 GeV assumptions in the light slepton model. Because of the democratic sleptons decay model, the single-τ_h channel produces the lowest signal sensitivity (i.e. branching ratio $\tau \rightarrow \tau_h$ effects plus softer average $p_T(\tau_h)$ due to τ decays to neutrinos). For the smallest value of $\Delta m = 1$ GeV, the 0ℓjj channel provides the best sensitivity, while the VBF soft-e and soft-μ channels provide the best sensitivity for the larger mass gap scenario with $\Delta m = 50$ GeV. Figure 6.40

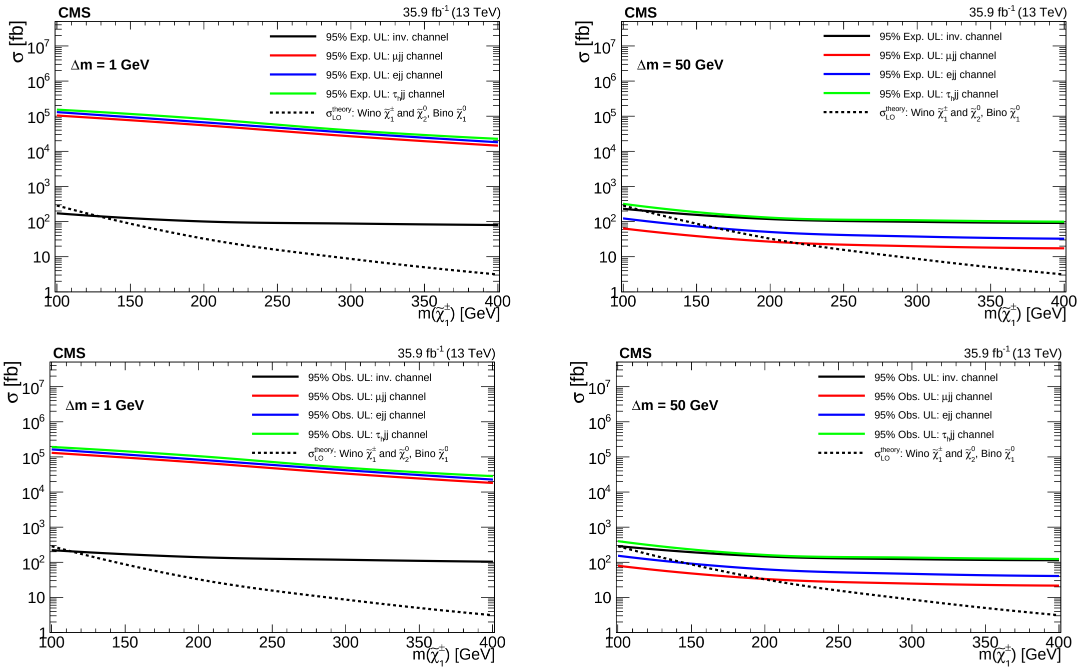

Figure 6.39: Combined 95% CL upper limit on the cross section as a function of $m_{\tilde{\chi}_1^\pm} = m_{\tilde{\chi}_2^0}$. The results correspond to $\Delta m = 1$ GeV (left) and $\Delta m = 50$ GeV (right) mass gaps between the chargino and the lightest neutralino. The Top row shows the expected limits and the bottom row shows the observed limits.

shows the expected and observed limits as well as the theoretical cross section as functions of $m_{\tilde{\chi}} = m_{\tilde{\chi}_2^0} = m_{\tilde{\chi}_1^\pm}$ for the combination of the VBF invisible and soft-lepton channels. Final exclusion limit plots are combined for all four channels and shown in Figure 6.41. Figure 6.41 (left) shows the 95% CL upper limit on the signal cross section as a function of $m(\widetilde{\chi}_1^\pm)$ and Δm, assuming $x_{\widetilde{\ell}} = 0.5$. Figure 6.41 (right) shows the 95% CL upper limit on the signal cross section, as a function of $m(\widetilde{\chi}_1^\pm)$, for two fixed Δm values of 1 and 30 GeV, and assuming $x_{\widetilde{\ell}} = 0.5$. The signal accep-

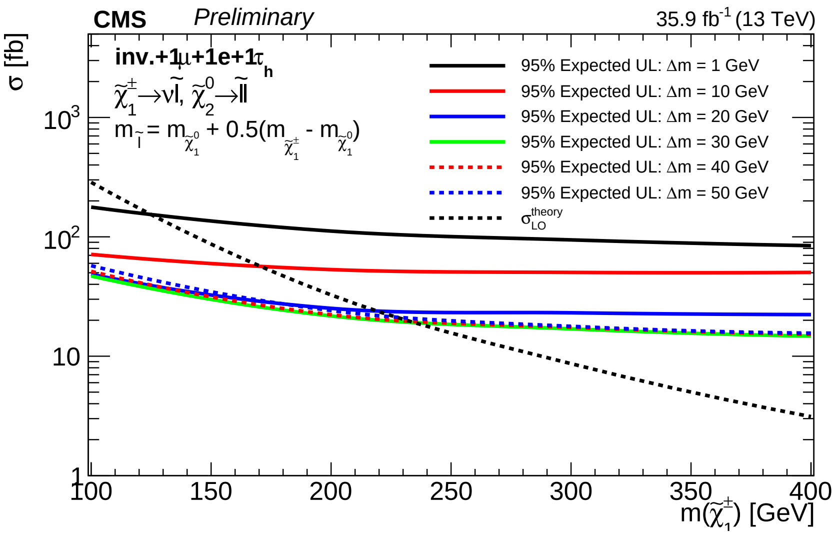

Figure 6.40: Combined limits for all four channels.

tance and mass shape are evaluated for each $\{m(\widetilde{\chi}_1^{\pm}), \Delta m\}$ combination and used in the limit calculation procedure described above. For the $\Delta m = \{1, 10, 30, 50\}$ GeV assumption, we have observed (expected) the exclusion on $\widetilde{\chi}_1^{\pm}/\widetilde{\chi}_2^0$ gaugino masses below $\{112, 159, 215, 207\}$ ($\{125, 171, 235, 228\}$) GeV for the combination of the four channels. For the compressed mass spectrum scenarios with $1 \leq \Delta m \leq 30$ GeV, the bounds on the $\widetilde{\chi}_1^{\pm}/\widetilde{\chi}_2^0$ gaugino masses are the most stringent to date. It is clear that for the $1 < \Delta m < 10$ GeV mass gaps considered in this analysis, the exclusions on $m(\widetilde{\chi}_1^{\pm})$ do not depend on the assumption that a light slepton exists (i.e. $m(\widetilde{\chi}_0^{\pm}) < m_{\widetilde{\ell}} < m(\widetilde{\chi}_1^{\pm})$). For $1 < \Delta m < 10$ GeV, the light slepton model and WZ model grant the same signal acceptance. For example, Figure 6.38(d) shows the expected m_{jj} signal distribution when the decays of the charginos and neutralinos proceed via W and Z bosons, resulting in a similar shape and normalization as the expectation for the light slepton scenario. However, the scenario changes for increasing values of Δm where $1l$jj channel becomes sensitive and limits are less stringent for WZ model as compared to light slepton model. This difference is the outcome of lower branching ratio of $\widetilde{\chi}_1^{\pm}/\widetilde{\chi}_2^0$ to leptonic final states in the WZ model. Fig-

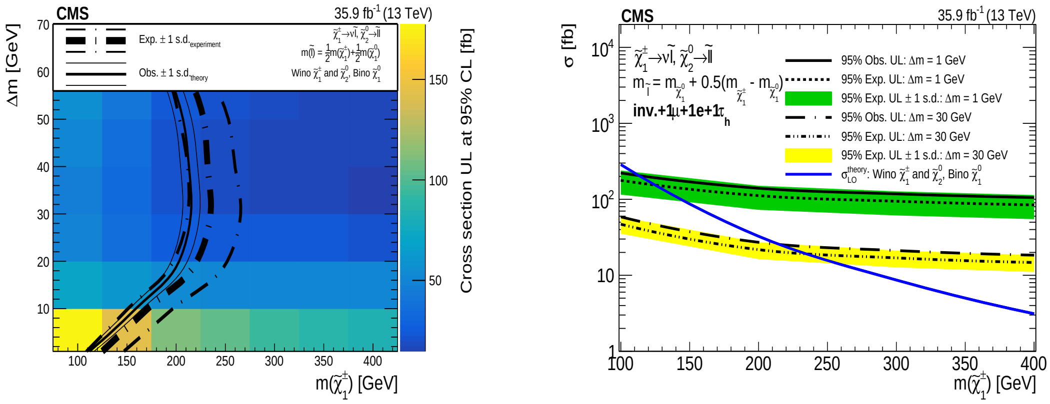

Figure 6.41: (Left) Expected and observed 95% confidence level UL on the signal cross section as a function of $m(\tilde{\chi}_1^\pm)$ and Δm, assuming the light slepton model with $x_{\tilde{\ell}} = 0.5$. (Right) Combined 95% CL upper limit on the cross section as a function of $m_{\tilde{\chi}_1^\pm} = m_{\tilde{\chi}_2^0}$ for $\Delta m = 1$ GeV and $\Delta m = 30$ GeV mass gaps between the chargino and the neutralino, assuming the light slepton model.

ure 6.42 shows the 95% CL upper limit assuming the WZ model on the signal cross section (left) as a function of $m(\tilde{\chi}_1^\pm)$ and Δm and (right) as a function of $m(\tilde{\chi}_1^\pm)$, for two fixed Δm values of 1 and 30 GeV. For the $\Delta m = \{1, 10, 30, 50\}$ GeV assumption, we have observed (expected) the exclusion on $\tilde{\chi}_1^\pm/\tilde{\chi}_2^0$ gaugino masses below $\{112, 146, 175, 162\}$ ($\{125, 160, 194, 178\}$) GeV. For the compressed mass spectrum scenarios with $1 \leq \Delta m < 5$ GeV and $25 \leq \Delta m < 50$ GeV, the bounds on the $\tilde{\chi}_1^\pm/\tilde{\chi}_2^0$ gaugino masses are also the most stringent to date.

Hence, to compile this Chapter, the present analysis has been performed for the search of noncolored SUSY particles in single hadronic tau final state using 35.87 fb^{-1} 2016 data collected with CMS detector at center-of-mass energy 13 TeV. These results are published in the *Journal of High Energy Physics* [29]. The VBF topology requires two well-separated jets that appear in opposite detector hemispheres, with large invariant mass m_{jj}. SUSY searches through VBF processes provide a complementary tool to probe compressed mass spectra scenarios which is otherwise difficult through direct searches. Also, $0ljj$ final state is the first-ever search for compressed electroweak SUSY sector. Since the data agree well within SM background predictions in the search bins of m_{jj} and $m_T(\tau, E_{\mathrm{T}}^{miss})$, no SUSY and New

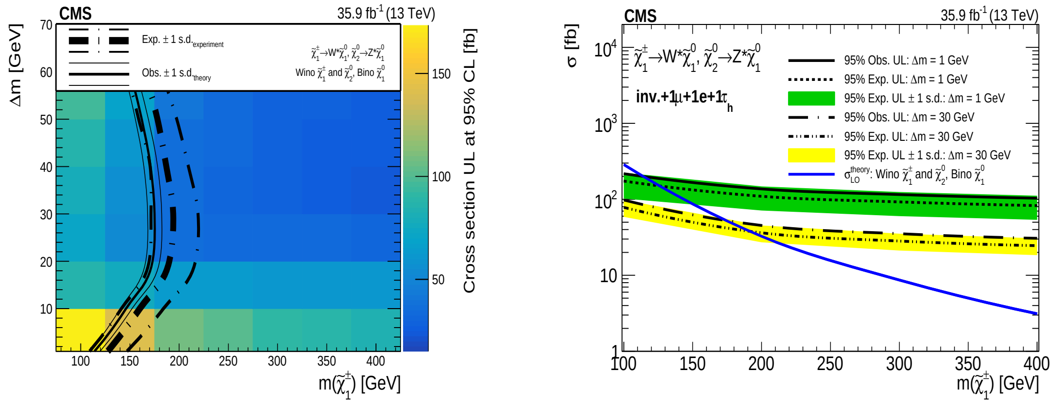

Figure 6.42: (Left) Expected and observed 95% confidence level UL on the signal cross section as a function of $m(\tilde{\chi}_1^{\pm})$ and Δm, assuming the $\tilde{\chi}_1^{\pm}$ and $\tilde{\chi}_2^0$ decays proceed via W^* and Z^*. (Right) Combined 95% CL upper limit on the cross section as a function of $m_{\tilde{\chi}_2^0} = m_{\tilde{\chi}_1^{\pm}}$, for $\Delta m = 1$ GeV and $\Delta m = 30$ GeV mass gaps between the chargino and the neutralino, assuming the $\tilde{\chi}_1^{\pm}$ and $\tilde{\chi}_2^0$ decays proceed via W^* and Z^*.

Physics signature has been revealed. However, exclusion limits at 95% CL are set on the masses of $\tilde{\chi}_1^{\pm}/\tilde{\chi}_2^0$. In compressed mass spectra scenario, for the sleptons model, masses of $\tilde{\chi}_1^{\pm}/\tilde{\chi}_2^0$ are excluded up to 112 (215) GeV for $\Delta m(m_{\tilde{\chi}_1^{\pm}} - m_{\tilde{\chi}_1^0}) =$ 1 (30) GeV and for W^* and Z^* model, masses up to 112 (175) GeV are excluded for $\Delta m(m_{\tilde{\chi}_1^{\pm}} - m_{\tilde{\chi}_1^0}) = 1$ (30) GeV. The present analysis obtains the most stringent limit to date on the production of charginos and neutralinos decaying to leptons in compressed mass spectrum scenarios defined by the mass separation $1 \leq \Delta m < 5$ GeV and $25 \leq \Delta m < 50$ GeV.

VBF $jj + e + E_{\mathrm{T}}^{miss}$ channel				(No. of Events)
Sample	$N_{\mathrm{BG}}^{\mathrm{MC/Data}}$(SR/CR)	SF^{CR1} or TF_1	SF^{CR2} or TF_2	$N_{\mathrm{BG}}^{\mathrm{Data}}$
Diboson	1.1± 0.6	—	—	1.1 ± 0.6
QCD	$0^{+1.2}$	—	—	$0^{+1.2}$
Single Top	0.1± 0.1	—	—	0.1 ± 0.1
W + jets	5.3 ± 1.0	0.97 ± 0.10	1.18 ± 0.09	6.1 ± 1.4
DY + jets	0.1±0.0	—	—	0.1 ± 0.0
$t\bar{t}$	11.4± 2.1	1.17 ± 0.09	0.82 ± 0.26	10.9 ± 4.1
SR BG Prediction	18.0±2.4	—	—	18.3 ± 4.6
$m(\tilde{\chi}_1^{\pm}), m(\tilde{\ell}), m(\tilde{\chi}_1^0) = 200, 195, 190$ GeV	—	—	—	14.2 ± 0.4
$m(\tilde{\chi}_1^{\pm}), m(\tilde{\ell}), m(\tilde{\chi}_1^0) = 200, 185, 170$ GeV	—	—	—	37.3 ± 0.7
$m(\tilde{\chi}_1^{\pm}), m(\tilde{\ell}), m(\tilde{\chi}_1^0) = 200, 175, 150$ GeV	—	—	—	36.5 ± 0.7
$m(\tilde{\chi}_1^{\pm}), m(\tilde{\ell}), m(\tilde{\chi}_1^0) = 300, 295, 290$ GeV	—	—	—	3.4 ± 0.1
$m(\tilde{\chi}_1^{\pm}), m(\tilde{\ell}), m(\tilde{\chi}_1^0) = 300, 285, 270$ GeV	—	—	—	12.2 ± 0.2
$m(\tilde{\chi}_1^{\pm}), m(\tilde{\ell}), m(\tilde{\chi}_1^0) = 300, 275, 250$ GeV	—	—	—	13.1 ± 0.2
Data Events	Unblinded	—	—	29

VBF $jj + \mu + E_{\mathrm{T}}^{miss}$ channel				(No. of Events)
Sample	$N_{\mathrm{BG}}^{\mathrm{MC/Data}}$(SR/CR)	SF^{CR1} or TF_1	SF^{CR2} or TF_2	$N_{\mathrm{BG}}^{\mathrm{Data}}$
Diboson	1.3 ± 0.6	—	—	1.3 ± 0.6
QCD	$0^{+0.2}$	—	—	$0^{+0.2}$
Single Top	2.3 ± 0.7	—	—	2.3 ± 0.7
W + jets	10.2 ± 2.1	1.10 ± 0.10	1.18 ± 0.09	13.2 ± 3.1
DY + jets	0.2 ± 0.1	—	—	0.2 ± 0.1
$t\bar{t}$	16.9± 2.6	0.97 ± 0.06	0.80 ± 0.20	13.1 ± 3.9
SR BG Prediction	30.9 ± 3.5	—	—	30.1 ± 5.1
$m(\tilde{\chi}_1^{\pm}), m(\tilde{\ell}), m(\tilde{\chi}_1^0) = 200, 195, 190$ GeV	—	—	—	26.2 ± 0.6
$m(\tilde{\chi}_1^{\pm}), m(\tilde{\ell}), m(\tilde{\chi}_1^0) = 200, 185, 170$ GeV	—	—	—	52.4 ± 0.8
$m(\tilde{\chi}_1^{\pm}), m(\tilde{\ell}), m(\tilde{\chi}_1^0) = 200, 175, 150$ GeV	—	—	—	47.2 ± 0.7
$m(\tilde{\chi}_1^{\pm}), m(\tilde{\ell}), m(\tilde{\chi}_1^0) = 300, 295, 290$ GeV	—	—	—	6.6 ± 0.1
$m(\tilde{\chi}_1^{\pm}), m(\tilde{\ell}), m(\tilde{\chi}_1^0) = 300, 285, 270$ GeV	—	—	—	17.9 ± 0.2
$m(\tilde{\chi}_1^{\pm}), m(\tilde{\ell}), m(\tilde{\chi}_1^0) = 300, 275, 250$ GeV	—	—	—	17.0 ± 0.2
Data Events	Unblinded	—	—	36

VBF $jj + \tau_h + E_{\mathrm{T}}^{miss}$ channel				(No. of Events)
Sample	$N_{\mathrm{BG}}^{\mathrm{MC/Data}}$(SR/CR)	SF^{CR1} or TF_1	SF^{CR2} or TF_2	$N_{\mathrm{BG}}^{\mathrm{Data}}$
Diboson	0.5 ± 0.4	—	—	0.5 ± 0.4
QCD	619.9 ± 52.6	0.037 ± 0.008	—	23.1 ± 5.0
Single Top	0.5 ± 0.2	—	—	0.5 ± 0.2
W + jets	5.7 ± 1.1	1.04 ± 0.13	1.18 ± 0.09	7.0 ± 1.7
DY + jets	0.1 ± 0.1	—	—	0.1 ± 0.1
$t\bar{t}$	3.7± 1.2	1.06 ± 0.19	1.3 ± 0.5	5.1 ± 2.7
SR BG Prediction	10.5 ± 1.7	—	—	36.3 ± 5.9
$m(\tilde{\chi}_1^{\pm}), m(\tilde{\ell}), m(\tilde{\chi}_1^0) = 200, 195, 190$ GeV	—	—	—	0.38 ± 0.07
$m(\tilde{\chi}_1^{\pm}), m(\tilde{\ell}), m(\tilde{\chi}_1^0) = 200, 185, 170$ GeV	—	—	—	2.5 ± 0.2
$m(\tilde{\chi}_1^{\pm}), m(\tilde{\ell}), m(\tilde{\chi}_1^0) = 200, 175, 150$ GeV	—	—	—	4.3 ± 0.2
$m(\tilde{\chi}_1^{\pm}), m(\tilde{\ell}), m(\tilde{\chi}_1^0) = 300, 295, 290$ GeV	—	—	—	0.085 ± 0.02
$m(\tilde{\chi}_1^{\pm}), m(\tilde{\ell}), m(\tilde{\chi}_1^0) = 300, 285, 270$ GeV	—	—	—	0.74 ± 0.05
$m(\tilde{\chi}_1^{\pm}), m(\tilde{\ell}), m(\tilde{\chi}_1^0) = 300, 275, 250$ GeV	—	—	—	1.4 ± 0.07
Data Events	Unblinded	—	—	38

Table 6.13: Predicted and observed rates in the signal region. As an example, the $t\bar{t}$ prediction is $N_{t\bar{t}}^{\mathrm{Data}} = N_{t\bar{t}}^{\mathrm{MC}}(\mathrm{SR\ cuts}) \cdot SF^{\mathrm{CR1}} \cdot SF^{\mathrm{CR2}}$.

Bibliography

[1] The CMS Collaboration, "Search for supersymmetry in pp collisions at $\sqrt{s}$=8 TeV in events with a single lepton, large jet multiplicity, and multiple b jets", *Phys. Lett. B*, vol. 733, (2014), https://doi.org/10.1016/j.physletb.2014.04.023.

[2] Farrar, Glennys R. and Fayet, Pierre, "Phenomenology of the production, decay, and detection of new hadronic states associated with supersymmetry ", *Phys. Lett. B*, vol. 76 (1978), http://dx.doi.org/10.1016/0370-2693(78)90858-4.

[3] The CMS Collaboration, "Combined search for electroweak production of charginos and neutralinos in proton-proton collisions at $\sqrt{s} = 13$ TeV", *JHEP*, vol. 03 (2018), http://dx.doi.org/10.1007/JHEP03(2018)160.

[4] The ATLAS Collaboration, "Search for the direct production of charginos and neutralinos in final states with tau leptons in $\sqrt{s} = 13$ TeV *pp* collisions with the ATLAS detector", *Eur. Phys. J. C*, vol. 78 (2018), http://dx.doi.org/10.1140/epjc/s10052-018-5583-9.

[5] The ATLAS Collaboration, "Search for electroweak production of supersymmetric states in scenarios with compressed mass spectra at $\sqrt{s} = 13$ TeV with the ATLAS detector", *Phys. Rev. D*, vol. 97 (2018), http://dx.doi.org/10.1103/PhysRevD.97.052010.

[6] The CMS Collaboration, "Search for new physics in events with two soft oppositely charged leptons and missing transverse momentum in proton-

proton collisions at $\sqrt{s} = 13$ TeV", *Phys. Lett. B*, vol. 782 (2018), http://dx.doi.org/10.1016/j.physletb.2018.05.062.

[7] B. Dutta et al., "Vector boson fusion processes as a probe of supersymmetric electroweak sectors at the lhc", *Phys. Rev. D*, vol. 87, (2013), https://doi.org/10.1103/PhysRevD.87.035029.

[8] The CMS Collaboration, "Search for supersymmetry in the vector-boson fusion topology in proton-proton collisions at $\sqrt{s} = 8$TeV", *JHEP*, vol. 11 (2015), http://dx.doi.org/10.1007/JHEP11(2015)189.

[9] Sjöstrand, Torbjorn and Ask, Stefan and Christiansen et al, "An introduction to PYTHIA 8.2", *Comput. Phys. Commun.*, vol. 191 (2015), http://dx.doi.org/10.1016/j.cpc.2015.01.024.

[10] Alwall, J. and Frederix, R. and Frixione, S. and Hirschi et al, "The automated computation of tree-level and next-to-leading order differential cross sections, and their matching to parton shower simulations", *JHEP*, vol. 07 (2014), http://dx.doi.org/10.1007/JHEP07(2014)079.

[11] Alioli, Simone and Nason, Paolo and Oleari, Carlo and Re, Emanuele, "NLO single-top production matched with shower in POWHEG s- and t-channel contributions", *JHEP*, vol. 09 (2009), http://dx.doi.org/10.1088/1126-6708/2009/09/111.

[12] Re, Emanuele, "Single-top Wt-channel production matched with parton showers using the POWHEG method", *Eur. Phys. J. C*, vol. 71 (2011), http://dx.doi.org/10.1140/epjc/s10052-011-1547-z.

[13] Czakon, Michał and Mitov, Alexander, "Top++: a program for the calculation of the top-pair cross-section at hadron colliders", *Comput. Phys. Commun.*, vol. 185 (2014), http://dx.doi.org/10.1016/j.cpc.2014.06.021.

[14] The CMS Collaboration, "Measurement of prompt J/ψ pair production in pp collisions at $sqrts = 7$ TeV", *JHEP*, vol. 09 (2014), http://dx.doi.org/10.1007/JHEP09(2014)094.

[15] The CMS Collaboration, "CMS luminosity measurements for the 2016 data-taking period", *CMS-PAS-LUM-17-001*, (2017), https://cds.cern.ch/record/2257069.

[16] The NNPDF Collaboration, "Parton distributions for the LHC Run II". *JHEP*, vol. 04 (2015), http://dx.doi.org/10.1007/JHEP04(2015)040.

[17] The CMS Collaboration, "Identification of heavy-flavour jets with the CMS detector in pp collisions at 13 TeV", *JINST*, vol. 13 (2018), http://dx.doi.org/10.1088/1748-0221/13/05/P05011.

[18] The CMS Collaboration, `https://twiki.cern.ch/twiki/bin/viewauth/CMS/BtagRecommendation`.

[19] The CMS Collaboration, "Reconstruction and identification of τ lepton decays to hadrons and ν_τ at CMS", *JINST*, vol. 11 (2016), http://dx.doi.org/10.1088/1748-0221/11/01/P01019.

[20] The CMS Collaboration, `https://twiki.cern.ch/twiki/bin/view/CMSPublic/SWGuidePFTauID`.

[21] The CMS Collaboration, "Performance of electron reconstruction and selection with the CMS detector in proton-proton collisions at $\sqrt{s} = 8$ TeV", *JINST*, vol. 10 (2015), http://dx.doi.org/10.1088/1748-0221/10/06/P06005.

[22] The CMS Collaboration, `https://twiki.cern.ch/twiki/bin/view/CMS/CutBasedElectronIdentificationRun2`.

[23] The CMS Collaboration, “Performance of the CMS muon detector and muon reconstruction with proton-proton collisions at $\sqrt{s} = 13$ TeV”, *JINST*, vol. 13 (2018), http://dx.doi.org/10.1088/1748-0221/13/06/P06015.

[24] The CMS Collaboration, `https://twiki.cern.ch/twiki/bin/view/CMS/SWGuideMuonIdRun2`.

[25] The CMS Collaboration, “Jet energy scale and resolution in the CMS experiment in pp collisions at 8 TeV”, *JINST*, vol. 12 (2017), http://dx.doi.org/10.1088/1748-0221/12/02/P02014.

[26] Cowan, Glen and Cranmer, Kyle and Gross, Eilam and Vitells, Ofer, “Asymptotic formulae for likelihood-based tests of new physics”, *Eur. Phys. J. C*, vol. 71 (2011), http://dx.doi.org/10.1140/epjc/s10052-011-1554-0.

[27] T. Junk, “Confidence level computation for combining searches with small statistics”, *Nucl. Instrum. Meth. A*, vol. 434 (1999), http://dx.doi.org/10.1016/S0168-9002(99)00498-2.

[28] Read, A. L., “Presentation of search results: the CL_s technique”, *J. Phys. G*, vol. 28 (2002), http://dx.doi.org/10.1088/0954-3899/28/10/313.

[29] The CMS Collaboration, “Search for supersymmetry with a compressed mass spectrum in the vector boson fusion topology with 1-lepton and 0-lepton final states in proton-proton collisions at $\sqrt{s} = 13$ TeV”, *JHEP*, vol. 08 (2019), http://dx.doi.org/10.1007/JHEP08(2019)150.

Chapter 7

Summary and Conclusions

The Standard Model (SM) which involves the fundamental particles and their interactions has 118 degrees of freedom and it explains most of the experimental observation in particle physics. However, some questions like the unification of forces, dark matter and dark energy absence, matter-antimatter asymmetry, and hierarchy problem are still unanswered. To solve these problems, many theories beyond the Standard Model (BSM) have been developed. Supersymmetry is one of the famous theories to solve these fundamental questions.

To discover small unknown particles, accelerators with higher energies are required, so in this regard, Large Hadron Collider (LHC), the world's most powerful accelerator has been built at CERN, Geneva, Switzerland. It is designed to operate at 14 TeV center-of-mass energy to explore SM physics as well as New Physics beyond the SM. The LHC's biggest achievement is the discovery of Higgs Boson in July 2012 by its two general-purpose detectors, Compact Muon Solenoid (CMS) and A Toroidal LHC AppratuS (ATLAS). After the discovery of Higgs boson, the main focus has been to search for superpartners of SM particles i.e. SUSY particles. The SUSY searches at LHC have achieved an exclusion limit on the gluinos and squarks mass up to the range of 1.9 TeV scale. However, limits on the electroweak sector are less constrained due to the low production cross section as compared to the colored sector. Hence, this is a possible window for LHC to explore New Physics.

This Thesis mainly reports two tasks: a) hardware work based on the aging study of Resistive Plate Chamber (RPC) detectors being used by CMS experiment b) Physics analysis for the search of SUSY particles using proton-proton collision data at 13 TeV with the CMS detector. The coming Sections contain a brief summary of these two tasks.

7.1 Aging Study of Resistive Plate Chambers

Compact Muon Solenoid (CMS) is mostly dedicated to the study related to muons as they act as the cleanest signal to explore New Physics signature. CMS muon system consists of various gas detectors like cathode strips chambers (CSC), drift tubes (DT), resistive plate chambers (RPC) and now during long shutdown (LS2), gas electrons multipliers (GEM) are going to be installed at the CMS experiment. RPCs are located in both barrel and endcap regions of the muon system covering pseudorapidity range up to $|\eta|$ =1.8 and provide good triggering and precise measurement of muon kinematics. Till now 1056 RPC chambers are located in the CMS muon system, but soon during long shutdown 3 (LS3), new chambers called improved RPC (*iRPC*) will be installed in the muon system covering up to $|\eta| = 2.4$. With the present luminosity accumulated so far, the RPCs are being operated with more than 97% efficiency. However, the integrated luminosity will increase five times more than the present luminosity 1×10^{34} to $5\times10^{34} cm^{-2}s^{-1}$ in the High-Luminosity LHC (HL-LHC) phase. So, it is very important to study the RPC detectors already placed in the muon system to check if they can sustain the huge amount of radiations during HL-LHC especially in the endcap region. The high radiation doze, mostly in the endcap region, can affect the RPC detector efficiency and accordingly muon identification which could be a challenge for the muon system.

The present RPC detectors that are already installed in CMS muon system have been checked for coming 10 years i.e. up to maximum background rates of 300 Hz/cm^2 and integrated charge (IC) of 50 mC/cm^2. However, at HL-LHC the background rates and IC will be much higher i.e. 600 Hz/cm^2 and 840 mC/cm^2, respectively (including safety factor of 3) and are different for RPC detectors compared to the time at their design. These harsher conditions could produce non-recoverable aging effects that can change the detector properties and performance.

So, to check the performance of current RPCs during HL-LHC, longevity or aging study is needed. Longevity study is performed in Gamma Irradiation Facility (GIF++) at CERN which is equipped with 13 TBq ^{137}Cs gamma source and a system of movable filters that allows to variate the gamma irradiation conditions same as of the HL-LHC. Hence it is possible to test real size RPC detectors in GIF++. For the longevity study, four endcap RPC detectors, two RE2/2 and two RE4/2 are placed in GIF++. Out of these four, one RE2/2 and one RE4/2 are continuously under radiations and the other two are turned on only from time to time and kept as a reference. The detector parameters like the dark current (current without background), noise rate are studied under different radiation conditions. The behaviour of dark current and noise rate is continuously monitored with increasing accumulated integrated charge. Till the time of writing this Thesis, IC of 650 mC/cm^2 and 362 mC/cm^2 is collected which means 77% and 43% of total IC (i.e. 840 mC/cm^2 - HL-LHC scenario) for RE2/2 and RE4/2 chambers, respectively. We have not observed any significant change in behaviour of these parameters with increasing IC so far. The study of detector current and rates with the background is also performed. To cancel out the effects of external parameters like gas humidity, temperature and pressure, the ratios of the irradiated and the reference RPC chambers are measured as a function of the integrated charge. Here also, we do not observe any degradation of current and rate for irradiated chambers with respect to the reference chambers.

Regarding, the performance of the RPC detector, time to time there is a muon test beam runs to check the efficiency, rates at detector working point for different irradiation conditions. The RPC detectors efficiency as a function of effective high voltage (voltage normalized at the standard temperature and pressure) is studied with and without background. Till now, the efficiency (98 %) is stable in time with a 2% decrease at the highest expected background rate i.e. 600 Hz/cm^2. This study has been published as "Longevity studies on the CMS-RPC system" in Journal of Instrumentation (JINST), volume 14 (2019).

7.2 Search for Supersymmetric Particles through Vector Boson Fusion (VBF) Processes at $\sqrt{s}$ = 13 TeV

The physics analysis "search for electroweakino particles (chargino and neutralino) through vector boson fusion (VBF) processes with proton-proton collision data having integrated luminosity of 35.87 fb^{-1} collected with the CMS detector at a center-of-mass energy 13 TeV" is presented in this Thesis. The R-parity conserving Minimal Supersymmetric Standard Model (MSSM) has been used to interpret the upper limits on the mass of charginos ($\tilde{\chi}_1^{\pm}$) and neutralinos ($\tilde{\chi}_2^0$) and both these SUSY particles are assumed as mass degenerate. In the VBF processes, two incoming partons fused together to produce pairs of chargino and neutralino along with two high p_{T} jets in the forward direction having large dijet invariant mass and large pseudorapidity gap. The chargino decay proceed as $\tilde{\chi}_1^{\pm} \rightarrow \tilde{l}^{\pm}\nu_l \rightarrow l\tilde{\chi}_1^0\nu_l$ and neutralino decay chain is: $\tilde{\chi}_2^0 \rightarrow \tilde{l}^{\pm}l^{\mp} \rightarrow ll^{\mp}\tilde{\chi}_1^0$. As a result, in VBF processes, we have multilepton, two VBF jets, E_{T}^{miss} due to neutrinos and lightest supersymmetric particle (LSP) in the final state. However, the analysis reported in this Thesis consists of single hadronic tau (τ_h), VBF jets, and E_{T}^{miss}. The LSP is considered as *bino* like and chargino and neutralino are *wino* like SUSY particles. Event selection criteria is divided into two parts: Central selections and VBF selections. The central selections consists of well reconstructed hadronic tau having $20 < p_T < 40$ GeV and $|\eta| < 2.1$, $E_{\mathrm{T}}^{miss} > 250$ GeV and $m_T(\tau, E_{\mathrm{T}}^{miss}) > 110$ GeV, while VBF selection takes care of having at least a jet pair with $p_T > 60$ GeV, $\Delta\eta > 3.8$, $\eta_1 \cdot \eta_2 < 0$ and $\mathrm{m}_{jj} >1$ TeV. The signal region (SR) contains both the central as well as VBF selections while some control regions (CR) are developed to estimate major backgrounds like QCD multijet background, W+jets followed by $t\bar{t}$. The QCD background is estimated by data-driven technique and W+jets, $t\bar{t}$ backgrounds are estimated by semi data-driven technique.

The m_T variable is the sensitive variable used to discriminate possible SUSY signal from backgrounds in this final state. The data and MC agree well within statistical and systematic uncertainties but unfortunately, no excess of the signal is found over SM background predictions and hence no evidence for SUSY and New Physics. Thus, an upper limit with 95% confidence level (CL) has been placed on the chargino and neutralino pair production cross section as a function of their masses. These limits are obtained by combining the data from four final states i.e. three 1-lepton (single tau, single muon, and single electron) channels and a 0-lepton channel, considering all systematic and statistical uncertainties along with their correlations. The calculation of the limits is performed using the $m_T(m_{jj})$ distribution in 1-lepton+jj (0-lepton+jj) by combined likelihood technique in bins of $m_T(m_{jj})$. The results have been presented in MSSM R-parity conserving scenarios with LSP ($\tilde{\chi}_1^0$), chargino($\tilde{\chi}_1^{\pm}$) and neutralinos ($\tilde{\chi}_2^0$). Two scenarios have been considered to interpret the final limits: a) “slepton model” i.e. the decay of chargino/neutralinos through “sleptons” which are next-to-lightest SUSY particles b) “WZ model” i.e. the decay of chargino/neutralino through W* and Z* as sleptons are too heavy. The main difference between the two models comes from the branching ratio of $\tilde{\chi}_1^{\pm}$ and $\tilde{\chi}_2^0$ to the leptonic final state. In the first scenario, the mass of slepton ($\tilde{l}$) is considered as the difference between the mass of chargino/neutralino and mass of LSP in terms of variable $x_{\tilde{l}}$ as:

$$m_{\tilde{\ell}} = m_{\tilde{\chi}_1^0} + x_{\tilde{\ell}}(m_{\tilde{\chi}_1^\pm} - m_{\tilde{\chi}_1^0}) \tag{7.1}$$

and here, $x_{\tilde{l}}$ is considered to be 0.5 as three sleptons ($m_{\tilde{l}} = m_{\tilde{e}} = m_{\tilde{\mu}} = m_{\tilde{\tau}}$) are considered to be light in "$\tilde{l}$-democratic" model. For the $\Delta m = \{1, 10, 30, 50\}$ GeV assumption, we have observed (expected) the exclusion on $\tilde{\chi}_1^\pm/\tilde{\chi}_2^0$ gaugino masses below$\{112, 159, 215, 207\}$ ($\{125, 171, 235, 228\}$) GeV for the combination of the four channels. For the compressed mass spectrum scenarios (where the mass difference between the parent particle and daughter particle is very small) with $1 \leq \Delta m \leq 30$ GeV, the bounds on the $\tilde{\chi}_1^\pm/\tilde{\chi}_2^0$ gaugino masses are the most stringent to date.

For $1 < \Delta m < 10$ GeV, the signal acceptance for the WZ model is similar to the signal acceptance for the light slepton model. However, with increasing mass gap where the 1-lepton+jj channels dominate the sensitivity, the exclusions on $m_{\tilde{\chi}_1^\pm}$ in the WZ model are less stringent than the ones in the light slepton model because of difference in low branching ratio of chargino and neutralino decaying through sleptons in WZ model.

In WZ model, for the $\Delta m = \{1, 10, 30, 50\}$ GeV assumption, we have observed (expected) the exclusion on $\tilde{\chi}_1^\pm/\tilde{\chi}_2^0$ gaugino masses below $\{112, 146, 175, 162\}$ ($\{125, 160, 194, 178\}$) GeV. For the compressed mass spectrum scenarios with $1 \leq \Delta m < 5$ GeV and $25 \leq \Delta m < 50$ GeV, the bounds on the $\tilde{\chi}_1^\pm/\tilde{\chi}_2^0$ gaugino masses are also the most stringent to date.

Just to summarize the results, in compressed mass spectra scenarios, for the sleptons model, masses of $\tilde{\chi}_1^\pm/\tilde{\chi}_2^0$ are excluded up to 112 (215) GeV for $\Delta m(m_{\tilde{\chi}_1^\pm} - m_{\tilde{\chi}_1^0}) = 1$ (30)and for W^* and Z^* model masses up to 112 (175) GeV are excluded for $\Delta m(m_{\tilde{\chi}_1^\pm} - m_{\tilde{\chi}_1^0}) = 1$ (30) GeV at 95% CL. The present analysis obtains the most stringent limit to date on the production of charginos and neutralinos decaying to leptons in compressed mass spectrum scenarios defined by the mass separation

$1 \leq \Delta m < 5$ GeV and $25 \leq \Delta m < 50$ GeV and this work has been published as "Search for supersymmetry with a compressed mass spectrum in the vector boson fusion topology with 1-lepton and 0-lepton final states in proton-proton collisions at $\sqrt{s} = 13$ TeV" in Journal of High Energy Physics (JHEP), volume 8 (2019).

7.3 Outlook

The analysis presented above is the first-ever SUSY search done through VBF topology in a single-lepton final state. The data used to put limits on chargino and neutralino production cross section correspond to 35.87 fb^{-1} collected by CMS detector during 2016. However, LHC Run II has been finished collecting the CMS data for 3.5 years and have accumulated 137 fb^{-1} integrated luminosity. The data analysis with full Run II data at 13 TeV center-of-mass energy has already been started considering the final states: a) single soft lepton + VBF jets + MET, b) dilepton + VBF jets + MET and c) 0-lepton + VBF jets + MET or invisible channel. This analysis will be carried out with full Run II data to gain more sensitivity towards the electroweak sector and hopefully would explore NEW PHYSICS.

Publications/Conferences

Publications and CMS Analysis Notes with Direct Contribution

1. CMS Collaboration, "Search for supersymmetry with a compressed mass spectrum in the vector boson fusion topology with 1-lepton and 0-lepton final states in proton-proton collisions at $\sqrt{s} = 13$ TeV", *JHEP*, vol. 09 p. 150 (2019), DOI: https://doi.org/10.1007/JHEP08(2019)150.

2. CMS Collaboration, "Searh for EWKinos in Vector Boson Fusion Processes with $\sqrt{s} = 13$ TeV", CMS AN-2017/025 (2017).

3. CMS Collaboration, "Search for dark matter and supersymmetry with a compressed mass spectrum in the vector boson fusion topology in proton-proton collisions at $\sqrt{s} = 13$ TeV.", CMS AN-2017/026 (2017).

* **CMS AN - CMS Analysis Note**

Conference papers in referred journals

1. Priyanka Kumari *et al.*, "Search for Supersymmetry in Vector Boson Fusion Topology Using Proton-Proton Collision Data at the LHC", *Springer Proc. Phys.*, vol. 203 (2018) p. 175-178, https://dx.doi.org/10.1007/978-3-319-73171-1_39.

2. Ram Krishan Sharma, Priyanka Kumari *et al.*, "Test Beam Study of Gas Electron Multiplier (GEM) Detectors for the Upgrade of CMS Endcap Muon System", *Springer Proc. Phys.*, vol. 203 (2018) p. 179-183, https://dx.doi.org/10.1007/978-3-319-73171-1_40.

Conference proceedings under review

1. CMS Collaboration, Priyanka Kumari *et al.*, “Search for Supersymmetry with a compressed mass spectrum in the vector boson fusion topology in single hadronic tau final state in pp collisions at $\sqrt{s} = 13$ TeV”, *Proceeding accepted in PoS* , **CMS CR-2019/084** (2019).
2. Priyanka Kumari *et al.*, “Aging study for Resistive Plate Chambers (RPC) of the CMS muon detector for HL-LHC”, *Proceeding under review in Springer Proc. Phys.*, **CMS CR-2019/085** (2019).
3. Priyanka Kumari *et al.*, “Search for Supersymmetry with a compressed mass spectrum in vector boson fusion topology with 1-lepton and 0-lepton final states in pp collisions at $\sqrt{s} = 13$ TeV with CMS detector”, *Proceeding under review in Springer Proc. Phys.*, **CMS CR-2019/166** (2019).

Papers presented in Conferences, Workshops and Symposium

1. Priyanka Kumari *et al.*, “Search for Supersymmetry with a compressed mass spectrum in vector boson fusion topology with 1-lepton and 0-lepton final states in pp collisions at $\sqrt{13}$ TeV with CMS”, **The 29th International Symposium on Lepton Photon Interactions at High Energies**, Aug 5th - 10th 2019, Toronto, Canada.
2. Priyanka Kumari *et al.*, “Use of PYTHON in CMS Framework”, **PYTHON Workshop**, Mar 1st - 2nd 2019, Department of Physics, Panjab University Chandigarh, India.
3. Priyanka Kumari *et al.*, “Aging Study for Resistive Plate Chambers (RPC) of the CMS muon detector for HL-LHC”, **XXIII DAE-BRNS HIGH ENERGY PHYSICS SYMPOSIUM 2018**, Dec 10th - 14th 2018, IIT Madras, India.

4. Priyanka Kumari *et al.*, “Search for Supersymmetry with a compressed mass spectrum in the vector boson fusion topology with single hadronic tau channel in pp collisions at $\sqrt{13}$ TeV”, **XXIII DAE-BRNS HIGH ENERGY PHYSICS SYMPOSIUM 2018**, Dec 10^{th} - 14^{th} 2018, IIT Madras, India.

5. Priyanka Kumari *et al.*, “Gas Electron Multiplier (GEM) Detectors For the Upgrade of CMS Endcap Muon System at the CERN LHC”, **International Conference in Nuclear Physics with Energetic Heavy Ion Beams**, March 15^{th} - 18^{th} 2017, Department of Physics, Panjab University Chandigarh, India.

6. Priyanka Kumari *et al.*, “Search for Supersymmetry with the Vector Boson Fusion tagging in pp collisions using CMS Detector at the LHC”, **11^{th} Chandigarh Science Congress (CHASCON)**, March 10^{th} - 12^{th} 2017, Panjab University Chandigarh, India.

7. Priyanka Kumari *et al.*, “Search for Supersymmetry with the Vector Boson Fusion Topology using proton-proton collisions at $\sqrt{8}$ TeV”, **XXII DAE-BRNS HIGH ENERGY PHYSICS SYMPOSIUM 2016**, Dec 12^{th} - 16^{th} 2016, University of Delhi, Delhi, India.

8. Priyanka Kumari *et al.*, “Search for Supersymmetry with the Vector Boson Fusion Topology using proton-proton collisions at $\sqrt{13}$ TeV”, **CMS Week**, Nov 12^{th} - 16^{th} 2016, TIFR Mumbai, India.

9. Priyanka Kumari *et al.*, “Search for Supersymmetry with the Vector Boson Fusion Topology using proton-proton collisions at $\sqrt{8}$ TeV”, **International Workshop on Frontiers in Electroweak Interactions of Leptons and Hadrons**, Nov 2^{th} - 6^{th} 2016, Aligarh Muslim University, Aligarh, India.

10. Priyanka Kumari *et al.*, “GEM Detector at CMS Muon System Upgrade At The CERN LHC”, **10^{th} Chandigarh Science Congress (CHASCON)**, Feb 29^{th} - 2^{nd} March 2016, Panjab University Chandigarh, India.

11. Priyanka Kumari *et al.*, “Performance of τ lepton identification in Compact Muon Solenoid (CMS) Detector”, **9^{th} Chandigarh Science Congress (CHASCON)**, Feb 25^{th} - 27^{th} 2015, Panjab University Chandigarh, India.

Publications as co-author with CMS Collaboration

1. CMS Collaboration, “Search for supersymmetry with a compressed mass spectrum in the vector boson fusion topology with 1-lepton and 0-lepton final states in proton-proton collisions at $\sqrt{s} = 13$ TeV”, *JHEP* **1908**, 150 (2019), `https://dx.doi.org/10.1007/JHEP08(2019)150`.
2. CMS Collaboration, “Search for supersymmetry in proton-proton collisions at 13 TeV in final states with jets and missing transverse momentum”, *JHEP* **1910** 244 (2019), `https://dx.doi.org/10.1007/JHEP10(2019)244`.
3. CMS Collaboration, “Search for anomalous electroweak production of vector boson pairs in association with two jets in proton-proton collisions at 13 TeV”, *Phys. Lett. B* **798**, 134985 (2019), `https://dx.doi.org/10.1016/j.physletb.2019.134985`.
4. CMS Collaboration, “Search for a low-mass $\tau^+\tau^-$ resonance in association with a bottom quark in proton-proton collisions at $\sqrt{s} = 13$ TeV”, *JHEP* **1905**, 210 (2019), `https://dx.doi.org/10.1007/JHEP05(2019)210`.
5. CMS Collaboration, “Search for supersymmetry in final states with photons and missing transverse momentum in proton-proton collisions at 13 TeV”, *JHEP* **1906**, 143 (2019), `https://dx.doi.org/10.1007/JHEP06(2019)143`.
6. CMS Collaboration, “An embedding technique to determine $\tau\tau$ backgrounds in proton-proton collision data”, *JINST* **14**, no. 06, P06032 (2019), `https://dx.doi.org/10.1088/1748-0221/14/06/P06032`.
7. CMS Collaboration, “Search for supersymmetry in events with a photon, jets, b -jets, and missing transverse momentum in proton-proton collisions at 13 TeV”, *Eur. Phys. J. C* **79**, no. 5, 444 (2019), `https://dx.doi.org/10.1140/epjc/s10052-019-6926-x`.
8. CMS Collaboration, “Measurement of electroweak WZ boson production and search for new physics in WZ + two jets events in pp collisions at $\sqrt{s} = 13$TeV”, *Phys. Lett. B* **795**, 281 (2019), `https://dx.doi.org/10.1016/j.physletb.2019.05.042`.

9. CMS Collaboration, “Inclusive search for supersymmetry in pp collisions at $\sqrt{s} = 13$ TeV using razor variables and boosted object identification in zero and one lepton final states”, *JHEP* **1903**, 031 (2019), `https://dx.doi.org/10.1007/JHEP03(2019)031`.

10. CMS Collaboration, “Search for supersymmetry in events with a photon, a lepton, and missing transverse momentum in proton-proton collisions at $\sqrt{s} = 13$ TeV”, *JHEP* **1901**, 154 (2019), `https://dx.doi.org/10.1007/JHEP01(2019)154`.

11. CMS Collaboration, “Search for dark matter in events with a leptoquark and missing transverse momentum in proton-proton collisions at 13 TeV”, *Phys. Lett. B* **795**, 76 (2019), `https://dx.doi.org/10.1016/j.physletb.2019.05.046`.

12. CMS Collaboration, “Search for heavy neutrinos and third-generation leptoquarks in hadronic states of two τ leptons and two jets in proton-proton collisions at $\sqrt{s} = 13$ TeV”, *JHEP* **1903**, 170 (2019), `https://dx.doi.org/10.1007/JHEP03(2019)170`.

13. CMS Collaboration, “Search for new physics in final states with a single photon and missing transverse momentum in proton-proton collisions at $\sqrt{s} = 13$ TeV”, *JHEP* **1902**, 074 (2019), `https://dx.doi.org/10.1007/JHEP02(2019)074`.

14. CMS Collaboration, “Performance of reconstruction and identification of τ leptons decaying to hadrons and ν_τ in pp collisions at $\sqrt{s} = 13$ TeV”, *JINST* **13**, no. 10, P10005 (2018), `https://dx.doi.org/10.1088/1748-0221/13/10/P10005`.

15. CMS Collaboration, “Search for supersymmetry in events with a τ lepton pair and missing transverse momentum in proton-proton collisions at $\sqrt{s} = 13$ TeV”, *JHEP* **1811**, 151 (2018), `https://dx.doi.org/10.1007/JHEP11(2018)151`.

16. CMS Collaboration, “Search for supersymmetric partners of electrons and muons in proton-proton collisions at $\sqrt{s} = 13$ TeV”, *Phys. Lett. B* **790**, 140 (2019), `https://dx.doi.org/10.1016/j.physletb.2019.01.005`.

17. CMS Collaboration, “Search for beyond the standard model Higgs bosons decaying into a $\mathrm{b\overline{b}}$ pair in pp collisions at $\sqrt{s} = 13$ TeV”, *JHEP* **1808**, 113 (2018), `https://dx.doi.org/10.1007/JHEP08(2018)113`.

18. CMS Collaboration, “Performance of the CMS muon detector and muon reconstruction with proton-proton collisions at $\sqrt{s} = 13$ TeV”, *JINST* **13**, no. 06, P06015 (2018), `doi:10.1088/1748-0221/13/06/P06015`.

19. CMS Collaboration, “Combined search for electroweak production of charginos and neutralinos in proton-proton collisions at $\sqrt{s} = 13$ TeV”, *JHEP* **1803**, 160 (2018), `https://dx.doi.org/10.1007/JHEP03(2018)160`.

20. CMS Collaboration, “Search for new physics in events with two soft oppositely charged leptons and missing transverse momentum in proton-proton collisions at $\sqrt{s} = 13$ TeV”, *Phys. Lett. B* **782**, 440 (2018), `https://dx.doi.org/10.1016/j.physletb.2018.05.062`.

21. CMS Collaboration, “Electroweak production of two jets in association with a Z boson in proton-proton collisions at $\sqrt{s} = 13$ TeV”, *Eur. Phys. J. C* **78**, no. 7, 589 (2018), `https://dx.doi.org/10.1140/epjc/s10052-018-6049-9`.

22. CMS Collaboration, “Search for new physics in final states with an energetic jet or a hadronically decaying W or Z boson and transverse momentum imbalance at $\sqrt{s} = 13$ TeV”, *Phys. Rev. D* **97**, no. 9, 092005 (2018), `https://dx.doi.org/10.1103/PhysRevD.97.092005`.

23. CMS Collaboration, “Search for supersymmetry in proton-proton collisions at 13 TeV using identified top quarks”, *Phys. Rev. D* **97**, no. 1, 012007 (2018), `https://dx.doi.org/10.1103/PhysRevD.97.012007`.

24. CMS Collaboration, “Search for supersymmetry in events with at least three electrons or muons, jets, and missing transverse momentum in proton-proton collisions at $\sqrt{s} = 13$ TeV”, *JHEP* **1802**, 067 (2018), `https://dx.doi.org/10.1007/JHEP02(2018)067`.

25. CMS Collaboration, “Search for supersymmetry in events with one lepton and multiple jets exploiting the angular correlation between the lepton and the missing transverse momentum in proton-proton collisions at $\sqrt{s} = 13$ TeV”, *Phys. Lett. B* **780**, 384 (2018), `https://dx.doi.org/10.1016/j.physletb.2018.03.028`.

26. CMS Collaboration, “Evidence for the Higgs boson decay to a bottom quark-antiquark pair”, *Phys. Lett. B* **780**, 501 (2018), `https://dx.doi.org/10.1016/j.physletb.2018.02.050`.

27. CMS Collaboration, “Observation of top quark production in proton-nucleus collisions”, *Phys. Rev. Lett.* **119**, no. 24, 242001 (2017), `https://dx.doi.org/10.1103/PhysRevLett.119.242001`.

28. CMS Collaboration, “Observation of electroweak production of same-sign W boson pairs in the two jet and two same-sign lepton final state in proton-proton collisions at $\sqrt{s} = 13$ TeV”, *Phys. Rev. Lett.* **120**, no. 8, 081801 (2018), `https://dx.doi.org/10.1103/PhysRevLett.120.081801`.

29. CMS Collaboration, “Search for electroweak production of charginos and neutralinos in multilepton final states in proton-proton collisions at $\sqrt{s} = 13$ TeV”, *JHEP* **1803**, 166 (2018), `https://dx.doi.org/10.1007/JHEP03(2018)166`.

30. CMS Collaboration, “Search for supersymmetry in events with at least one photon, missing transverse momentum, and large transverse event activity in proton-proton collisions at $\sqrt{s} = 13$ TeV”, *JHEP* **1712**, 142 (2017), `https://dx.doi.org/10.1007/JHEP12(2017)142`.

31. CMS Collaboration, “Search for natural supersymmetry in events with top quark pairs and photons in pp collisions at $\sqrt{s} = 8$ TeV”, *JHEP* **1803**, 167 (2018), `https://dx.doi.org/10.1007/JHEP03(2018)167`.

32. CMS Collaboration, “Search for electroweak production of charginos and neutralinos in WH events in proton-proton collisions at $\sqrt{s} = 13$ TeV”, *JHEP* **1711**, 029 (2017), `https://dx.doi.org/10.1007/JHEP11(2017)029`.

33. CMS Collaboration, “Particle-flow reconstruction and global event description with the CMS detector”, *JINST* **12**, no. 10, P10003 (2017), `https://dx.doi.org/10.1088/1748-0221/12/10/P10003`.

34. CMS Collaboration, “Search for Supersymmetry in pp Collisions at $\sqrt{s} = 13$ TeV in the Single-Lepton Final State Using the Sum of Masses of Large-Radius Jets”, *Phys. Rev. Lett.* **119**, no. 15, 151802 (2017), `https://dx.doi.org/10.1103/PhysRevLett.119.151802`.

35. CMS Collaboration, “Search for supersymmetry in multijet events with missing transverse momentum in proton-proton collisions at 13 TeV”, *Phys. Rev. D* **96**, no. 3, 032003 (2017), `https://dx.doi.org/10.1103/PhysRevD.96.032003`.

36. CMS Collaboration, "Search for physics beyond the standard model in events with two leptons of same sign, missing transverse momentum, and jets in protonproton collisions at $\sqrt{s} = 13\,\text{TeV}$", *Eur. Phys. J. C* **77**, no. 9, 578 (2017), `https://dx.doi.org/10.1140/epjc/s10052-017-5079-z`.

37. CMS Collaboration, "Search for dark matter produced with an energetic jet or a hadronically decaying W or Z boson at $\sqrt{s} = 13$ TeV", *JHEP* **1707**, 014 (2017), `https://dx.doi.org/10.1007/JHEP07(2017)014`.

38. CMS Collaboration, "Search for new phenomena with multiple charged leptons in proton-proton collisions at $\sqrt{s} = 13$ TeV", *Eur. Phys. J. C* **77**, no. 9, 635 (2017), `https://dx.doi.org/10.1140/epjc/s10052-017-5182-1`.

39. CMS Collaboration, "Search for dark matter and unparticles in events with a Z boson and missing transverse momentum in proton-proton collisions at $\sqrt{s} = 13$ TeV", *JHEP* **1703**, 061 (2017), Erratum: [JHEP **1709**, 106 (2017)], `https://dx.doi.org/10.1007/JHEP01(2018)056,10.1007/JHEP09(2017)106,10.1007/JHEP03(2017)061`.

40. CMS Collaboration, "Search for light bosons in decays of the 125 GeV Higgs boson in proton-proton collisions at $\sqrt{s} = 8$ TeV", *JHEP* **1710**, 076 (2017), `https://dx.doi.org/10.1007/JHEP10(2017)076`.

41. CMS Collaboration, "Search for supersymmetry in the all-hadronic final state using top quark tagging in pp collisions at $\sqrt{s} = 13$ TeV", *Phys. Rev. D* **96**, no. 1, 012004 (2017), `https://dx.doi.org/10.1103/PhysRevD.96.012004`.

42. CMS Collaboration, "Search for supersymmetry in events with photons and missing transverse energy in pp collisions at 13 TeV", *Phys. Lett. B* **769**, 391 (2017), `https://dx.doi.org/10.1016/j.physletb.2017.04.005`.

*** Complete list of **332** published papers as a co-author in CMS : Inspire-HEP_PriyankaKumari

Conferences, Schools, Symposiums and Workshops attended

1. August 28- September 06, 2019, **CERN-Fermilab HCP Summer School**, CERN, Geneva, Switzerland.
2. August 5-10, 2019, **The 29th International Symposium on Lepton Photon Interactions at High Energies**, Toronto, Canada.
3. March 1-2, **Python Workshop**, Department of Physics, Panjab University, Chandigarh.
4. December 10-14, 2018, **XXIII DAE-BRNS HIGH ENERGY PHYSICS SYMPOSIUM**, IIT Madras, India.
5. March 15-18, 2017, **International Conference in Nuclear Physics with Energetic Heavy Ion Beams**, Department of Physics, Panjab University Chandigarh, India.
6. March 10-12, 2017, **11th Chandigarh Science Congress (CHASCON-2017)**, Panjab University Chandigarh.
7. December 10-14, 2016, **XXII DAE-BRNS HIGH ENERGY PHYSICS SYMPOSIUM**, University of Delhi, Delhi, India.
8. November 12-16, 2016, **CMS Week**, TIFR Mumbai, India.
9. November 2-6, 2016, **International Workshop on Frontiers in Electroweak Interactions of Leptons and Hadrons**, Aligarh Muslim University, Aligarh, India.
10. April 19- May 9, 2016, **X SERC School on Experimental High Energy Physics**, Department of Physics and Astrophysics, University of Delhi, Delhi, India.
11. March 15-18, 2016, **National School cum Workshop in Accelerator Physics**, Panjab University, Chandigarh, India.
12. February 29-March 02, 2016, **10th Chandigarh Science Congress (CHASCON-2016)**, Panjab University Chandigarh, India.

13. November 23-24, 2015, **HGCAL workshop**, TIFR-Mumbai, India.

14. March 16-17, 2015, **Workshop on High Performance Computing**, Department of Physics, Panjab University Chandigarh, India.

15. February 25-27, 2015, **9th Chandigarh Science Congress (CHASCON-2015)**, Panjab University Chandigarh, India.

Selected Reprints

Published for SISSA by Springer

Received: *May 30, 2019*
Accepted: *August 6, 2019*
Published: *August 27, 2019*

Search for supersymmetry with a compressed mass spectrum in the vector boson fusion topology with 1-lepton and 0-lepton final states in proton-proton collisions at $\sqrt{s} = 13\,\mathrm{TeV}$

The CMS collaboration

E-mail: cms-publication-committee-chair@cern.ch

Abstract: A search for supersymmetric particles produced in the vector boson fusion topology in proton-proton collisions is presented. The search targets final states with one or zero leptons, large missing transverse momentum, and two jets with a large separation in rapidity. The data sample corresponds to an integrated luminosity of $35.9\,\mathrm{fb}^{-1}$ of proton-proton collisions at $\sqrt{s} = 13\,\mathrm{TeV}$ collected in 2016 with the CMS detector at the LHC. The observed dijet invariant mass and lepton-neutrino transverse mass spectra are found to be consistent with the standard model predictions. Upper limits are set on the cross sections for chargino ($\tilde{\chi}_1^{\pm}$) and neutralino ($\tilde{\chi}_2^{0}$) production with two associated jets. For a compressed mass spectrum scenario in which the $\tilde{\chi}_1^{\pm}$ and $\tilde{\chi}_2^{0}$ decays proceed via a light slepton and the mass difference between the lightest neutralino $\tilde{\chi}_1^{0}$ and the mass-degenerate particles $\tilde{\chi}_1^{\pm}$ and $\tilde{\chi}_2^{0}$ is 1 (30) GeV, the most stringent lower limit to date of 112 (215) GeV is set on the mass of these latter two particles.

Keywords: Hadron-Hadron scattering (experiments), Supersymmetry

ArXiv ePrint: 1905.13059

https://doi.org/10.1007/JHEP08(2019)150

Contents

JHEP08(2019)150

1 Introduction

Supersymmetry (SUSY) [1–7] is a theory that can simultaneously describe the particle nature of dark matter (DM) and solve the gauge hierarchy problem of the standard model (SM). However, for all of its attractive features, there is as yet no direct evidence to support this theory. The masses of the strongly produced gluinos ($\widetilde{\mathrm{g}}$) as well as the squarks ($\widetilde{\mathrm{q}}$) of the first and second generations have been excluded below approximately 2 TeV in certain simplified model scenarios [8–13]. On the other hand, the values of the masses of the weakly produced charginos ($\widetilde{\chi}^{\pm}_{\mathrm{i}}$) and neutralinos ($\widetilde{\chi}^{0}_{\mathrm{i}}$) are less constrained at the CERN LHC where these particles have much smaller production cross sections. The chargino-neutralino sector of SUSY plays an important role in establishing a connection between SUSY models and DM. The lightest neutralino $\widetilde{\chi}^{0}_{1}$, as the lightest supersymmetric particle (LSP), is the canonical DM candidate in R-parity conserving SUSY extensions of the SM [14].

A common strategy to search for charginos and neutralinos is through Drell-Yan (DY) production processes of order α^2_{EW} (electroweak coupling squared) involving virtual W and Z bosons (W*/Z*), $\mathrm{q}\overline{\mathrm{q}}' \to \mathrm{W}^* \to \widetilde{\chi}^{\pm}_{\mathrm{i}}\widetilde{\chi}^{0}_{\mathrm{j}}$, followed by their decay to final states with one or more charged leptons (ℓ) and missing transverse momentum ($p_{\mathrm{T}}^{\mathrm{miss}}$). These processes can include, for example, $\widetilde{\chi}^{\pm}_{1}\widetilde{\chi}^{0}_{2}$ pair production followed by $\widetilde{\chi}^{\pm}_{1} \to \ell^{\pm}\nu_{\ell}\widetilde{\chi}^{0}_{1}$ and $\widetilde{\chi}^{0}_{2} \to \ell^{\pm}\ell^{\mp}\widetilde{\chi}^{0}_{1}$ via virtual SM bosons or a light slepton $\widetilde{\ell}$, where $\widetilde{\chi}^{\pm}_{1}$ ($\widetilde{\chi}^{0}_{2}$) is the lightest (next-to-lightest) chargino (neutralino), and where the LSP $\widetilde{\chi}^{0}_{1}$ is presumed to escape without detection leading to significant missing momentum. However, these searches are experimentally difficult in cases where the mass of the LSP is only slightly less than the masses of other charginos and neutralinos, making these so-called compressed spectrum scenarios important search targets using new techniques. While the exclusion limits in refs. [15–17] can be as stringent as $m_{\widetilde{\chi}_1^\pm} < 650\,\text{GeV}$ for a massless $\widetilde{\chi}_1^0$, they weaken to only approximately $100\,\text{GeV}$ for $\Delta m \equiv m_{\widetilde{\chi}_1^\pm} - m_{\widetilde{\chi}_1^0} = 2\,\text{GeV}$, assuming decays of the $\widetilde{\chi}_1^\pm$ and $\widetilde{\chi}_2^0$ to leptonic final states proceed through the mediation of virtual W and Z bosons [18, 19]. As the mass difference between SUSY particles decreases, the momenta available to the co-produced SM particles are small, resulting in "soft" decay products having low transverse momentum (p_T). Therefore, the traditional searches using DY processes suffer in the compressed spectrum scenarios since the SM particles used for discrimination become more difficult to reconstruct as their momenta decrease. In contrast, chargino and neutralino production via vector boson fusion (VBF) processes of order α_EW^4 are very useful in tackling these interesting compressed SUSY scenarios [20]. In VBF processes, electroweak SUSY particles are pair-produced in association with two high-p_T oppositely-directed jets close to the beam axis (forward), resulting in a large dijet invariant mass (m_jj). The use of two high-p_T VBF jets in the event topology effectively suppresses the SM background while, simultaneously, creating a recoil effect that facilitates both the detection of p_T^miss in the event and the identification of the soft decay products in compressed-spectrum scenarios because of their natural kinematic boost [21, 22]. Figure 1 shows the Feynman diagrams for two of the possible VBF production processes: chargino-neutralino and chargino-chargino production.

The CMS collaboration reported the first results of a SUSY search using the VBF dijet topology for charginos and neutralinos in the minimal supersymmetric standard model (MSSM), using a data sample corresponding to an integrated luminosity of $19.7\,\text{fb}^{-1}$ of proton-proton collision data at $\sqrt{s} = 8\,\text{TeV}$ [23]. That analysis considered SUSY models with light staus ($\widetilde{\tau}$) leading to leptonic decay modes of the charginos and neutralinos (e.g., $\widetilde{\chi}_2^0 \to \tau^\pm\widetilde{\tau}^\mp \to \tau^-\tau^+\widetilde{\chi}_1^0$). In the presence of a light slepton, it is likely that $\widetilde{\chi}_1^\pm$ decays to $\ell^\pm\nu_\ell\widetilde{\chi}_1^0$ and $\widetilde{\chi}_2^0$ decays to $\ell^+\ell^-\widetilde{\chi}_1^0$. Thus, charginos and neutralinos were probed using final states with two leptons and two additional jets consistent with the VBF topology. In the compressed mass spectrum scenario, where the mass difference between the $\widetilde{\chi}_1^0$ and $\widetilde{\chi}_2^0/\widetilde{\chi}_1^\pm$ particles was taken to be $50\,\text{GeV}$, $\widetilde{\chi}_2^0$ and $\widetilde{\chi}_1^\pm$ masses below $170\,\text{GeV}$ were excluded.

In this paper, a search is presented for the electroweak production of SUSY particles in the VBF topology using data collected in 2016 with the CMS detector and corresponding to an integrated luminosity of $35.9\,\text{fb}^{-1}$ of proton-proton collisions at a center-of-mass energy of $\sqrt{s} = 13\,\text{TeV}$. Besides the two oppositely directed forward jets (j) that define the VBF configuration, the search requires the presence of zero or one soft lepton and large p_T^miss. The events are classified into two categories based on the lepton content, 0ℓjj and 1ℓjj, with the latter having three different final states: ejj, μjj, and $\tau_\mathrm{h}$jj, where τ_h denotes a hadronically decaying τ lepton. The 0ℓjj final state (also referred to as the "invisible" channel) provides the best sensitivity to the $\Delta m < 10\,\text{GeV}$ scenarios, where the leptons from the $\widetilde{\chi}_2^0/\widetilde{\chi}_1^\pm$ decays are "lost", either because their momenta are too low to reconstruct or because they fail to satisfy the identification requirements. The soft single-lepton channels were not

JHEP08(2019)150

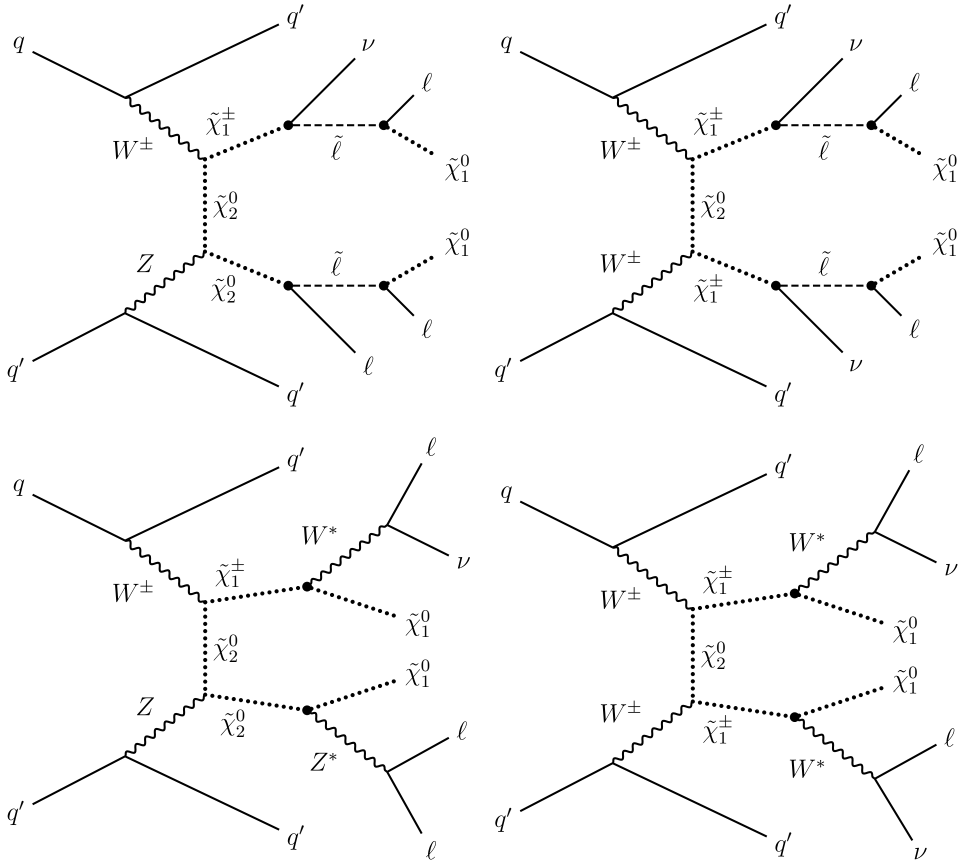

Figure 1. Representative Feynman diagrams of (left) chargino-neutralino and (right) chargino-chargino pair production through vector boson fusion, followed by their decays to leptons and the LSP $\tilde{\chi}_1^0$ via a light slepton (top row) or a W^*/Z^* (bottom row). Although these representative diagrams show multiple leptons in the final state, the compressed mass spectra scenarios of interest result in low-p_T leptons, making it unlikely to reconstruct and identify more than one lepton.

utilized in the 8 TeV search and thus this analysis extends the previous search performed only in the two-lepton final state. The dijet invariant mass distribution m_{jj} is the sensitive variable used to discriminate possible SUSY signal from background in the 0ℓjj channel, while the transverse mass m_T between the lepton and p_T^{miss} is used in the 1ℓjj channels.

The backgrounds are evaluated using data wherever possible. The general strategy is to define control regions, each dominated by a different background process and with negligible contamination from signal events, through modification of the nominal selection requirements. These control regions are used to measure the m_{jj} and m_T shapes and probabilities for background events to satisfy the VBF selection requirements. If the background contribution from a particular process is expected to be small or if the above approach is not feasible, the m_{jj} and m_T shapes are taken from simulation. In these cases, scale factors, defined as the ratio of efficiencies measured in data and simulation, are used to normalize the predicted rates to the data.

The paper is organized as follows. The CMS detector is described in section 2. The reconstruction of electrons, muons, τ_h leptons, jets, and $p_\mathrm{T}^\mathrm{miss}$ is presented in section 3. The simulated SUSY signal and background samples are discussed in section 4, followed by the description of the event selection in section 5 and the background estimation in section 6. Systematic uncertainties are summarized in section 7, and the results are presented in section 8. Section 9 contains a summary of the paper.

2 The CMS detector

The central feature of the CMS apparatus is a superconducting solenoid of 6 m internal diameter, providing a magnetic field of 3.8 T. Located within the solenoid volume are silicon pixel and strip detectors, a lead tungstate electromagnetic calorimeter (ECAL), and a brass and scintillator hadron calorimeter (HCAL). Muons are measured in gas-ionization detectors embedded in the steel flux-return yoke outside the solenoid. Extensive forward calorimetry complements the barrel and endcap detectors by covering the pseudorapidity range $3.0 < |\eta| < 5.2$.

The inner silicon tracker measures charged tracks with $|\eta| < 2.5$ and provides an impact parameter resolution of approximately 15 μm and a transverse momentum resolution of about 1.5% for 100 GeV charged particles. Collision events of interest are selected using a two-tiered trigger system. The first level trigger (L1), composed of custom hardware processors, selects events at a rate of around 100 kHz. The second level trigger, based on an array of microprocessors running a version of the full event reconstruction software optimized for fast processing, reduces the event rate to around 1 kHz before data storage. A detailed description of the CMS detector, along with a definition of the coordinate system and relevant kinematic variables, can be found in ref. [24].

3 Event reconstruction and particle identification

The particle-flow (PF) algorithm is used to reconstruct the jets and $p_\mathrm{T}^\mathrm{miss}$ used in this analysis [25]. The PF technique combines information from different subdetectors to produce a mutually-exclusive collection of particles (namely muons, electrons, photons, charged hadrons, and neutral hadrons) that are used as input for the jet clustering algorithms. The missing transverse momentum vector $\vec{p}_\mathrm{T}^\mathrm{miss}$ is defined as the negative vector sum of the momenta of all reconstructed PF candidates in an event, projected on the plane perpendicular to the beam axis. The magnitude of $\vec{p}_\mathrm{T}^\mathrm{miss}$ is $p_\mathrm{T}^\mathrm{miss}$ [26]. The production of undetected particles such as SM neutrinos and the SUSY $\widetilde{\chi}_1^0$ is inferred by the measured $p_\mathrm{T}^\mathrm{miss}$. The reconstructed vertex with the largest value of summed physics-object p_T^2 is taken to be the primary pp interaction vertex. The physics objects are the jets, clustered using the jet finding algorithm [27, 28] with the tracks assigned to the vertex as inputs, and the associated missing transverse momentum, taken as the negative vector sum of the p_T of those jets.

Jets are clustered using the FastJet anti-k_T algorithm [27, 28], with a distance parameter of 0.4. Only jets that satisfy the identification criteria designed to reject particles from multiple proton-proton interactions (pileup) and anomalous behavior in the calorimeters are considered in this analysis [29]. The jet energy scale and resolution are calibrated through correction factors that depend on the p_{T} and η of the jet [30]. Jets with $p_{\mathrm{T}} > 60\,\mathrm{GeV}$ have a reconstruction-plus-identification efficiency of approximately 99%, while 90–95% of pileup jets are rejected [31]. Jets originating from the hadronization of bottom quarks (b quark jets) are identified using the combined secondary vertex (CSV) algorithm [32], which exploits observables related to the long lifetime of B hadrons. For jets with $p_{\mathrm{T}} > 20\,\mathrm{GeV}$ and $|\eta| < 2.4$, the b tagging algorithm is operated at a working point such that the probability of correctly identifying a b quark jet is approximately 60%, while the probability of misidentifying a jet generated from a light-flavor quark or gluon as a b quark jet is approximately 1% [32].

Muons are reconstructed using the inner silicon tracker and muon detectors [33]. Quality requirements based on the minimum number of measurements in the silicon tracker, pixel detector, and muon detectors are applied to suppress backgrounds from decays-in-flight and hadron shower remnants that reach the muon system. Electrons are reconstructed by combining tracks produced by the Gaussian-sum filter algorithm with ECAL clusters [34]. Requirements on the track quality, the shape of the energy deposits in the ECAL, and the compatibility of the measurements from the tracker and the ECAL are imposed to distinguish prompt electrons from charged pions and from electrons produced by photon conversions. The electron and muon reconstruction efficiencies are >99% for $p_{\mathrm{T}} > 8\,\mathrm{GeV}$.

The electron and muon candidates are required to satisfy isolation criteria in order to reject non-prompt leptons from the hadronization of quarks and gluons. Relative isolation is defined as the scalar sum of the p_{T} values of reconstructed charged and neutral particles within a cone of radius $\Delta R \equiv \sqrt{(\Delta\eta)^2 + (\Delta\phi)^2} = 0.4$ (where ϕ is the azimuthal angle in radians) around the lepton-candidate track, divided by the p_{T} of the lepton candidate. To suppress the effects of pileup, tracks from charged particles not associated with the primary vertex are excluded from the isolation sum, and the contribution to pileup from reconstructed neutral hadrons is subtracted [29]. The contribution from the electron or muon candidate is removed from the sum. The value of the isolation variable is required to be ≤ 0.0821 for electrons and ≤ 0.25 for muons [33, 34].

The total efficiency for the muon identification and isolation requirements is 96% for muons with $p_{\mathrm{T}} > 10\,\mathrm{GeV}$ and $|\eta| < 2.1$. The rate at which pions undergoing $\pi^{\pm} \to \mu^{\pm}\nu_{\mu}$ decay are misidentified as prompt muons is 10^{-3} for pions with $p_{\mathrm{T}} > 10\,\mathrm{GeV}$ and $|\eta| < 2.1$. The total efficiency for the electron identification and isolation requirements is 85 (80)% for electrons with $p_{\mathrm{T}} > 10\,\mathrm{GeV}$ in the barrel (endcap) region [34]. The jet$\to$ e misidentification rate is 5×10^{-3} for jets with $p_{\mathrm{T}} > 10\,\mathrm{GeV}$ and $|\eta| < 2.1$ [34].

Hadronic decays of τ leptons are reconstructed and identified using the hadrons-plus-strips algorithm [35], which is designed to optimize the performance of the τ_{h} reconstruction by considering specific τ_{h} decay modes. To suppress backgrounds in which light-quark or gluon jets can mimic τ_{h} decays, a τ_{h} candidate is required to be spatially isolated from other energy deposits in the event. The isolation variable is calculated using a multivariate boosted decision tree technique within a cone of radius $\Delta R = 0.5$ around the direction of the τ_{h} candidate and considering the energy deposits of particles not included in the reconstruction of the τ_{h} decay mode. Additionally, τ_{h} candidates are required to be distinguishable from electrons and muons in the event by using dedicated criteria based on the consistency among the measurements in the tracker, calorimeters, and muon detectors. With these requirements, the contribution from electrons and muons being misidentified as genuine τ_{h} candidates is negligible ($\ll$0.1%).

The identification and isolation efficiency at the tight working point used in this analysis is approximately 50% for a τ_{h} lepton with $p_{\mathrm{T}} > 20\,\mathrm{GeV}$ and $|\eta| < 2.1$, while the probability for a jet to be misidentified as a τ_{h} is 1–5%, depending on the p_{T} and η values of the τ_{h} candidate [35]. Although the tight working point is used to define the τ_{h}jj signal region, a loose working point is used to obtain multijet enriched control samples for estimation of the background rate in the signal region. The identification and isolation efficiency for a τ_{h} lepton at the loose working point used in this analysis is approximately 60%, while the probability for a jet to be misidentified as a τ_{h} is about 10%.

The event selection criteria used in each search channel are summarized in section 5.

4 Signal and background samples

The SM background composition depends on the final state of each channel considered in the analysis. The main backgrounds in the four channels considered in the analysis are estimated using data-driven methods. Negligible or minor backgrounds are obtained directly from simulation. For the ejj and μjj channels, the main backgrounds are from $\mathrm{t\bar{t}}$ production and W boson production in association with jets (W+jets). Subdominant background sources come from single top quark, diboson (WW, WZ, and ZZ, collectively referred to as VV) and Z+jets production. For the τ_{h}jj channel, the main source of background consists of SM events only containing jets produced via the strong interaction, referred to as quantum chromodynamics (QCD) multijet events, followed by W+jets and $\mathrm{t\bar{t}}$ production. In the 0ℓjj channel, the main backgrounds are W/Z+jets and QCD multijet events, with a minor contribution from $\mathrm{t\bar{t}}$ and diboson production.

The W+jets, $\mathrm{t\bar{t}}$, and single top quark processes produce events with genuine leptons, $p_{\mathrm{T}}^{\mathrm{miss}}$, and jets. The Z+jets process contributes to the background composition when one of the leptons is lost as a result of detector acceptance or inefficiencies in the reconstruction and identification algorithms. Although jets in QCD events have a 1–5% probability of being misidentified as a τ_{h}, the large QCD multijet production cross section results in a substantial contribution of this background to the τ_{h}jj channel.

In the 0ℓjj channel, the Z+jets background produces genuine $p_{\mathrm{T}}^{\mathrm{miss}}$ when the Z boson decays into neutrinos. The W+jets process also has real $p_{\mathrm{T}}^{\mathrm{miss}}$ when the W boson decays leptonically, but it results in a similar 0ℓjj final state when the lepton is not observed as a consequence of the detector acceptance or is not properly reconstructed or identified because of inefficiencies in the corresponding algorithms. The QCD multijet events can also have significant $p_{\mathrm{T}}^{\mathrm{miss}}$ from mismeasurement of jet energies.

Simulated samples of signal and background events are generated using Monte Carlo (MC) event generators. The signal event samples are generated with the MadGraph5_aMC@NLO v2.3.3 generator [36] at leading order (LO) precision, considering pure electroweak pair production of $\widetilde{\chi}_1^{\pm}$ and $\widetilde{\chi}_2^0$ gauginos ($\widetilde{\chi}_1^{\pm}\widetilde{\chi}_1^{\pm}$, $\widetilde{\chi}_1^{\pm}\widetilde{\chi}_1^{\mp}$, $\widetilde{\chi}_1^{\pm}\widetilde{\chi}_2^0$, and $\widetilde{\chi}_2^0\widetilde{\chi}_2^0$) with two associated partons. Models with a bino-like $\widetilde{\chi}_1^0$ and wino-like $\widetilde{\chi}_2^0$ and $\widetilde{\chi}_1^{\pm}$ are considered. The signal events are generated requiring a pseudorapidity gap $|\Delta\eta| > 3.5$ between the two partons, with $p_{\mathrm{T}} > 30\,\mathrm{GeV}$ for each parton. This parton level $|\Delta\eta|$ requirement is verified to provide no bias with respect to the final requirement on the reconstructed dijet pseudorapidity gap. The LO cross sections in this paper are obtained with these parton-level requirements. Note that VBF $\widetilde{\chi}_1^{\pm}\widetilde{\chi}_2^0$ production is the dominant process in the models considered, composing about 60% of the total signal cross section, while the VBF $\widetilde{\chi}_1^{\pm}\widetilde{\chi}_1^{\mp}$ process is the second-largest contribution, composing about 30% of the total signal cross section. The VBF $\widetilde{\chi}_1^{\pm}\widetilde{\chi}_1^{\pm}$ and $\widetilde{\chi}_2^0\widetilde{\chi}_2^0$ processes compose about 10% of the total signal cross section. The $\mathrm{Z}/\gamma^*(\to \ell^+\ell^-)$+jets, $\mathrm{Z}(\to \nu_\ell\overline{\nu}_\ell)$+jets, and $\mathrm{W}(\to \ell\nu_\ell)$+jets backgrounds are also simulated at LO precision using MadGraph5_aMC@NLO, where up to four partons in the final state are included in the matrix element calculation. The background processes involving the production of a single vector boson in association with two jets exclusively through pure electroweak interactions are simulated at LO via MadGraph5_aMC@NLO. The interference effect between pure electroweak and mixed electroweak-QCD production of V+jets events has been studied and found to be small [37]. The effect is neglected in our analysis and the sum of these two samples is henceforth referred to as Z+jets. The QCD multijet background is also simulated at LO using MadGraph5_aMC@NLO. Single top quark and $\mathrm{t\overline{t}}$ processes are generated at next-to-leading order (NLO) using the POWHEG v2.0 generator [38–42]. The leading order PYTHIA v8.212 generator is used to model the diboson processes. The POWHEG and MadGraph generators are interfaced with the PYTHIA v8.212 [43] program, which is used to describe the parton shower and the hadronization and fragmentation processes with the CUETP8M1 tune [44]. The NNPDF3.0 LO and NLO [45] parton distribution functions (PDFs) are used in the event generation. Double counting of the partons generated with MadGraph5_aMC@NLO and POWHEG interfaced with PYTHIA is removed using the MLM [46] matching scheme. The LO cross sections are used to normalize simulated signal events, while NLO cross sections are used for simulated backgrounds [36, 42, 47, 48].

For both signal and background simulated events, additional pileup interactions are generated with PYTHIA and superimposed on the primary collision process. The simulated events are reweighted to match the pileup distribution observed in data. The background samples are processed with a detailed simulation of the CMS apparatus using the Geant4 package [49], while the CMS fast simulation package [50] is used to simulate the CMS detector for the signal samples.

5 Event selection

Events are selected using a trigger with a threshold of 120 GeV on both $p_{\mathrm{T,trig}}^{\mathrm{miss}}$ and $H_{\mathrm{T,trig}}^{\mathrm{miss}}$. The variable $p_{\mathrm{T,trig}}^{\mathrm{miss}}$ corresponds to the magnitude of the vector $\vec{p}_{\mathrm{T}}$ sum of all the PF candidates reconstructed at the trigger level, while $H_{\mathrm{T,trig}}^{\mathrm{miss}}$ is computed as the magnitude of the vector $\vec{p}_{\mathrm{T}}$ sum of all jets with $p_{\mathrm{T}} > 20\,\mathrm{GeV}$ and $|\eta| < 5.0$ reconstructed at the trigger level. The energy fraction attributed to neutral hadrons in these jets is required to be smaller than 0.9. This requirement suppresses anomalous events with jets originating from detector noise. To be able to use the same trigger for selecting events in the muon control samples used for background prediction, muon candidates are not included in the $p_{\mathrm{T,trig}}^{\mathrm{miss}}$ nor $H_{\mathrm{T,trig}}^{\mathrm{miss}}$ computation. The $p_{\mathrm{T}}^{\mathrm{miss}}$ threshold defining the search regions is chosen to achieve a trigger efficiency greater than 95%.

While the compressed mass spectrum SUSY models considered in this analysis result in final states with multiple leptons [20, 22], the compressed mass spectra scenarios of interest also result in low-p_{T} visible decay products, making it difficult to reconstruct and identify multiple leptons. For this reason, events are required to have zero or exactly one well-identified soft lepton. In the μjj channel, an additional lepton veto is applied by rejecting events containing a second muon ($p_{\mathrm{T}} > 8\,\mathrm{GeV}$), an electron ($p_{\mathrm{T}} > 10\,\mathrm{GeV}$), or a τ_{h} candidate ($p_{\mathrm{T}} > 20\,\mathrm{GeV}$). Similarly, ejj and τ_{h}jj channel events are required not to contain another electron, muon, or τ_{h} candidate. The 0ℓjj channel selects events without a well-identified electron, muon, or τ_{h} candidate. The veto on additional leptons maintains high efficiency for compressed mass spectra scenarios and simultaneously reduces the SM backgrounds. To further suppress QCD multijet background events containing large $p_{\mathrm{T}}^{\mathrm{miss}}$ from jet mismeasurements, the minimum azimuthal separation between any jet with $p_{\mathrm{T}} > 30\,\mathrm{GeV}$ and the direction of the missing transverse momentum vector is required to be greater than 0.5 ($|\Delta\phi_{\mathrm{min}}(\vec{p}_{\mathrm{T}}^{\mathrm{miss}}, j)| > 0.5$). Muon, electron, and τ_{h} candidates must have $8 < p_{\mathrm{T}} < 40\,\mathrm{GeV}$, $10 < p_{\mathrm{T}} < 40\,\mathrm{GeV}$, and $20 < p_{\mathrm{T}} < 40\,\mathrm{GeV}$, respectively. The upper bound on lepton p_{T} suppresses the $\mathrm{Z} \to \ell\ell$ and $\mathrm{W} \to \ell\nu_{\ell}$ backgrounds where the average $p_{\mathrm{T}}(\ell)$ is about $m_{\mathrm{Z}}/2$ and $m_{\mathrm{W}}/2$, respectively. The lower bound on τ_{h} p_{T} is larger because of known difficulties reconstructing lower-p_{T} τ_{h} candidates, namely that they do not produce a narrow jet in the detector, which makes them difficult to distinguish from quark or gluon jets. All leptons are required to have $|\eta| < 2.1$ in order to select high quality and well-isolated leptons within the tracker acceptance. This requirement is 99% efficient for signal events. Lepton candidates are also required to pass the reconstruction, identification, and isolation criteria described in section 3.

In addition to the 0ℓ or 1ℓ selection, the following requirements are imposed. The event is required to have $p_{\mathrm{T}}^{\mathrm{miss}} > 250\,\mathrm{GeV}$, which largely suppresses the $\mathrm{Z} \to \ell\ell$ and QCD multijet backgrounds. In order to reduce top quark pair contamination, the event is required not to have any jet identified as a b quark jet, following the description in section 3; only jets with $p_{\mathrm{T}} > 30\,\mathrm{GeV}$, $|\eta| < 2.4$, and separated from the leptons by $\Delta R > 0.3$ are considered for b tags. In the 1ℓ channels, a minimum threshold on the transverse mass between the lepton and the $p_{\mathrm{T}}^{\mathrm{miss}}$ is imposed to minimize backgrounds with W bosons. It is required that $m_{\mathrm{T}}(\ell, p_{\mathrm{T}}^{\mathrm{miss}}) > 110\,\mathrm{GeV}$, i.e., beyond the Jacobian m_{W} peak. The lepton- and $p_{\mathrm{T}}^{\mathrm{miss}}$-based requirements described in this paragraph will be referred to as the "central selection."

The VBF signal topology is characterized by the presence of two jets in the forward direction, in opposite hemispheres, and with large dijet invariant mass [51–58]. On the other hand, the jets in background events are mostly central and have small dijet invariant

JHEP08(2019)150

masses. Additionally, the outgoing partons in VBF signal processes must carry relatively large p_{T} since they must have enough energy (and be within the detector acceptance) to produce a pair of heavy SUSY particles (as shown in figure 1). Therefore, the "VBF selection" is imposed by requiring at least two jets with $p_{\mathrm{T}} > 60\,\mathrm{GeV}$ and $|\eta| < 5.0$. In the 1ℓjj channels, only jets separated from the leptons by $\Delta R > 0.3$ are considered. All pairs of jet candidates passing the above requirements and having $|\Delta\eta| > 3.8$ and $\eta_1\eta_2 < 0$ are combined to form VBF dijet candidates. In the rare cases (<1%) where selected events contain more than one dijet candidate satisfying the VBF criteria, the VBF dijet candidate with the largest dijet mass is chosen since it is 97% likely to result in the correct VBF dijet pair for signal events. Selected dijet candidates are required to have $m_{\mathrm{jj}} > 1\,\mathrm{TeV}$.

The signal region (SR) is defined as the events that satisfy the central and VBF selection criteria.

6 Background estimation

The general methodology used for the estimation of background contributions in the SR is similar for all search channels and is based on both simulation and data. Background-enriched control regions (CR) are constructed by applying selections orthogonal to those for the SR. These CRs are used to measure the efficiencies of the VBF and central selections (the probability for a background component to satisfy the VBF and central selection criteria), determine the correction factors to account for these efficiencies, and derive the shapes of the m_{T} and m_{jj} background distributions in the SR. The correction factors are determined by assessing the level of agreement in the yields between data and simulation. The shapes of distributions are derived directly from the data in the CR, whenever possible, or from the MC simulated samples when correct modeling by simulation is validated in the dedicated CRs. For each final state, the same trigger is used for the CRs as for the corresponding SR.

The production of $\mathrm{t\bar{t}}$ events represents the largest background source in the ejj and μjj channels (approximately 57–64% of the total background), and the second largest background source for the τ_{h}jj channel (approximately 29% of the total background). In the 0ℓjj final state, since the combination of the lepton and b jet vetoes reduces this background to only approximately 5% of the total background rate, its contribution is determined entirely from simulation. The $\mathrm{t\bar{t}}$ background yields in the 1ℓjj channels are evaluated using the following equation:

$$N_{\mathrm{t\bar{t}}}^{\mathrm{pred}} = N_{\mathrm{t\bar{t}}}^{\mathrm{MC}}\, SF_{\mathrm{t\bar{t}}}^{\mathrm{CR}}, \tag{6.1}$$

where $N_{\mathrm{t\bar{t}}}^{\mathrm{pred}}$ is the predicted $\mathrm{t\bar{t}}$ background yield in the SR, $N_{\mathrm{t\bar{t}}}^{\mathrm{MC}}$ is the $\mathrm{t\bar{t}}$ rate predicted by simulation for the SR selection, and $SF_{\mathrm{t\bar{t}}}^{\mathrm{CR}}$ is the data-over-simulation correction factor, given by the ratio of observed data events to the $\mathrm{t\bar{t}}$ yield in simulation, measured in a $\mathrm{t\bar{t}}$ enriched CR. The numerator in the calculation of each correction factor is estimated by subtracting from data the contribution from other background events different from that under study, and the statistical uncertainty is propagated to the $SF_{\mathrm{t\bar{t}}}^{\mathrm{CR}}$ uncertainty.

The event selection criteria used to define the $\mathrm{t\bar{t}}$ CR must not bias the correction factor $SF^{\mathrm{CR}}_{\mathrm{t\bar{t}}}$. The simulated samples are used to check the closure of this method, ensuring that the lepton kinematics, the composition of the events, and the m_{T} and m_{jj} shapes are similar between the CRs and the SR. The closure tests demonstrate that the background determination techniques, described in detail below, reproduce the expected background distributions in both rate and shape to within the statistical uncertainties. Various control samples are also utilized to validate the correct determination of the correction factors with the data.

The $\mathrm{t\bar{t}}$ CR is obtained with similar selections to the SR, except requiring one jet tagged as a b quark jet. These control samples with 1 b-tagged jet are referred to as $\mathrm{CR_e}$, CR_{μ}, and $\mathrm{CR}_{\tau_\mathrm{h}}$. The 1 b-tagged jet requirement significantly increases the $\mathrm{t\bar{t}}$ purity of the control samples while still ensuring that those control samples contain the same kinematics and composition of misidentified leptons as the SR. The $\mathrm{t\bar{t}}$ purity of the resulting data CR, determined from simulation, depends on the final state, ranging from 67 to 83%. The measured data-over-simulation correction factors $SF^{\mathrm{CR}}_{\mathrm{t\bar{t}}}$ are 0.8 ± 0.3, 0.8 ± 0.2, and 1.3 ± 0.5 for the ejj, μjj, and $\tau_\mathrm{h}$jj channels, respectively. The quoted uncertainties are based on the statistics in data and the simulated samples. Systematic uncertainties are discussed in section 7. Figure 2 contains the m_{T} distributions for the $\mathrm{t\bar{t}}$ control regions: (upper left) $\mathrm{CR_e}$, (upper right) CR_{μ}, and (lower left) $\mathrm{CR}_{\tau_\mathrm{h}}$. The correction factors $SF^{\mathrm{CR}}_{\mathrm{t\bar{t}}}$ have been applied to the MC simulation distributions shown in figure 2. The m_{T} shapes between data and simulation are consistent within statistical uncertainties (the bands in the data over background (BG) ratio distributions represent the statistical uncertainties of the data and simulated samples). Therefore, the $\mathrm{t\bar{t}}$ m_{T} shapes in the SR are taken directly from simulation.

In general, the W+jets and Z+jets backgrounds represent an important contribution in the 0ℓjj and 1ℓjj channels, and their contributions to the SR are evaluated using two control regions CR1 and CR2 (defined below for each BG component) and using the equation:

$$N^{\mathrm{pred}}_{\mathrm{BG}} = N^{\mathrm{MC}}_{\mathrm{BG}}\, SF^{\mathrm{CR1}}_{\mathrm{BG}}(\mathrm{central})\, SF^{\mathrm{CR2}}_{\mathrm{BG}}(\mathrm{VBF}), \tag{6.2}$$

where $N^{\mathrm{pred}}_{\mathrm{BG}}$ is the predicted BG yield in the SR, $N^{\mathrm{MC}}_{\mathrm{BG}}$ is the rate predicted by simulation (with BG = W+jets and Z+jets) for the SR selection, $SF^{\mathrm{CR1}}_{\mathrm{BG}}(\mathrm{central})$ is the data-over-simulation correction factor for the central selection, given by the ratio of data to the BG simulation in control region CR1, and $SF^{\mathrm{CR2}}_{\mathrm{BG}}(\mathrm{VBF})$ the data-over-simulation correction factor for the efficiency of the VBF selections as determined in another background enriched control sample CR2.

The production of $\mathrm{Z}(\to \nu\bar{\nu})$+jets is the main SM background to the 0ℓjj SR, with a similar signal topology from the neutrino contributions to $p_{\mathrm{T}}^{\mathrm{miss}}$, and is therefore mostly irreducible. The strategy for the $\mathrm{Z}(\to \nu\bar{\nu})$+jets background estimation is to use simulation to model the $p_{\mathrm{T}}^{\mathrm{miss}}$ distribution, and jet and lepton vetoes. The background yields predicted by the MC simulated samples are corrected for observed differences with respect to the data in the CRs, and scaled to the fraction of events passing the VBF selection, derived from data. The modeling of the m_{jj} distribution is checked in the CRs. Two CRs are used to verify the MC simulation, estimate acceptance corrections used to scale the MC simulation

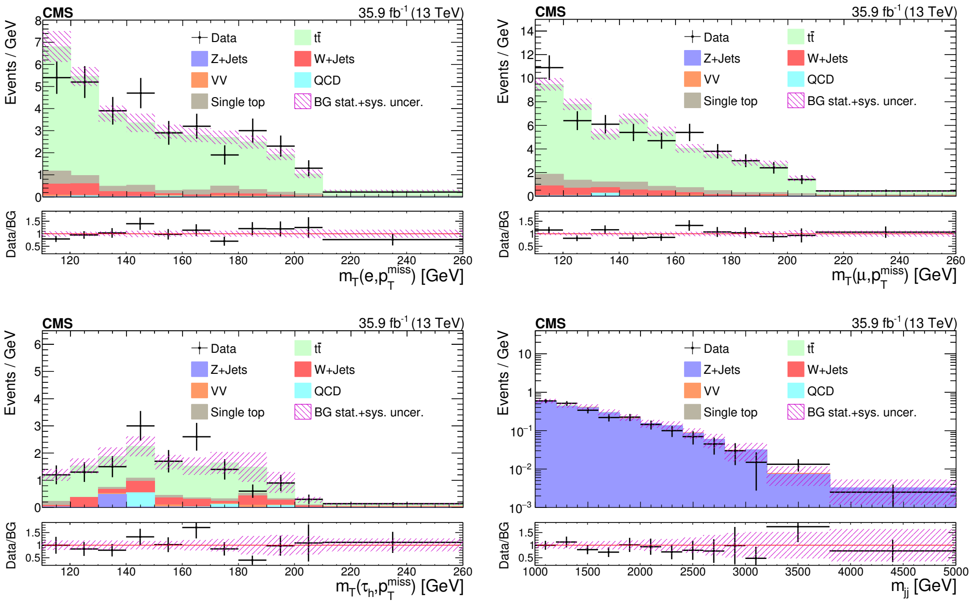

Figure 2. The m_{T} distributions in the $\mathrm{t\bar{t}}$ control regions: (upper left) $\mathrm{CR1_e}$, (upper right) $\mathrm{CR1}_\mu$, and (lower left) $\mathrm{CR1}_{\tau_\mathrm{h}}$; (lower right) the m_{jj} distribution for $\mathrm{Z}(\to \nu\overline{\nu})$+jets CR2 of the 0ℓjj channel.

yields, and measure the fraction of events passing the VBF selection. The control regions are defined by treating muons as neutrinos in the $\mathrm{Z} \to \mu^+\mu^-$ decay mode. The first control region ($\mathrm{CR1_Z}$) is a $\mathrm{Z}(\to \mu^+\mu^-)$+two jets sample used to validate modeling of geometric and kinematic acceptance of leptons. The invariant mass of the opposite-sign dimuon system must be consistent with the Z-boson mass (60-120 GeV). The two muons are treated as neutrinos, excluding the muon p_{T} vectors from $\vec{p}_{\mathrm{T}}^{\,\mathrm{miss}}$, and require $p_{\mathrm{T}}^{\mathrm{miss}} > 250\,\mathrm{GeV}$ together with a veto on b-tagged jets and additional leptons, as in the SR. The measured data-over-simulation correction factor is $0.95 \pm 0.02\,(\mathrm{stat})$. Adding the VBF selection defines $\mathrm{CR2_Z}$. The Z+jets prediction from simulation in $\mathrm{CR2_Z}$ is corrected with the measured data-over-simulation correction factor from $\mathrm{CR1_Z}$ to ensure $SF^{\mathrm{CR2}}_{\mathrm{BG}}$ represents a correction for the efficiency of the VBF selection (correlations between the uncertainties of $\mathrm{CR2_Z}$ and $\mathrm{CR1_Z}$ are also taken into account). The ratio of $\mathrm{CR2_Z}$ to $\mathrm{CR1_Z}$ events in the data gives the fraction of $\mathrm{Z}(\to \nu\overline{\nu})$+jets events passing the VBF topology selection. The measured data-over-simulation correction factor in $\mathrm{CR2_Z}$ is $0.92 \pm 0.12\,(\mathrm{stat})$. Figure 2 (lower right) shows the m_{jj} distribution in $\mathrm{Z}(\to \nu\overline{\nu})$+jets $\mathrm{CR2_Z}$, which shows agreement between the data and the corrected Z+jets prediction from simulation.

The production of W+jets events presents another important source of background for all the search channels. For the 1ℓjj channels, control samples enriched in W+jets events, with about 65% purity according to simulation, are obtained by requiring similar criteria to the SR, except with an inverted VBF selection (failing the VBF selection as defined in section 5). The inverted VBF selection enhances the W+jets background yield by two orders of magnitude, while suppressing the VBF signal contamination to negligible levels. This control region, $\mathrm{CR1_W}$, is used to obtain a correction factor for the efficiency of the central selection, $SF^{\mathrm{CR1}}_{\mathrm{W+jets}}(\mathrm{central})$. This correction factor is determined to be 0.97 ± 0.10 and

1.10±0.10, for the ejj and μjj channels, respectively. The quoted uncertainties are based on the statistics in data and the simulated samples. For the τ_{h}jj channel, it is difficult to obtain a control sample enriched in W+jets events because there is a significant contribution from QCD multijet events. Therefore, the average of the correction factors obtained for the ejj and μjj channels, 1.04±0.13, is used to scale the W+jets prediction from simulation in the τ_{h}jj channel. This approach is justified since the W($\rightarrow \tau\nu_\tau$)+jets prediction from simulation is corrected to account for slight differences in the τ_{h} identification efficiency observed in data. This is further supported by the fact that the modeling of the VBF efficiency at simulation level is uncorrelated with the decay of the W boson. The relatively small difference in mass between W and Z bosons (compared to the energy scale of the SR), which allows the use of a control sample (CR2$_{\mathrm{W}}$) enriched with Z+jets events to measure the VBF selection efficiency for the W+jets background in the 1ℓjj channels. This second control sample is obtained by selecting events containing two muons with $p_{\mathrm{T}} > 30\,\mathrm{GeV}$, treating only one muon as a neutrino to recalculate $\vec{p}_{\mathrm{T}}^{\,\mathrm{miss}}$, and otherwise similar selections to the SR. Since the efficiency and momentum scale of muons are known at the 1–2% level, any disagreement between data and simulation in this Z($\rightarrow \mu^+\mu^-$)+jets control sample is used to measure the correction factor for the modeling of the VBF selection efficiency in W+jets events. The correction factor $SF^{\mathrm{CR2}}_{\mathrm{W+jets}}$(VBF) determined from the CR2$_{\mathrm{W}}$ control sample is measured to be 1.18 ± 0.09 (correlations between the uncertainties of $SF^{\mathrm{CR2}}_{\mathrm{W+jets}}$ and $SF^{\mathrm{CR2}}_{\mathrm{Z+jets}}$ are taken into account). To validate the correction factors, the W+jets rate in samples with $m_{\mathrm{T}} < 110\,\mathrm{GeV}$ is scaled by $SF^{\mathrm{CR1}}_{\mathrm{W+jets}}$(central) and $SF^{\mathrm{CR2}}_{\mathrm{W+jets}}$(VBF), and agreement between the data and the corrected W+jets prediction from simulation is observed.

In the 0ℓjj channel, W($\rightarrow \ell\nu_\ell$)+jets events can enter the SR, because of the contribution to $p_{\mathrm{T}}^{\mathrm{miss}}$ from the neutrino, if the accompanying charged lepton fails the lepton veto criteria. To determine the contribution of W($\rightarrow \ell\nu_\ell$)+jets background to the 0ℓjj SR, a similar procedure to the Z($\rightarrow \nu\overline{\nu}$)+jets background estimation methodology is used. The muon veto is replaced with a one-muon requirement to obtain a W($\rightarrow \mu\nu_\mu$) plus two jets sample, requiring $60 < m_{\mathrm{T}}(\mu, p_{\mathrm{T}}^{\mathrm{miss}}) < 100\,\mathrm{GeV}$, treating the muon as undetected, and requiring $p_{\mathrm{T}}^{\mathrm{miss}} > 250\,\mathrm{GeV}$ as in the SR selection. The simulated samples are used to demonstrate that substituting the muon veto for a one-muon requirement does not affect the shapes of the $p_{\mathrm{T}}^{\mathrm{miss}}$ and VBF jet kinematic distributions. The measured data-over-simulation correction factor is $0.90 \pm 0.02\,(\mathrm{stat})$. The control region is obtained by adding the VBF topology selection, and has a measured data-over-simulation correction factor of $0.90 \pm 0.08\,(\mathrm{stat})$.

The QCD multijet background is only important in the 0ℓjj and τ_{h}jj channels. Among the main discriminating variables against QCD multijet events are the VBF selection criteria, the minimum separation between $\vec{p}_{\mathrm{T}}^{\,\mathrm{miss}}$ and any jet $|\Delta\phi_{\mathrm{min}}(\vec{p}_{\mathrm{T}}^{\,\mathrm{miss}}, j)|$, and τ_{h} isolation. Thus, the QCD multijet background estimation methodology utilizes CRs obtained by inverting these requirements. In the τ_{h}jj channel, the QCD multijet background is estimated using a completely data-driven approach which relies on the matrix ("ABCD") method. The regions are defined as follows:

- CRA: inverted VBF selection; pass the nominal (tight) τ_{h} isolation;
- CRB: inverted VBF selection; fail the nominal τ_{h} isolation but pass loose τ_{h} isolation;

JHEP08(2019)150

- CRC: pass the VBF selection; fail the nominal τ_h isolation but pass loose τ_h isolation and;

- CRD: pass the VBF selection; pass the nominal τ_h isolation

The QCD multijet component $N^\mathrm{i}_\mathrm{QCD}$ in regions $i = \mathrm{CR}A, \mathrm{CR}B, \mathrm{CR}C$ is estimated by subtracting non-QCD backgrounds (predicted using simulation) from data ($N^\mathrm{i}_\mathrm{QCD} = N^\mathrm{i}_\mathrm{Data} - N^\mathrm{i}_{\neq\mathrm{QCD}}$). The QCD multijet component in CRD (i.e., the SR) is then estimated to be $N^{SR}_\mathrm{QCD} = N^\mathrm{CRA}_\mathrm{QCD}\, N^\mathrm{CRC}_\mathrm{QCD}/N^\mathrm{CRB}_\mathrm{QCD}$, where $N^\mathrm{CRC}_\mathrm{QCD}/N^\mathrm{CRB}_\mathrm{QCD}$ is referred to as the "pass-to-fail VBF" transfer factor (TF_VBF). Said differently, the yield of QCD multijet events in data with an inverted VBF selection is extrapolated to the SR using the transfer factor TF_VBF, which is measured in data samples enriched with QCD multijet events that fail the nominal τ_h isolation criteria but satisfy the loose τ_h isolation working point (henceforth referred to as "inverted τ_h isolation" or "nonisolated τ_h"). The purity of the QCD multijet events is approximately 53–77% depending on the CR. The shape of the $m_\mathrm{T}(\tau_\mathrm{h}, p_\mathrm{T}^\mathrm{miss})$ distribution is obtained from CRB (from the nonisolated τ_h plus inverted VBF control sample). This "ABCD" method relies on TF_VBF being unbiased by the τ_h isolation requirement. A closure test of this assumption is provided using the simulated QCD multijet samples, resulting in agreement at a 5% level and within the statistical uncertainties.

In the 0ℓjj channel, the contribution from QCD multijet production is estimated using the number of events passing the analysis selection except the $|\Delta\phi_\mathrm{min}(\vec{p}_\mathrm{T}^\mathrm{miss}, j)|$ requirement. The QCD multijet purity in this CR is about 74% according to simulation. The m_jj distribution of the non-QCD background is subtracted from the m_jj data distribution, and the resultant QCD multijet m_jj distribution from data is scaled by the efficiency to inefficiency ratio of the $|\Delta\phi_\mathrm{min}(\vec{p}_\mathrm{T}^\mathrm{miss}, j)|$ requirement, $TF_{\Delta\phi}$. The transfer factor $TF_{\Delta\phi} = 0.06 \pm 0.01$ is determined using the simulated QCD multijet samples and validated using data control samples obtained by selecting events that fall in the dijet mass window $500 < m_\mathrm{jj} < 1000\,\mathrm{GeV}$.

7 Systematic uncertainties

The main contributions to the total systematic uncertainty in the background predictions arise from the closure tests and from the statistical uncertainties associated with the data CRs used to determine the $SF^\mathrm{CR1}_\mathrm{BG}$(central), $SF^\mathrm{CR2}_\mathrm{BG}$(VBF), TF_VBF, and $TF_{\Delta\phi}$ factors. The relative systematic uncertainties on the product $SF^\mathrm{CR1}_\mathrm{BG}$(central)$SF^\mathrm{CR2}_\mathrm{BG}$(VBF) related to the statistical precision in the CRs range between 8 and 42%, depending on the background component and search channel. For TF_VBF and $TF_{\Delta\phi}$, the statistical uncertainties lie between 13 and 22%. The systematic uncertainties in the $SF^\mathrm{CR1}_\mathrm{BG}$(central), $SF^\mathrm{CR2}_\mathrm{BG}$(VBF), TF_VBF, and $TF_{\Delta\phi}$ factors, evaluated from the closure tests and cross-checks with data, range from 9 to 33%, depending on the channel. Additionally, although the background m_T and m_jj shapes between data and simulation are consistent within statistical uncertainties, data/BG ratios of the m_T and m_jj distributions are fit with a first-order polynomial, and the deviation of the fit from unity, as a function of m_T or m_jj, is conservatively taken as the systematic uncertainty on the shape. This results in up to ≈10% systematic uncertainty in a given m_T or m_jj bin.

Less significant contributions to the systematic uncertainties arise from contamination by non-targeted background sources to the CRs used to measure $SF_{\rm BG}^{\rm CR1}$(central) and $SF_{\rm BG}^{\rm CR2}$(VBF), and from the uncertainties in these correction factors caused by uncertainties in the lepton identification efficiency, lepton energy and momentum scales, $p_{\rm T}^{\rm miss}$ scale, and trigger efficiency.

The efficiencies for the electron and muon reconstruction, identification, and isolation requirements are measured with the "tag-and-probe" method [33, 34] with a resulting uncertainty of $\leq$2%, dependent on $p_{\rm T}$ and η. The total efficiency for the $\tau_{\rm h}$ identification and isolation requirements is measured from a fit to the $\rm Z \to \tau\tau \to \mu\tau_{\rm h}$ visible mass distribution in a sample selected with one isolated muon trigger candidate with $p_{\rm T} > 24\,\rm GeV$, leading to a relative uncertainty of 5% per $\tau_{\rm h}$ candidate [35]. The $p_{\rm T}^{\rm miss}$ scale uncertainties contribute via the jet energy scale (2–5% depending on η and $p_{\rm T}$) and unclustered energy scale (10%) uncertainties, where "unclustered energy" refers to energy from a reconstructed object that is not assigned to a jet with $p_{\rm T} > 10\,\rm GeV$ or to a lepton with $p_{\rm T} > 10\,\rm GeV$. A $p_{\rm T}^{\rm miss}$-dependent uncertainty in the measured trigger efficiency results in a 3% uncertainty in the signal and background predictions that rely on simulation. The trigger efficiency is measured by calculating the fraction of W+jets events (selected with the same single-μ trigger), that also pass the same trigger that is used to define the SR.

The signal and minor backgrounds, estimated solely from simulation, are affected by similar sources of systematic uncertainty. For example, the uncertainties in the lepton identification efficiency, lepton energy and momentum scale, $p_{\rm T}^{\rm miss}$ scale, trigger efficiency, and integrated luminosity uncertainty of 2.5% [59] also contribute to the systematic uncertainty in the signal.

The signal event acceptance for the VBF selection depends on the reconstruction and identification efficiency and jet energy scale of forward jets. The total efficiency for the jet reconstruction and identification requirements is >98% for the entire η and $p_{\rm T}$ range, as validated through the agreement observed between data and simulation in the η distribution of jets, in particular at high η, in CRs enriched with $\rm t\bar{t}$ background events. Among the dominant uncertainties in the signal acceptance is the modeling of the kinematic properties of jets, and thus the efficiency to select VBF topologies for forward jets in the MadGraph simulation. This is investigated by comparing the predicted and measured $m_{\rm jj}$ spectra in the Z+jets CRs. The level of agreement between the predicted and observed $m_{\rm jj}$ spectra is better than 9%, which is assigned as a systematic uncertainty in the VBF efficiency for signal samples. The dominant uncertainty in the signal acceptance arises from the partial mistiming of signals in the forward region of the ECAL endcaps, which led to a reduction in the L1 trigger efficiency. A correction for this effect was determined using an unbiased data sample. This correction was found to be about 8% for $m_{\rm jj}$ of $1\,\rm TeV$ and increases to about 19% for $m_{\rm jj}$ greater than $3.5\,\rm TeV$. The uncertainty in the signal acceptance from the PDF set used in simulation is evaluated in accordance with the PDF4LHC recommendations [60] by comparing the results obtained using the CTEQ6.6L, MSTW08, and NNPDF10 PDF sets [61–63] with those from the default PDF set. It should be noted that the combined uncertainty on the signal yields and $m_{\rm jj}/m_{\rm T}$ shapes due to scale variations on renormalization, factorization, and jet matching is found to be about 2%, which is small

Process	μjj	ejj	τ_{h}jj	0ℓjj
DY+jets	0.20 ± 0.07	0.10 ± 0.04	0.10 ± 0.04	3714 ± 760
W+jets	13 ± 3	6 ± 1	7 ± 2	2999 ± 620
VV	1.7 ± 0.7	1.5 ± 0.6	0.9 ± 0.9	77 ± 18
$\mathrm{t\bar{t}}$	13 ± 4	11 ± 4	5 ± 3	577 ± 128
Single top quark	2.2 ± 0.9	0.2 ± 0.1	0.6 ± 0.3	104 ± 10
QCD	$0^{+0.2}_{-0}$	$0^{+1.2}_{-0}$	23 ± 5	546 ± 69
Total BG	31 ± 5	19 ± 5	37 ± 6	8017 ± 992
Data	36	29	38	8408

Table 1. The number of observed events and corresponding pre-fit background predictions, where "pre-fit" refers to the predictions determined as described in the text, before constraints from the fitting procedure have been applied. The uncertainties include the statistical and systematic components.

compared to our estimate of 9% using the Z+jets CRs. Other dominant uncertainties that contribute to the m_{jj} and m_{T} shape variations include the $p_{\mathrm{T}}^{\mathrm{miss}}$ energy scale, τ_{h} energy scale, and jet energy scale uncertainties.

8 Results and interpretation

Table 1 lists the number of observed events in data as well as the predicted background contributions in the SR for each channel, integrating over m_{jj} and m_{T} bins. Figure 3 shows the predicted SM background, expected signal, and observed data rates in bins of m_{T} for the 1ℓjj channels and bins of m_{jj} in the 0ℓjj channel. The bin sizes in the distributions of figure 3 are chosen to maximize the signal significance of the analysis. No significant excess of events is observed above the SM prediction in any of the search regions. Therefore the search does not reveal any evidence for new physics.

To illustrate the sensitivity of this search, the results are presented in the context of the R-parity conserving MSSM and considering cases such as those shown in figure 1 for pure electroweak VBF production of charginos and neutralinos. As mentioned previously, models with a bino-like $\widetilde{\chi}_1^0$ and wino-like $\widetilde{\chi}_2^0$ and $\widetilde{\chi}_1^\pm$ are considered. Since in this case the $\widetilde{\chi}_2^0$ and $\widetilde{\chi}_1^\pm$ belong to the same gauge group multiplet, the $\widetilde{\chi}_2^0$ mass is set to $m_{\widetilde{\chi}_2^0} = m_{\widetilde{\chi}_1^\pm}$ and results are presented as a function of this common mass and mass difference $\Delta m \equiv m(\widetilde{\chi}_2^0) - m(\widetilde{\chi}_1^0)$. Two scenarios have been considered: (*i*) the "light slepton" model where $\widetilde{\ell}$ is the next-to-lightest SUSY particle; and (*ii*) the "WZ" model where sleptons are too heavy and thus $\widetilde{\chi}_1^\pm$ and $\widetilde{\chi}_2^0$ decays proceed via W* and Z*. The main difference between the two models is the branching ratio of $\widetilde{\chi}_1^\pm$ and $\widetilde{\chi}_2^0$ to leptonic final states. It should be noted that the branching fractions to leptons are adapted to off-shell W and Z bosons. In the models shown in the top row of figure 1, the mass $m_{\widetilde{\ell}}$ of the intermediate slepton is parameterized in terms of a variable $x_{\widetilde{\ell}}$ as

$$m_{\widetilde{\ell}} = m_{\widetilde{\chi}_1^0} + x_{\widetilde{\ell}}(m_{\widetilde{\chi}_1^\pm} - m_{\widetilde{\chi}_1^0}), \tag{8.1}$$

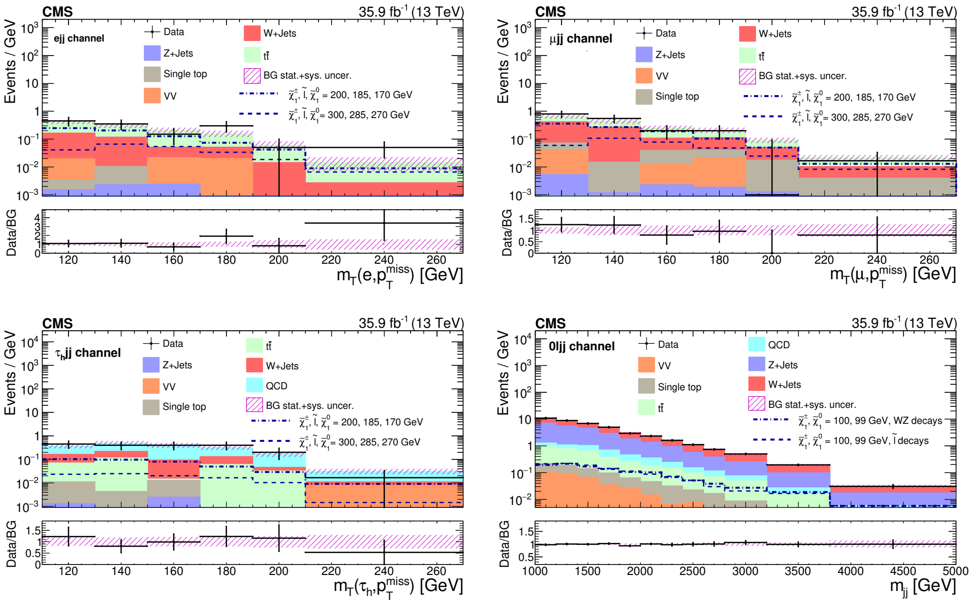

Figure 3. The observed m_{T} and m_{jj} distributions in the ejj (upper left), μjj (upper right), τ_{h}jj (lower left), and 0ℓjj (lower right) signal regions compared with the post-fit SM background yields from the fit described in the text. The pre-fit background yields and shapes are determined using data-driven methods for the major backgrounds, and based on simulation for the smaller backgrounds. Expected signal distributions are overlaid. The last bin in the m_{T} distributions of the 1ℓjj channels include all events with $m_{\mathrm{T}} > 210\,\mathrm{GeV}$. The last bin of the m_{jj} distributions of the 0ℓjj channel include all events with $m_{\mathrm{jj}} > 3800\,\mathrm{GeV}$.

where $0 < x_{\tilde{\ell}} < 1$. Results are presented for $x_{\tilde{\ell}} = 0.5$ in the "$\tilde{\ell}$-democratic" model where three sleptons ($m_{\tilde{\ell}} = m_{\tilde{\mathrm{e}}} = m_{\tilde{\mu}} = m_{\tilde{\tau}}$) are light [15]. The results are interpreted by assuming branching fractions $\mathcal{B}(\tilde{\chi}_2^0 \to \ell\tilde{\ell} \to \ell\ell\tilde{\chi}_1^0) = 1$ and $\mathcal{B}(\tilde{\chi}_1^{\pm} \to \nu_\ell\tilde{\ell} \to \nu_\ell\ell\tilde{\chi}_1^0) = 1$. To highlight the evolution of the search sensitivity for compressed spectra with mass gap Δm, values between $\Delta m = 1$ and $50\,\mathrm{GeV}$ are studied for both the light slepton and WZ interpretations. The signal selection efficiency for the 1μjj (1ejj) channel in the light slepton model, assuming $\Delta m = 30\,\mathrm{GeV}$, is 0.9 (0.7)% for $m(\tilde{\chi}_1^{\pm}) = 100\,\mathrm{GeV}$ and 2.5 (1.8)% for $m(\tilde{\chi}_1^{\pm}) = 300\,\mathrm{GeV}$. Similarly, the signal selection efficiency for the 0ℓjj channel, assuming $\Delta m = 1\,\mathrm{GeV}$, is 2.8% for $m(\tilde{\chi}_1^{\pm}) = 100\,\mathrm{GeV}$ and 5.3% for $m(\tilde{\chi}_1^{\pm}) = 300\,\mathrm{GeV}$.

The calculation of the exclusion limit is obtained by using the m_{T} (m_{jj}) distribution in the 1ℓjj (0ℓjj) to construct a combined profile likelihood ratio test statistic [64] in bins of m_{T} (m_{jj}) and computing a 95% confidence level (CL) upper limit (UL) on the signal cross section using the asymptotic $\mathrm{CL_s}$ criterion [64–66]. Systematic uncertainties are taken into account as nuisance parameters, which are removed by profiling, assuming gamma function or log-normal priors for normalization parameters, and Gaussian priors for mass spectrum shape uncertainties. The combination of the four search channels requires simultaneous analysis of the data from the individual channels, accounting for all statistical and systematic uncertainties and their correlations. Correlations among backgrounds, both

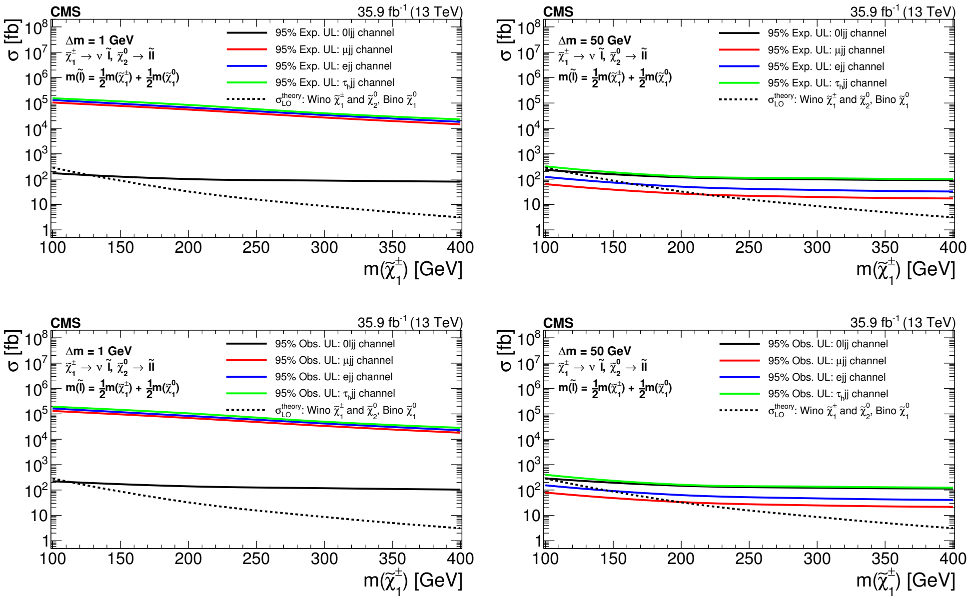

Figure 4. Combined 95% CL UL on the cross section as a function of $m_{\tilde{\chi}_2^0} = m_{\tilde{\chi}_1^\pm}$. The results correspond to $\Delta m = 1\,\text{GeV}$ (left) and $\Delta m = 50\,\text{GeV}$ (right) mass gaps between the chargino and the lightest neutralino in the light slepton model. The top row shows the expected limits, and the bottom row shows the observed limits.

within a channel and across channels, are taken into consideration in the limit calculation. For example, the uncertainty in the integrated luminosity is treated as fully correlated across channels. The uncertainties in the predicted signal yields resulting from the event acceptance variation with different sets of PDFs in a given m_T or m_{jj} bin are treated as uncorrelated within a channel and correlated across channels. The uncertainties from the closure tests are treated as uncorrelated within and across the different final states.

Figure 4 shows the expected and observed limits as well as the theoretical cross section as functions of $m_{\tilde{\chi}_1^\pm}$ for the $\Delta m = 1$ and $50\,\text{GeV}$ assumptions in the light slepton model. For the smallest value of $\Delta m = 1\,\text{GeV}$, the 0ℓjj channel provides the best sensitivity, while the VBF soft-e and soft-μ channels provide the best sensitivity for the larger mass gap scenario with $\Delta m = 50\,\text{GeV}$. The four channels are combined and the results are presented in figure 5. Figure 5 (left) shows the 95% CL UL on the signal cross section, as a function of $m(\tilde{\chi}_1^\pm)$ and Δm, assuming $x_{\tilde{\ell}} = 0.5$. Figure 5 (right) shows the 95% CL UL on the signal cross section, as a function of $m(\tilde{\chi}_1^\pm)$, for two fixed Δm values of 1 and $30\,\text{GeV}$, and assuming $x_{\tilde{\ell}} = 0.5$. The signal acceptance and mass shape are evaluated for each $\{m(\tilde{\chi}_1^\pm), \Delta m\}$ combination and used in the limit calculation procedure described above. For the $\Delta m = \{1, 10, 30, 50\}\,\text{GeV}$ assumption, the combination of the four channels results in an observed (expected) exclusion on the $\tilde{\chi}_2^0$ and $\tilde{\chi}_1^\pm$ gaugino masses below $\{112, 159, 215, 207\}$ $(\{125, 171, 235, 228\})$ GeV. For the compressed mass spectrum scenarios with $1 \leq \Delta m \leq 30\,\text{GeV}$, the bounds on the $\tilde{\chi}_2^0$ and $\tilde{\chi}_1^\pm$ gaugino masses are the most stringent to date.

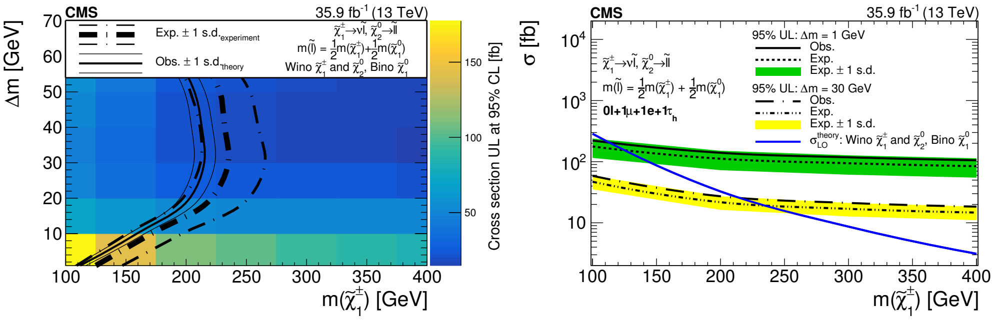

Figure 5. (Left) Expected and observed 95% confidence level upper limit (UL) on the signal cross section as a function of $m(\widetilde{\chi}_1^\pm)$ and Δm, assuming the light slepton model with slepton mass defined as the average of the $\widetilde{\chi}_2^0$ and $\widetilde{\chi}_1^\pm$ masses, $x_{\widetilde{\ell}} = 0.5$. The lower left edge of each bin represents the $\{m(\widetilde{\chi}_1^\pm), \Delta m\}$ combination used to calculate the UL on the signal cross section. For example, the lowest and leftmost bin corresponds to the UL on the signal cross section for the scenario with $m(\widetilde{\chi}_1^\pm) = 100\,\text{GeV}$ and $\Delta m = 1\,\text{GeV}$. (Right) Combined 95% CL UL on the cross section as a function of $m_{\widetilde{\chi}_2^0} = m_{\widetilde{\chi}_1^\pm}$, for $\Delta m = 1\,\text{GeV}$ and $\Delta m = 30\,\text{GeV}$ mass gaps between the chargino and the neutralino, assuming the light slepton model.

It is noted that for the $1 < \Delta m < 10\,\text{GeV}$ mass gaps considered in this analysis, the exclusions on $m(\widetilde{\chi}_1^\pm)$ do not depend on the assumption that a light slepton exists (i.e. $m(\widetilde{\chi}_1^0) < m_{\widetilde{\ell}} < m(\widetilde{\chi}_1^\pm)$). For $1 < \Delta m < 10\,\text{GeV}$, the signal acceptance for the WZ model is similar to the signal acceptance for the light slepton model. For example, figure 3 (lower right) shows the expected m_{jj} signal distribution when the decays of the charginos and neutralinos proceed via W and Z bosons, resulting in a similar shape and normalization as the expectation for the light slepton scenario. However, for increasing Δm values where the 1ℓjj channels dominate the sensitivity, the exclusions on $m(\widetilde{\chi}_1^\pm)$ in the WZ model are less stringent than the ones in the light slepton model. This difference is a result of the lower branching ratio of $\widetilde{\chi}_1^\pm$ and $\widetilde{\chi}_2^0$ to leptonic final states in the WZ model.

Figure 6 (left) shows the 95% CL UL on the signal cross section, as a function of $m(\widetilde{\chi}_1^\pm)$ and Δm, assuming the WZ model. Figure 6 (right) shows the 95% CL UL on the signal cross section, as a function of $m(\widetilde{\chi}_1^\pm)$, for two fixed Δm values of 1 and 30 GeV, and assuming the WZ model. For the $\Delta m = \{1, 10, 30, 50\}$ GeV assumption, the combination of the four channels results in an observed (expected) exclusion on the $\widetilde{\chi}_2^0$ and $\widetilde{\chi}_1^\pm$ gaugino masses below $\{112, 146, 175, 162\}$ $(\{125, 160, 194, 178\})$ GeV. For the compressed mass spectrum scenarios with $1 \leq \Delta m < 3\,\text{GeV}$ and $25 \leq \Delta m < 50\,\text{GeV}$, the bounds on the $\widetilde{\chi}_2^0$ and $\widetilde{\chi}_1^\pm$ gaugino masses in the WZ model are also the most stringent to date, surpassing the bounds from the LEP experiments [67–70].

9 Summary

A search is presented for noncolored supersymmetric particles produced in the vector boson fusion (VBF) topology using data corresponding to an integrated luminosity of $35.9\,\text{fb}^{-1}$ collected in 2016 with the CMS detector in proton-proton collisions at $\sqrt{s} = 13\,\text{TeV}$. The search utilizes events in four different channels depending on the number and type of

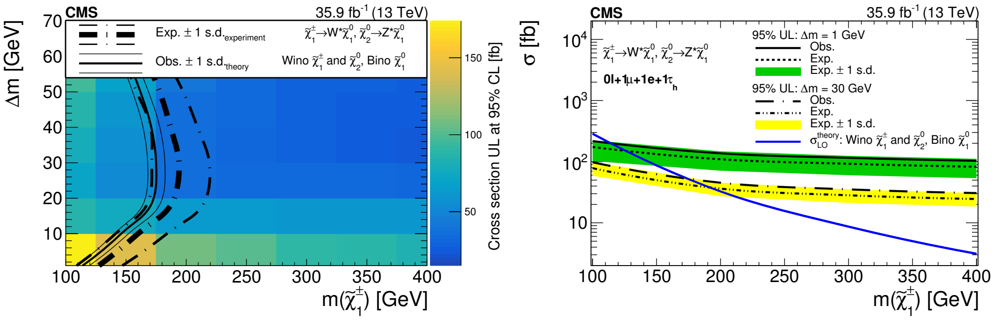

Figure 6. (Left) Expected and observed 95% confidence level upper limit (UL) on the signal cross section as a function of $m(\widetilde{\chi}_1^{\pm})$ and Δm, assuming the $\widetilde{\chi}_1^{\pm}$ and $\widetilde{\chi}_2^0$ decays proceed via W^* and Z^*. The lower left edge of each bin represents the $\{m(\widetilde{\chi}_1^{\pm}), \Delta m\}$ combination used to calculate the UL on the signal cross section. For example, the lowest and leftmost bin corresponds to the UL on the signal cross section for the scenario with $m(\widetilde{\chi}_1^{\pm}) = 100\,\text{GeV}$ and $\Delta m = 1\,\text{GeV}$. (Right) The 95% CL UL on the cross section as a function of $m_{\widetilde{\chi}_2^0} = m_{\widetilde{\chi}_1^{\pm}}$, for $\Delta m = 1\,\text{GeV}$ and $\Delta m = 30\,\text{GeV}$ mass gaps between the chargino and the neutralino, after combining 0 lepton and 1 lepton channels, assuming the $\widetilde{\chi}_1^{\pm}$ and $\widetilde{\chi}_2^0$ decays proceed via W^* and Z^*.

leptons: 0ℓjj, ejj, μjj, and τ_{h}jj, where τ_{h} denotes a hadronically decaying τ lepton. While ref. [71] reported a search using the VBF dijet topology with a zero-lepton final state in proton-proton collision data at $\sqrt{s} = 8\,\text{TeV}$, this is the first search for the compressed electroweak supersymmetry (SUSY) sector using the 0ℓjj final state. This is also the first search for SUSY in the VBF topology with single soft-lepton final states. The VBF topology requires two well-separated jets that appear in opposite hemispheres, with large invariant mass m_{jj}. The observed m_{jj} and transverse mass $m_{\mathrm{T}}(\ell, p_{\mathrm{T}}^{\text{miss}})$ distributions do not reveal any evidence for new physics. The results are used to exclude a range of $\widetilde{\chi}_1^{\pm}$ and $\widetilde{\chi}_2^0$ gaugino masses. For a compressed mass spectrum scenario, in which $\Delta m \equiv m(\widetilde{\chi}_1^{\pm}) - m(\widetilde{\chi}_1^0) = 1$ (30) GeV and in which $\widetilde{\chi}_1^{\pm}$ and $\widetilde{\chi}_2^0$ branching fractions to light sleptons are 100%, $\widetilde{\chi}_1^{\pm}$ and $\widetilde{\chi}_2^0$ masses up to 112 (215) GeV are excluded at 95% CL. For the scenario where the sleptons are too heavy and decays of the charginos and neutralinos proceed via W^* and Z^* bosons, $\widetilde{\chi}_1^{\pm}$ and $\widetilde{\chi}_2^0$ masses up to 112 (175) GeV are excluded at 95% CL for $\Delta m = 1$ (30) GeV. While many previous studies at the LHC have focused on strongly coupled supersymmetric particles, including searches for charginos and neutralinos produced in gluino or squark decay chains, and a number of studies have presented limits on the Drell-Yan production of charginos and neutralinos, this analysis obtains the most stringent limits to date on the production of charginos and neutralinos decaying to leptons in compressed mass spectrum scenarios defined by the mass separation $1 \leq \Delta m < 3\,\text{GeV}$ and $25 \leq \Delta m < 50\,\text{GeV}$.

Acknowledgments

We congratulate our colleagues in the CERN accelerator departments for the excellent performance of the LHC and thank the technical and administrative staffs at CERN and at other CMS institutes for their contributions to the success of the CMS effort. In addition, we gratefully acknowledge the computing centers and personnel of the Worldwide LHC

Computing Grid for delivering so effectively the computing infrastructure essential to our analyses. Finally, we acknowledge the enduring support for the construction and operation of the LHC and the CMS detector provided by the following funding agencies: BMBWF and FWF (Austria); FNRS and FWO (Belgium); CNPq, CAPES, FAPERJ, FAPERGS, and FAPESP (Brazil); MES (Bulgaria); CERN; CAS, MoST, and NSFC (China); COLCIENCIAS (Colombia); MSES and CSF (Croatia); RPF (Cyprus); SENESCYT (Ecuador); MoER, ERC IUT, PUT and ERDF (Estonia); Academy of Finland, MEC, and HIP (Finland); CEA and CNRS/IN2P3 (France); BMBF, DFG, and HGF (Germany); GSRT (Greece); NKFIA (Hungary); DAE and DST (India); IPM (Iran); SFI (Ireland); INFN (Italy); MSIP and NRF (Republic of Korea); MES (Latvia); LAS (Lithuania); MOE and UM (Malaysia); BUAP, CINVESTAV, CONACYT, LNS, SEP, and UASLP-FAI (Mexico); MOS (Montenegro); MBIE (New Zealand); PAEC (Pakistan); MSHE and NSC (Poland); FCT (Portugal); JINR (Dubna); MON, RosAtom, RAS, RFBR, and NRC KI (Russia); MESTD (Serbia); SEIDI, CPAN, PCTI, and FEDER (Spain); MOSTR (Sri Lanka); Swiss Funding Agencies (Switzerland); MST (Taipei); ThEPCenter, IPST, STAR, and NSTDA (Thailand); TUBITAK and TAEK (Turkey); NASU and SFFR (Ukraine); STFC (United Kingdom); DOE and NSF (U.S.A.).

Individuals have received support from the Marie-Curie program and the European Research Council and Horizon 2020 Grant, contract Nos. 675440, 752730, and 765710 (European Union); the Leventis Foundation; the A.P. Sloan Foundation; the Alexander von Humboldt Foundation; the Belgian Federal Science Policy Office; the Fonds pour la Formation à la Recherche dans l'Industrie et dans l'Agriculture (FRIA-Belgium); the Agentschap voor Innovatie door Wetenschap en Technologie (IWT-Belgium); the F.R.S.-FNRS and FWO (Belgium) under the "Excellence of Science — EOS" — be.h project n. 30820817; the Beijing Municipal Science & Technology Commission, No. Z181100004218003; the Ministry of Education, Youth and Sports (MEYS) of the Czech Republic; the Lendület ("Momentum") Program and the János Bolyai Research Scholarship of the Hungarian Academy of Sciences, the New National Excellence Program ÚNKP, the NKFIA research grants 123842, 123959, 124845, 124850, 125105, 128713, 128786, and 129058 (Hungary); the Council of Science and Industrial Research, India; the HOMING PLUS program of the Foundation for Polish Science, cofinanced from European Union, Regional Development Fund, the Mobility Plus program of the Ministry of Science and Higher Education, the National Science Center (Poland), contracts Harmonia 2014/14/M/ST2/00428, Opus 2014/13/B/ST2/02543, 2014/15/B/ST2/03998, and 2015/19/B/ST2/02861, Sonatabis 2012/07/E/ST2/01406; the National Priorities Research Program by Qatar National Research Fund; the Ministry of Science and Education, grant no. 3.2989.2017 (Russia); the Programa Estatal de Fomento de la Investigación Científica y Técnica de Excelencia María de Maeztu, grant MDM-2015-0509 and the Programa Severo Ochoa del Principado de Asturias; the Thalis and Aristeia programs cofinanced by EU-ESF and the Greek NSRF; the Rachadapisek Sompot Fund for Postdoctoral Fellowship, Chulalongkorn University and the Chulalongkorn Academic into Its 2nd Century Project Advancement Project (Thailand); the Welch Foundation, contract C-1845; and the Weston Havens Foundation (U.S.A.).

References

[1] P. Ramond, *Dual theory for free fermions*, *Phys. Rev.* **D 3** (1971) 2415 [INSPIRE].

[2] Yu. A. Golfand and E.P. Likhtman, *Extension of the algebra of Poincaré group generators and violation of p invariance*, *JETP Lett.* **13** (1971) 323 [INSPIRE].

[3] S. Ferrara and B. Zumino, *Supergauge invariant Yang-Mills theories*, *Nucl. Phys.* **B 79** (1974) 413 [INSPIRE].

[4] J. Wess and B. Zumino, *Supergauge transformations in four-dimensions*, *Nucl. Phys.* **B 70** (1974) 39 [INSPIRE].

[5] A.H. Chamseddine, R.L. Arnowitt and P. Nath, *Locally supersymmetric grand unification*, *Phys. Rev. Lett.* **49** (1982) 970 [INSPIRE].

[6] R. Barbieri, S. Ferrara and C.A. Savoy, *Gauge models with spontaneously broken local supersymmetry*, *Phys. Lett.* **119B** (1982) 343 [INSPIRE].

[7] L.J. Hall, J.D. Lykken and S. Weinberg, *Supergravity as the messenger of supersymmetry breaking*, *Phys. Rev.* **D 27** (1983) 2359 [INSPIRE].

[8] CMS collaboration, *Search for new phenomena with the M_{T2} variable in the all-hadronic final state produced in proton-proton collisions at $\sqrt{s} = 13$ TeV*, *Eur. Phys. J.* **C 77** (2017) 710 [`arXiv:1705.04650`] [INSPIRE].

[9] CMS collaboration, *Search for supersymmetry in multijet events with missing transverse momentum in proton-proton collisions at* 13 *TeV*, *Phys. Rev.* **D 96** (2017) 032003 [`arXiv:1704.07781`] [INSPIRE].

[10] ATLAS collaboration, *Search for squarks and gluinos in events with an isolated lepton, jets and missing transverse momentum at $\sqrt{s} = 13$ TeV with the ATLAS detector*, *Phys. Rev.* **D 96** (2017) 112010 [`arXiv:1708.08232`] [INSPIRE].

[11] ATLAS collaboration, *Search for squarks and gluinos in final states with jets and missing transverse momentum using $36\,fb^{-1}$ of $\sqrt{s} = 13$ TeV pp collision data with the ATLAS detector*, *Phys. Rev.* **D 97** (2018) 112001 [`arXiv:1712.02332`] [INSPIRE].

[12] J. Alwall, P. Schuster and N. Toro, *Simplified models for a first characterization of new physics at the LHC*, *Phys. Rev.* **D 79** (2009) 075020 [`arXiv:0810.3921`] [INSPIRE].

[13] LHC NEW PHYSICS WORKING GROUP collaboration, *Simplified models for LHC new physics searches*, *J. Phys.* **G 39** (2012) 105005 [`arXiv:1105.2838`] [INSPIRE].

[14] G.R. Farrar and P. Fayet, *Phenomenology of the production, decay and detection of new hadronic states associated with supersymmetry*, *Phys. Lett.* **76B** (1978) 575 [INSPIRE].

[15] CMS collaboration, *Combined search for electroweak production of charginos and neutralinos in proton-proton collisions at $\sqrt{s} = 13$ TeV*, *JHEP* **03** (2018) 160 [`arXiv:1801.03957`] [INSPIRE].

[16] ATLAS collaboration, *Search for electroweak production of supersymmetric particles in final states with two or three leptons at $\sqrt{s} = 13$ TeV with the ATLAS detector*, *Eur. Phys. J.* **C 78** (2018) 995 [`arXiv:1803.02762`] [INSPIRE].

[17] ATLAS collaboration, *Search for chargino-neutralino production using recursive jigsaw reconstruction in final states with two or three charged leptons in proton-proton collisions at* $\sqrt{s} = 13$ *TeV with the ATLAS detector*, *Phys. Rev.* **D 98** (2018) 092012 [`arXiv:1806.02293`] [INSPIRE].

[18] ATLAS collaboration, *Search for electroweak production of supersymmetric states in scenarios with compressed mass spectra at* $\sqrt{s} = 13$ *TeV with the ATLAS detector*, *Phys. Rev.* **D 97** (2018) 052010 [`arXiv:1712.08119`] [INSPIRE].

[19] CMS collaboration, *Search for new physics in events with two soft oppositely charged leptons and missing transverse momentum in proton-proton collisions at* $\sqrt{s} = 13$ *TeV*, *Phys. Lett.* **B 782** (2018) 440 [`arXiv:1801.01846`] [INSPIRE].

[20] B. Dutta et al., *Vector boson fusion processes as a probe of supersymmetric electroweak sectors at the LHC*, *Phys. Rev.* **D 87** (2013) 035029 [`arXiv:1210.0964`] [INSPIRE].

[21] G.F. Giudice, T. Han, K. Wang and L.-T. Wang, *Nearly degenerate gauginos and dark matter at the LHC*, *Phys. Rev.* **D 81** (2010) 115011 [`arXiv:1004.4902`] [INSPIRE].

[22] A.G. Delannoy et al., *Probing dark matter at the LHC using vector boson fusion processes*, *Phys. Rev. Lett.* **111** (2013) 061801 [`arXiv:1304.7779`] [INSPIRE].

[23] CMS collaboration, *Search for supersymmetry in the vector-boson fusion topology in proton-proton collisions at* $\sqrt{s} = 8$ *TeV*, *JHEP* **11** (2015) 189 [`arXiv:1508.07628`] [INSPIRE].

[24] CMS collaboration, *The CMS experiment at the CERN LHC*, 2008 *JINST* **3** S08004 [INSPIRE].

[25] CMS collaboration, *Particle-flow reconstruction and global event description with the CMS detector*, 2017 *JINST* **12** P10003 [`arXiv:1706.04965`] [INSPIRE].

[26] CMS collaboration, *Performance of missing energy reconstruction in 13 TeV pp collision data using the CMS detector*, CMS-PAS-JME-16-004 (2016).

[27] M. Cacciari, G.P. Salam and G. Soyez, *The anti-*k_t *jet clustering algorithm*, *JHEP* **04** (2008) 063 [`arXiv:0802.1189`] [INSPIRE].

[28] M. Cacciari, G.P. Salam and G. Soyez, *FastJet user manual*, *Eur. Phys. J.* **C 72** (2012) 1896 [`arXiv:1111.6097`] [INSPIRE].

[29] M. Cacciari and G.P. Salam, *Pileup subtraction using jet areas*, *Phys. Lett.* **B 659** (2008) 119 [`arXiv:0707.1378`] [INSPIRE].

[30] CMS collaboration, *Jet energy scale and resolution in the CMS experiment in pp collisions at 8 TeV*, 2017 *JINST* **12** P02014 [`arXiv:1607.03663`] [INSPIRE].

[31] CMS collaboration, *Pileup jet identification*, CMS-PAS-JME-13-005 (2013).

[32] CMS collaboration, *Identification of heavy-flavour jets with the CMS detector in pp collisions at* 13 *TeV*, 2018 *JINST* **13** P05011 [`arXiv:1712.07158`] [INSPIRE].

[33] CMS collaboration, *Performance of the CMS muon detector and muon reconstruction with proton-proton collisions at* $\sqrt{s} = 13$ *TeV*, 2018 *JINST* **13** P06015 [`arXiv:1804.04528`] [INSPIRE].

[34] CMS collaboration, *Performance of electron reconstruction and selection with the CMS detector in proton-proton collisions at* $\sqrt{s} = 8$ *TeV*, 2015 *JINST* **10** P06005 [`arXiv:1502.02701`] [INSPIRE].

[35] CMS collaboration, *Reconstruction and identification of* τ *lepton decays to hadrons and* ν_τ *at CMS*, 2016 *JINST* **11** P01019 [`arXiv:1510.07488`].

[36] J. Alwall et al., *The automated computation of tree-level and next-to-leading order differential cross sections and their matching to parton shower simulations*, *JHEP* **07** (2014) 079 [`arXiv:1405.0301`] [INSPIRE].

[37] CMS collaboration, *Electroweak production of two jets in association with a Z boson in proton–proton collisions at* $\sqrt{s} = 13\,TeV$, *Eur. Phys. J.* **C 78** (2018) 589 [`arXiv:1712.09814`] [INSPIRE].

[38] R. Frederix, E. Re and P. Torrielli, *Single-top t-channel hadroproduction in the four-flavour scheme with POWHEG and aMC@NLO*, *JHEP* **09** (2012) 130 [`arXiv:1207.5391`] [INSPIRE].

[39] P. Nason, *A new method for combining NLO QCD with shower Monte Carlo algorithms*, *JHEP* **11** (2004) 040 [`hep-ph/0409146`] [INSPIRE].

[40] S. Frixione, P. Nason and C. Oleari, *Matching NLO QCD computations with Parton Shower simulations: the POWHEG method*, *JHEP* **11** (2007) 070 [`arXiv:0709.2092`] [INSPIRE].

[41] S. Alioli, P. Nason, C. Oleari and E. Re, *A general framework for implementing NLO calculations in shower Monte Carlo programs: the POWHEG BOX*, *JHEP* **06** (2010) 043 [`arXiv:1002.2581`] [INSPIRE].

[42] E. Re, *Single-top Wt-channel production matched with parton showers using the POWHEG method*, *Eur. Phys. J.* **C 71** (2011) 1547 [`arXiv:1009.2450`] [INSPIRE].

[43] T. Sjöstrand et al., *An introduction to PYTHIA 8.2*, *Comput. Phys. Commun.* **191** (2015) 159 [`arXiv:1410.3012`] [INSPIRE].

[44] CMS collaboration, *Event generator tunes obtained from underlying event and multiparton scattering measurements*, *Eur. Phys. J.* **C 76** (2016) 155 [`arXiv:1512.00815`] [INSPIRE].

[45] NNPDF collaboration, *Parton distributions for the LHC Run II*, *JHEP* **04** (2015) 040 [`arXiv:1410.8849`] [INSPIRE].

[46] J. Alwall et al., *Comparative study of various algorithms for the merging of parton showers and matrix elements in hadronic collisions*, *Eur. Phys. J.* **C 53** (2008) 473 [`arXiv:0706.2569`] [INSPIRE].

[47] S. Alioli, P. Nason, C. Oleari and E. Re, *NLO single-top production matched with shower in POWHEG: s- and t-channel contributions*, *JHEP* **09** (2009) 111 [*Erratum ibid.* **1002** (2010) 011] [`arXiv:0907.4076`] [INSPIRE].

[48] M. Czakon and A. Mitov, *Top++: a program for the calculation of the top-pair cross-section at hadron colliders*, *Comput. Phys. Commun.* **185** (2014) 2930 [`arXiv:1112.5675`] [INSPIRE].

[49] GEANT4 collaboration, *GEANT4 — a simulation toolkit*, *Nucl. Instrum. Meth.* **A 506** (2003) 250 [INSPIRE].

[50] CMS collaboration, *The fast simulation of the CMS detector at LHC*, *J. Phys. Conf. Ser.* **331** (2011) 032049 [INSPIRE].

[51] B. Dutta et al., *Probing compressed bottom squarks with boosted jets and shape analysis*, *Phys. Rev.* **D 92** (2015) 095009 [`arXiv:1507.01001`] [INSPIRE].

[52] B. Dutta et al., *Probing compressed top squark scenarios at the LHC at* 14 *TeV*, *Phys. Rev.* **D 90** (2014) 095022 [`arXiv:1312.1348`] [INSPIRE].

[53] B. Dutta et al., *Probing compressed sleptons at the LHC using vector boson fusion processes*, *Phys. Rev.* **D 91** (2015) 055025 [`arXiv:1411.6043`] [INSPIRE].

[54] A. Flórez et al., *Searching for new heavy neutral gauge bosons using vector boson fusion processes at the LHC*, *Phys. Lett.* **B 767** (2017) 126 [`arXiv:1609.09765`] [INSPIRE].

PROCEEDINGS OF SCIENCE

Search for Supersymmetry with a compressed mass spectrum in vector boson fusion topology with 1-lepton and 0-lepton final states in pp collisions at $\sqrt{s}$ = 13 TeV with CMS

Priyanka Kumari[*][†] [a] , **Nitish Dhingra** [a,b], **JB Singh** [a], **Vipin Bhatnagar** [a]
On behalf of the CMS Collaboration
[a] *Panjab University (PU), Chandigarh, India*
[b] *G.H.G Khalsa College, Ludhiana, India*
E-mail: `priyanka.kumari@cern.ch`

Searching for Supersymmetry (Susy) is one of the major physics goals of the Large Hadron Collider. A large number of physics analyses are being performed in CMS (and ATLAS) experiments to detect signatures of Susy particles. The search presented here aims for observing Susy particles produced in the Vector Boson Fusion (VBF) topology, leading to a final state having zero or one lepton, large missing E_T, two jets with high p_T and large rapidity separation. The analysis is performed using 35.9 fb^{-1} of proton-proton collision data collected with the CMS detector during year 2016 at center-of-mass energy of 13 TeV. The background estimation is performed using data-driven/semi data-driven techniques, and the observed dijet invariant mass as well as lepton transverse mass spectra are found to be consistent with the Standard Model (SM) background predictions and no signal signature is observed. Hence, upper limits are set on the cross sections for chargino ($\tilde{\chi}_1^{\pm}$) and neutralino ($\tilde{\chi}_2^0$) production along with two associated jets, assuming the lightest scalar leptons to be lighter than $\tilde{\chi}_1^{\pm}$. For a compressed mass spectra in which the mass difference between the Lightest Supersymmetric Particle (LSP) $\tilde{\chi}_1^0$ and the mass-degenerate particles $\tilde{\chi}_1^{\pm}$ and $\tilde{\chi}_2^0$ is 30 (1) GeV, the most stringent mass upper limit to date is set for the latter two particles.

XXIX International Symposium on Lepton Photon Interactions at High Energies - LeptonPhoton2019
August 5-10, 2019
Toronto, Canada

---

[*] Speaker.

[†] I am sincerely thankful to CMS Collaboration at LHC experiment, my VBF-SUSY colleagues for the outstanding results presented in this conference, to the LP2019 organizers for a great conference and last but not the least, to the Department of Science and Technology, India for providing me financial support to participate in this major conference in the field of High Energy Physics.

1. Introduction

The discovery of the Higgs Boson is considered as the biggest success for the SM as well as for the CMS and ATLAS experiments. Nevertheless, SM still fails to explain a few unsolved problems like unification of forces, hierarchy problem, neutrino oscillations, matter-antimatter asymmetry, nature of dark matter and energy. Supersymmetry (Susy) [1] is considered to be one of the best extensions of the SM that can explain simultaneously the particle nature of dark matter (DM) and solves the gauge hierarchy problem of the SM. Susy associates every SM fermion with its "super-partner" boson and vice-versa which differs by half-integral spin. Despite having attractive features, Susy has no direct evidence of its existence to date. Susy searches at LHC are mostly focused on the colored sector because of its large cross-section, however strongly produced gluinos ($\tilde{g}$), as well as the squarks ($\tilde{q}$) of the first and second generations, have been excluded up to ~ 2 TeV in certain scenarios. On the other hand, the limits are weaker on the masses of weakly produced charginos ($\widetilde{\chi}^{\pm}_{\mathrm{i}}$) and neutralinos ($\widetilde{\chi}^{0}_{\mathrm{i}}$). The lightest neutralino $\tilde{\chi}^0_1$ (LSP) is the canonical DM candidate in R-parity conserving Susy extensions of the SM. CMS and ATLAS have performed various Susy searches covering most of the parameter space. This paper focuses on the result based on the search for the electroweak production of Susy particles in the Vector Boson fusion (VBF) topology using 2016 proton-proton collision data collected with the CMS detector and corresponding to an integrated luminosity of 35.9 fb^{-1} at a center-of-mass energy $\sqrt{s}$ of 13 TeV.

2. Analysis strategy and background estimation

The charginos and neutralinos are produced in association with two forward jets, in opposite hemispheres of the detector, having large dijet invariant mass and large pseudorapidity. These pair-produced charginos and neutralinos decay to sleptons ($\tilde{l}$) which further decay to the leptons ($\tau_h/e/\mu$) and lightest neutralinos ($\tilde{\chi}^0_1$) which is LSP. The Susy search with 2016 data at $\sqrt{s}$ = 13 TeV has been performed in 4 final states namely: $0ljj$, ejj, μjj, and $\tau_h jj$ (hadronically decaying tau). For the *Central Selections*, events are selected using a trigger based on MET and MHT (magnitude of negative vectorial sum of transverse momentum of all jets) and having a threshold of 120 GeV on both $p^{miss}_{T,trig}$ and $H^{miss}_{T,trig}$. The compressed mass spectra scenario results in low-p_T visible decay products, making it difficult to reconstruct and identify multiple leptons. Hence, events are required to have zero or exactly one well identified soft lepton. In the $\tau_h jj$ channel, an additional lepton veto is applied by rejecting events containing a second tau ($p_T > 20$ GeV), an electron ($p_T > 10$ GeV), or a muon candidate ($p_T > 8$ GeV). Similarly, in ejj and μjj channels, events are required not to contain another electron, muon, or τ_h candidate. For the $0ljj$ channel, a well-identified e, μ or τ_h candidate is rejected. Muon, electron, and τ_h candidates must have $8 < p_T < 40$ GeV, $10 < p_T < 40$ GeV, and $20 < p_T < 40$ GeV and "tight", "medium" and "tight" ID respectively with $|\eta| < 2.1$. The events are required to have $E^{miss}_T > 250$ GeV to suppress the DY$\to$ ll and QCD multijet backgrounds and no b-jets condition to reduce the $t\bar{t}$ background. A cut on $m_T(l, E^{miss}_T) > 110$ GeV, i.e. beyond the jacobian m_W peak (jacobian peak at $p_T = m_w/2$) to reduce the backgrounds coming from W boson. The *VBF selections* require the presence of two VBF jets with $p_T > 60$ GeV and $|\eta| < 5.0$ in opposite hemispheres $(\eta_1 \cdot \eta_2 > 0)$, large pseudorapidity gap $|\Delta\eta| > 3.8$ and separated from the leptons by $\Delta R > 0.4$. The VBF dijet candidate with the largest dijet mass is chosen and is required to have $m_{jj} > 1$ TeV. The signal region (SR) is defined as the events that satisfy the central and VBF selection criteria. Main backgrounds such as QCD multijet (major for τ_h), $t\bar{t}$ (large for e and μ) and W+jets are estimated by defining control regions (CR) which are orthogonal to signal region selection. CRs are defined in such a way that they don't bias our m$_T$ (m$_{jj}$) distribution in the signal region for 1-lepton (0-lepton).

3. Results and conclusion

Figure 1 shows the predicted SM background, expected signal, and observed data rates in bins of m_T for $\tau_h + jj + E_T^{miss}$ final state [2]. The bin sizes in the distributions are chosen to maximize the signal significance of the analysis. No excess of events above the SM prediction in any of the search regions is observed and hence no new physics. For the R-parity conserving MSSM models, results are presented in two scenarios: (i) the "light slepton" model where $\widetilde{\ell}$ is the next-to-lightest Susy particle; and (ii) the "WZ" model where sleptons are too heavy and thus $\widetilde{\chi}_1^{\pm}$ and $\widetilde{\chi}_2^0$ decays proceed via W^* and Z^*. The main difference between the two models is the branching ratio of $\widetilde{\chi}_1^{\pm}$ and $\widetilde{\chi}_2^0$ to leptonic final states. Middel plot in Figure $\mathring{\text{l}}$imit1shows that for a compressed mass spectrum scenario, in which $\Delta m = m(\tilde{\chi}_1^{\pm}) - m(\tilde{\chi}_1^0) = 1$ (30) GeV and in which $\tilde{\chi}_1^{\pm}$ and $\tilde{\chi}_2^0$ branching fractions to light sleptons are 100%, $\tilde{\chi}_1^{\pm}$ and $\tilde{\chi}_2^0$ masses up to 112 (215) GeV are excluded at 95% CL. Bottom plot shows that for the scenario where the sleptons are too heavy and decays of the charginos and neutralinos proceed via W^* and Z^* bosons, $\tilde{\chi}_1^{\pm}$ and $\tilde{\chi}_2^0$ masses up to 112 (175) GeV are excluded at 95% CL for $\Delta m = m(\tilde{\chi}_1^{\pm}) - m(\tilde{\chi}_1^0) = 1$ (30) GeV.

References

[1] Ramond P., "Dual Theory for Free Fermions", *Phys. Rev. D*, vol. 3, (1971), https://dx.doi.org/10.1103/PhysRevD.3.2415.

[2] The CMS Collaboration, "Search for supersymmetry with a compressed mass spectrum in the vector boson fusion topology with 1-lepton and 0-lepton final states in proton-proton collisions at $\sqrt{s}$ = 13 TeV", *JHEP*, vol. 8 (2019), https://doi.org/10.1007/JHEP08(2019)150.

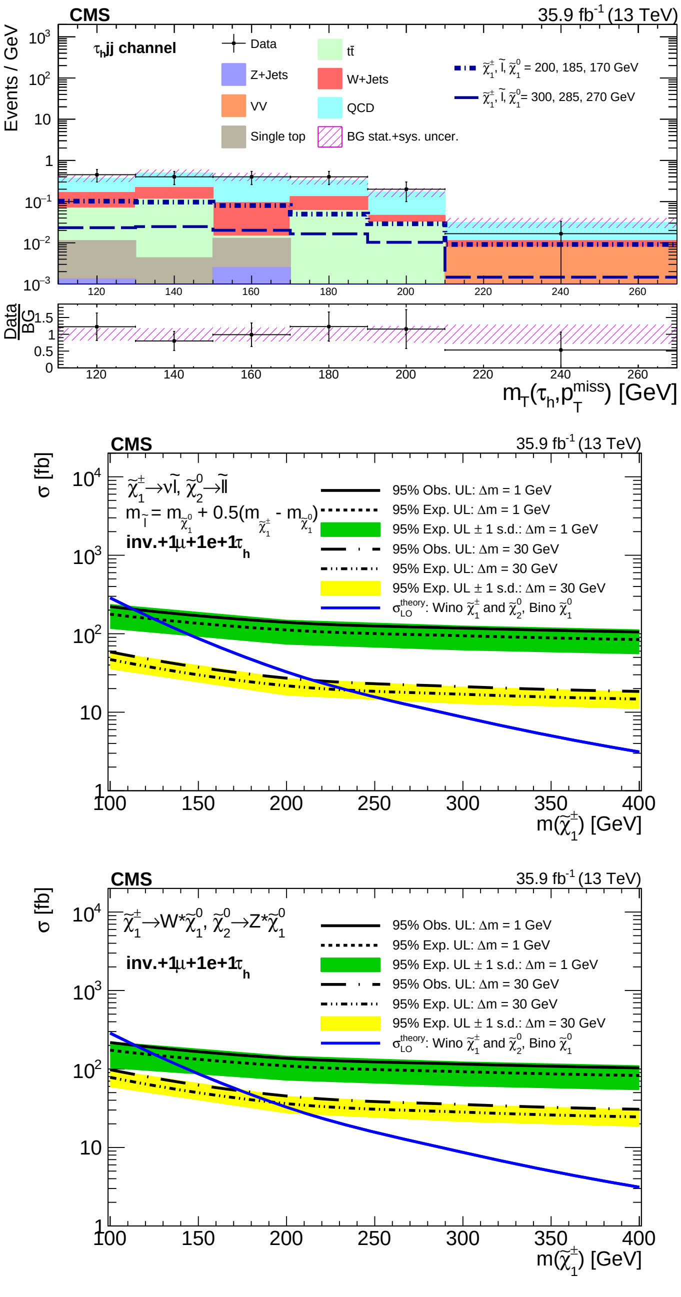

Figure 1: Top plot shows the m_T distribution for $\tau_h + jj + E_T^{miss}$, middle and bottom shows the limit plots for slepton and WZ model respectively.

LP2019

CERTIFICATE OF PARTICIPATION

This is to certify that

Priyanka Kumari

has presented the poster entitled

“*Search for Supersymmetry with a compressed mass spectrum in vector boson fusion topology with 1-lepton and 0-lepton final states in pp collisions at √s = 13 TeV with CMS***”**

at the **Lepton Photon 2019** conference
held at the Westin Harbour Castle from August 5 to 10, 2019
in Toronto, Ontario, Canada.

W Trischuk

William Trischuk, Co-Chair

Hirohisa Tanaka

Hirohisa Tanaka, Co-Chair

Lepton Photon 2019
Conference Secretariat c/o Venue West Conference Services
#301-1040 Hamilton Street - Vancouver, BC - V6B 2R9 - Canada
www.leptonphoton2019.ca | email: lp2019@venuewest.com

Certificate of Participation

This is to certify that

Ms. Priyanka Kumari

Panjab University Chandigarh

has successfully participated in the

XXII DAE-BRNS HIGH ENERGY PHYSICS SYMPOSIUM
(December 12-16, 2016)

held at the

Department of physics and Astrophysics,
University of Delhi, Delhi, India

and presented a talk on
Search for Supersymmetry with the Vector Boson Fusion tagging in pp collisions using CMS detector at the LHC

Dr. Md. Naimuddin
Convener

Kirti Ranjan
Dr. Kirti Ranjan
Jt. Convener